Caracterización de superficies funcionales modelo con control de estructura atómica y composición: capas orgánicas y superficies de óxidos

Luis E. Garzón Muñoz

Tesis presentada al Departamento de Física
de la Universitat Autònoma de Barcelona
para optar al grado de Doctor en Ciencias Físicas

Institut de Ciència de Materials de Barcelona
Consejo Superior de Investigaciones Científicas
Supervisor: Prof. Carmen Ocal

Tutor: Prof. Javier Rodriguez Viejo
Departamento de Física
Universitat Autònoma de Barcelona

2013

Universitat Autònoma de Barcelona

Characterization of model functional surfaces with
control of atomic structure and composition:
organic layers and oxide surfaces

Programa de Doctorado:
Ciència de Materials

Facultad de Ciencias
Departamento de Física

Luis E. Garzón Muñoz
2013

ABSTRACT

The discovery of new and novel materials, process and phenomena at the nanoscale, as well as the new experimental and theoretical methods provide opportunities for the development of innovative nanosystems. Nature shows how builds macroscopic objects from small molecular building blocks with defined shapes, properties, high order and degree of structural control in atomic scale materials. Under this evidence, nowadays is possible to assemble any kind of device or functional system, ranging from functional surfaces materials. This attractive concept is presented to profit from the order of the arrangement of molecules or inorganic surfaces in well-ordered patterns to interlink the molecular or building block to other macro-systems in a bottom-up strategy.

The present work lies within the scope of the mechanical and electrical characterization of functional surfaces, organics and inorganics, at the nanoscale by using the Scanning Force Microscopy (SFM) with their modes Friction Force Microscopy (FFM), Conductive Scanning Force Microscopy (C-SFM) and Kelvin Probe Force Microcopy (KPFM) which comprises of 7 chapters. Chapter 2 introduces the fundamental description about the technique, instrumentation and components for the data acquisition. A description of the main operation modes and the forces that can be measured is presented. The first experimental part of this work describes the sample preparation, protocols and strategies to obtain layers or multilayers of a π-conjugated organic aromatic thiol anchored on a gold surface.

Chapter 3 describes the morphological characterization of Self Assembled Monolayers of the aromatic thiol mercapto-methyl terphenyl carboxylic acid (MMTA) for solutions using different solvents, concentrations and their influence on the molecular packing. We show how to control the self-assembly and the formation of 3D structures from the aromatic thiol adsorbed on Au(111) and patterned gold surfaces by means of microcontact-printing (μCP). Moreover, we present how to control the size of the 3D structures by using a thermal treatment.

The chapter 4 describes the tribological studies mainly on low and tall islands obtained by using different solvents after annealing. Chapter 5 shows the electronic transport measurements carried out on the MMTA molecular films obtained with or without annealing. Complementary studies of KPFM (Kelvin Probe Force Microscopy) were mainly performed at low relative humidity over these surfaces.

Chapter 6 is devoted to study the inorganic surface of complex oxides type perovskite, case STO(001), as a functional surface model by exploding the presence of both TiO_2 and SrO chemical terminations. It is known that both terminations are presents in a random distribution in as-received surfaces, however under annealing chemical segregation can appear. We show that $SrTiO_3$ surfaces can be used as a versatile template for growing ordered organic and inorganic nanostructures.

Finally in chapter 7 we will present the characterization of the MMTA films after annealing by means of the PM-IRRAS technique. A first attempt of selective growth with dinuclear copper(II) acetate complexes ($Cu_2(CH_3COO)_4 \bullet 2H_2O$) on the MMTA islands is studied by SFM. This chapter gives an outlook for the future implication of the selective growth on differentiate chemical terminations.

This thesis have been typeset using a LaTeX typesetting system.

RESUMEN

El descubrimiento de nuevos y novedosos materiales, procesos y fenómenos a escala manométrica, así como los nuevos métodos experimentales y teóricos proveen oportunidades para el desarrollo de sistemas innovadores a esa escala. La naturaleza muestra como construye objetos macroscópicos desde unidades básicas con formas definidas, propiedades, orden y control estructural en materiales. Este concepto es utilizado para la construcción de macro-sistemas, orgánicos e inorgánicos, desde una estrategia "bottom-up".

El trabajo de la tesis se ha centrado en el estudio experimental de sistemas modelo muy diferenciados (uno orgánico y otro inorgánico): i) películas autoorganizadas (self-assembled monolayers, SAMs) de organosulfuros sobre Au(111), en concreto ($C_{20}H_{16}O_2S$, mercaptomethyl therphenyl carboxylic acid, MMTA) y ii) substratos óxidos tipo perovskita, en concreto $SrTiO_3$ (STO). La técnica que se ha utilizado es la microscopia de fuerzas de barrido (Scanning Force Microscopy, SFM) tambien llamado microscopio de fuerzas atómicas (Atomic Force Microscopy, AFM) con el fin de obtener información sobre las propiedades estructurales, mecánicas y electrónicas (transporte y electrostáticas) de estas superficies y establecer correlaciones entre las propiedades y la funcionalidad. El presente trabajo consta de 7 capítulos, los primeros 5 capítulos describen la completa caracterizacion del sistema pi-conjugado MMTA. Una introducción a la técnica SFM en sus diversos modos de uso, preparacion de substratos, soluciones y procesos termicos involucrados para observar posibles cambios morfólogicos son abordados en el capítulo 2.

El capítulos 3 de la tesis describe el trabajo realizado desde la preparación de las capas hasta su caracterización. Para poder estudiar la influencia de los solventes en la estructura y propiedades de las superficies, se ha utilizano toda una serie de protocolos en los que se han variado todos los parámetros involucrados en la preparación: solventes (etanol (EtOH, 99.8%), ácido acético (AA, 99%), tetrahydrofuran (THF) y ácido trifluroacético (TFA, 99%)), concentraciones (de 1 µM hasta 1 mM) y tratamientos térmicos (25°C y 120°C y post-annealing). También se incluye en la tesis la funcionalización confinada lateralmente de superficies de oro con MMTA utilizando la técnica de *microcontact printing* (µ-CP) con sellos de Poly(dimethylsiloxane) PDMS impregnados en la concentración óptima de la solución molecular. Un arduo trabajo de pruebas han llevado a concluir la metodología adecuada para obtener películas de una o dos alturas, cuya terminación consecuentemente es diferente (COOH o SH) proporcionando diferente respuesta tanto en propiedades tribológicas (fricción) como en propiedades electrónicas (corriente y potencial de superficie), cuyos resultados son presentados en los capítulos 4 y 5. Algunas de las novedades más resaltables implican la

diferenciación y establecimiento de la transición ente mecanismos de transporte (e.g. túnel coherente a bajos voltajes y Fowler-Nordheim a mayores campos) a través de las películas y en función del espesor de la película y de la fuerza aplicada*.*

El capítulo 6 esta dedicado al segundo sistema modelo, el óxido tipo perovskita STO, es el substrato por excelencia para el crecimiento de óxidos complejos. La estructura cristalina de estos óxidos, con fórmula general ABO_3 contiene planos alternados de composiciones atómicas AO (A=Sr) y BO_2 (B=Ti) de tal manera que las superficies (001) pueden tener esas dos posibles terminaciones químicas. Durante la tesis se ha puesto en evidencia que la terminación de la superficie (dependiente del modo de obtención) es determinante, por ejemplo, en la secuencia de empaquetamiento de películas depositadas o en la reactividad de la propia superficie. Como principal conclusión que obtener superficies SrO(001) y TiO_2(001) bien caracterizadas es de gran importancia. En coordinación con el grupo del Prof. Fontcuberta se ha demostrado que, variando las condiciones de tratamientos térmicos (temperatura y tiempo de calentamiento) a que se someten los cristales, se puede controlar la coexistencia y separación espacial de las dos terminaciones en la misma superficie, obteniendo patrones químicos a escala nanométrica. Y, en particular ha permitido el crecimiento selectivo tanto de películas delgadas de óxidos funcionales como para la obtención de materiales híbridos orgánico/inorgánico mediante la adsorción selectiva de monocapas orgánicas autoensambladas. Por último, la técnica PM-IRRAS fue empleada para la caracterización de la película molecular MMTA obtenida con tratamiento térmico y líneas abiertas de trabajo de investigación para futuros estudios de crecimiento selectivo usando metal-orgánicos (dinuclear copper (II) acetate complexes ($Cu_2(CH_3COO)_4$ 2H2O)) son expuestos en el capítulo 7.

El trabajo presentado en esta tesis doctoral evidencia que la estrategia combinada de diferentes modos de microscopía de fuerzas de barrido (Scanning Force Microscopy, SFM) en condiciones de ambiente controladas es la adecuada para, tanto para SAMs como substratos de STO, determinar las características superficiales a nivel de estructura molecular y morfología con gran precisión y obtener, simultáneamente, la información a escala nanométrica de las propiedades tribológicas (estabilidad mecánica, fricción) y electrónicas (transporte, potencial de superficie) de las superficies modelo bajo estudio. De tal modo, como novedad a destacar en conjunto, se ha establecido la correlación entre las características estructurales y las propiedades de las superficies en el marco del transporte electrónico (C-SFM) para diferentes morfologías dependiendo del método de obtención, y de cómo la terminación superficial modifica los potenciales de contacto superficiales de los substratos de partida (Au en el caso de SAMs y el "as-received" STO), mediante Kelvin Probe Force Microscopy (KPFM).

ACKNOWLEDGMENTS

ACRONYMS LIST

SPM	Scanning Probe Microscopy
SFM	Scanning Force Microscopy
C-SFM	Conductive Scanning Force Microscopy
KPFM	Kelvin Probe Force Microscopy
EFM	Electrostatic Force Microscopy
AM-AFM	Amplitude Modulation-Atomic Force Microscopy
DSP	Digital Signal Processor
2D	Bidimensional
2D-FFT	2D-Fast Fourier Transformed
3D	Three-dimensional
SAMs	Self-Assembled Monolayers
MMTA	Mercapto Methyl Terphenyl Carboxylic Acid
PDMS	Polydimethylsiloxane
μCP	Microcontact Printing
DMT	Derjaguin Muller Toporov Model
IRRAS	Infrared Reflection Absorption Spectroscopy
PM-IRRAS	Polarization Modulation-IRRAS
IR	Infrared Spectroscopy
GIXRD	Grazing Incident X-ray Diffraction
LEED	Low Energy Electron Diffraction
NEXAFS	Near Edge X-Ray Absorption Fine Structure
RAIRS	Reflection Absorption Infrared Spectroscopy
NN	Nearest Neighbor
NNN	Next-Nearest Neighbor
THF	Tetrahydrofuran
STO	$SrTiO_3$ (Strontium Titanate)
BTO	$BaTiO_3$ (Barium Titanate)

"Happiness is not doing what you want, but wanting what you do."

– Jean-Paul Sartre

CONTENTS

CHAPTERS

LIST OF FIGURES

LIST OF TABLES

CHAPTER 1

INTRODUCTION

During the last two decades, self-assembled monolayers (SAMs) of organics molecules on metal surfaces (gold, cooper, silver) have been extensively studied due to their technological promise in areas that involve surface modification and patterning for a number of applications such as chemical sensors, control of charge transfer, organic-based electronic functionality. In the past the majority of related studies have been carried out for thiol-based SAMs with aliphatic backbones which can be prepared on gold surfaces by immersion or evaporation. However, recently aromatic SAMs have become the focus of interest due to their extended π-system and potential applications directly related to molecular electronics [1, 2, 3, 4, 5], (i.e. molecular switching, molecular conductivity or molecular transistors) where in some cases, the structural quality of the oligophenyl thiols SAMs is superior to those of alkanethiolates.

1.1 State of the Art of functional surfaces

In contrast to alkanethiol-based SAMs, whose most structure is found to be independent of the chain length, the ordering mechanism and structure of aromatic SAMs is more complex. Such complexity has been shown in SAMs formed out of biphenyl derivatives BPn $(CH_3(C_6H_4)_2(CH_2)_nSH$, as changing the parameter n from odd to even leads to strong changes in the molecular film structure [6, 7, 8]. Since aromatic SAMs structure is determined for complex factors (i.e. molecule substrate-bonding, molecular interactions, immersion times or solvents used) preparation of high quality molecular films requires precise knowledge of these factors.

Nowadays, there is a pronounced interest in the preparation of structurally well-defined organic surfaces with different functional groups. The chemical composition of the surface formed on the substrate is controlled by the termination of the organothiols,

in case of the alkanethiols the -CH$_3$ termination or -COOH (acid terminated alkanethiol, MHDA). In the present work, as a first part we show the characterization results obtained by using the aromatic thiol $4'' - (mercaptomethyl) - [1, 1' : 4', 1'' - terphenyl]$-4-carboxylic acid or MMTA on gold substrates. The MMTA is an aromatic thiol with an alkyl chain between the thiol group and the three aromatic rings and functionalized with a carboxylic acid group. One of the most interesting functions is the carboxylic group, since -COOH-terminated surfaces are of interest in surface science, biology, sensor development or electrochemistry. Early works carried out by Patel et al. [9] have shown the immmobilization of the protein catalasa onto carboxylate-terminated SAMs made from 3-mercaptopropanoic acid (3-MPA), 11-mercaptoundecanoic acid (11-MUA), and a mixture of both acid thiols utilizing water-soluble carbodiimide and N-hydroxysuccinimidde (NHS). The immobilization of catalasa involves the formation of an NHS ester with the carboxylate-terminated SAMs, where the side-chain amino groups of lysine residues on the protein surface displace the terminal NHS groups, resulting in covalent immobilization of the protein.

Moreover, several studies to immobilize metallic complex (dinuclear copper II acetate complexes) on SAMs by means of different types of interactions (covalent bonding, specific adsorption or nonspecific adsorption) in both alkane and aromatic thiols have been reported [10]. For non-specific adsorption case on thiols SAMs surfaces involves electrostatic and hydrophobic interactions, whereas the covalent bonding is attractive due to their high stability and binding strength. The specific interaction refers to a characteristic that is unique to a couple of binding partners (selective growth process). Metallization of aromatic thiol-coverage surfaces, in particular dithiol SAMs, offer the possibility that the free -SH groups bind chemically to the deposited metal atoms and thus prevent their diffusion through the SAM as showed Rajalingam et al. [11].

Lastly, and as second part of this work, we present the characterization of functional surfaces of a perovskite oxide, in particular the SrTiO$_3$ substrate widely used in the growth of complex oxides and possible candidate to grow molecular organics [12].

The quality of thin films is strongly dependent of the quality of the substrate on which they are deposited. Smooth substrate surfaces atomically flat plane are essential for perfecting the epitaxial growth of transition metal oxide films. By using

the epitaxial growth of films with perovskite structure, single crystal substrates must follow specifications by which the lattice constant, thermal expansion coefficients of the substrates should closely match those of the growing films. Moreover, the substrate should not have phase transitions.

The role of the chemical surface termination of $SrTiO_3$ has been investigated down to the atomistic level and, because titanium dioxide (TiO_2) terminated surfaces are preferred in a wide range of applications, obtaining nanostructured surfaces having tailored TiO_2 termination is of enormous interest for further developments. The cubic perovskite $SrTiO_3$ viewed in the $\langle 001 \rangle$ directions is made up from a stack of alternating neutral TiO_2 and SrO layers. It is known that both terminations are randomly distributed on the as-received substrates surface, and the SrO surface segregation can appear under annealing at high temperature and oxidizing conditions. Bachelet et al. [13, 14] have shown that by means of appropriate thermal treatments, the SrO termination self-organize, forming, along the substrate step-edges, a well-ordered array of half-unit-cell-deep trenches coexisting with atomically flat TiO_2 terraces in between. As a real example of a selective growth, using such nanopatterned surfaces they have fabricated ordered arrays of conducting epitaxial $SrRuO_3$ nanostripes separated by insulating trenches.

1.2   Motivation and Objetives

Based on the observation of Gordon Moore in 1965 about the technological limitations to arise the miniaturization of electronic components following a top-down strategy and since the size of semiconductor based electronic circuits shrinks it has been suggested to build up electronic devices with a bottom-up approach by using single or small molecular ensembles by which detailed knowledge of the fundamental growth process is desirable. In this sense, the study of new nanostructured materials as thiol based SAMs on the very well-known metallic substrates such as (gold, silver, cooper) as well as other organic molecules on oxides, in particular, $SrTiO_3$ have been major motivations.

Our main objective is to establish the correlations between structural characteristics and properties of the surfaces. The influence of these correlations will be analyzed by

investigating the electronic transport (Conductive-Scanning Force Microscopy) through thin films (organic or inorganic) for different morphologies depending on the method of production, and how these films modifying the surface contact potentials of the starting substrates by using the Kelvin Probe Force Microscopy (KPFM). To this end, two sets of very different model systems (one organic and another inorganic) will be studied: i) self-organized films (self-assembled monolayers, SAMs) of organosulfur compounds on Au (111) and ii) perovskite oxide substrates, namely $SrTiO_3$ (STO).

CHAPTER 2

EXPERIMENTAL TECHNIQUES

2.1 Introduction

Scanning probe methods have become successful tools in surface science due to their ability to characterize metallic, semiconductors or insulator surfaces in real space at the atomic scale. Surface relief, electronic and vibrational properties, measurements of adhesion, friction, studies of lubrication, dielectric and magnetic properties, molecular manipulation are outlines under Scanning Probe Microscopy (SPM) studies. Within the family of SPM a variety of methods to characterize the surface properties have been performed to date. The Scanning Tunneling Microscope is based on the control of tunneling current and/ or the voltage parameters by obtaining image formation; however, one of their limitations is the requirement of conductive samples. This limitation was overcome in 1986 when Gerg Binning, Calvin Quate and Christoph Gerber proposed a new type of microscope, the AFM, in which instead of measuring tunneling currents between a probe tip and sample, any type of forces between a sharp tip and conductor and insulator samples at the atomic scale were measured [15]. Afterwards, the idea derived in other scanning probes microscopes such as the friction force microscope (FFM), magnetic force microscope (MFM) and the electrostatic force microscope (EFM).

2.2 Background of Scanning Force Microscopy (SFM)

Atomic Force Microscopy (AFM), or known also as Scanning Force Microscopy (SFM), was invented by Binnig and co-workers in 1986 [15, 16]. The physical quantity that is measured is the force experimented between a sharp conical tip, with a terminal radius often less than 10nm and located at the free end of a long cantilever, and a sample surface. In a force measurements the sample is moved up and down by applying a voltage to the piezoelectric ceramic, onto which the sample is mounted. Experimented

forces of only few pN cause vertical deflections of the cantilever being detected by using an optical system such as the laser-PSD(position-sensitive detector). The measured cantilever deflections enable the computer to generate a map of the surface topography.

2.2.1   Description of the SFM System

The results presented in this work have been obtained by using two different microscope systems. The first one is a home-made SFM following the design suggested by Kolbe et al. [17] with an SPM100 electronic control unit fabricated in the UAM (Segainvex Workshop), and the second one is a complete commercial SPM from Nanotec [18]. Both equipments follow the common characteristics to most commercial SFMs.

2.2.1.1   The Force Sensor

A small tip, which is mounted at the end of a small sensor lever or cantilever form the heart of the SFM because it is brought in closest contact with the surface allowing detecting of vertical deflection with picometer resolution. Commercial tip-lever assemblies are fabricated from silicon (Si) or silicon nitride (Si_3N_4) and typical dimensional values of cantilever are length L (100-300)μm, width w (10-40)μm, thickness t (0.3-8)μm, tip height(3-15)μm and tip radius R (4-200)nm; by this way, a wide range of spring constants are obtained. There are two main designs for cantilevers, the "V" shaped and the single-arm kind. By developing this work, V-shaped and rectangular cantilevers with nominal force constants between $k = 0.01 \, N \cdot m^{-1}$ and $k = 0.5 \, N \cdot m^{-1}$ were mainly employed for the structural and frictional characterization of Self Assambled Monolayers (SAMs) of MMTA on gold, whereas the electrical measurements have been performed with rectangular conductive diamond or Cr-Pt coated cantilevers of nominal force constant of $k = 0.2 \, N \cdot m^{-1}$ for contact mode [19, 20] and $k = 2.8 \, N \cdot m^{-1}$ for dynamic mode [19]. Rectangular conductive diamond coated cantilevers with nominal force constants $k = 48 \, N \cdot m^{-1}$ and Cr-Pt coated cantilever $k = 40 \, N \cdot m^{-1}$ have been used to characterize $SrTiO_3$ and complex oxides thin films of perovskite type. Figure 2.1 shows two cantilever geometries used mainly for contact and non-contact mode from commercial SPM probes: (a) rectangular and triangular probes on a silicon chip [21] (b) SEM image of a silicon tip and (c) cantilever coated (i.e. Ag, Al, Cr, Ir, Pt, Ti, W) on detector side as well as the tip[19]. (d) shows the geometry of a V-shaped

and uniform rectangular cantilever, where the cantilever length, width and thickness, and the tip height are denoted by L, w, t, and h, respectively. The working principle is
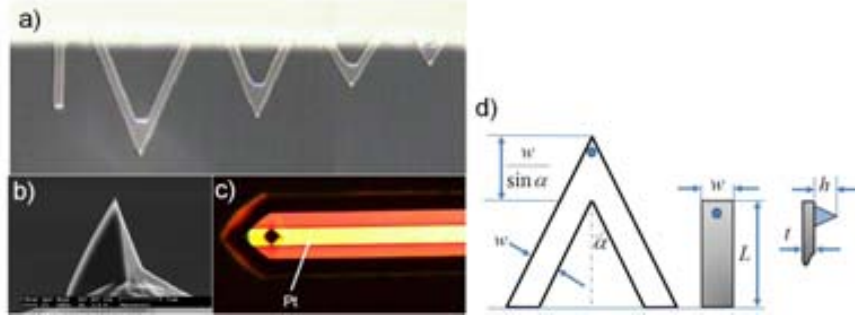
Figure 2.1. Cantilever geometries used from commercial SPM probes. (a) Rectangular and V-shaped Si_3N_4 probes from Veeco Instruments, now Bruker[21]. Silicon tip (b) and cantilever Pt-coated (c) from Nanosensors[19] are shown. (d) Geometry of a V-shaped and a beam cantilever are described: L is the parameter describing the cantilever length, the height of the tip is h and the thickness is t for a width w that corresponds, in the case of the triangular cantilever, to the width of one of its arms.

similar for both geometries, normal forces acting on the tip and perpendicular to the lever plane produce a vertical deflection while lateral forces perpendicular to the long axis cause the torsion of the cantilever. By correlating the corresponding displacements (Δz and Δx) and the forces, the cantilever response is approximated by a spring in each direction by means of the Hook´s law, so

$$F_n = k_Z \cdot \Delta z \tag{2.1}$$

$$F_L = k^T \cdot \Delta x \tag{2.2}$$

The determination of k_Z and k^T is fundamental to obtain quantitative information of the SFM measurements. In this work, information supplied by the manufacturer have been used for the vertical deflection k_Z to obtain the value of the normal force applied.

Alternatively, the resonance frequency of the cantilever was always measured to verify that the nominal value was statistically representative[1].

Although manufactures provide data sheet for the different probes employed, some times these values are at least up to a factor of two compared to their true value. Theoretical studies have been proposed to determine the nominal values of k_Z and k^T for both rectangular and triangular cantilevers with its own advantages and disadvantages [22, 23, 24].

2.2.1.2 Optical Detection System

SFM can detect forces by measuring the vertical deflection or lateral torsion of the cantilever due to the repulsive or attractive forces during scanning. The conventional optical lever or beam-bounce method is employed on most commercial SFMs. In this frame, a laser beam is reflected from the reflective backside of the cantilever onto a position-sensitive photodetector consisting of two side-by side photodiodes. The vertical force is measured by monitoring the difference between top and bottom sectors, and the lateral forces are measured by monitoring the difference between left and right sectors; both topography and frictional image may be measured simultaneously.

A small deflection or torsion of the cantilever will deviate the reflected beam and changing its position on the photodetector. The difference between the signals from the photodetector indicates the position of the laser spot and thus the angular deflection or torsion, this last referred as lateral force (see Figure 2.2).

2.2.1.3 The Scanning System

The piezo scanner generally consist of lead-zirconate-titanate (PZT) ceramic materials placed between two metal electrodes. When a voltage difference is applied between the electrodes, the piezoelectric ceramic expands or contracts in a direction that is perpendicular to the applied electric field. The motion of the ceramic is controlled by the polarity and magnitude of the applied voltage. The piezo scanner of our SFM was designed with a concentric tubular form with an electrode on the inner surface and four

---

[1]Equation relating the resonance frequency of an object with its force constant k and effective mass m: $f_{res} = \frac{1}{2\pi}\sqrt{\frac{k}{m}}$
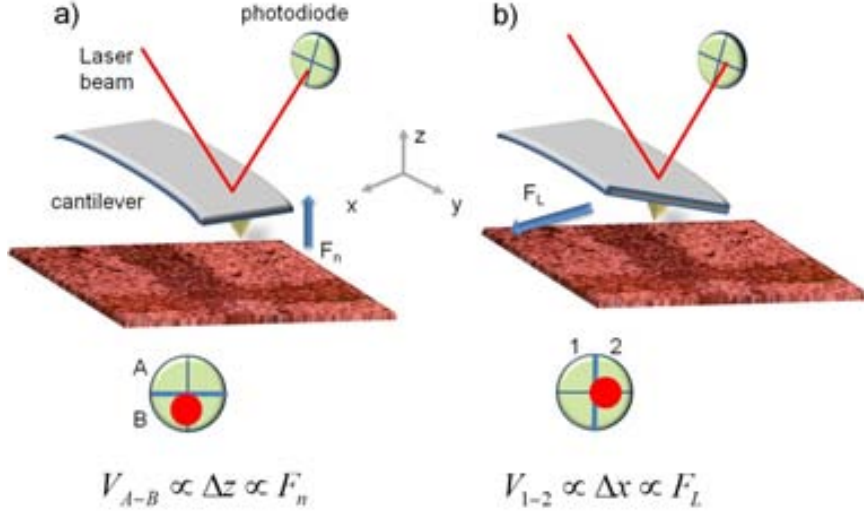
Figure 2.2. Schematic of the optical detection system used to measure the cantilever deflection produced by normal (a) and lateral forces (b).

equally spaced electrodes on the outer surface. Biasing the inner electrode controls the vertical movement($\pm z$), this displacement can be referred as Δz. Biasing two opposite outer electrodes moves the tube in the $\pm x$ and $\pm y$ directions. Δx and Δy provide the scan area (Δx, Δy) on the surface plane of a SPM image. We have employed different scanners whose nm/V ratios vary between 10-30nm/V for the vertical displacement and 40-250nm/V for the lateral movement which allows measuring a wide variety of scan ranges from 10μm to 70μm and of 2μm to 12μm, respectively. Although the scanners are calibrated by manufactures, they must be in-situ verified and calibrated again periodically.

Figure 2.3 (a) shows a SFM 3D image of the grating employed to calibrate the piezo scanner. A nominal steps height of 18.5$\pm$1nm and periodicity of 3$\pm$0.05μm are provided by the manufacturer [25]. For small scan areas, the surface of the Au(111) has been used to calibrate the vertical displacement due to their monoatomic height step is known (0.235nm) (b), whereas the lateral-resolved image (c) of the hexagonal periodicity (0.289nm) is used to calibrate the lateral movement.
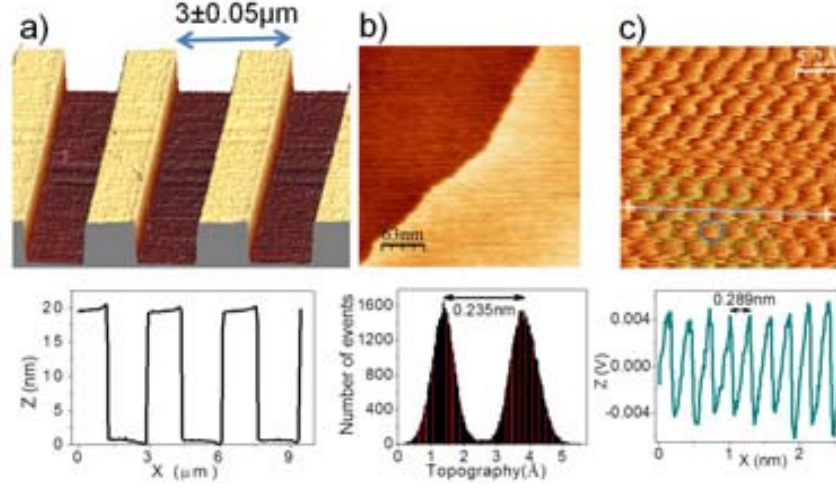
Figure 2.3. (a)3D SFM image of the commercial gratings used to calibrate the piezo scanner. Topographic (b) and lattice resolved(c) images of the Au(111) surface.

2.2.1.4   The Electronic Control Unit

A high voltage unit connected to a digital signal processor (DSP) inside a PC complete our SFM equipment. The DSP board is mainly in charge of collecting the signals coming from the photodiode and controlling the displacement of the piezo scanner. Due to the limited voltage range of the DSP ($\pm$3V) and the high voltage required by the piezo scanner (up to 300V) to work, the signal must be amplified and supplied to the microscope through a high voltage unit. The amplification gain is selected by the user depending on the vertical and lateral scales of the sample: lower gains imply smaller scanned area but increased resolution.

The DSP board is also in charge of the so-called feedback loop, a way to control the vertical distance between tip and sample by maintaining a selected magnitude fixed to a preset value during the scanning. Commonly, the normal deflection of the cantilever is used as feedback. By means of the feedback loop, this deflection and the preset setpoint value are continually compared at each point of the image. If they are not equal, a voltage is applied to the scanner in order to move the sample closer to or further from the probe, to maintain constant the normal load. This applied voltage signal is used for generating the SFM image. The control unit as well as the WSxM [26]

software employed for data acquisition and image processing are from Nanotec [18].

2.2.1.5   Vibration Isolation

As a system employed for studies at the atomic scale, vibration isolation is of crucial concern. To avoid typical mechanical vibrations coming from stepping on the floor or motion of the entire building itself (0.1 - 50)Hz and acoustic noise ($\approx$20Hz) or electronic noise ($\approx$60Hz) from electric circuits, those must be eliminated. To this end, a design is common for both SFM equipments. Each SFM is mounted on a rigid granite plate, which are supported by a table that acts as a low resonant frequency support. A hood covers each scanning force microscope head(tip, sample, detection system and piezo actuator) which provides an acoustic isolation and allows controlling the relative humidity of the working atmosphere, in addition of a metallic box to minimize electrical noise. An hygrometer TES-1364/1365 Datalogging Humidity Temperature meter was employed to measure the relative humidity and temperature inside and outside of the hood with an accuracy of $\pm$3% RH(in the 2%-98% range) and $\pm$0.8°C (in the -20°C to 60°C range).

2.2.2   Forces that we can Measure

In SFM, several forces such as van der Waals forces, capillary forces, frictional forces, magnetic forces and electrostatic forces contribute to the deflection or torsion of the cantilever. As a first approximation, the forces contributing to the deflection of an SFM cantilever are the van der Waals forces and the interatomic repulsive forces, which can be derived from the Lennard-Jones Potential. In the contact regime, the cantilever is held less than a few angstroms from the sample surface, and the interatomic force between the cantilever and the sample is repulsive. In the non-contact regime, the cantilever is held on the order of tens to hundreds of angstroms from the sample surface, and the interatomic forces between the cantilever and the sample is attractive.

Under measurement conditions such as ultrahigh vacuum (UHV), in air or liquids the SFM is employed to obtain the so-called Force-Distance (Fz) measurements. This type of measurements allows to deduce the attractive forces between the probing tip and the explored surface. Figure 2.4 shows a force distance curve for a Si_3Ni_4 tip approaching to and retracting from a clean Au(111) surface (RH$\approx$5%). The curve shows

the deflection of the cantilever as a function of distance between the gold surface and the AFM-tip, which is driven by the piezo-scanner. This deflection is measured in a split photodetector by the laser light reflected from the back of the cantilever. At the piezo displacement labelled (1) the cantilever with the AFM-tip is far apart from the sample and the cantilever deflection is nearly zero. The tip remains free as long as the piezo-scanner approches the surface and when both tip and surface reaching the close proximity a jump-to contact occurs (2). At this point the gradient of the attracting force between tip and surface becomes higher than the spring constant of the cantilever. The piezo-scanner drive pushes the AFM-tip further on the hard gold surface until (3) where the motion of the piezo-scanner is reversed. On retraction, partial wetting of the tip by the explored surface generates a capillary bridge that extends far more than the initial position of the sample surface before loading. In this point, the tip snaps out (pull-off force) (4) of is continued until the tip comes free again (5). The force acting on the cantilever immediately before coming out of contact (pull-off force) is a measure for the adhesion force between AFM tip and the explored surfaces.
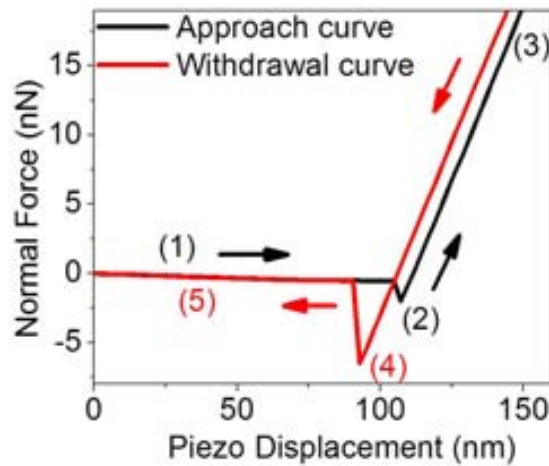
Figure 2.4. Force distance curve (Fz) obtained on a clean Au(111) surface at relative humidity (RH≈5%). Labelled points are illustrating the atracttive and repulsive regimes where the jump-to-contact (approach) and jump-off-contact (withdrawal) occur and the maximum value of the attractive force (pull-off force).

From the measured pull-off force the surface energy γ of the surfaces in contact can be calculated by applying the models developed for the adhesion of elastic spheres on flat surfaces by Johnson-Kendall-Roberts (JKR) or Derjaguin-Muller-Toporov (DMT) as follow:

$$F_{pull-off}(JKR) = -\frac{3}{2}\pi R \gamma \tag{2.3}$$

$$F_{pull-off}(DMT) = -2\pi R \gamma \tag{2.4}$$

Characteristics of the JKR theory include infinite tensile stress at the contact area perimeter, a non-zero contact area and a minimum stable normal load which still exhibits a non-zero contact area. When surface forces are short range compared to the resulting elastic deformations (i.e. compliant materials, large sphere radii, and strong, short-range adhesion forces), the JKR model describes the contact area accurately. JKR model neglects long range forces outside the contact area and considers only short range forces inside the contact region. In the DMT model, the elastic sphere is deformed according to Hertz theory, but in addition to the external load, the forces acting between the two bodies outside the contact region are taken into account. If an external load is applied, the area of contact is increased and if a negative load is applied, the contact area goes to zero at the pull-off force. DMT model is applicable for systems with low adhesion and samll tip radii.

2.2.2.1   van der Waals Force

The van der Waals force between atoms and/or molecules is the contribution of three different forces [27], i.e. the Keesom Force, the Induction or Debye Force and the dispersion or London force, all being proportionals to r^{-n}, r the distance between molecules or atoms and $n=6$. Keesom force is the angle-average dipole-dipole interaction between two atoms or molecules and its potential described as,

$$w_K(r) = -\frac{1}{r^6}\frac{\mu_1^2\mu_2^2}{3k_BT\left(4\pi\epsilon_0\epsilon\right)^2} \tag{2.5}$$

μ_1, μ_2 represent the dipole moments, ϵ the dielectric constant of the medium, k_B the Boltzmann constant and T the temperature.

The Debye force is the angle averaged dipole- induced-dipole interaction between two atoms or molecules, being its potential as follow,

$$w_D(r) = -\frac{1}{r^6} \frac{\mu_1^2 \alpha_{02} + \mu_2^2 \alpha_{01}}{(4\pi\epsilon_0\epsilon)^2} \tag{2.6}$$

α_{01}, α_{02} represent the molecular polarization values.

The last force so-named London Force has the most important contribution to van der Waals. The range of interaction goes from few nanometers to Å between all atoms or molecules. This force is referred as the instantaneous dipole-induced dipole interaction and its potential is,

$$w_L(r) = -\frac{3}{2r^6 (4\pi\epsilon_0\epsilon)^2} \frac{\alpha_{01}\alpha_{02}(h\nu_1)(h\nu_2)}{(h\nu_1 + h\nu_2)} \tag{2.7}$$

The total contribution at van der Waals potential will be adding the potentials w_K, w_D and w_L, so

$$w_{VdW}(r) = -\frac{1}{r^6 (4\pi\epsilon_0)^2} \left[\left(\mu_1^2 \alpha_{02} + \mu_2^2 \alpha_{01}\right) + \frac{\mu_1^2 \mu_2^2}{3k_B T} + \frac{3\alpha_{01}\alpha_{02}}{2} \frac{(h\nu_1)(h\nu_2)}{(h\nu_1 + h\nu_2)} \right] \tag{2.8}$$

The van der Waals interaction between atoms at the end of the tip and the surface explored is taken into account by summing the interactions of all pair of atoms, but the full system contains billons of atoms and impossible to estimate all the interactions. For simplicity, only the contribution of the London force is evaluated based on the material and structure of the tip. The dispersion or London force can be simplified as,

$$w_L(r) = -\frac{C_6}{r^6} \tag{2.9}$$

being C_6 constant defined by London and specific to the identity of the interacting atoms. Forward, Hamaker calculated the total interaction potential under assumptions for two macroscopic bodies allowing obtaining the total force for two arbitrary shaped bodies,

$$F_{VdW} = -\rho_1 \rho_2 \int_{v2} \int_{v1} \nabla w_L(r) dV_1 dV_2 \tag{2.10}$$

ρ_1 and ρ_2 are the number of densities, and V_1 and V_1 represents the volumes of bodies involved. More elaborated expressions to obtain the van der Waals force between a

conical tip with angle γ and a sphere of radius R at the end with a flat plane were derived by Argento and French [28]. In this sense, they suggested a parametric tip force-distance relation to adequate the existing power-law sphere-plane models. The Figure 2.5 shows the geometric model used to describe the integration of the interaction force, consisting of a cylindrical followed by a conical section and a spherical cap.
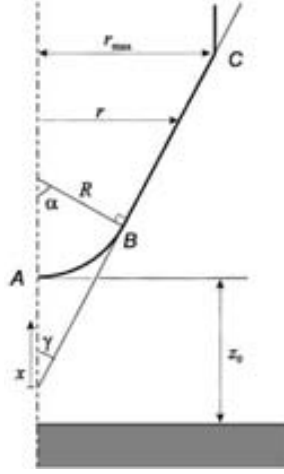
Figure 2.5. Parametric tip model. R is the tip radius of the spherical section, γ and α are angle for the conical and spherical sections. From Argento et al.[28]

$$F_{VdW} = \frac{HR^2 \left(1 - \sin\gamma - z_0 \sin\gamma - R - z_0\right)}{6z_0^2 \left(R + z_0 - R\sin\gamma\right)^2}$$
$$- \frac{H\tan\gamma \left[z_0 \sin\gamma + R\sin\gamma + R\cos\left(2\gamma\right)\right]}{6\cos\gamma \left(z_0 + R - R\sin\gamma\right)^2} \tag{2.11}$$

From equation 2.11 the first term corresponds to the contribution of the conical section to the total force, whereas the second term represents the contribution of the spherical cap to the total force.

2.2.2.2 Capillarity Forces

SFM experiments carried out under ambient condition must take into account the role that the presence of water plays between surfaces covered by molecular films and

the probing tip. A meniscus is formed provoking strongly draws the tip toward the sample. The interaction can be described by the Laplace pressure by

$$P = \gamma \left(\frac{1}{r_1} + \frac{1}{r_2} \right) = \frac{\gamma}{r_K} \tag{2.12}$$

with γ is the surface tension, r_1 and r_2 are the radii of the meniscus and r_K called the Kelvin radius. The capillarity force can be obtained by multiplying the Laplace pressure by the contact area of the meniscus A,

$$F_{cap} = \frac{\gamma A}{r_K} = \frac{\gamma 2\pi R d}{r_K} \tag{2.13}$$

being R the tip radius and d the tip penetration depth into the liquid. Capillary forces can be roughly estimated by $F \approx 4\pi R\gamma$, some reported values for saturation vapor pressure, surface tension and the Kelvin lengths[2] are summarized in table 2.1.

The adhesion force, F_{adh}, between the tip and the surface under the presence of the

Substance	P_0 Pa	γ mN/m	λ_K nm
Water	3169	71.99	0.52
Toluene	3790	27.93	1.20
Chloroform	26200	26.67	0.88
Ethanol	7870	21.97	0.52
Acetone	30800	23.46	0.70

Table 2.1. Saturation vapor pressure P_0, surface tension γ, and λ_K at 25°C.

water bridge can be written by summing van der Waals, capillary forces and the force due to surface tension of a liquid film,

$$F_{adh} = F_{VdW} + F_{cap} + F_{st} \tag{2.14}$$

Most SFM equipments have implemented the Force Volume Imaging in which the tip detects forces on the surface and then the deflection experimented by the cantilever

---

[2]calculated as $\lambda_K = \frac{\gamma V_m}{RT}$, with $R = 8.314$ J·mol^{-1}K^{-1} the molar gas constant, T the temperature and V_m the molar volume of the liquid.

is recorded as the tip approaches, contact and retract from the surface collecting an array of force curves over the entire sample area. In these sense, each force curve is recorded at a fixed (x-y) position over the area, and force curves from an array of (x-y) positions are combined into a volume of force data. We employed this method to obtain adhesion maps over *a priori* SH and COOH terminations given by two morphologies of MMTA islands presented in chapter 4.

2.2.2.3 Electrostatic force
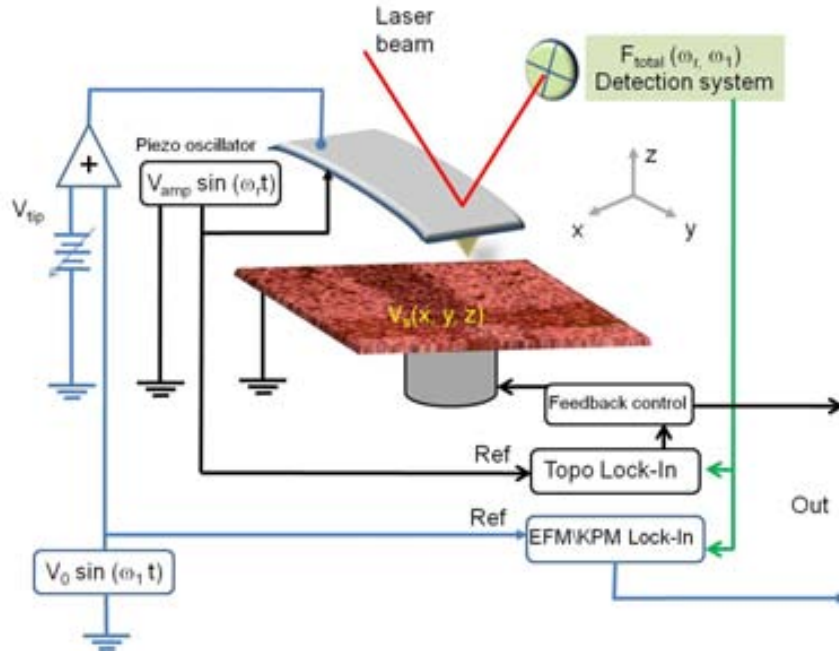
Figure 2.6. Experimental set-up for most commercial SFMs. $V_s(x, y, z)$ is the surface potential that one wants to measure.

Modeling the tip-sample ensemble as a capacitor, where dq represents a charge element and dU the necessary energy to bring it from the positive electrode at potential V to other electrode, one obtains,

$$dU_{surface} = V dq = \frac{q}{C} dq$$

$$U_{surface} = \frac{Q^2}{2C} = \frac{1}{2} C V^2$$

(2.15)

2.2 Background of Scanning Force Microscopy (SFM)

By considering a conducting AFM tip and conducting sample with different work functions and both electrically connected, electrons flow from the material with smaller work function to the material with higher work function. The diffusion current builds up a double layer at the interface resulting in an electrostatic potential (CPD)[3] referred as, Contact Potential Difference $\Delta\Phi$. In Figure 2.6, the total energy between the tip-sample ensemble is,

$$U_{total} = \frac{1}{2}kx^2 + U_{surface} = \frac{1}{2}kx^2 + \frac{1}{2}(CV)^2_{tip-sample} \tag{2.16}$$

electrostatic forces experimented by the cantilever-tip system are attractive forces interacting in the middle range distance of about 10nm. These forces exerted on a conductive AFM tip held at constant distance z above sample surface is given by

$$\begin{aligned} F &= -\frac{dU_{total}}{dz} \\ &= -\frac{1}{2}\frac{dC}{dz}V^2 \end{aligned} \tag{2.17}$$

where V is the electrostatic potential difference between AFM tip potential and sample surface potential, $V = V_{tip}$ - V_{sample}, and $\frac{dC}{dz}$ is the first derivative of AFM tip-sample coupling capacitance. If an AC voltage, $V_{ac}\sin(\omega t)$ with adjustable offset V_{dc} is applied to the conducting AFM tip, the electrostatic force interaction between the electrodes becomes

$$\begin{aligned} F_{elect} &= -\frac{1}{2}\frac{dC}{dz}(\Delta V)^2 \\ &= -\frac{1}{2}\frac{dC}{dz}\left[\Delta\Phi + (V_{dc} + V_{ac}\sin(\omega t))\right]^2 \end{aligned} \tag{2.18}$$

by expanding the expression F_{elect}, the spectral components at DC and frequencies ω and 2ω are,

$$\begin{aligned} F_{dc} &= -\frac{1}{2}\frac{dC}{dz}\left\{(\Delta\Phi + V_{dc})^2 + \frac{V_{ac}^2}{2}\right\} \\ F_{\omega} &= -\frac{dC}{dz}(\Delta\Phi + V_{dc})V_{ac}\sin(\omega t) \\ F_{2\omega} &= \frac{1}{4}\frac{dC}{dz}V_{ac}^2\cos(2\omega t) \end{aligned} \tag{2.19}$$

as a result of the F_{ω} and $F_{2\omega}$, the tip starts vibrating. If the frequency of the applied AC voltage equals the resonant frequency of the cantilever, the vibration amplitude at

---

[3]The sign of the measured $\Delta\Phi$ will be positive/negative if the nullifying voltage is applied to the sample/tip respectively.

frequency ω is directly proportional to the spectral component of F_ω. If the DC offset V_{dc} applied to the tip is equal in magnitude and opposite in sign to the CPD of the sample, the spectral components at frequency ω of the tip vibration amplitude, as well as of the force acting on the tip will become zero. KPFM technique is based on nullifying tip vibration amplitude at the resonant frequency by applying an adjustable DC voltage by a feedback circuit to record V_{dc} as a function of position (x, y) and to obtain a map of the electrostatic surface potential. In the present work, in order to minimize cantilever contributions, often Kelvin Probe Microscopy measurements are carried out in gradient force mode [29].

$$\frac{dF}{dz} = -\frac{1}{2}\frac{d^2C}{dz^2}(\Delta V)^2$$
$$\frac{dF_\omega}{dz} = -\frac{d^2C}{dz^2}(\Delta\Phi + V_{dc})V_{ac}\sin(\omega t)$$

(2.20)

2.2.3 Operation Modes in SFM

In agreement with the wide variety of forces that can be detected in SFM, several alternative ways of acquiring data of surface properties from contact and non-contact mode have been developed. The first developed mode was the contact mode, in which the tip and the explored surface are in direct mechanical contact. By measuring vertical and lateral deflections of the sensor as the tip scans the sample surface, topography and friction maps can be simultaneously obtained. Other operation modes are the so-called dynamic modes where the lever is oscillated near its resonance frequency at a given distance from the surface. Depending on the amplitude of oscillation, compared to the tip-sample distance, the tip may either not contact the sample or intermittently contact the sample surface. By measuring the changes in amplitude, phase or frequency of the oscillating cantilever in response to the existing tip-sample interactions, it is possible to obtain information about the surface properties such as electrostatic or magnetic maps, dissipation, surface potential, apart of the topographic images.

2.2.3.1 Contact Mode

As mentioned before, forces are detected by a probe tip mounted on a flexible lever which causes the cantilever deflection. This deflection is kept constant to a pre-set setpoint value when the tip contacts the surface by mean of a feedback loop of the

electronic control unit. With the cantilever deflection held constant, the applied force to the sample during the scan is also constant obtaining a profile of constant atomic or molecular force over the surface. The nature and strength of the forces experimented by the tip-sample can vary depending of their separation distance achieving forces in the μN to nN range. The most typical potential employed to model the intermolecular forces is the Lennard-Jones potential,

$$V_z = 4\epsilon \left[\left(\frac{\sigma}{z}\right)^{12} - \left(\frac{\sigma}{z}\right)^6 \right] \tag{2.21}$$

The Lennard-Jones potential in equation 2.21 describes the attractive van der Waals force, the sixth-power term, whereas the twelfth-power term describes an empirical potential accounting for the core-core repulsive force that is dominating at small distances. From force-distance curve, it is possible to distinguish between the normal and the total force applied to the sample. From equation 2.1, the normal force is obtained from the cantilever deflection and, when the feedback is enabled, it is the set-point value multiplied by k_Z, whereas the total force is the sum of the normal force and the adhesion force. This fact implies that to acquire an image in contact mode the minimum set-point value is close to the adhesion. Furthermore, if the zero deflection is defined as the cantilever deflection in the absence of forces, this means a negative set-point and a total applied force close to zero, measuring at this minimum set-point reduces possible damage of soft sample surfaces.

- Image formation: images are formed by recording the effects of the interaction forces between the tip-sample system. The SFM electronics drives the scanner across the first line of the scan and back (forward and backward), it then steps in the perpendicular direction and starts a second scan line forward and backward, then a third line, an so forth. As the cantilever scanned over the surface, a topographic image is recorded storing the vertical control signals sent by the feedback loop to the scanner moving it up and down to follow the surface morphology while keeping the constant force.

- Lateral Forces, Friction and lattice-resolved images: by using the Friction Force Microscopy based on the detection of the torsion of the cantilever, a lateral force image is obtained at each point of scanned area for both forward and backward

directions. The standard measurement in FFM is made by means of friction loop where the lateral force acting on the tip is recorded for the forward and backward scan directions being the dissipated energy the loop area [30]. For image analysis, the forward and reverse signals on the same scan line are subtracted and the mean lateral force is,

$$F(r) = F_L^{mean} = \frac{1}{2}\left(F_L^{Fw} - F_L^{Bw}\right) \tag{2.22}$$

where F_L^{Fw} and F_L^{Bw} are in the forward and backward directions, respectively. On small scanned areas an average friction force is calculated over N lines of lateral force images; however, some results are presented by making a friction map subtracting both forward and backward lateral force images and dividing between two, correcting previously any possible drift on the images. Small scan areas have been used to study the atomic periodicity of gold substrates as well as the molecular order of the islands of self-assembled of the mercapto-methyl terphenyl carboxylic acid (MMTA). High resolution lateral force images show a typical stick-slip behaviour that can be understood as an oscillator represented by the tip and a periodically potential of the surface. If the tip is brought to the surface and pushed laterally, it will remain at that minimum "sticking", until the restoring force of the cantilever overcomes the energy barrier causing the tip jump or slip to the nearest local equilibrium position, being locked again [31, 32]. Quality of these images can be affected by the quality of the surface (vacancies, contamination, electronic noise, speed of the scanning).

- Current maps: Simultaneously to the topography and friction images, one of our microscopes allows obtaining maps of electronic transport and usually called current maps. In current maps, the current flowing between a conductive tip and the sample surface is recorded at each position for a fixed applied voltage. A high sensitivity internal IV-converter allows acquisition in the total range (100nA), whereas an external Low-Noise Current Preamplifier (Model SR570) Stanford Research Systems allows obtaining range from picoampere (pA) to miliampere (mA).

2.2.3.2   Dynamic Modes

Amplitude Modulated-Atomic Force Microscopy (AM-AFM) is a dynamic force microscopy mode where the cantilever-tip ensemble is mounted on a piezoelectric element that is oscillating with amplitude F_0 at angular frequency ω, usually near or at the free resonance frequency. The three degrees of freedom of an oscillating cantilever called, amplitude, frequency and the phase difference between excitation and oscillation can be used as feedback parameters to image the sample surface, in particular Martin et al. [33] proposed an analytical model for small vibration amplitudes to correlate their changes respect to derivative of the force experimented by the cantilever.

Unlike pioneering work developed by Martin, few years later Zhong et al. [34] introduced an alternative way to measure with large oscillation amplitudes by using stiff cantilever on silica optical fiber samples; this alternative of measuring was called tapping mode or intermittent contact. Interestingly, both alternatives small and large vibration amplitudes form part of the solutions of the equation movement of an oscillating cantilever-tip ensemble close to the surface. A first approach is to consider the oscillating cantilever-tip system as a point-mass spring, with an effective mass m^*, if the oscillating cantilever-tip system is far from the sample (tip and surface are not interacting, $F_{ts}=0$), then the system can be described by the motion of a forced harmonic oscillator with damping as follows,

$$m^* \ddot{z}(t) + \alpha \dot{z}(t) + k \, z(t) = F_0 \cos(\omega t) \tag{2.23}$$

by defining terms as $\omega_0^2 = \frac{k}{m^*}$ the resonant frequency of the free oscillating cantilever, $Q = m^* \frac{\omega_0}{\alpha}$ the dimensionless quality factor being inversely proportional to the damping coefficient, m^* the effective cantilever-tip mass[4], then the equation 2.23 can be written as,

$$\ddot{z}(t) + \frac{\omega_0}{Q} \dot{z}(t) + \omega_0^2 \, z(t) = \frac{F_0}{m^*} \cos(\omega t) \tag{2.24}$$

The solution of a harmonic oscillator with damping has a transient and steady term,

$$z(t) = B \exp(-\alpha t) \cos(\omega_r t + \beta) + A \cos(\omega t - \phi) \tag{2.25}$$

---

[4]$m^* = 0.2427 m_c + m_t$, where $m_c = w_c \cdot t \cdot L \cdot \rho$ is the mass of the cantilever and m_t the mass of the tip. ω_c, t, L and ρ are the width, the thickness, the length and the mass density of the cantilever, respectively.

In the absence of intermolecular forces between tip-sample surface, but applying a periodic excitation to the cantilever with ω close to the resonance frequency, a linear combination of two regimes, a transient term and a steady solution are obtained. Starting from rest and switching on the excitation at t=0 to the piezo, the amplitude will increase from zero to a final value and after a time of $\frac{2Q}{\omega_0}$ to arise a steady state, leaving the amplitude, phase and frequency stay constant over time. The steady term is a harmonic function with a phase lag with respect to the excitation force,

$$z_s(t) = A_0 \sin(\omega t - \varphi) \tag{2.26}$$

the dependence of the amplitude with the excitation frequency is,

$$A_0(\omega) = \frac{\frac{F_0}{m^*}}{\sqrt{\left(\omega_0^2 - \omega^2\right)^2 + \left(\frac{\omega_0}{Q}\right)^2 \omega^2}} \tag{2.27}$$

and the phase shift by,

$$\varphi = \arctan\left(\frac{\omega\omega_0}{Q(\omega_0^2 - \omega^2)}\right) \tag{2.28}$$

For slow resonance frequencies and $\omega = \omega_0$, the amplitude goes as $\frac{QF_0}{k}$; whereas the damping coefficient modifies the resonance frequency as $\omega_r = \omega_0 \left(1 - \frac{1}{2Q^2}\right)^{1/2}$. More complex interactions can be assumed between tip-sample, this fact makes computationally expensive to find the solution of the tip movement. Discussions, theoretical calculations and simulations can be followed in [35, 36, 37, 38].

- Three-dimensional (3D) modes: a successful tool to perform several and simultaneously measurements in SFM are the so-called 3D modes [39]. Measurements carried out with this mode can be understood as an extension of a force distance-curve where, in addition to the normal force, other distance dependence parameters of a distinct magnitude can be obtained. Let $F_k = (X_i, Y_j)$ a magnitude that depends of other two, being X_i and Y_j, the fast and slow scans, respectively. Within each scanning direction, parameters such as, voltage(V), frequency(ω), distance (z), various images can be simultaneously recorded [40, 41].

- 3D modes for friction measurements: by applying this mode for friction measurements, a single line along the surface of the sample is chosen and associated to X_i,

whereas the z-piezo movement is chosen to Y_j parameter. For a given tip-sample distance, the tip scans the line forward as well as backward; once done that, the piezo scanner moves a new tip-sample distance and the scan is repeated along the same line, as is depicted in Figure 2.7. By this way, normal and lateral forces images are recorded simultaneously during the scanning, generating two sets of 3-dimensional images: a pair of normal force (left and right scan) and a pair of lateral force (left and right scan) images, as shown in Figure 2.7(b) and 2.8 (a, b). The lateral force image, exhibits opposite contrasts in the forward and backward scans. When a horizontal profile of the forward and backward scans of the lateral force images are plotted together (see Figure 2.8(d)), a friction loop is formed at the selected z distance of normal force $F_n=(X, z)$. The net friction is taken to be the half of the difference of the forward and backward scans of the friction loop. By doing this, over the entire lateral forces images a friction map is obtained as shown in figure 2.8(c). By means of a friction map, different friction regions can be deduced.

- 3D modes for transport measurements: these data acquisition were performed over a single point on the explored surface, that is, the lateral scan movement is disable, being the fast scan direction the bias voltage applied to the tip (X_i=V), while the slow scan direction is the piezo movement in the vertical direction (Y_j=z), in this case, the voltage is varied at each tip-sample distance. The magnitudes under study are the current flowing between the conducting tip and sample (I) and the normal force (F_n).

2.3   Sample Preparation

We used glass substrates coated successively with a 50Å thick layer of chromium and 200nm thick layer of gold purchased from Arrandee™and atomically flat Au(111) surfaces epitaxially grown on mica and purchased from Georg Albert PVD-Beschichtungen (Heidelberg, Germany). Polycrystalline Au substrates prepared by evaporating 5nm buffer layer of titanium (99.8%, Chempur) and subsequently 100 nm of gold (99.9%, Chempur) onto polished silicon-wafers (Wacker silicone) at room temperature in an eva-
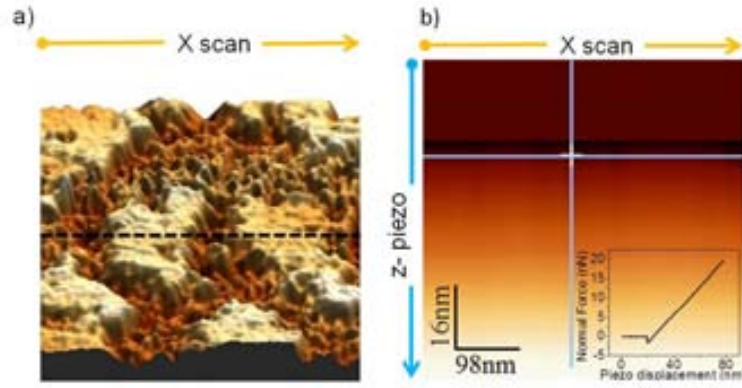
Figure 2.7. (a) 3D SFM topographic image of MMTA islands on gold substrate and (b) $F_n=(X,z)$ recorded on a single line by using 3D modes. The normal force image looks the same in both forward and backward scans. Inset: force-distance curve obtained from vertical gray line.
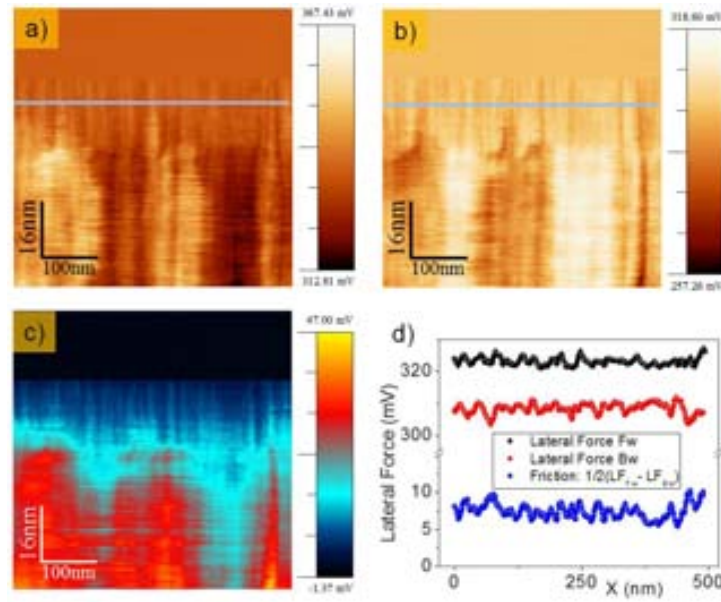
Figure 2.8. Lateral force images acquired by means of 3D modes. LF (X, z) forward (a) and backward (b) are used to obtain a friction map (c).

poration chamber operating at a base pressure of about 10^{-7} mbar were also employed and generously supplied by Prof. C. Wöll group from Ruhr-Universität Bochum.

2.3.1 Gold Substrates Preparation

Gold surface has been chosen because it forms a strong bond with the thiol group (-SH) used as the headgroup; in addition, the gold is an inert metal in air compared to others, such as cooper or silver. In common with other close-packed metals the (111) surface is the most thermodynamically stable. For clean gold surfaces in (111),(100) and (110) planes, the surface energies of the three high index surfaces have been reported as 0.05 eV/$Å^2$, 0.08 eV/$Å^2$ and 0.100 eV/$Å^2$ respectively.

Gold substrates from Arrandee™were soaked in piranha solution (H_2SO_4:H_2O_2; 3:1) for 20 minutes and taken out to be rinsed with Milli-Q water and finally dried under a stream of nitrogen. Afterwards, these substrates were annealed in a butane gas flame for several seconds to get large terraces of about 0.4μm to 0.8μm width and orientation Au(111). The Au(111) on mica substrates were not immersed into piranha solution, but were stored in a small container with Argon as-received until the adsorption experiments were carried out; some substrates were annealed in a butane gas flame also to obtain large terraces prior to the experiments. Gold onto polished silicon-wafers were exclusively immersed into piranha solution for 20 minutes and rinsed with enough Milli-Q water and dried with a stream nitrogen.

All gold substrates were observed in our microscopes previously to the immersion in thiol solutions. Measuring in lateral force mode allows enhancing atomic lattice resolution as shown in Figure 2.9 for the Au(111) surface. This mode has been used to calibrate the piezo scanner for small scanned areas and to study the molecular order of the MMTA organic layer. The monoatomic steps of known height (0.235nm) are used to calibrate the vertical displacement (see Figure 2.10) whereas lattice-resolved images of the hexagonal periodicity (a_{Au-Au}=0.289nm) are used to calibrate the lateral dimension. The high lateral resolution force images show the so-called stick-slip behavior revealing the periodicity of the atomic lattice of the surface and being extremely useful for surface structural characterization.

Large terraces are normally achieved after some minutes of annealing, when samples are heated to the point where a dim reddish/orange glow is observed on the gold surface.
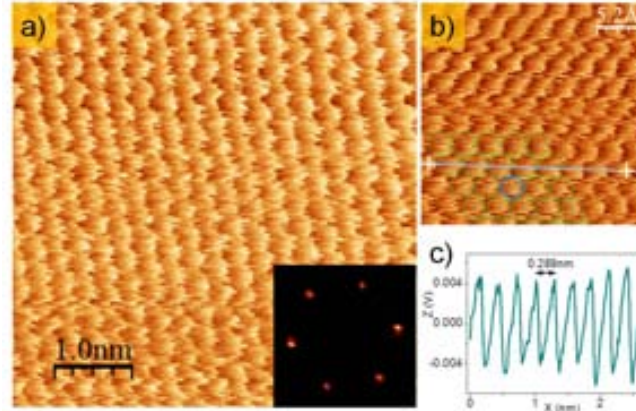
Figure 2.9. High resolution lateral force images measured on a flat terrace of gold (a, b) are shown. Inset in (a) shows the hexagonal symmetry by means of 2D-Fast Fourier Transformed (2D-FFT) filtered image. Profile in (c) taken along the line in (b) shows the periodicity (2.89Å) on the Au(111) surface.
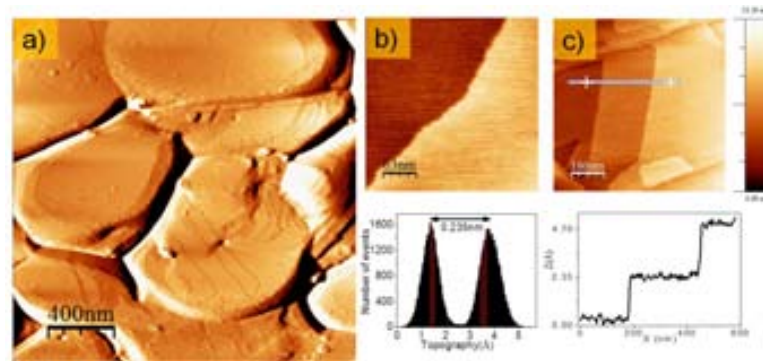
Figure 2.10. Gold surface Arrandee image after annealing (a) and Georg Albert PVD gold substrates (b, c) mentioned in the text. Derivative image (a) from topography of gold on glass shows the lateral grain size larger than 400nm with larges terraces separated by monoatomic steps of 2.35Å in height (b) (histogram). The topographic image of gold on mica with monoatomic steps after annealing with butane gas flame is presented in (c).

This process induces the formation of large grains and contamination free surfaces; despite the roughness due to the deep grain boundaries formed, the surface of the grains consists of flat terraces separated by monoatomic steps.

2.3.2   SAMs Preparation

Self-Assembled Monolayers(SAMs) can be spontaneously formed on substrates by adsorption from solutions as well as evaporation methods. During this work, self-assembled monolayers were mainly prepared by immersion; however, the drop casting method was also used for MMTA aromatic thiols on gold substrates as well as stearic acid on nanostructured bifunctional terminated $SrTiO_3$ substrates. Other strategy to obtain SAMs on gold surfaces was by means of the so-called "soft lithography" micro-contact printing μCP technique. The immersion of substrates in thiol solutions for short (seconds) or longer times (days) at room temperature and appropriate concentrations were manly employed. For SAMs prepared at low concentration (below 2μM), longer immersion times are required to form a dense SAM. Immersion times for SAM formation is 10 - 24 hours, where the physisorption process on the gold surface takes a few minutes and the chemisorption process to organize and form an ordered layer takes several hours.

In order to minimize contamination by exposing the substrates and samples for long times to the environment conditions, fresh samples were immediately studied under a nitrogen environment, as described in section 2.2. Molecules employed to organize self-assembled monolayers on substrates typically consist of three parts:

1. A headgroup which is anchored to the substrate immobilizing the molecules via chemical interaction between the headgroup and the substrate. The headgroups that bind to specific metals, semiconductors or metal oxides comprises a wide variety, i.e. thiols (-SH) bind to gold via a S-Au or to silver via S-Ag bonds, carboxylic acids bind to silver by means of an ionic COO^- Ag^+ interaction or adsorbates with a carboxylate function on oxide surfaces, whereas organosilanes bind to hydroxylated surfaces by means of Si-O interaction.

2. A backbone or spacer that connects headgroup and end-group. The backbone is mainly responsible of the intermolecular interactions and orientation or packing.

3. The end-group localized on the outer surface of the film. Several functional groups have been employed to achieve different surface properties such as carboxyl (-COOH), methyl (-CH$_3$), thiol (-SH), hydroxyl (-OH), porphyrines (-NH$_2$) or trifluoromethyl (-CF$_3$).

Like n-alkanethiols, the aromatic thiol SAMs formation process can also be described as a two-step mechanism:

- a fast adsorption step.

- a much slower ordering step. The kinetics of this step is governed by the interchain interactions.

The following equation describes the first step:

$$X-Ph-Ph-SH(sol) \rightleftharpoons X-Ph-Ph-SH \cdot Au_n \rightleftharpoons X-Ph-Ph-S^-Au^+ \cdot Au_n + \frac{1}{2}H_2 \quad (2.29)$$
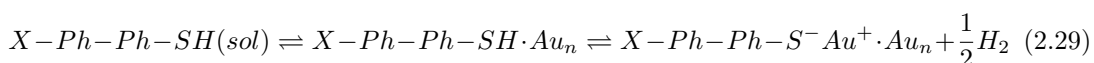
Liao and co-workers have studied the adsorption kinetic of functionalized-4-mercapto-biphenyls on gold surfaces by using the Quartz Crystal Microbalance (QCM) technique [42]. Their results suggested that the first step occurs within the first few minutes and proposed the lattice-gas adsorption model providing much better fits to experimental data than the Langmuir isotherm model used for alkanethiols. The kinetics of the first step is a physical and chemical adsorption process governed by the surface and the headgroup interaction. The Langmuir isotherm model assumes there is no interaction between molecules and fits the adsorption kinetic of n-alkanethiols on gold surfaces successfully [43]; however, the model fails for aromatic thiols. The lattice-gas adsorption model takes into account the interaction between neighbor molecules indicating from fits that repulsive interaction between aromatic thiol molecules dominate over the attractive van der Waals forces.

2.3.3 Solutions Preparation and Protocols

Samples were prepared by immersion in thiol solutions for a wide range of immersion times from few seconds until several days. The immersion time and the concentration of the solution as well as the solvent employed allow obtaining monolayer or multilayer structures. The range of the concentrations employed vary from 0.05μM to 100μM, being the most relevant at 2μM and 100μM. All fresh samples were thoroughly rinsed with the appropriate solvent (ethanol, acetic acid, tetrahydrofuran THF) and dried under a stream of nitrogen. Additional strategies were performed for every protocol of samples preparation to obtain possibles morphological changes of the organic films, such as:

- immersion process without annealing

- annealing samples in furnace

  - under controlled N_2 environment

  - in air

- annealing the solution + samples in a hot plate

- annealing the solution + samples within a thermal bath

We used a furnace in which it was possible to control the nitrogen environment by using two programs. The first one, with annealing rate of $120°C \cdot h^{-1}$ and final temperature of $370°C$ and the second one, with annealing rate of $200°C \cdot h^{-1}$ and final temperature of $190°C$, both with a nitrogen stream of $12cc \cdot min^{-1}$. The sublimation temperature of $375.85°C$ (649 K) for p-terphenyl was taken into account for all experiments with post-annealing [44].

2.3.3.1   Ethanol Solutions

0.9μg of MMTA powder was diluted in 25ml of ethanol PRS (99.5%) from Panreac or ultrapure Romil SpS^{TM} (99.8%) super purity solvent. Sonication was necesary for 20 minutes or more, because the organic material is hardly diluted. By doing this, concentrations of 100μM were obtained. However, saturated solutions were filtered by using Whatman filter papers No.42 maintaining always the established concentration. More diluted concentrations were prepared from 100μM.

2.3.3.2   Ethanol plus Acetic Acid Mixture Solution

For this case, diluted ethanolic solution 2μM was obtained from the initial 100μM. Mixture solutions were obtained by adding 5% or 10% of acetic acid of the total volume.

2.3.3.3   Acetic Acid Solutions

For solutions by using acetic acid, the ultrapure Romil SpS^{TM} (99.8%) super purity solvent was employed. To obtain a concentration of 100μM as before, 0.9μg of MMTA powder was diluted in acetic acid. More diluted solutions were prepared from the initial

100μM. Sonication for 20 minutes or more was required; saturated solutions under this protocol were also filtered with a syringe filter type PTFE 0.2μm.

2.3.3.4 Toluene and THF solutions

The tetrahydrofuran (THF) solvent was obtained directly of the MBrawn solvent purification system MB-SPS-800, whereas the toluene (HPLC grade) solvent was supplied by Panreac Quimica and used as received. Solutions using toluene or tetrahydrofuran (THF) as solvents have been prepared by diluting 0.9μg of MMTA into an afforated volumetric flask of 10ml or 25ml. Once the solution in toluene or THF was prepared a sonication process for 15 minutes was performed. Depending of its appearance the sonication time was prolonged to 30 minutes. Saturated solutions under this protocol were filtered with a syringe filter type PTFE 0.2μm. More diluted solutions were obtained starting from the 100μM concentration.

2.4 Patterning Gold Surfaces by using μCP

Microcontact Printing (μCP) is one of the first and maybe the most important technique in Soft Lithography. An elastomeric stamp is formed from a solid template or master. Molecules are immobilized to this stamp by inking techniques and subsequently transferred to a substrate by printing. μCP technique was developed in Whitesides´s group making elastomeric stamps of poly(dimethylsiloxane)(PDMS) by replicating a relief of a master by inking molecules into the surface which are then transferred to the substrate by contact [45, 46].

Several approaches have been developed in the group of Whitesides such as Replica Molding (REM) in which an elastomeric stamp duplicates the information, i.e. the shape, the morphology, and the structure present in a master. It also allows duplication of three-dimensional topologies in a single step, whereas photolithography is not able to replicate such structures [47]; Micromolding in Capillaries (MIMIC) or Inverse Microcontact Printing [48] where the stamp is placed on a substrate and then the resulting channels are filled with a material, which is molded onto the substrate; Solvent-assisted Micromolding (SAMIM) in which the solvent is placed into the suppressions of the stamp. A substrate carries a polymer sensitive to this solvent and after bringing both into contact the solvent removes the polymer in the suppressions [49] and Microtransfer

Molding (μTM) in which microstructures are formed by filling microchannels on the surface of an elastomeric mold with a liquid precursor, and then bringing the mold into contact with a planar or contoured substrate. The liquid precursor is caused to solidify in situ either thermally or photochemically. The elastomeric mold is then peeled away, leaving the resulting microstructures on the surface of the substrate [50]. Nowadays, new replication process for microstructures [51, 52] using soft lithography have been introduced to be applicable various fields as microfluidics, optics, as well as the semiconductor industry.

The idea to transfer polar molecules into the gold surfaces to obtain patterned areas has had relevant difficulties. It has been necessary to find the appropriate solvent to dilute the molecular compound and to avoid any damage of the polymeric stamp or to find an easy method to transform a hydrophobic into hydrophilic surface.

The solubility of Mercapto Methyl-Terphenyl carboxylic Acid (MMTA) is low when we used ethanol, for this reason we follow a protocol using others solvents as acetic acid or toluene. However, stamps of Poly(Dimethylsiloxane) PDMS can be swelled using solvents with solubility parameter near to $\delta = 7.3$ cal$^{1/2}$ cm$^{-3/2}$. For two materials to be soluble, their cohesive energy densities must be similar, since this energy must be overcome to separate the molecules of the solute to allow the molecules of solvent to insert. Ethanol and water are considered as low solubility solvents generally have $\delta > 9.9$ cal$^{1/2}$ cm$^{-3/2}$, whereas toluene can be considered as highly soluble $\delta = 8.9$ cal$^{1/2}$ cm$^{-3/2}$. A list of solvents are shown in Figure 2.11 from [53], these are numbered in order of decreasing swelling ability(i.e. "1" has the most swelling ability and "38" has the least swelling ability. The dashed line shows the solubility value of PDMS ($\delta = 7.3$ cal$^{1/2}$ cm$^{-3/2}$). By using solvents close to PDMS solubility parameter, a greater degree of swelling or damage of the polymer is observed.

2.4.1 Patterned MMTA Surface with Poly(dimethylsiloxane) PDMS

The central process in μCP technique is the conformal contact between the flexible elastomeric stamp (PDMS) and the substrate, which transfer the molecular ink onto the surface. The mechanical properties of the stamp are crucial to obtain excellent pattern transfer; moreover, polar inks, do not spontaneously wet the elastomeric stamp and surface hydrophilization of PDMS stamps is required for microcontact printing.
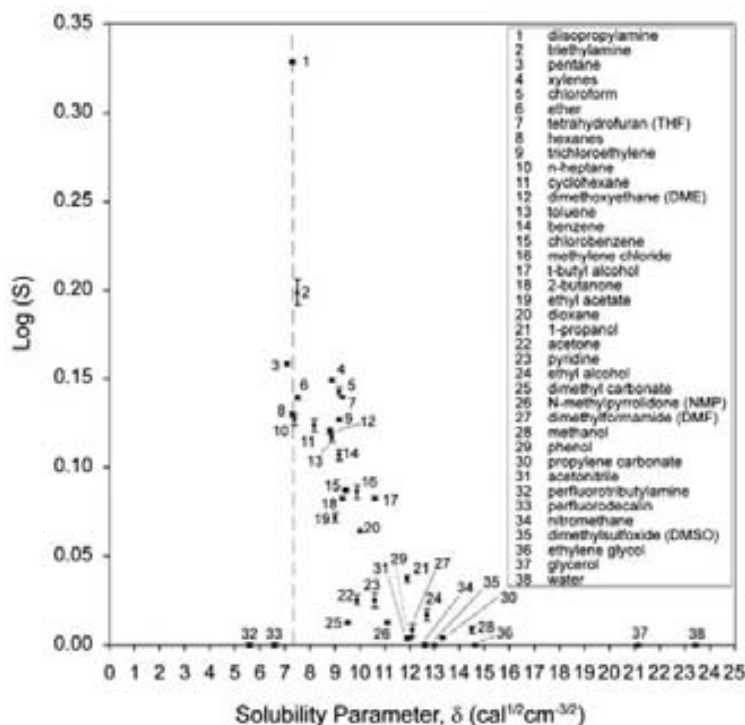
Figure 2.11. Relationship between swelling ratio (Log(S)) of PDMS in various solvents and the solubility parameter δ of the solvents. These are numbered in order of decreasing swelling ability where a greater degree of swelling is observed with solvents that have a value of δ similar to that of PDMS.

Polydimethylsiloxane (PDMS) stamps were fabricated by using Sylgard 184 Silicone Elastomer and curing agent (Dow Corning, Germany) in a 10:1 weight ratio. During the process, several cycles of vacuum were performed to eliminate bubbles of air in the compound and then this compound was poured onto a silicon master. After curing at 60°C for 16 hours, the PDMS template was carefully removed of the surface of the master obtaining round microstructures of 2μm, 3μm and 5μm in diameter and squares of 3$\times$3 μm^2. Taking into account the hydrophilic character of the MMTA molecule and the hydrophobic character of the PDMS stamp due to its repetitive chemical structure$[-Si\,(CH_3)_2 - O-]$, several strategies to modify the stamp surface were followed. A way to modify this characteristic is exposing the surface to oxygen plasma which introduces silanol $(Si - OH)$ groups destroying the methyl groups $(Si - CH_3)$

and leading to a hydrophilic surface [54]. Stamps treated of this way, can be stored in water or polar organic solvents keeping their hydrophilic character [53]. To increase the hydrophilicity of our stamps, we stored the PDMS stamps in MilliQ(18MΩ, 1ppm) water for several days without using additional treatments. Some works have suggested to use surfactants such as Triton X-100 or Sodium Dodecyl Sulphate (SDS)[55, 56] previously the ink hydrophilic proteins to the stamps and so to increase the transferring of proteins into the surface.
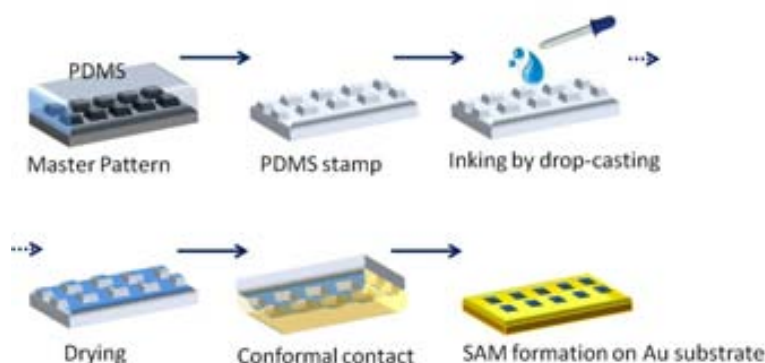
Figure 2.12. Schematic of the microcontact printing μCP process. The relief patterns of the silicon master are transferred as negatives to the PDMS stamp.

The steps for patterning surfaces with μCP technique are depicted schematically in Figure 2.12. The more important step is the conformal contact between the PDMS stamp and the surface. The first step replicates the relief of the silicon master, then this system is cured and peeled off from the master. Drop-casting or wet inking method, denotes the transfer of the aromatic thiol from a solution of ink in which is deposited on the surface of the patterned PDMS. Once the stamp has been inked (by drop-casting or immersion methods) and dried, the elastomeric stamp is then briefly pressed against the gold substrate via mechanical contact, and the molecules transfer from the stamp to the substrate where they self-assemble into patterns determined by the relief patterns of the stamp. PDMS stamps were soaked in 2μM (ethanolic, toluene) solutions of MMTA for few seconds, below 1 minute, to avoid the swelling on the elastomeric stamp. By

drop-casting method, only a drop of solution was poured on topmost on the patterned relief.

CHAPTER 3

STRUCTURAL AND MORPHOLOGICAL CHARACTERIZATION OF ORGANICS FUNCTIONAL SURFACES

3.1 Introduction

It is known that both, the headgroup-substrate and intermolecular interactions play an important role in SAMs formation. Zharnikov et al. [57] elucidated the relative importance of these interactions using NEXAFS and Photoelectron Spectroscopy for aliphatic and aromatic thiol-derived SAMs. Their results revealed that the headgroup-substrate interaction for alkanethiols play a dominant role for the structure and packing density, whereas for aromatic thiols SAMS, the main role is due to the intermolecular interactions.

The anchoring of sulfur atoms on the gold surface defines the free space available for the molecular assembling. SAMs of alkanethiols ($CH_3(CH_2)_nSH$) on Au(111) surfaces have been previously studied by several experimental techniques such as scanning tunneling microscopy [58], infrared (IR) spectroscopy [59], electron [60] and X-ray diffraction [61]. As result of these studies is that, the monolayer adopts a commensurate $(\sqrt{3} \times \sqrt{3})R30°$ structure of absorbed molecules with an intermolecular spacing of 4.97Å and estimated an area per molecule of 21.4Å^2 and average tilt angle in a range of $28° - 40°$ from the surface normal.

Although the exact adsorption site and the amount of charge transfer is still debated in the literature, a large number of adsorption models have been proposed describing the sulfur-gold interaction of alkanethiols on Au(111). First models assumed the adsorption of the sulfur head atom at the fcc three-fold hollow-site [62, 63], the 2-fold bridge-site of the substrate [64] or the so-called bri-fcc site (shifted from the bridge site towards

the fcc site) [65]. Recent findings proposed a mechanism including single gold adatoms as an important component in the thiol binding mechanism [66, 67, 68]

Figure 3.1 shows the FCC structure for metal and the $(\sqrt{3} \times \sqrt{3})R30°$ and $p\left(3 \times 2\sqrt{3}\right)$ structure commensurate for alkanethiol on Au(111) surface.
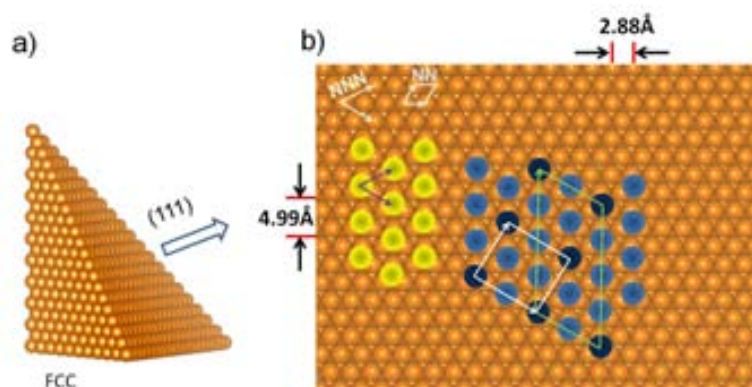
Figure 3.1. a) Face cubic centered FCC structure of gold and b) sulfur atoms of alkanethiols show a $(\sqrt{3} \times \sqrt{3})R30°$ structure commensurate with the underlying Au(111) and the $p\left(3 \times 2\sqrt{3}\right)$ superlattice and usually written as $c\left(4 \times 2\right)$. The nearest-neighbor (NN) and next-nearest-neighbor (NNN) direction of the Au(111) have been marked.

Structural studies of aromatic molecules based on benzene, biphenyl, oligophenyl and oligophenylethynyl thiols adsorbed on Au(111) have revealed that the molecular chain orients on the substrate with a slightly smaller tilt angle than alkanethiols and the herringbone-shaped structure seems to be the most common structure measured from these thiol molecules [69, 70, 71, 7, 72, 73, 74].

The average molecular tilt angle of 28° for the terphenylthiol and terpenylmethanethiol (TPT, TPMT) SAMs was found by NEXAFS[1] and IRRAS[2] data [70] and (28±4)° and (24±4)° by IRRAS[75] in the case of MMTA[3].

---

[1]Au(111) immersed in $10\mu M$ ethanolic solution for a period of between 15 and 24 hours at room temperature.

[2]Gold substrates immersed into ethanolic solution at 62°C (335K).

[3]By immersing the Au(111) substrates for 24 hours in $100\mu M$ ethanolic and THF solutions.

3.2 Self-Assembled Monolayers and Crystalline Structure of MMTA on Au(111)

Figure 3.2 shows the molecular lengths for terphenyl (TP_n, n=1-3) and MMTA molecules by considering a tilt angle of 20° [76]. Early studies carried out on COOH-therphenyl-methanethiols (Carboxy Terphenylmethanethiol, CTPMT now MMTA) in ethanolic solutions by means of NEXAFS and XPS spectra have shown an average tilt angle for molecular axis of 17°±5° from the surface normal and thickness of 3.4±0.3 nm and 1.8nm, corresponding to the presence of a double and a single layer, respectively[77].

Arnold et al.[75] determined the thicknesses of 1.96nm and 3.29nm (monolayer and bilayer) for MMTA SAMs in ethanolic and THF solutions from the intensity ratios of the Au 4f to the C1s excitations XPS spectra, respectively. A possible discrepancy between thickness found and the 1.6nm expected thickness for single layer can be due to environment contaminants adsorbed on the surface [78].
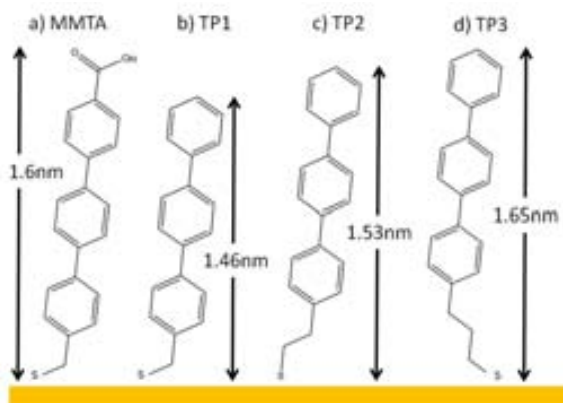
Figure 3.2. Single conjugated molecules systems of a) mercapto-methyl-terphenyl carboxylic acid (MMTA); b) terphenyl-methanethiol (TP1); c) terphenyl-ethanethiol (TP2) and d) terphenyl-propanethiol (TP3).

3.2   Self-Assembled Monolayers and Crystalline Structure of MMTA on Au(111)

In this section we present a study of the formation, structure and morphological changes of the mercapto-methyl-terphenyl carboxylic acid (MMTA) SAMs on gold substrates and the effects of the chain alkyl, the immersion time and after annealing within a variety of samples by using different solvents.

Friction Force Microscopy (FFM) and indentation experiments have been used to identify the carboxylic (-COOH) and thiol (-SH) end groups of low and tall islands obtained after annealing. Lastly, the μCP technique is employed to pattern the gold surface with the polar MMTA molecules.

3.2.1   Effect of the Alkyl Chain

The adsorption process of self-assembled monolayer of conjugated molecules have been recently studied such as Terphenyl (TP) and Biphenyl (BP) derivatized thiols. Molecular mechanics calculations performed by Sabatani et al. [79] with the aromatic compounds p-biphenyl mercaptan (BPM) and p-terphenyl mercaptan (TPM) and experimental observations by Tao et al. [80] suggested that BPM and TPM SAMs on Au(111) may contain large zones of a $(\sqrt{3} \times \sqrt{3})$R30° structure when a methylene unit inserted between the phenyl ring and the thiol headgroup was present. Systematic investigations carried out by Azzam et al. [81, 82] by using STM and IRRAS and LEED revealed that different SAMs[4] (TP$_n$, n=1-6; BP$_n$, n=3 and 4) on Au(111) substrates were found to adopt different lateral structures for different solvent temperatures (see Table 3.1) and the influence of the spacer chain on the structure. The molecular films of odd-numbered TP$_n$ and BP$_n$ revealed a $(2\sqrt{3} \times \sqrt{3})$R30° arrangement.

Heister et al. [6] used synchrotron-based high resolution X-ray photoelectron spectroscopy (HRXPS) to study the SAM-metal interface and odd-even effects in the aliphatic chain of the biphenyl-substituted alkanethiols (BP$_n$, n=1-4) on Au(111) and Ag(111) substrates. Their results on Au(111) revealed that these effects occurs with the length variation of the aliphatic part in the BP$_n$ molecular film and related to periodical change in the packing density and tilt angle of the film.

Similar investigations were carried out by Frey et al. [71] on SAMs formed from thiophenol (TP), biphenyl-thiol (BPT), Terphenyl-thiol (TPT) and anthracene (AnT) on polycrystalline Au and Ag substrates by means of X-ray photoelectron spectroscopy (XPS) and NEXAFS spectroscopy. The studied systems do not have the alkyl chains between the thiol group and the aromatic ring and, from their results the average

---

[4]BP$_3$ and BP$_4$ were prepared in 100μM ethanolic solution for 24 and 48 hours whereas TP$_n$ monolayers were obtained in ethanolic solutions (2.5μM) for 24 hours.

3.2 Self-Assembled Monolayers and Crystalline Structure of MMTA on Au(111)

Thiols	Structure at @298K	Structure at @333K
TP1	$(2\sqrt{3} \times \sqrt{3})R30°$	$(2\sqrt{3} \times \sqrt{3})R30°$
TP2	$(2\sqrt{3} \times \sqrt{3})R30°$	$c(5\sqrt{3} \times 3)$
TP3	$(2\sqrt{3} \times \sqrt{3})R30°$	$(2\sqrt{3} \times \sqrt{3})R30°$
TP4	$c(5\sqrt{3} \times 3)$	$c(5\sqrt{3} \times 3)$
TP5	$(2\sqrt{3} \times \sqrt{3})R30°$	$(2\sqrt{3} \times \sqrt{3})R30°$
TP6	$c(5\sqrt{3} \times 3)$	$c(5\sqrt{3} \times 3)(\alpha)$
BP3	$(2\sqrt{3} \times \sqrt{3})R30°$	$(2\sqrt{3} \times \sqrt{3})R30°$
BP4	$(5\sqrt{3} \times 3)\text{rect}$	$(5\sqrt{3} \times 3)\text{rect}$

Table 3.1. Structures adopted by the TP_n and BP_n SAMs by using two different preparation temperatures. Adapted from [81, 82].

tilt angle for TP, BPT, TPT, and AnT SAMs were 49°, 23°, 20° and 23° in the case SAMs/Au, whereas 24°, 18°, 16° and 14° in the case SAMs/Ag. On both Au and Ag substrates, the average tilt angles for TP, BPT, TPT revealed that the molecular orientation becomes less tilted with increasing length of the aromatic chain assuming that the intermolecular forces responsible for self-assembling become stronger with increasing number of aromatic units.

3.2.2   Islands and Coverage Analysis

In recent years SAMs have attracted significant attention due to their technological promise in areas that involve surface modification and patterning. Experimental evidences suggest that the molecular layer generally forms via stepwise process, where two-dimensional clusters of close-packed, vertically oriented molecules, nucleate, grow and coalesce from a less dense surface phase [83, 84]. By performing analysis of several topographic images of samples with the thermal treatment, we observed aggregation and formation of cluster of single molecular layer as well as the presence of multilayer regions. The existence of islands showing a range of heights represent an image analysis tremendous cost, moreover very short islands may not be recognized in the island counting procedure. Therefore, we have taken each image and established a cutoff threshold of 1.85nm to determine the height range for the low islands. By doing this,

we determine coverages using the flooding method on topographic images for different height values.
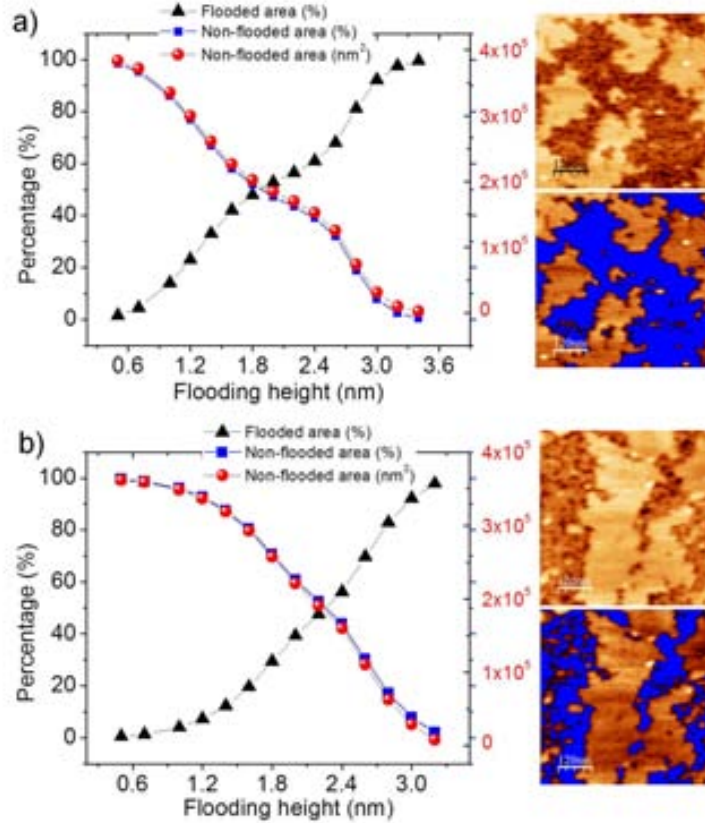
Figure 3.3. (a, b) Flooding analysis of MMTA islands on Au(111) after immersing in a 100μM acetic acid solution of MMTA for 17 hours and after annealing at $100°$C for 16 hours. (a, b) Percentages of flooded and non-flooded areas versus the flooding height (Z_{flood}). Right: original and flooded AFM topographic images (blue level with Z_{flood}=1.85nm).

Figure 3.3 shows the flooding analysis of MMTA islands on Au(111) after immersion in a 100μM acetic acid solution of MMTA for 17 hours and after annealing at $100°$C for 16 hours (a, b) for two different samples. The SFM topographic images were analyzed using WSxM software 4.0 develop 12.21 [26] to estimate coverages by means of flooded and non-flooded areas, as well as a possible morphology of the low islands. Flooded and

3.2 Self-Assembled Monolayers and Crystalline Structure of MMTA on Au(111)

emergent areas versus flooding height (Z_{flood}), percentages (%) vs. Z_{flood} were analyzed through the 0.6×0.6 μm^2 images. It is worthy to note that images of the Au(111) on mica showed monoatomic steps of heights of two atomic planes (0.47nm). Considering small and flat areas of substrate (without monoatomic steps) flooding measurements were carried out.

Then, denoting as h the height of the non-flooded islands and varying the flooding height Z_{flood}, we can estimate the non-flooded area of the low as well as tall islands. Bare gold substrate less than 3% was measured by taking $Z_{flood} = 0.4 \pm 0.15$ for several images within small areas (0.6×0.6 μm^2). The percentage of Au(111) covered by low islands for cutoff threshold of 1.85nm is about 45% for long immersion times and after annealing. The lateral size of the tall islands obtained for 17 hours of immersion revealed dimensions of 350 ± 50 nm, three times longer than the lateral size of tall islands obtained for 30 minutes, both after simultaneous annealing.

Figure 3.4 shows the area estimation and percentage of low islands when the topographic image of 60×60 nm^2 of the marked region in (b) is flooded in a controlled mode. SFM topographic image of a gold surface after immersing in a 100μM acetic acid solution of MMTA for 30 minutes and after annealing at 100°C for 16 hours is shown in (b).

The height value of 1.6 ± 0.15nm for the low islands measured from topographic images has been taken into account to establish the threshold height of 1.85nm. A percentage of about 7% of non-flooded area of the low island is measured for the threshold height. A closer inspection on the scatter plots, we observe that as the flooding height (Z_{flood}) increases, the non flooded area as well as the percentage (%) of area decreases of a non-linear way. This negative non-linear trend will be analyzed by means of known geometries such as the cone frustum and a ellipsoid body. Zones with bare gold substrate was measured less than 2%, as described before.

Figure 3.5 shows the percentages of flooded area and non-flooded islands as well the non-flooded area as a function of the flooding height. By taking the 0.6×0.6 μm^2 SFM topographic images, we obtained the percentage of flooded area (coverage) around of 35% of the low islands in cutoff threshold of 1.9nm and the non-flooded area of 65% for bilayer islands with lateral size of 90nm.
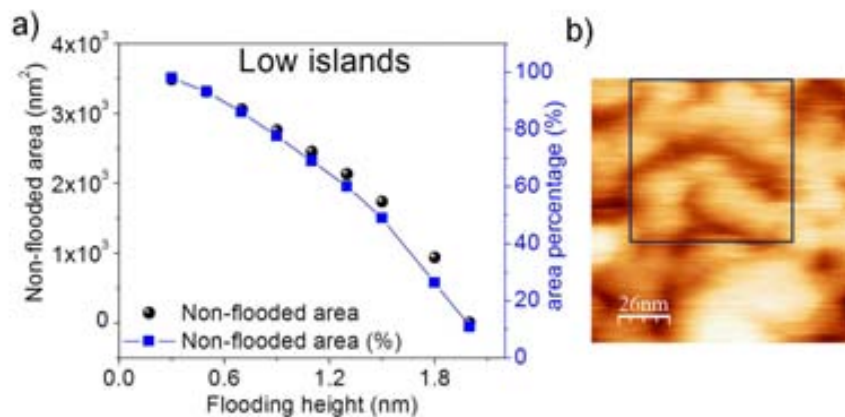
Figure 3.4. Coverage analysis of MMTA low islands on Au(111) after immersing in a $100\mu M$ acetic acid solution of MMTA for 30 minutes and after annealing at 100°C for 16 hours. Non-flooded area and percentage of the low islands versus the flooding height (Z_{flood}) obtained from marked region in (b).
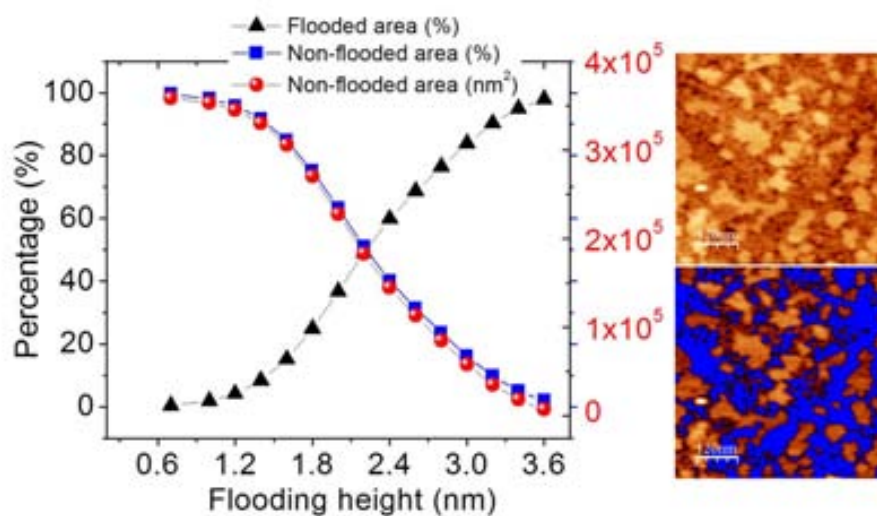
Figure 3.5. Flooding analysis of MMTA islands on Au(111) after immersing in a $100\mu M$ acetic acid solution of MMTA for 30 minutes and after annealing at 100°C for 16 hours. Percentages of flooded and non-flooded area of the islands versus the flooding height. Right: original and flooded AFM topographic images (blue level with Z_{flood}=1.9nm).

3.2 Self-Assembled Monolayers and Crystalline Structure of MMTA on Au(111)

Figure 3.6 shows the flooding analysis performed for the samples prepared from toluene solutions of MMTA in 100μM and 2μM for long immersion times and after annealing. Flooding analysis performed in topographic image (0.65×0.65 μm^2) (a) without annealing, gave $\approx 20\%$ of bilayers on the Au(111) substrate for cutoff threshold of 1.85nm. Above this height, a almost constant trend is observed for percentages and the non-flooded area. Could indicate this fact a different morphology for MMTA islands for different solutions?. The topographic iamge of (0.65×0.65 μm^2) in (b), the low concentration and long immersion times with the thermal proces revealed a 35% of the Au(111) covered with low islands for the threshold height of 1.85nm and tall islands with lateral dimensions of about 100nm.
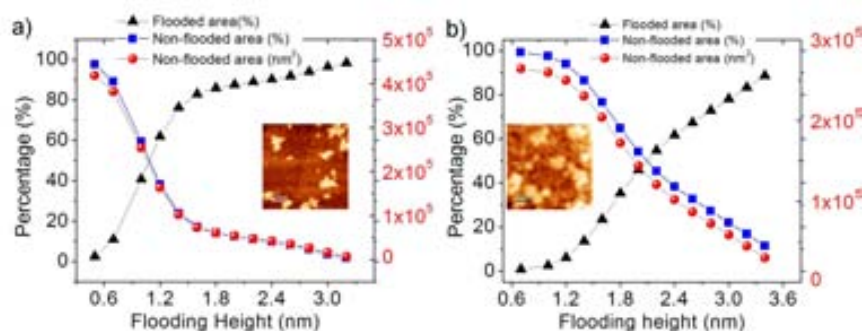
Figure 3.6. Flooding analysis of MMTA islands on Au(111) after immersing in a 100μM toluene solution of MMTA for 20 hours (a) and 2μM for 20 hours after annealing at 120°C for 24 hours (b). (a, b) Percentages of flooded area and non-flooded islands versus the flooding height. Inset: SFM topographic image without annealing (a) and after annealing (b).

Au(111) substrates after immersing in acetic acid and toluene solutions of MMTA and annealing have shown bilayer formation. Larger areas of tall islands have been obtained for longer immersion times and after annealing of about 70%. By comparing the results of coverage in Figures described above, we found the same non-linear trend of the curves below the threshold of 1.85nm, range of heights, in which the low islands have been flooded.

The thermal treatment at 100°C induced morphology changes on the molecular film of MMTA forming low and tall islands on Au(111) that expand laterally. From

flooding analysis of these samples, bare gold substrate ($\approx$2%) was estimated, which it makes minimum the distances between the low islands to coalesce into laterally larger islands. In order to understand the experimental evidence described above, we analyzed the morphologies of the low islands by idealizing their morphologies as formed by an representative geometry. The first approximation is a cone frustum denoting the upper radius r_1, the lower radius r_2, the non-flooded height h and the height of side face g, as shown the cartoon in Figure 3.7(a, right). The surface area (S) of the cone frustum is given by

$$S = \pi \left(r_1 + r_2 \right) \sqrt{\left(r_2 - r_1 \right)^2 + h^2} + \pi \left(r_1 \right)^2 + \pi \left(r_2 \right)^2 \tag{3.1}$$

By replacing $h = k$ - Z_{flood}, being k a positive arbitrary constant (i.e the total height of the low islands), then we observe the negative trend of the curve in (a). For Z_{flood} values below k the area decreases as Z_{flood} increases. If Z_{flood}=0, then we measure the maximum area of the cone frustum. Each new flooding value implies new values of r_2 in which we approximate as $\delta r_2 = r_2(k$ - $Z_{flood})/$ k, following proportionality between triangles. However, the non-linear trend observed do not corresponds to the flooding curves below 1.85nm.

The second approximation is by means of a quadratic surface type ellipsoid. The equation of a standard axis-aligned ellipsoid body in an xyz- cartesian coordinate system is $\frac{x^2}{a_x^2} + \frac{y^2}{a_y^2} + \frac{z^2}{c^2} = 1$, where a_x and a_y are the transverse radii and c the polar radius (along the z-axis). If all three radii are equal, $a_x = a_y = c$, the solid body is a sphere; if two radii are equal, $a_x = a_y > c$, the ellipsoid is an spheroid [5]. The equations 3.2 and 3.3 represent the surface area (S) of a spheroid, prolate and oblate respectively.

$$
\begin{aligned}
S &= \pi \cdot a \cdot c \left\{ \frac{\arcsin m - \arcsin q}{m} + \frac{a}{c} - (1 - \frac{h}{c})\sqrt{1 - q^2} \right\} \\
m &= \sqrt{1 - \frac{a^2}{c^2}} \\
q &= (1 - \frac{h}{c})\sqrt{1 - \frac{a^2}{c^2}}
\end{aligned}
\tag{3.2}
$$

where m is the ellipticity of the prolate spheroid.

---

[5] if $a_x = a_y > c$, is an oblate spheroid; if $a_x = a_y < c$, is a prolate spheroid. For three unequal sides, $a_x > a_y > c$, is a scalene ellipsoid.

3.2 Self-Assembled Monolayers and Crystalline Structure of MMTA on Au(111)
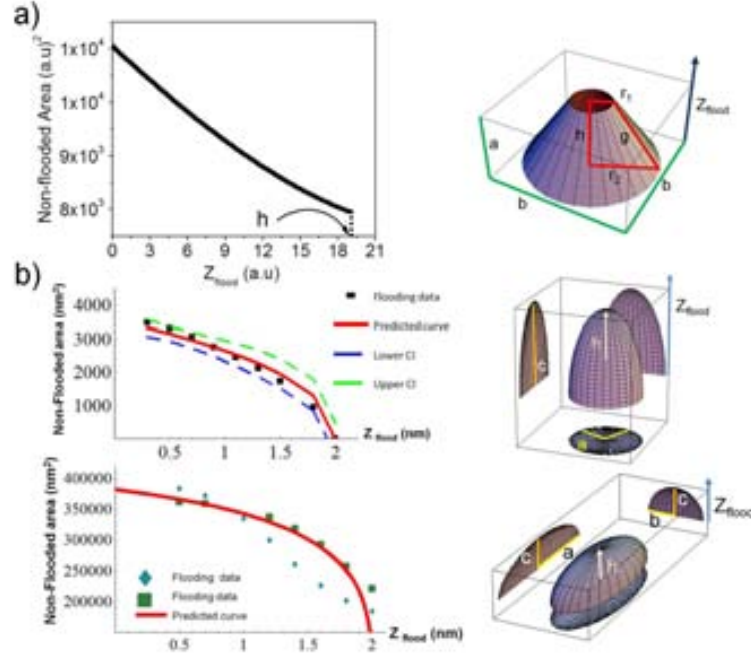
Figure 3.7. Possible morphologies of the low islands after annealing treatment. (a) Cone frustum model (right) and simulated curve of the surface vs. flooding height (Z_{flood}) (left). The h value represents the height of the non-flooded island. (b) Ellipsoid body : prolate spheroid (right, top) and oblate spheroid (right, down). Data from flooding measurements are fits to the oblate spheroid model (upper cap) for a range of flooding below 1.85nm. Semi-axes and height are shown as a, b, c and h, respectively. Legend in (b) indicates the experimental data from flooding (black box), the predicted curve (red line), and the upper and lower confidence interval.

$$S = 2\pi \left\{ a^2 + \frac{c^2}{\sin\alpha} \cdot \ln\frac{1+\sin\alpha}{\cos\alpha} \right\}$$
$$\alpha = \arcsin(\frac{a}{c}) \tag{3.3}$$

Assuming that the low islands follow the same morphology with $c < a \cong b$, a spheroidal model is an acceptable approximation for low percolated islands. Taking into account this constrains we used the approximated formula for any spheroidal body given by Knud Thomsen´s Formula [6] as,

---

[6]This approximation has been discussed and analyzed by Mathematician David W. Cantrell in sci.math newsgroup. Knud Thomsen's formula for the surface area of a general ellipsoid yield a relative error of 1.061% if $p \approx 1.6075$. Discussion and analysis can be followed in http://www.numericana.com/

$$S \approx 4\pi \left(\frac{a_x^p a_y^p + a_x^p c^p + a_y^p c^p}{3} \right)^{\frac{1}{p}} \tag{3.4}$$

In this case, we only analyzed the upper area of the spheroidal cap. The surface area (S) of the spheroidal cap is given by the semi-axes a, b, c and and the height h of upper cap (non-flooded area), as shown in Figure 3.7(b, right) for prolate and oblate spheroids. We simulate the curve in agreement to the equation 3.4 for a half surface area (upper hemisphere) of the non-flooded spheroidal cap, as shown in inset (b, left down). By doing this, we focused on the rate of change of spheroid´s area with $h = (1.85\text{-}Z_{flood})^{p \cdot n}$. The surface area decreases as Z_{flood} increases, then by applying the chain rule to surface area S, $(\frac{dS}{dh} \cdot \frac{dh}{dZ_{flood}})$, we obtain the surface area as a function of Z_{flood}, where n value allows modulate the c value. By taking only the area of the cap (excluding the base) we observed a better non-linear fit of the data (3.7, left top) from flooding performed in Figure 3.4. For a value of Z_{flood}=0, the surface area (S) is maximum, then $h = c$, where $c = 1.85$ nm is the cutoff threshold or the total height of the cap. The fitting results show the raw data (black box), fitted curve (red line) and the 95% conficence intervals (upper and lower CI) for the predicted response of single observations. Expected radii a and b are below 20nm that corresponds to the lateral dimensionns of the low islands, with $n = 0.76$. Floding data from figure 3.3 below 1.85nm were also fitted with expected radii of $a = 5$nm, $b = 55$nm and $c = 1.85$nm, whith $n = 0.69$, as shown (3.7 b, left down). Non-linear fitting was performed using the commercial software Mathematica 5.1 [85].

From physical parameters such as radii and height obtained from fits suggest that the low islands follow a morphology as a ellipsoidal surface, the oblate spheroid. Altough, the AFM artifacts (tip-sample convolution) is an inherent feature of SFM images, the ultra-sharp silicon tip employed during experiments (radii $\approx$ 5nm) reduces the effect.

3.2.3 Influence of the Solvent, Concentration and Immersion Times

It is shown that very well ordered monolayer films of alkanethiols can be obtained by immersion in ethanolic solution. However, because of the low solubility of aromatic

---

answer/ellipsoid.htm#thomsen.

derivatives, longer immersion times and elevated concentration values can lead to a possible formation of multilayers on the substrate. In the present work, we show the influence of these parameters on the molecular film for samples prepared at room temperature and then the thermal treatment.

3.2.3.1 Morphologies from Tetrahydrofuran Solutions of MMTA

MMTA samples obtained in 100μM THF solutions of MMTA were prepared to study the morphological changes, structure and their electrical response prior to and after annealing. Atomically flat Au(111) substrates previously described in section 2.3 were employed. Au(111) substrates were immersed in tetrahydrofuran (THF) solution of MMTA for 30 minutes, then taken out of the solution and rinsed with the pure solvent THF to remove physisorbed molecules.

By using THF solutions of MMTA, we observed low surface coverage for 30 minutes of immersion, so longer immersion times are needed for monolayer formation; unlike other solutions with different solvents. This fact, reveals the importance of the solvent used in SAMs formation, i.e. the terphenyl methanethiol (TPMT) and carboxy-terphenyl methanethiol (CTPMT, nowadays MMTA) in ethanolic solution for 24 hours form well-ordered monolayer or bilayers, whereas CTPMT bilayers of 3.4 ± 0.3nm immersed into trifluoroacetic acid could form single layers thickness of 1.8nm, which it has been shown by means of XPS data[77].

Scratching experiments performed on the molecular film by using both Au(111) on glass and mica allow measuring the molecular film thickness having the bare gold as reference, as shown in Figures 3.8 and 3.9. The molecular surface in Figure 3.8 looks rough and like percolated and there are no monoatomic steps visible (a) before and (c) after scratching. Once done the scratching on the film, the height difference was found to be 1.4 ± 0.1nm from profiles taken on the film that could correspond to a single molecular layer.

An homogeneous molecular film following the relief of the gold substrate can be observed from Figure 3.9 and some monoatomic steps are visible. After scratching the surface, and then re-imaging, the square scratched area can be seen that MMTA molecules have been removed as material accumulation on the border and the under-
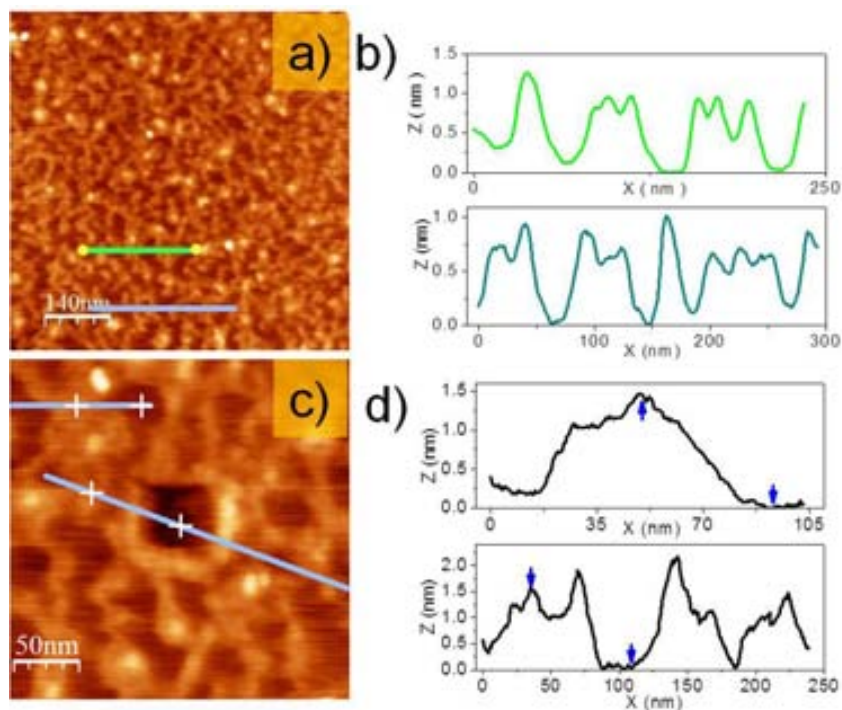
Figure 3.8. Topographic images (a, c) show small cluster of islands like a percolated. Cross-sectional profiles (b, d) allow to compare the island cluster heights prior to and after scratching the molecular film, respectively. Au(111) on glass from Arrrandee was used. Total z-scale: (a, c) 0-5nm.

lying monoatomic steps. Left and right sides of profile in Figure 3.9(b) reveal a height molecular film of 1.3±0.1nm, by zooming in the scratched region, inset in (c), shows three atomically flat terraces (2.38Å) of Au(111), as shown in (c).

3.2.3.2 Morphologies and Structure from Acetic Acid Solutions of MMTA

Self-Assembled monolayers were prepared by using acetic acid solutions with concentrations ranging from 0.5 μM to 100μM for 30 minutes of immersion time. Low coverages on the surface were observed in the range 0.5μM to 2μM, whereas at higher molecular coverage (100μM) the Au(111) surface is hardly covered with the MMTA molecules as shown in Figure 3.10. Topographic images (a, b, c) show MMTA molecules adsorbed on Au(111) substrate, thus allowing to recognize the monoatomic step between

3.2 Self-Assembled Monolayers and Crystalline Structure of MMTA on Au(111)
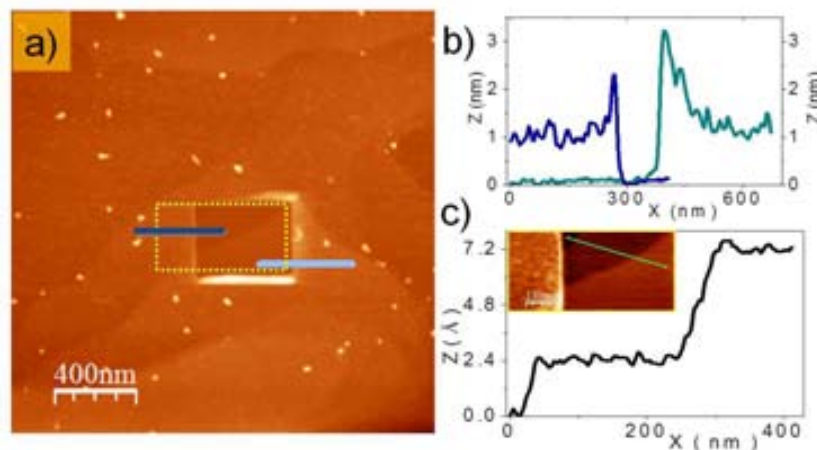
Figure 3.9. SFM of a region scratched into a MMTA molecular film. (a) Topographic image of MMTA molecular film on Au(111) on mica. (b) Left and right profiles show an homogeneous molecular film following the relief of monoatomic gold terraces out of the scratched area. (c) Profile on the monoatomic steps of the gold surface pointed out with the dashed line. Total z-scale: (a) 0-17nm.

underlying terraces and some regions with defects like holes in the morphology in a lower number, as observed for other thiol SAMs. Cross-sectional topographic line scan along the molecular film in (c) shows that the depressions are around 0.3 nm, as shown in Figure 3.10 (d).

Despite the difficulty for measuring the structure dimension of the samples prepared for 30 minutes of immersion time, the corresponding high-resolution lateral force image indicates the presence of a degree of lateral order and domains rotated by $=120°$ with respect to each other, reflecting the substrate symmetry (see Figure 3.11). High resolution lateral force images (a, c, d) revealed that molecular domains exhibit an oblique unit cell described with dimensions $\mathbf{a} = 1.05\pm 0.5$ nm and $\mathbf{b} = 0.55\pm0.03$ nm, which suggest the $(2\sqrt{3} \times \sqrt{3})$R30° molecular arrangement already reported for odd-numbered terphenyls and biphenyls (TP_n, BP_n) SAMs on Au(111), as shown in 2D-FFT image (b).

For longer immersion times we observed high coverage of the substrate using 100μM solutions of MMTA , instead of the molecular islands or 3D structures observed on substrates soaked in ethanolic solutions of MMTA. Figure 3.12 (a, b) shows topographic
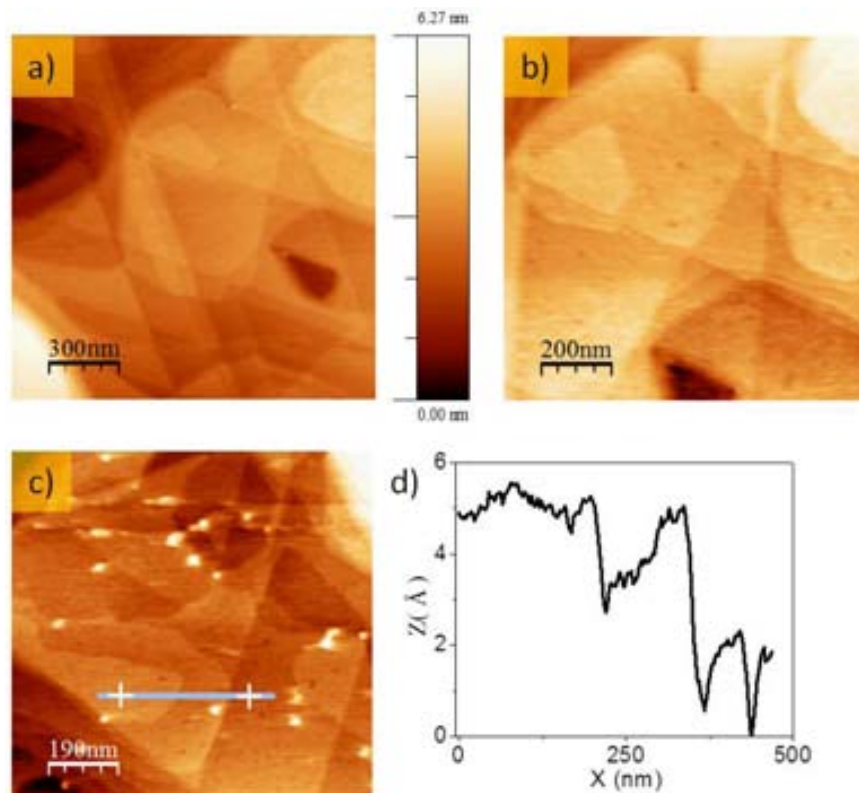
Figure 3.10. SFM images of MMTA on Au(111) after immersing in 100μM acetic acid solution of MMTA for 30 minutes. Topographic images (a, b, c) show adsorbed molecules on monoatomic terraces of Au (111) (a, b, c) and the presence of holes on the molecular film. (d) Cross-sectional topographic line along the direction marked in (c) reveals the size of holes.

images in contact mode and statistically representative of the morphology's layers. Cross-sectional profiles (c) taken on the molecular film in (b) revealed a height difference of 0.24nm between consecutive Au(111) steps.

3.2.3.3 Morphologies and Structure from Ethanolic Solutions of MMTA

Figure 3.13 (a) shows large scan area SFM recorded for Au(111) on glass covered with 3D-structures and monolayers of MMTA molecular film, formed after $\approx$ 5 days from 2μM ethanolic solution of MMTA. We observed three-dimensional structures formed by several layers stacking (b, by zooming in the image a). A range of heights

3.2 Self-Assembled Monolayers and Crystalline Structure of MMTA on Au(111)
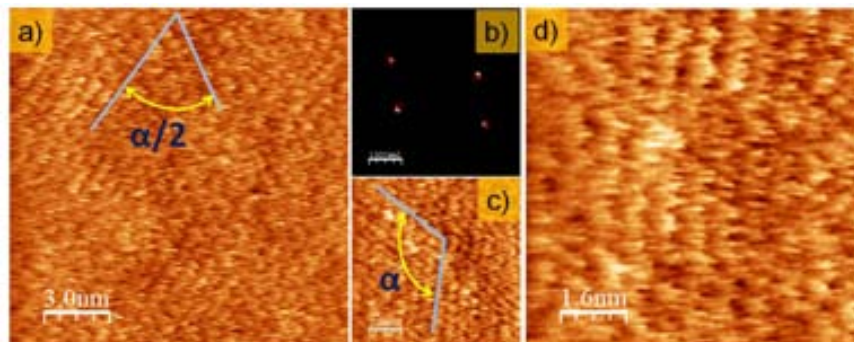
Figure 3.11. High-resolution lateral force images (a, c, d) for Au(111) substrates immersed in a 100μM acetic acid solution of MMTA for 30 minutes. Some domains, and directions can be observed and the unit cell of the $(2\sqrt{3} \times \sqrt{3})$R30° structure can be measured in 2D-FFT as well as high resolution lateral forces images. 2D-Fast Fourier Transformed filtered image for the whole image in (a) is shown in (b).
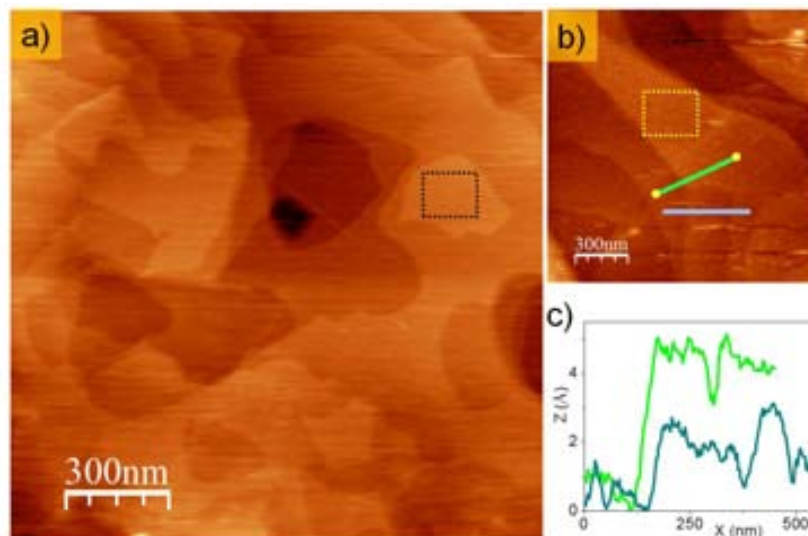
Figure 3.12. Topography (a, b) images of MMTA on Au(111) substrate immersed in acetic acid solution at 100μM for 17 hours. Profiles in (c) show several height values for the same organic layer. RMS roughness of 0.6 ± 0.15 Å was estimated on rectangular areas in (a, b). Total z-scale: (a) 0-3nm; (b) 0-4nm.

from 1 nm to 30 nm were observed for some 3D-structures of the bilayer stacks, as shown in (d) from profile taken in (b). Interestingly, small cluster of molecules on the
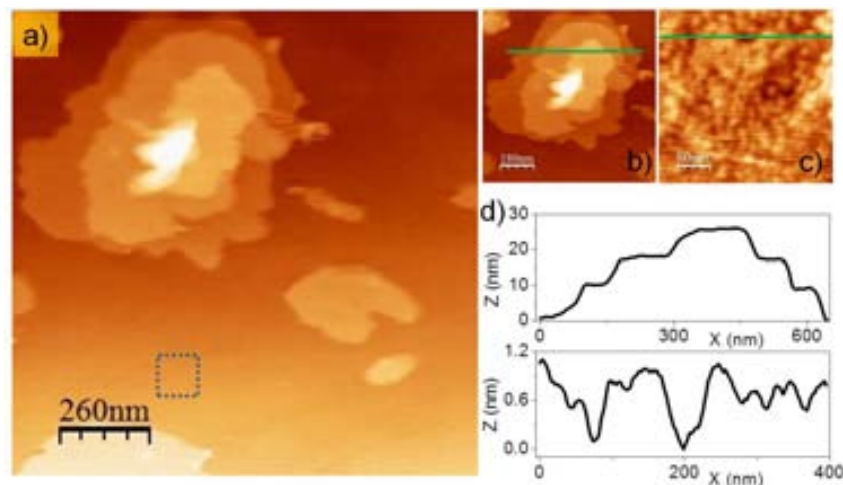
Figure 3.13. SFM images showing the Au(111) surface after immersing in a 2μM ethanolic solution of MMTA for ≈ 5 days. Topographic (a, b) images of 3D-structures and the image in (c) obtained by zooming in the molecular growth within the marked zone in (a). Total z-scale: (a)0-78nm; (c)0-2nm.

substrate (c, by zooming in the marked zone in a) were observed with a height difference of 1.0±0.1 nm.

A closer inspection to the three levels of the multilayer surface (see Figure 3.14), in particular the second level with height of ≈ 20nm leads to observe an incomplete formation of the layer. By taking a profile on this zone of the layer, one can measure a height difference of ≈ 1.6nm. This observation allow us to consider that each level of the 3D-structure is formed by the stack and close-packed of molecules. Histogram of heights performed on the colored topographic image of this structure revealed high events close to 2.5nm, 12nm, 20nm, 25nm and 28nm, thus allowing to estimate the forming of the second level of at least seven layers.

Figure 3.15 shows the morphological changes of fresh molecular films measured in contact (a, b, c, e) and dynamic (d, f) modes. For few seconds of immersion times, some characteristic of the first step of molecular adsorption can be observed, (i.e. defects on the molecular layer, vacancies), whereas at least for 30 minutes an ordered molecular film is formed due to their interchain interactions. Usually monolayers at low concentration values ($\approx 2\mu$M) are obtained after 24 hours of immersion in ethanolic
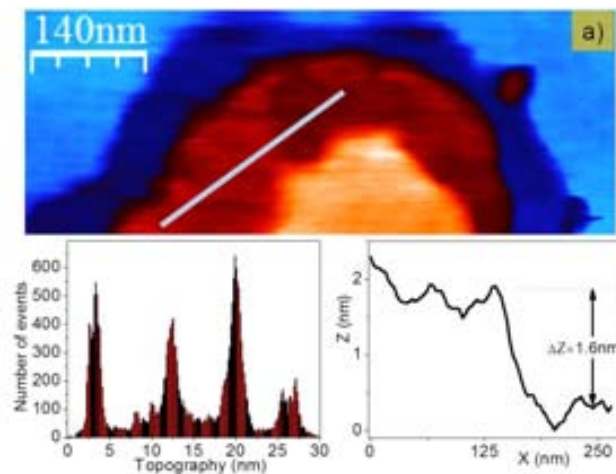
Figure 3.14. Topographic image (a) showing several levels of the 3D nanostructure. Histogram represents the height distribution for those area, whereas a topographic profile is drawn to show a height difference of $\approx$ 1.6nm within the same level.
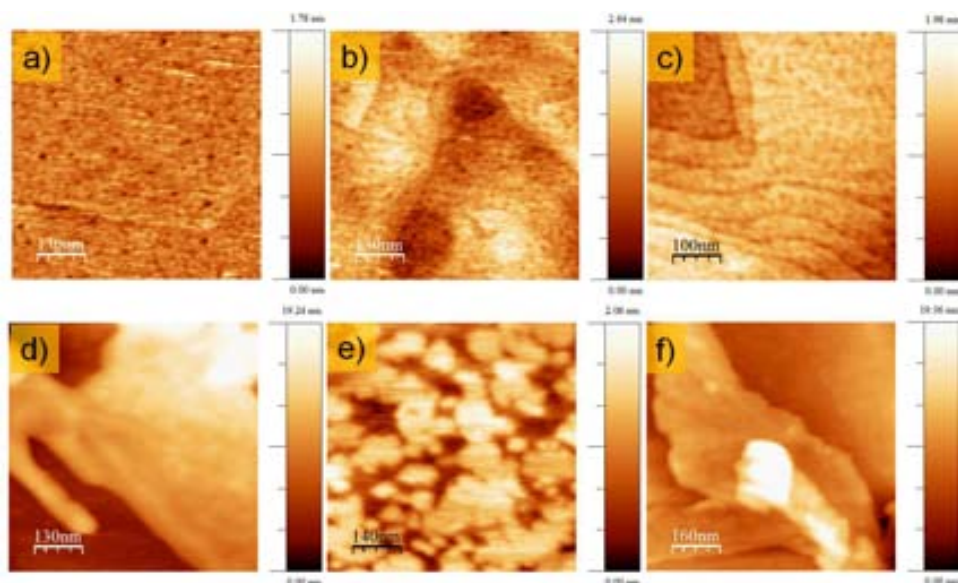
Figure 3.15. Morphological evolution into 3D structures. SFM topographic images showing the Au(111) surface after immersing in a 100μM ethanolic solution of MMTA for (a) 10s ;(b) 30s; (c) 30 minutes; (d) 4 hours; (e) 18 hours and (f) 20 hours.
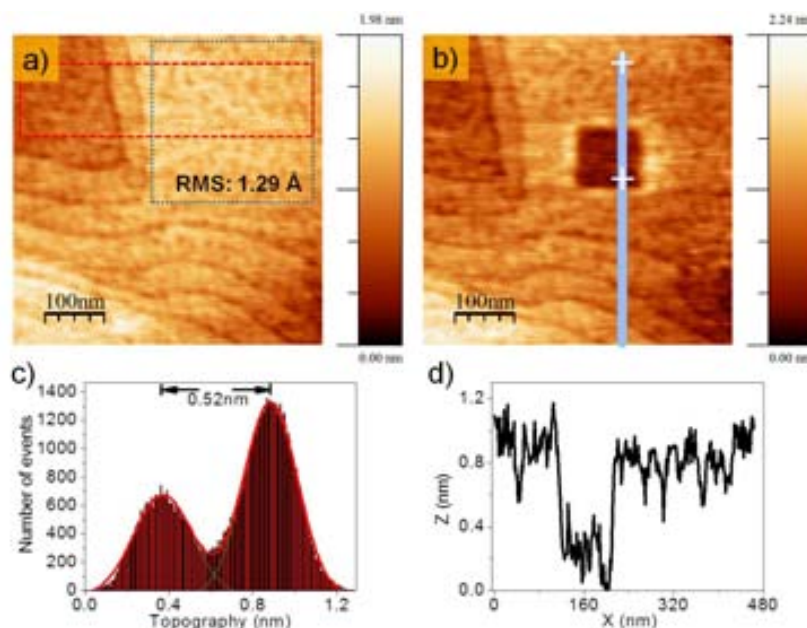
Figure 3.16. Topographic (a, b) images before and after scratching experiment. A RMS roughness of 0.13nm was measured on the marked zone with a gray dashed line, whereas on the rectangular zone marked with a red dashed line the height difference of 0.52 nm the corresponding to 2 monoatomic steps was measured. Profile across of the scratching zone is showed in (d). Au(111) substrates after immersing in 100μM ethanolic solution for 30 minutes of immersion time.

solutions of MMTA; however, for $\approx 100\mu$M, we observed islands and 3D structures on the surface from immersion times above 4 hours.

For 30 minutes of immersion time (see Figure 3.16), we observed terraces of Au(111) covered by the molecular film following the relief of the substrate. We also performed a scratching on a flat region of the film which revealed a height difference of 1.1±0.1 nm for the layer thickness (see Figure 3.16)(b, d). Two monoatomic steps were measured from the histogram (c) for the rectangular area with the dashed red line in (a), whereas a RMS roughness of 0.13nm on a flat area and marked with a dashed line was measured. On the contrary, for low concentration (0.05μM - 0.09μM) range, we did not observe islands or 3D structures even for longer immersion times, at least 11 days.

Two molecular films of MMTA on Au (111) formed after 11 and 2 days by using 0.05μM and 100μM solutions are shown in Figure 3.17(a, b), respectively. From earlier

3.2 Self-Assembled Monolayers and Crystalline Structure of MMTA on Au(111)
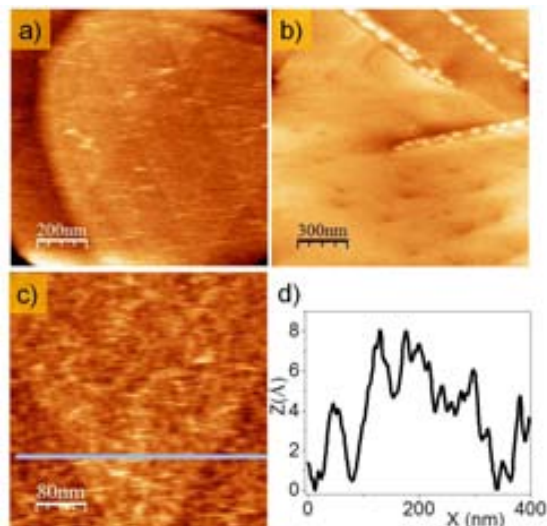
Figure 3.17. Topographic (a, b, c) images of Au(111) substrates immersed in ethanolic solutions of MMTA. (a, c) Topographic images of the sample immersed 11 days in a $0.05\mu M$ solution and (b) topographic image of the sample prepared for 2 days in $100\mu M$ solution. (c) Topographic profile taken between monoatomic steps covered with the molecular film is shown in (d). Total z-scale: (a) 0-6nm; (b) 0-22nm; (c) 0-1.7nm.

studies in alkanethiols, it is known that the minimum concentration for forming a dense SAM is $1\mu M$ but it takes a long immersion time [86]. The immersion time for SAM formation at this concentration is between 12 and 24 hours, where the first process to attach the molecules on the substrate takes a few minute and the second process to organize the adsorbates and form ordered layers takes several hours. This fact is observed in SFM topographic images (a, c) recorded for lower concentration ($0.05\mu M$) in a long immersion period. A RMS roughness value of 0.17nm was estimated for the whole image in (c). From topographic profile taken along the line in (c), we can deduce that at lower concentrations the molecular film is not ordered and the first phase (lying-down molecules) is occurring even for longer immersion times. On the contrary, ordered and compactness molecular layers were obtained by using 100μ solutions after immersing for 2 days, as shown in (b).

Some samples were prepared by means of drop-casting method employing low concentrations ($2\mu M$) to avoid high coverages on the gold surface. Au(111) on mica
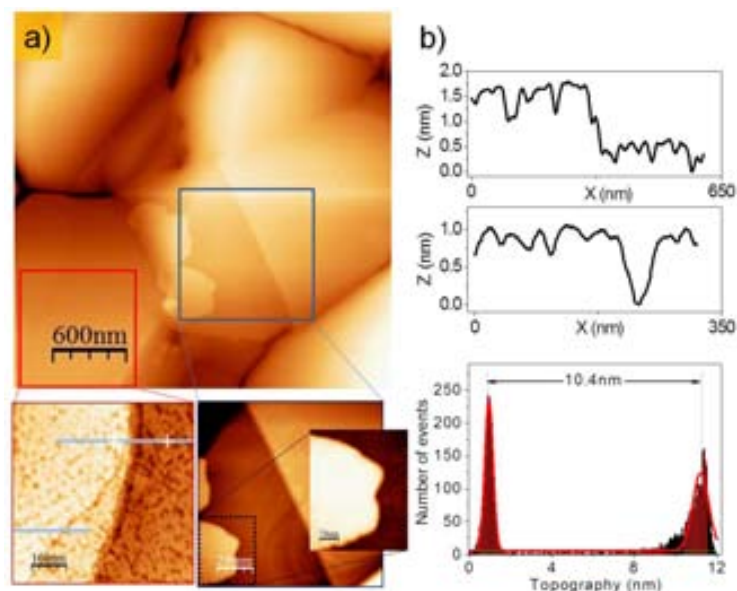
Figure 3.18. Left: topographic image (a) of flat terraces covered by the molecular film with some 3D structures formed on Au(111) substrate. Covered terraces and 3D structure in (a) are shown (down), by zooming in the images. Right: topographic profiles taken along the lines in (zooming in the image a) show an incomplete monolayer, whereas an histogram shows the height difference value for the 3D structure. Drop-casting method using a 2μM ethanolic solution.

and Au(111) on glass surfaces were used, as described in chapter 2. By using this method, we observed partial coverages of the surface, which allowed the self-assembly of the MMTA molecules like single molecular thickness in addition of the 3D structures.

3D structures were observed by immersion as well as drop-casting method using 2μM ethanolic solutions of MMTA. The first one, after immersing the Au(111) substrates into solutions for $\approx$5 days while the second one, by depositing a drop of solution on the Au(111) surface which is evaporated in few minutes.

Figure 3.18 shows the topographic image (a) with two marked zones to show the molecular film on the gold terraces and their respective profiles in panel (b), an histogram was performed to determine the height of the 3D structure. The measured height for this first layer showed values of 1.2$\pm$0.1nm and above 5nm for the 3D structures, in particular of about 10.4nm for the histogram in panel (b). Several and reproducible 3D structures were obtained by drop-casting method in 2μM ethanolic

solutions of MMTA.
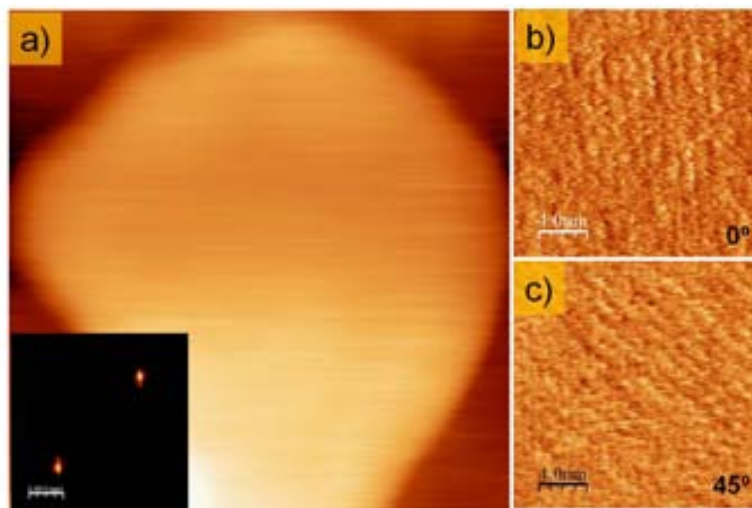
Figure 3.19. Topographic (a) and high resolution lateral force images (b, c). Inset in (a) shows the 2D-FFT filtered image of lateral force image in (c).

To study possible molecular arrangements on the 3D structures, we used the FFM acquisition mode. High resolution lateral force images on the 3D structure revealed a striped pattern as shown the Figure 3.19 (b, c). The inset in (a) shows its 2D-Fast-Fourier Transformed filtered image. A periodicity of 1.1 ± 0.05 nm was measured from (2D-FFT) image recorded at 0° (b) and 45° (c). This periodicity corresponds to the $2\sqrt{3}$ length of the unit cell of terphenyl-methanethiol structures on Au(111).

Dynamic force microscopy (DFM) has been used in the non-contact attractive regime to explore the molecular surface over large areas prior to any experiment (see Figure 3.20). In dynamic mode, we observed 3D structures (a) and by applying a voltage to the tip some layers of topmost surface were removed after passing to the contact mode, as shown in (b) in dynamic mode again. From numbered (1) topographic profile taken along the line in (a) prior to peeling, a height difference of ≈16nm for the 3D structure was measured. After peeling of the layer, we observed height differences as shown numbered profiles (2 and 3) taken along the lines in (b). Profiles (1 and 3) taken prior to and after peeling of the 3D structure revealed height differences of 1.47nm,
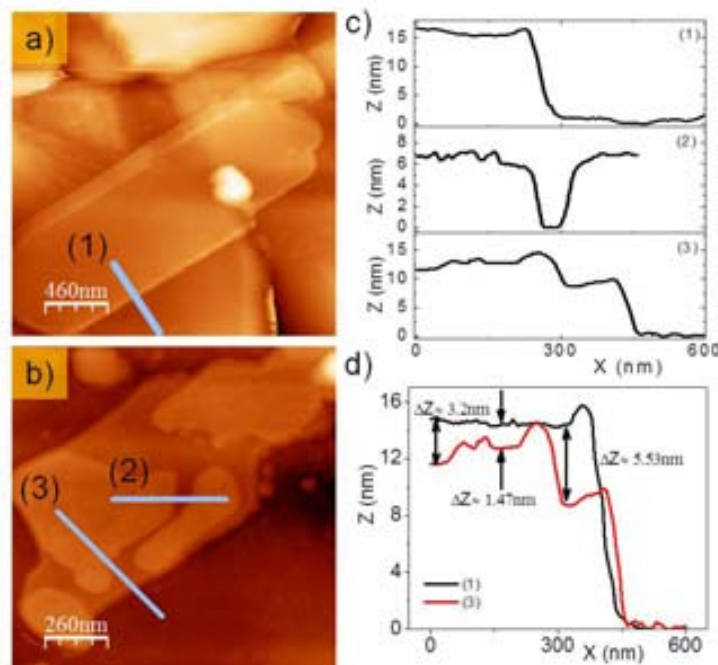
Figure 3.20. Topography image recorded from dynamic mode (a) prior to (b) after peeling the surface. Image (b) shows some removed layers after applying a low voltage to the tip. Topographic profiles taken along the lines in (a, b) are show in (c), whereas numbered profiles (1) and (3) are used to determine the height difference of the removed layers (d).

3.2nm and 5.53nm the corresponding single and bilayer lengths, as shown in (d). In this case, we show that low positive voltages (1.5V) are capable of peeling away the surface of a molecular film, as reported in TTF derivatives [87].

SFM topographic images recorded over large areas revealed both 3D structures and terraces of the substrate covered with the MMTA molecular film. A closer inspection on the molecular film showed a RMS roughness of 0.12nm and height of about 0.6nm (see Figure 3.21) (a, b); in addition, lateral force images revealed different friction for some small regions of the scanned area. Lateral force (c, d) images show bright/dark regions in forward/backward scan directions that correspond at the lowest in topographic image and associated to the gold substrate. The high resolution lateral force images on the domain arrangement could provide information on the molecular structure of the

multilayers.
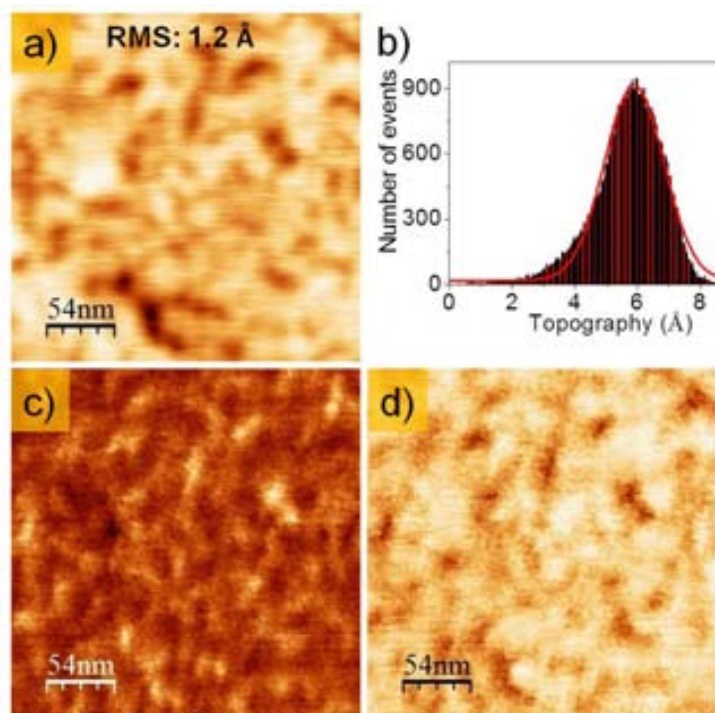
Figure 3.21. Topographic image (a) on a small region of the gold terrace. Histogram shows a height value of 0.6nm and RMS roughness of 0.12nm for the whole image. Lateral force images (Fw&Bw) (c, d) show less friction on the islands for forward than backward scan directions. Total z-scale: (a) 0-0.8nm; (c)-125mV to -16mV; (d)-192mV to -80mV.

Figure 3.22 shows topographic image (a), the lateral force (b, c) images (Fw&Bw), high lateral resolution image taken on flat areas in (a) is displayed in (d). By Zooming in the marked area in (d) is displayed in (e). According to the molecular lengths obtained from high lateral resolution images and 2D-FFT filtered image (d, inset), a structural model for the MMTA self-assembly is shown in (f). In spite of the rough appearance of the images at these scales, high resolution images show molecular order.

A closer inspection in (d) indicates two main directions rotated 120° and marked by the gray color line in which the domains of 60nm^2, of the order of the contact area, are arranged in a quasi-hexagonal fashion with an oblique lattice as seen in the 2D-FFT
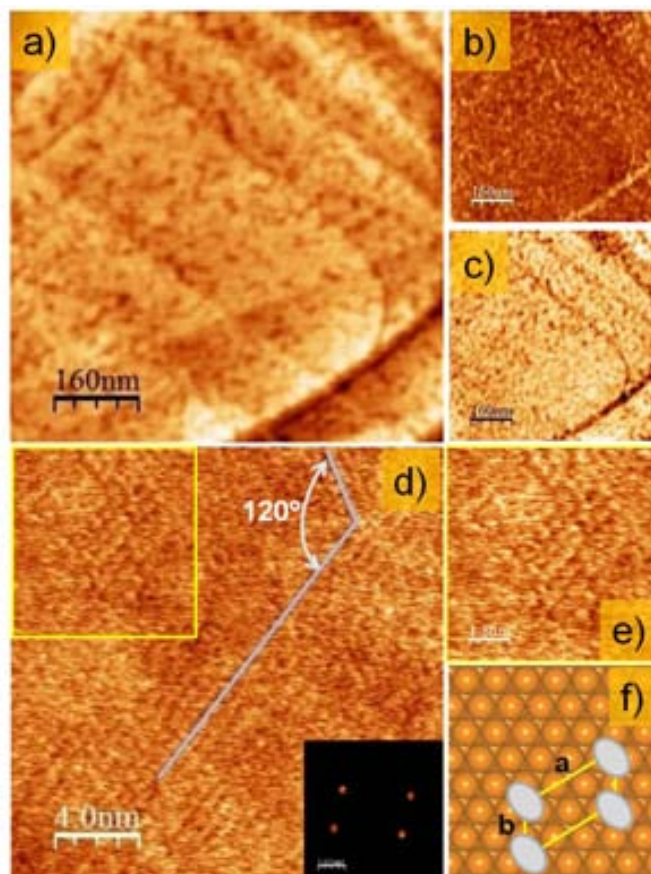
Figure 3.22. Au (111) terraces covered with MMTA molecular film (a) and lateral forces images (b, c) for Fw&Bw scan directions are shown. Panel (d) displays the high lateral force image showing the presence of small molecular domains on the substrate. Panel (e) shows the marked region by the yellow line in (d). Top view of a $(2\sqrt{3}\times\sqrt{3})$R30° structure model for MMTA on Au(111) according to the measured lengths and data from 2D-FFT filtered image (d, inset) in (f). The oval shape represents the projected area of the van der Waals dimensions of the phenyl ring on the substrate.

image (d, inset) and by zooming in the image, as shown in (e). The dimensions of the unit cell have been measured by taking profiles on the high resolution image (d) and magnified areas of the same terrace (e) as well as measuring directly on the 2D-FFT image. These measurements yielded values of **a**=1.01±0.08 nm and **b**=0.5±0.05 nm. By comparing such dimensions with the underlying substrate lattice Au(111) suggests the existence of a $(2\sqrt{3}\times\sqrt{3})R30°$ structure showed in Figure 3.22 (f), where the oval

61

shape represents the projected area of the van der Waals dimensions[7] of the phenyl ring on the substrate.

In previous studies, Fuxen [70] proposed a structural model for adlayer of TPT (Terphenyl thiol) and TPMT (Terphenylmethanethiol) on Au(111) using ethanolic solution at 2.5μM. Their results by LEED studies have shown a $(2\sqrt{3} \times \sqrt{3})$R30° superstructure for monolayer films of TPT and TPMT annealing in UHV between 370-470K. Aguilar et al. [88] and Su et al. [89] have also shown a $(2\sqrt{3} \times \sqrt{3})R30°$ structure for monolayer prepared by immersing Au(111) electrodes in ethanolic solution (2μM-100μM) of BP$_n$ thiols after annealing between 12-15 hours at 60°C-90°C by means of STM using organic solvents, in particular for n=3 (BP3) SAMs. From these results, a $(2\sqrt{3} \times \sqrt{3})R30°$ structure is common for BP$_{odd}$, TP$_{odd}$ and MMTA (functionalized TP$_{odd}$) showing the relevance of the alkyl spacer in all cases.

3.2.3.4   Bilayers from Toluene Solutions of MMTA

Figure 3.23 shows two stages of molecular film formation. Cluster of tall islands in topographic image (a) are formed on the terraces following the relief of the underlying Au(111) surface; a different region of the sample was explored revealing the bilayer formation. Height profiles taken along the lines in (c) are displayed in (e) where a height difference of 3.3±0.2nm was estimated, whereas the histogram in (d) revealed for the tall islands a height difference of 2.6nm. Magnified topographic images revealed slight height variations consisting of brighter spots close to the holes with heights of about 50nm.

The occupied volume for the excess of material close to/or inside the holes was correlated to the holes observed on the bilayer, in agreement with the area and volume dimensions measured from profiles and image analysis. Flooding procedure was performed on the topographic images by separating both holes and accumulated material (brighter spots) to estimated their areas. Flooding height of 3.1±0.1 was used to know the area and volume of holes. Afterwards, by flooding a small area where the accumulated area was present, we obtained a volume value of the non-flooded area. These values were also calculated by taking several profiles on the studied area (see

---

[7]van der Waals dimensions for the phenyl group of 6.4Å by 3.3Å were considered by Fuxen et al.
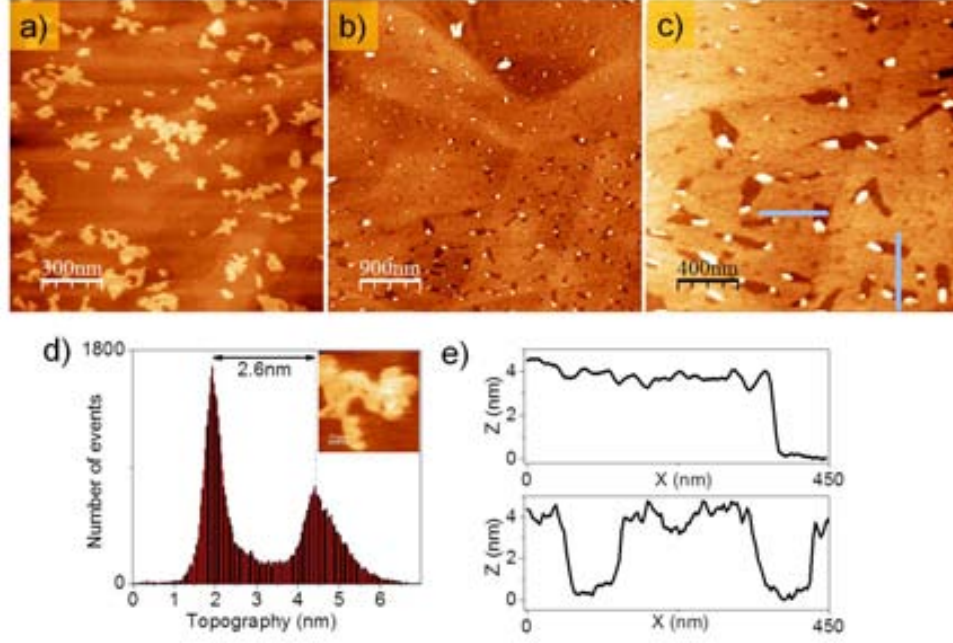
Figure 3.23. SFM images of Au(111) on mica after immersing in a 100μM toluene solution of MMTA for 20 hours. Topographic (a, b, c) images show SAM islands in two stages of film formation. Histogram in (d) and profiles taken along the lines in (c) show the height difference for the islands for the bilayer case (e). Total z-scale: (a)0-7nm; (b) 0-61nm; (c)0-23nm.

Figure 3.24)(a, b, c). Some values of volume of holes and accumulated material are shown in table 3.2 and the absolute error between calculated magnitudes.

Hole	V_h nm^3	$V_{acc.}$ nm^3	$|error|$ $\approx (\%)$
1	57312	58740	3
2	44403	39110	11
3	33000	36496	10
4	48666	47268	3
5	13189	12000	9

Table 3.2. Volume of numbered holes, V_h and Volume of the accumulated material inside or next to holes, $V_{acc.}$. Absolute error values are estimated as $\frac{V_h - V_{acc}}{V_h}$.

3.2 Self-Assembled Monolayers and Crystalline Structure of MMTA on Au(111)
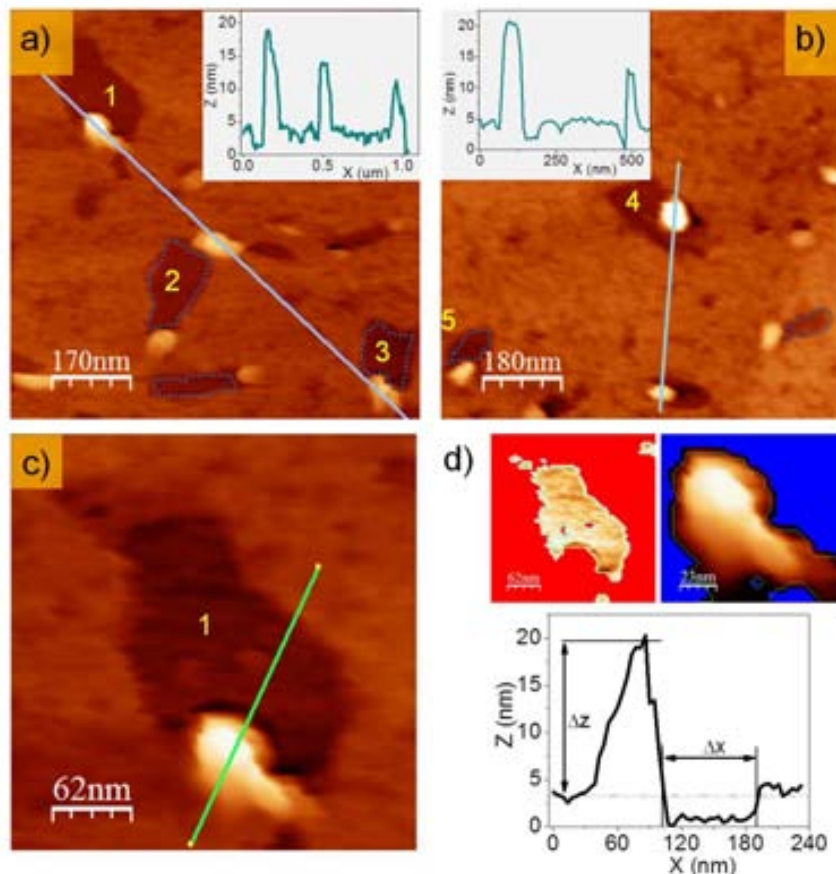
Figure 3.24. SFM images of Au(111) on mica after immersing in a 100μM toluene solution of MMTA for 20 hours. Topographic (a, b, c) images show holes on the bilayer. A closer inspection on the scanned area shows brighter spots next to or inside the holes. Topographic profiles along the lines in (b, c) are shown in insets. Some hole areas have been numbered and marked with dashed lines in (a, b). The volume of the holes and the accumulated material (brighter spots) have been estimate by flooding procedure. The image in (c) of the numbered hole (1) is used to flood and estimate the hole area and volume for a flooding height (d, left). The volume of the accumulated material is calculated by software or by taking profiles to estimate an average height (d, right).

In agreement to the stages of bilayer formation observed in figure (3.23), the tall islands follow a nucleation mechanism: groups of molecules adsorb to the substrate and growth into structured domains forming also domain boundaries. Because the domains may not be oriented in the same direction, the lateral van der Waals interactions

between domains are disrupted. Also, several factors such as the cleanliness of the substrate, purity of the solution or reconstruction of the surface during assembly produce defects in SAMs.

The accumulated material and correlated with the volume of holes could be due to two process: the first one, a desorption process at the defect sites in the molecular film and then at random nucleation site within the well-organized regions of the film. The second one, due to the weakened lateral interactions at domain boundaries of the clustered tall islands.

3.2.4   Thermal Treatment Effect

As shown in previous results, 3D structures have been obtained using ethanolic solutions of MMTA for longer immersion times as well as drop-casting without annealing. However, the annealing process could form high quality or close packed SAMs and 3D nanostructures due to reduction of defects, coalescence of small domains into larger ones and allowing measuring at submonolayer scale [90, 91]. In this section, we will show the effect on the SAMs morphology after annealing process.

3.2.4.1   Morphologies from Tetrahydrofuran Solutions of MMTA
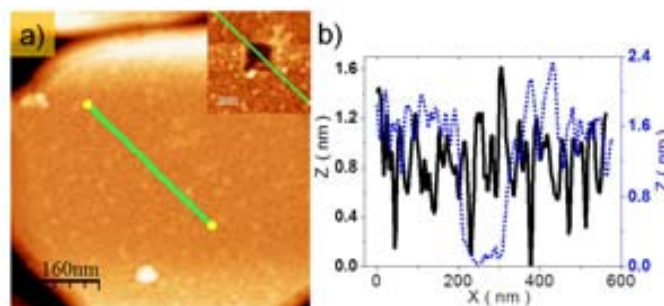
Figure 3.25. SFM images of Au(111) on glass after immersing in a 100μM THF solution of MMTA for 30 minutes and after annealing at $126°$C for 15 hours. Topographic image (a) without and with scratch (inset) on the surface is showed. Panel (b) shows both profiles taken on the surface previous (continuous line) and after scratching (dashed line).

3.2 Self-Assembled Monolayers and Crystalline Structure of MMTA on Au(111)
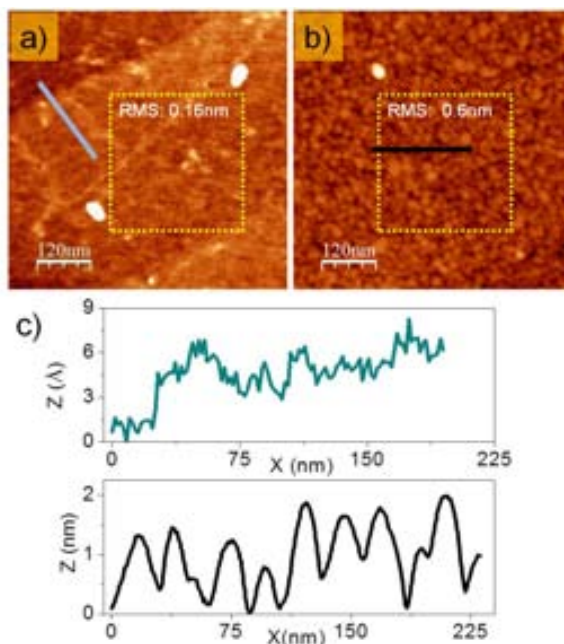
Figure 3.26. SFM images showing the Au(111) on mica surface after immersing in a 100μM THF solution of MMTA for 30 minutes. Topographic image before (a) and after (b) annealing process. Topographic profiles in (c) were taken along the lines in (a) and (b) with two different colors. A RMS roughness value prior to and after annealing was measured within regions marked with yellow dashed line.

Once done morphological characterization on fresh samples, these were annealed at 126°C for 15 hours using a furnace in air. Morphological changes were observed after the thermal treatment to the samples using Au(111) on glass/mica substrates. SFM images of Au(111) on glass after immersing in a 100μM THF solution of MMTA for 30 minutes and after annealing are shown in Figure 3.25.

Topographic image 3.25 (a) reveals low MMTA islands of height 1.6±0.1nm and lateral dimensions below 10nm from profiles taken on the same area, prior to and after scratching (inset) the surface to compare heights as shown the continuous and dashed line in panel (b), respectively. Bilayer islands below 20nm in lateral dimensions were observed using Au(111) on glass. MMTA islands with longer lateral dimensions were observed using Au(111) after annealing for 30 minutes and 18 hours of immersion time.

As we can observe in the Figure 3.26 (a) the morphology of the molecular film at

66

room temperature is characterized by a lot of islands and their height correspond to an atomic step of the gold substrate, as shown topographic profile (c) take along the line in (a, top). After annealing of the sample at 126°C for 15 hours we observed that these islands are now bigger and wider, as revealed topographic profile (c, down) taken along the line in (b). Marked regions in (a, b) show the RMS roughness of 0.16nm and 0.6nm prior to and after annealing, respectively. Larger tilt angles reduce the geometrical thickness of the film. Panel (c) shows two profiles taken on the surface without and with annealing in which we observe low islands of a single molecular thickness on the thermally treated sample correspondy to a tilt angle of $\approx 20°$.
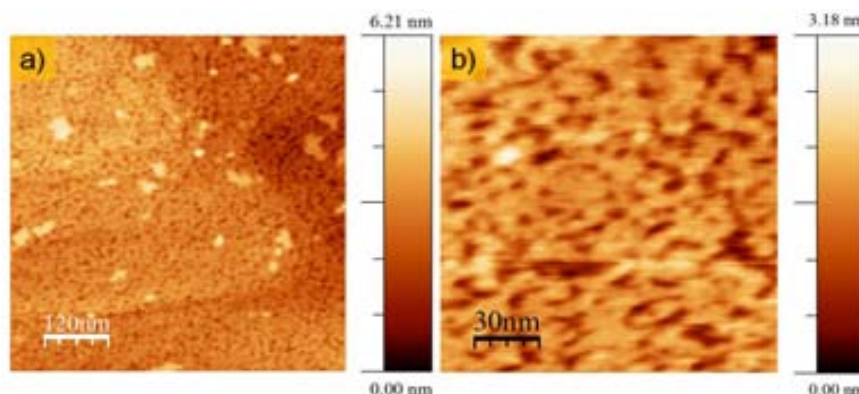
Figure 3.27. SFM images of Au(111) on mica after immersing in a $100\mu M$ THF solution of MMTA for 16 hours and after annealing at 120°C for 16 hours. Topographic (a, b) images show the low islands and some tall islands on the surface.

In Figure 3.27 we present topographic images of Au(111) on mica after immersing in a $100\mu M$ THF solution of MMTA for 16 hours and after annealing at 120°C for 16 hours. Topographic images reveal an incomplete monolayer formation after annealing and RMS roughness of 0.4nm for the whole image in (b). Bilayer islands were rarely observed for several preparations and measurements using this solvent.

After annealing process, for both Au(111) on mica and Au(111) on glass few bilayer islands were observed for 30 minutes as well as 16 hours of immersion times. This fact suggest that the use of THF solvent allows the formation of single molecular thickness

of MMTA on Au(111) substrates at submonolayer scale by means of the annealing process.

3.2.4.2   Morphologies, Indentation and Structure from Acetic Acid Solutions of MMTA
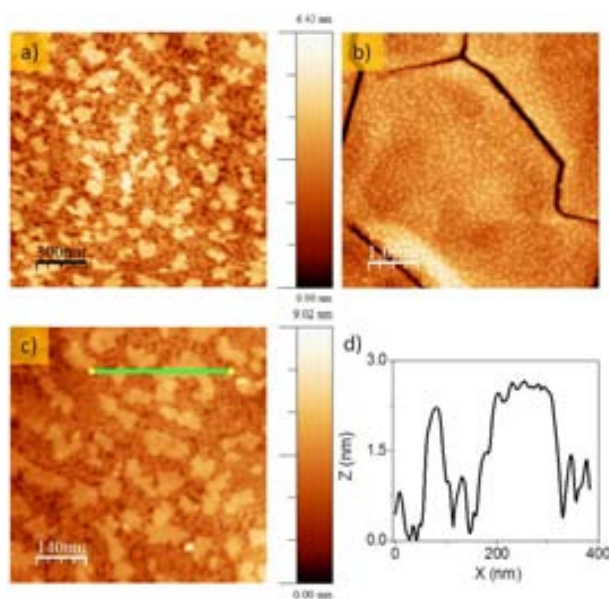
Figure 3.28. SFM topographic images of Au(111) on mica after immersing in a 100μM acetic acid solution of MMTA for 30 minutes and after annealing at $100°$C for 16 hours.

SFM topographic images of Au(111) on mica after immersing in a 100μM acetic acid solution of MMTA for 30 minutes and after annealing at $100°$C for 16 hours are shown in Figure 3.28. Low and tall islands are observed at larger scan areas as shown in (b). Topographic details of the molecular film is easily measured for small areas of scan (less than 1×1 μm^2). Profile taken along the line in (c) shows a height difference between low and tall islands of about 1.5nm.

In agreement with the coverage analysis performed in section 3.2.2 for the acetic acid solutions, the percentage of non-flooded area for the tall islands for 30 minutes of immersion and after annealing at $100°$C for 16 hours corresponds to $\approx$ 45% of coverage and minimum areas of tall islands of about 100×100 nm^2. Lateral dimensions
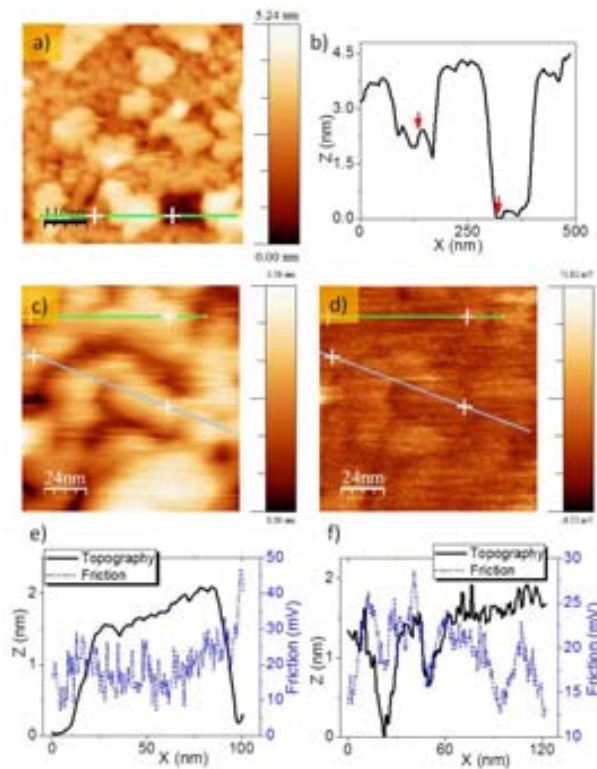
Figure 3.29. SFM topographic images showing the Au(111) on mica after immersing in a 100μM acetic acid solution of MMTA for 30 minutes and after annealing at $100°$C for 16 hours. Topographic images (a, c) show the heights of low and tall islands and (b) profile taken along the line in (a). The scratched area in (a) allowed obtaining the bare gold as reference. Simultaneous profiles taken along the lines in (c, d) correlate the morphology and the friction on the low islands.

of bilayer islands obtained at low immersion times (30 minutes) and after annealing were measured about 100nm being $\approx 25\%$ less than lateral dimensions of the samples for longer immersion times (16-18 hours) and same annealing conditions for images of $0.6{\times}0.6$ μm^2.

Figure 3.29 shows topography images (a, c) and a friction map (d) of low and tall islands of MMTA. Scratching experiments carried out on the surface in (a) lead to see two heights for the islands, the first one of 1.6±0.2nm and the second one to 3.4±0.3nm, as shown in (b) from profile taken along the line in (a). Topographic and friction images for low worm like islands are shown in (c, d). Morphological details of the low
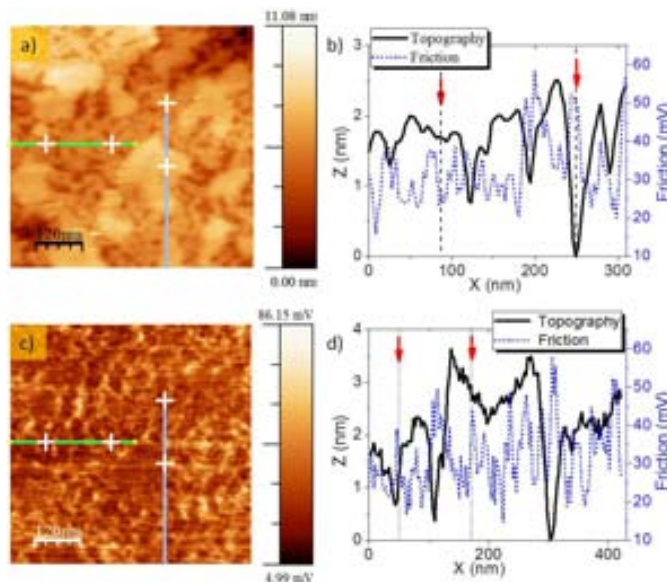
Figure 3.30. Topographic(a) and friction(c) images are shown. Horizontal profile (b) taken along the line in (a, c) shows the height of low islands and compares with friction signal in (c). The vertical profile (d) taken along the line in (a, c) correlates the height of the islands and the friction signal. Adhesion force:-4nN; applied force:2nN at $RH < 5\%$.

islands permit to observe that their topmost surface is not completely homogeneous as also show in the topographic and friction profiles (e, f). Measurement conditions of $RH < 5\%$, applied force of 1nN and adhesion force of -3nN were used. Several samples obtained in 100μM acetic acid solution of MMTA and low immersion times after annealing have revealed similar morphologies.

The Figure 3.30 shows topographic (a) and friction map (c) of MMTA islands on Au(111). Topographic profiles taken along the lines in (a) reveal heights of about 1.6nm for low islands (horizontal) and 3.2nm for bilayer case (vertical profile) (b, d), respectively.

Inhomogeneous surfaces and different friction on both low and tall islands were measured in the adhesion regime as revealed the topographic profiles (continuous line) and friction (dashed line) in panel (b, d). These heights correspond to a single molecular layer and bilayer with (-COOH) and (-SH) end groups, respectively. Although the size of domain of the islands allow hardly to determine a frictional response for each

termination (-COOH and -SH), different friction between the bare substrate, low and tall islands was observed. More detailed analysis are presented in the chapter 4.
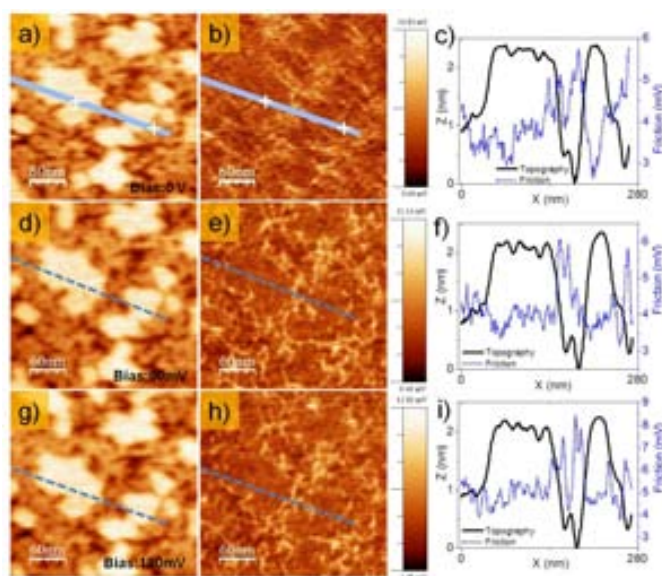
Figure 3.31. Topography (a, d, g) and friction (b, e, h) images recorded while a bias voltage to the tip is applied. Measurements performed with a conductive tip (k=0.2 N·m^{-1}) by applying a voltage ramp until 180mV with steps of 20mV.

To identify the gold substrate and measure the molecular thickness of the islands several current maps were carried out. By applying relatively small forces to avoid damage on the molecular film, in addition to bias voltage to the conductive tip, different friction values for both terminations were observed. During this experiment, the applied force was kept at 7nN, and a voltage ramp until 180mV with step of 20mV for each acquisition image was applied; the adhesion force was -5.5nN.

Figure 3.31 shows topographic (a, d, g) and friction maps (b, e, h) of low and tall islands. Simultaneous profiles taken along the lines in all images are shown in panels (c, f, i). Brighter regions in the friction map correspond to the bare gold. Though no current was detected for these voltages, a change of friction on the islands by increasing the bias voltage is observed, as shown in (b, e, h). We suggest that after applying a bias voltage to the tip and scanning several times on the molecular film at 7nN, the

presence of unbounded molecules or adlayer of contaminants can be removed and a real contact between the tip and molecular film can be assumed.

Figures 3.30 and 3.31 revealed that applying forces in the range 2nN to 7nN a friction difference can be measured between both low and tall MMTA islands. The low current signal measured after applying forces of about 7nN and heights of about 1.8nm for the low islands suggest the presence of a thin contaminant film on the surface for the samples obtained in acetic acid solution of MMTA after annealing.

Figure 3.32 (a) compares the friction values for zero and 180mV of applied bias voltage at 7nN of applied force. The topographic profiles (b) for several applied voltages do not revealed morphological damage on the film. Though no damages on the islands were observed, a height difference $\Delta Z \approx 0.3$nm between the topographic profiles at zero and 180mV was measured. This difference of ≈ 0.3nm was measured on topmost surface in contact mode in adhesion as well as repulsive regimen with and without using conductive cantilevers of low nominal force constants.
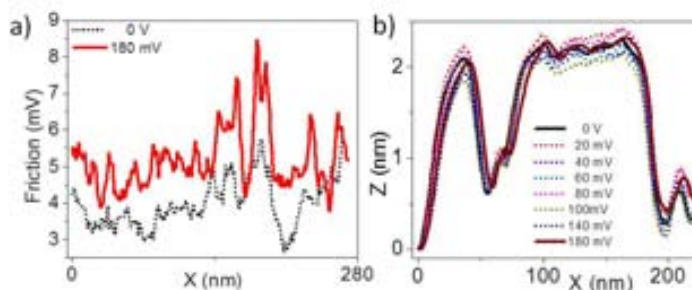
Figure 3.32. Cross-sectional friction profile (a) along the lines showed in figure (3.31) with/without applying low bias voltages. The higher value of friction correlates with the bare gold surface. Only few millivolts can be measured between tall and low islands. (b) Simultaneous topographic profiles on the same islands were taken on recorded images from zero to 180mV bias voltages.

Specific experiments such as nanoindentation by using the 3D modes were employed to identify more accurately the mechanical properties of both low and tall islands. We investigate the nanoindentation of low MMTA islands using a sharp tip-AFM by means of the 3D modes over a single point as well as X selected line. Nanoindentation of soft

materials is a growing research field, demanding sophisticated models and methods to extract accurate information from these materials. Many works have been analyzed within the framework of the Hertz model, assuming that indentation depths are much smaller than sample thickness, in which case the Hertz model provides good accuracy [92, 93, 94, 95, 96].
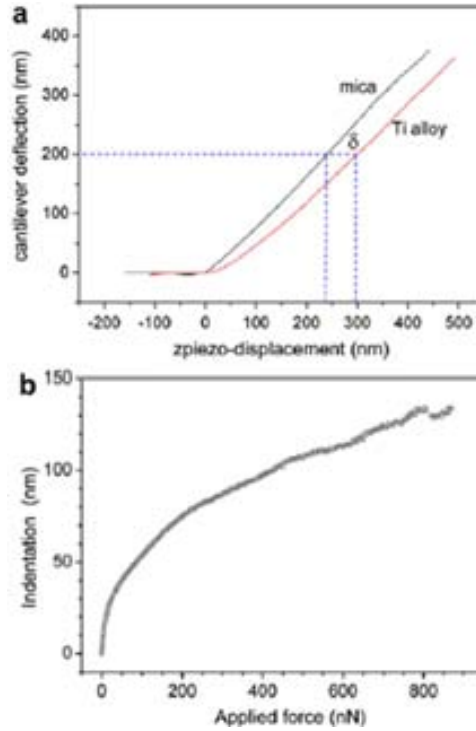
Figure 3.33. (a) Force vs. displacement curves on a freshly cleaved mica surface and on the as-received Ti-7Nb-6Al sample surface. An equal displacement of the z-piezo results in a smaller cantilever deflection on the titanium alloy surface compared to the mica surface due to elastic indentation. (b) Indentation vs. applied force curve calculated from the curves in (a). Taken from [95].

Following the procedure described first by Radmacher and co-workers [97], the indentation curve of a material surface can be obtained by comparing the slope of the force vs. distance curve of this material with that of a hard surface. As the surface of the hard material is not indented by the tip, the cantilever deflection is proportional to the z-piezo movement and, therefore, the force vs. displacement curve has a constant

3.2 Self-Assembled Monolayers and Crystalline Structure of MMTA on Au(111)

slope as soon as the tip contacts the surface. However, on a compliant material the tip indents into the sample and the same cantilever deflection is obtained only after an additional piezo travel. The indentation (δ) at a given deflection value is given by the extra z-piezo motion needed to achieve the same cantilever deflection as on the hard material. The calculated indentation values are plotted as a function of the applied force, which is directly obtained multiplying the cantilever deflection by the spring constant, as shown in Figure 3.33. In order to determine the indentation depth (δ), the cantilever response obtained on the gold surface as the surface of the hard material reference and the curves on the MMTA islands are compared, as shown in Figure 3.34. A closer inspection in the force-distance curve recorded on the bare gold shows that the piezo displacement z while in contact will lead to a deflection d of the cantilever that is identical to z, $d=z$. In the case of the MMTA islands the same movement z will lead to smaller deflection of the cantilever as a result of an elastic indentation δ, $z=d+\delta$. The loading force F is proportional to the force constant k and the deflection d of the cantilever, $F=k \cdot d=k \cdot (z-\delta)$.

By using the 3D modes for tribological and electrical studies (chapters 4 and 5), we observed variations or steps in the force-distance curve within small ranges of force after contacting the molecular surface. These steps seem to indicate a tilt angle experimented for the molecules under the applied load. Following the procedure described in section 2.2.3.2 for friction measurements by means of the 3D modes, the approaching cycle begins with the cantilever position far away above the molecular surface, where there is no interaction between them, so that the cantilever deflection is zero. As the piezoelectric moves in z-direction, the cantilever approaches closer to the sample and the tip starts touching and compressing the molecular film, generating a measurable non-zero deflection value.

For both in a single point or a selected line of the scan direction on the molecular film, revealed high reproducibility of the force-distance curves in the compression regime. We performed indentation analysis by comparison force distance curves on low and tall islands respect the force distance curve obtained for a hard surface like the gold substrate. The typical tip radius of AFM probes is of the order of tens of nanometers, and for indentation depths comparable to the tip radius, the spherical indenter model
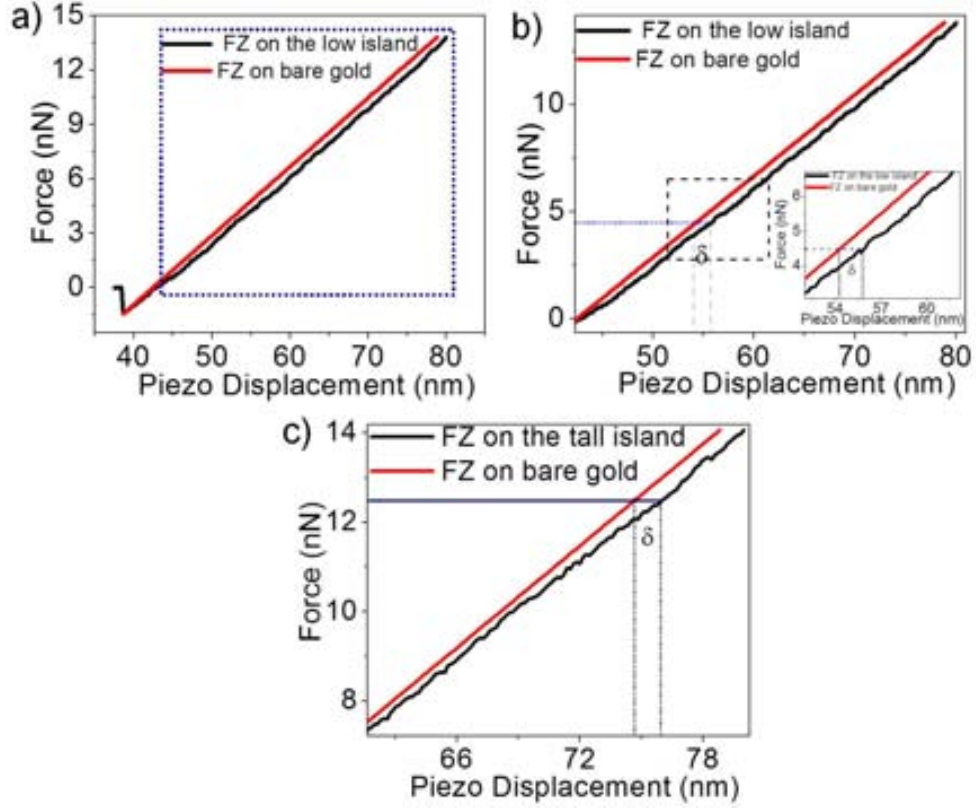
Figure 3.34. (a) Force versus displacement curves on the MMTA islands on Au(111). The image in (b) was obtained by zooming in the marked area with dashed blue line in (a). Inset in (b) shows more detailed ranges in the force vs. displacement curve for the low islands. (c) shows the force vs. displacement curve recorded on tall islands. Force vs. displacement curves in red line correspond to the gold substrate as the hard surface reference.

should be used. The classic Hertz model relates the load F and the penetration depth δ during a frictionless elastic indentation of an infinitely stiff indenter in a sample with elastic modulus E and the Poisson coefficient ν.

$$F_{Sphere} = \frac{4}{3} E^* R^{1/2} d^{3/2} \tag{3.5}$$

$$F_{Cone} = \frac{2}{\pi} E^* \tan \alpha \, \delta^2 \tag{3.6}$$

3.2 Self-Assembled Monolayers and Crystalline Structure of MMTA on Au(111)

Assuming that the tip and the sample are both isotropically elastic, the following expression for E* must be employed, $E^* = \frac{4}{3}\left(\frac{1-\nu_i^2}{E_i} + \frac{1-\nu_j^2}{E_j}\right)^{-1}$.

Equations 3.5 and 3.6 are derived from the Hertzian contact theory where both expressions are particular cases of the generalized Hertzian contact theory developed by Sneddon [98], that states that load-displacement relationships obey a power law $F \propto \delta^n$, where the exponent n and the proportionality factor depend on the indenter geometry.

Indentation analysis on samples after annealing have shown similar results; in particular, for low islands with lateral dimensions of 30nm, as shown in Figure 3.35. The X dashed line in topographic image (a) represents the place where the feedback is disabled to start the 3D acquisition only over the chosen line. Horizontal gray line in (b) image has been drawn to show the coordinates where the island is modified by the applied load ($\approx$ 4nN), whereas the vertical gray line is the background reference of the gold surface. Numbered profiles (1, 2 and 4) were taken on low islands with lateral dimensions between 10nm and 40nm. Image (c) shows the 3D representation of the $F_n = (X, z)$ for low and tall islands and the bare surface to compare the force distance curves.

From indentation profiles (d) we determined small force ranges where the indentation remains constant. An indentation of 0.3nm is measured in the range -1.5nN to 2.5nN that we associated to contaminants adsorbed on the molecular film, whereas in the range 3nN to 4nN we suggest that the contaminant layers are removed and the real contact between the molecular film and the tip is done. In the force range from 5nN to 7nN, we observed a constant δ value by which a new tilt angle of the molecular arrangement previous the total compressing and damage is suggested.

Alternatively, we can extract from the indention-force curves a height value of the low islands. The constant value of indentation above 10nN indicates that the low island is completely compressed, but below 7nN there is a regimen where the island is modified, we suggest that is tilted around $(48\pm5)°$. In table 3.3, we indexed with n three levels of indentation for each force range. The first level $n=0$ a smooth indentation is observed, at level $n=1$ these values are statistically representative for several analysis in the low islands. For $n=1$ we have called the position "REF A" for a real contact
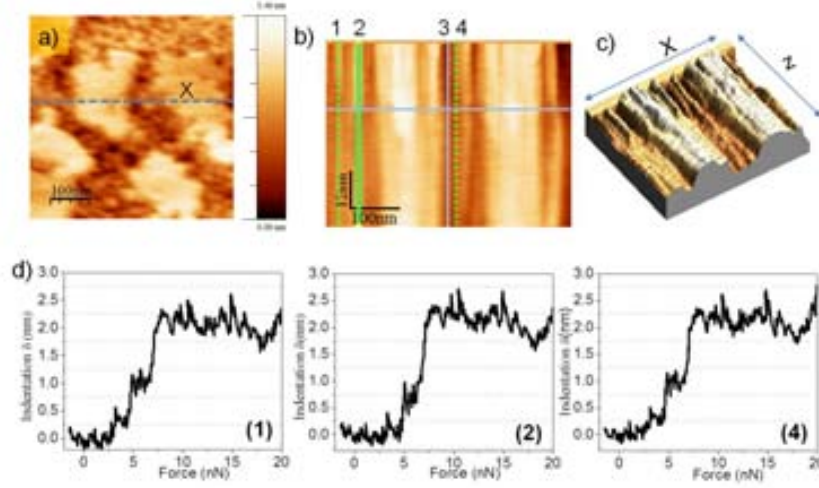
Figure 3.35. SFM topography image (a), Fn(X, z) image and their three-Dimensional representation obtained from 3D modes (b, c), respectively. Bottom panel (d) represents the indentation curves for the numbered low islands taken along the vertical lines in (b). The dashed line X in (a) shows the place where the feedback is disable to start the 3D acquisition.

tip-molecular film where the contaminants are removed at this force range, whereas in the level $n=2$ a new molecular tilt is obtained due to the applied force and called "REF B". By calculating Δd between the n levels, we have measured the heights of the low island $d_3 - d_0 = d_{30}$, $d_3 - d_1 = d_{31}$ or $d_3 - d_2 = d_{32}$; being $d_{31} = 1.54 \pm 0.03$nm the single molecular length and $d_{32} = 0.99 \pm 0.11$nm the height suggested when the molecular arrangement is tilted.

In agreement with experimental data obtained from 3D modes over a selected point or line on the islands, we suggest a model to explain the presence of several heights measured on the molecular islands of MMTA. Cartoon in Figure 3.36 shows the contact between the rigid sphere (AFM-tip) and an elastic half-space with a displacement of the points on the surface in the contact area.

Figure 3.37 shows the indentation results performed on the MMTA islands, as described before. Numbered lines (1 to 8) taken on the $F_n = (X, z)$ image were employed to determine the numbered indentation plots. The force-displacement curve on the gold substrate was obtained by taking the profile on the yellow line. Numbered lines (2, 3, 4,

3.2 Self-Assembled Monolayers and Crystalline Structure of MMTA on Au(111)

Level n	Force Range nN	Indentation $\delta(nm)$	Thickness d(nm)	Tilt angle $^\circ degree$	$\Delta Thickness$ $\Delta d(nm)$
0	-1.44 to 2.54	0.01	d_0		d_0
1	2.75 to 4.50	0.33 0.30 0.35	d_1	20	$d_{10} = 0.32 \pm 0.02$
2	4.7 to 6.70	0.95 0.73 0.95	d_2	48	$d_{21} = 0.55 \pm 0.08$
3	7.3 to 17	1.85 1.85 1.9	d_3		$d_{30} = 1.85 \pm 0.10$ $d_{31} = 1.54 \pm 0.03$ $d_{32} = 0.99 \pm 0.11$

Table 3.3. Indentation versus force values. n levels are presented to indicate the applied force ranges, the indentation δ value, the parameter d_n to calculate the thickness and the average tilt angle.
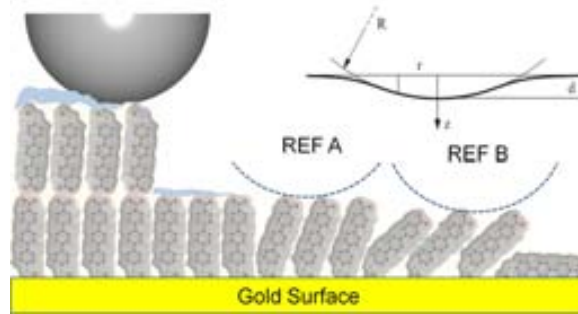
Figure 3.36. Illustration of tall (bilayer) and low MMTA islands on Au(111). REF A and REF B are positions where the contaminant layers have been removed and the molecular assembling has been tilted.

7 and 8) were drawn on the low islands, whereas numbered lines (1 and 5) were drawn on tall islands.

We payed special attention on the numbered curves where the successive value
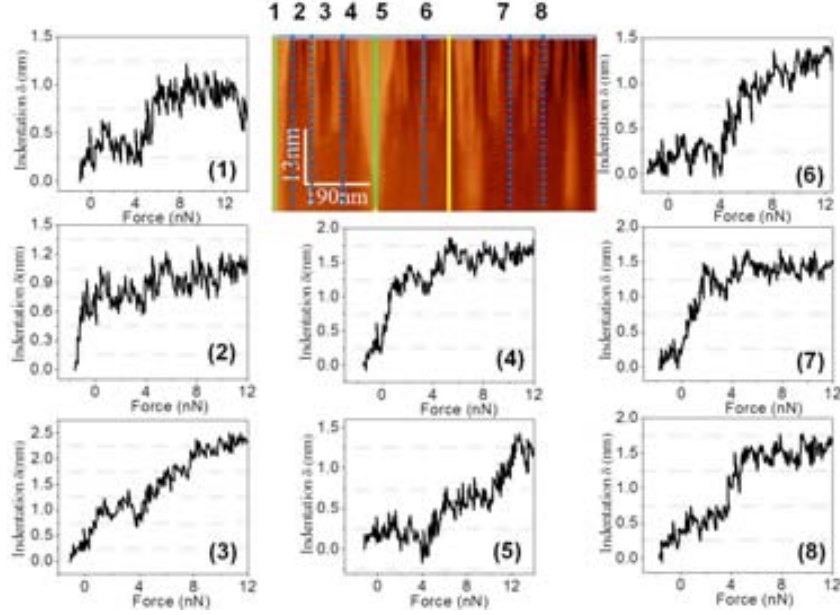
Figure 3.37. Indentation versus applied force panels for low islands after annealing treatment. Blue dashed lines represent the profiles taken on the low islands of the F_n=(X, z) image (filtered to enhance details), green lines on tall islands and the yellow line represents the force distance curve measurement on the bare gold substrate as hard surface reference.

of indentation (δ) increases or remain constant as the value of the force increases. That is, the preceding values are less than or equal to successive values as follow, if $F_1 < F_2$ then $\delta(F_1) \leq \delta(F_2)$, from -2nN to 4nN range force (F). A non-constant value of indentation-load curve within a range of force could obey a power law $F \propto \delta^n$, as described before.

By plotting δ versus F from experimental data as shown both Figures 3.37 and 3.35, we determined each labeled indentation distance from several profiles taken on the F_n=(X, z) image. From indentation plots we observed that for islands with lateral dimensions less than 10nm low forces are required to penetrate/compress the film as shown the numbered profiles (2, 4 and 7) whereas low islands with larger lateral dimensions required forces of about 3nN (profiles 3 and 8).

Indentation experiments performed on the bilayer islands revealed that forces in repulsive regimen ($\approx$ 5nN) were required *a priori* to penetrate, tilt or compress the

molecular layer (numbered profiles 1 and 5). The compressing limit before damage for low and tall islands was measured of about 5nN and 12nN, respectively.

Samples obtained from 100μM acetic acid solution of MMTA for longer immersion times ($\approx 18h$) and after annealing at $(110\pm 5)°$C have shown interesting morphological changes. Two kind of morphologies can be observed for most samples studied. The first one, consist of small clusters of islands with heights of 1.35 ± 0.2nm forming percolated. These islands do not present a flat surface and their topology is worm like and the dimensions indicate than correspond to a single molecular layer. The second one, taller islands with heights of 3.3 ± 0.25nm and lateral dimensions larger than the islands obtained for 30 minutes with the same preparation conditions.
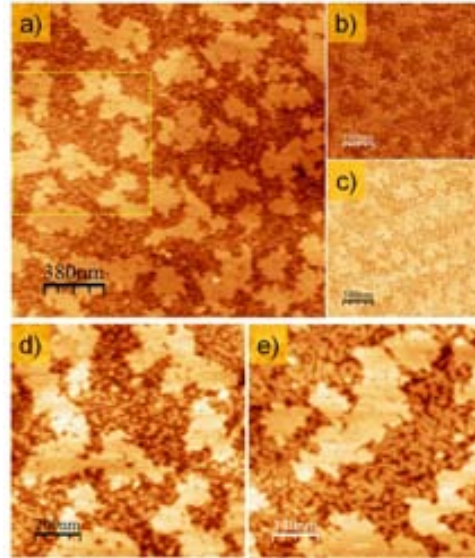
Figure 3.38. SFM images of Au(111) on mica after immersing in 100μM acetic acid solution of MMTA for 18 hours and after annealing at $(110\pm 5)°$C for 18 hours. Topographic (a, d, e) and lateral force (Fw&Bw) (b, c) images are displayed. The image (e) was recorded in a different region of the sample. Total z-scale: (a) 0-8nm; (b) 0.14 to 0.17 V ; (c) 0.13 to 0.16 V; (d) 0-5nm; (e) 0-4.5nm. The measurements were performed by applying -2nN, adhesion force -5nN.

Figure 3.38 shows topographic images (a, d, e), the magnified area (d) marked with yellow dashed line in (a) and lateral force (b, c) images of the low and tall islands for scanned areas of $\approx 4\mu$m^2. Tall islands (bilayer) show less torsion signal of the cantilever
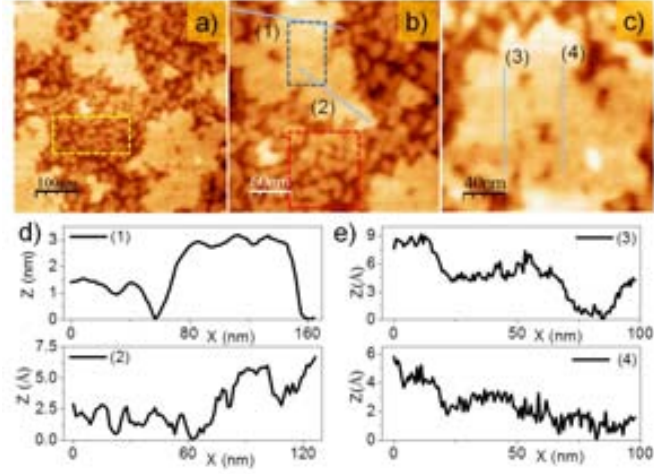
Figure 3.39. Top row: SFM topographic images (a, b, c) of low and tall islands of MMTA on Au(111). An average height of 1.38±0.02nm was measured for low islands in the zone marked with yellow and red dashed lines in (a, b). Flat area ($\approx$ 50×50 nm^2) on the tall island is marked with a blue rectangular box in dashed line in (b). (d) Bottom row: numbered profiles on tall islands reveal the corresponding heights for low and tall islands (1) and inhomogeneous on topmost surface of tall islands (2, 3 and 4).
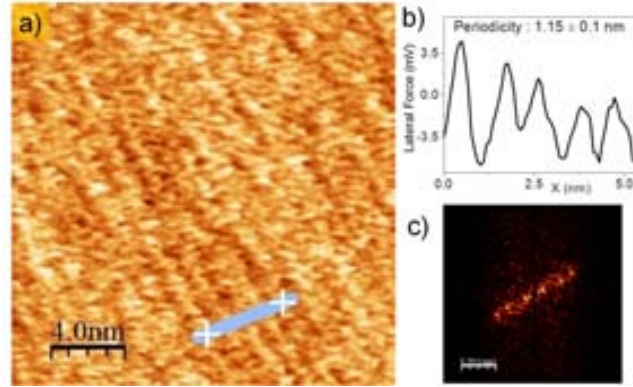
Figure 3.40. High resolution lateral force image (a) acquired on the topmost of the surface of a tall island. (b) A stripes periodicity of 1.15±0.1nm was measured along the line in (a). A unit cell length can be deduced from (b) with dimension **a**=1.15±0.1 nm of the $(2\sqrt{3} \times \sqrt{3})$R30° structure. 2D-FFT image (c) was obtained from the whole image in (a).

3.2 Self-Assembled Monolayers and Crystalline Structure of MMTA on Au(111)

in forward than backward scan directions in lateral force images, in agreement with preparations for 30 minutes of immersion times and after annealing. Topographic images recorded on different regions of the sample as in (e) revealed the same morphology for the MMTA islands. Different friction between tall and low islands allow us suggest the presence of both (-COOH) and (-SH) end groups (see chapter 4).

Topographic images have revealed that the surface of the tall islands are not completely flat. In fact, height differences of about 2.5±0.5Å were measured on the inhomogeneous surface of the tall islands. We suggest that a thin contaminant layer is adsorbed on the surface during the process (thermal treatment and measuring) which can be removed by applying forces in repulsive regime($\approx$ 2nN) in agreement with indentation data shown above. Bilayer islands obtained at high immersion times and post annealing have shown larger surface area than bilayers obtained at low immersion times and post annealing as shown in section 3.2.2. Despite the inhomogeneous surface of the tall islands (bilayer), flat regions can be observed with a RMS roughness 0.2±0.05Å , as shown in Figure 3.39 in the rectangular box in (b). Profiles taken on low islands marked in yellow and red dashed box (a, b) revealed average heights of 1.38±0.02nm and tall islands heights of 3.3±0.25nm, whereas numbered profiles (2, 3 and 4) show inhomogeneous surfaces on the tall islands.

High resolution lateral force images on the tall islands surface revealed striped periodicities of 1.15±0.1nm, as shown in Figure 3.40 by taking profile (b) along the line in (a). 1-D FFT image in (c) was obtained from the whole image in (a). The periodicity $\mathbf{a}$=1.15±0.1 nm corresponds to the $2\sqrt{3}$ length of unit cell already found. This fact indicates that the tall islands (bilayer) forms the same $(2\sqrt{3} \times \sqrt{3})$R30° structure already described.

In addition to measurements at low relative humidity (RH), we were also interested to know the possible influence of humidity and how different can be the results at high RH values. Although there was not fundamental morphological changes, we determined a different response for adhesion, friction and surface potential measurements as will be described in more detail in chapters 4 and 5.

3.2.4.3 Morphologies and Structure from Ethanolic Solutions of MMTA

A thermal treatment was carried out on different samples prepared in ethanolic solution to get very-well packed molecular layers or to dismiss the degree of defects on the layers. Three-dimensional structures have been seen for longer immersion times at high concentrations and one goal with the annealing process is to arise very well ordered and packed islands at submonolayer scale. However, the high coverage of the surface makes nearly impossible to have a good reference for height measurements, because several layers of the organic material adsorbed on the Au(111) surface. In this case, we observed a well defined molecular arrangement on the top flat of the 3D structure.
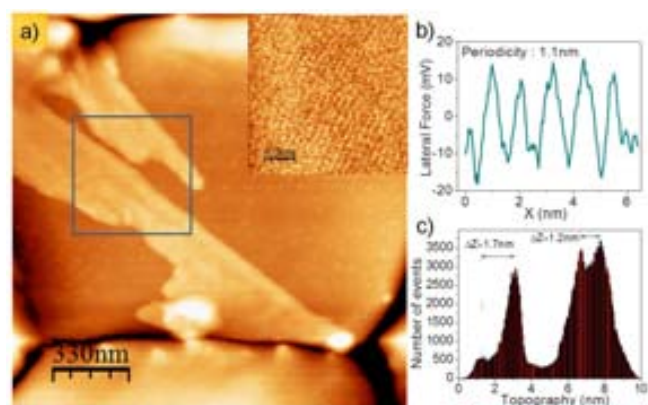
Figure 3.41. SFM images of Au(111) on glass after immersing in a $100\mu M$ ethanolic solution of MMTA for 20 hours and forwards a thermal treatment at 110°C for 24 hours. Topographic image (a) shows the 3D structure on the substrate. Inset in (a) shows the stripes on the high resolution lateral force image. Profile (b) taken on the high resolution image reveals the stripe periodicity of 1.1nm. Histogram (c) was obtained on the marked area in (b) of the 3D structure.

In Figure 3.41 we observe on a gold grain a molecular film and the inhomogeneous 3D structure with heights between 6nm and 8nm, as shown in the marked area in topographic image (a) and histogram (c). The measured heights are in agreement with the single and bilayer dimensions that finally forms the 3D structure. Inset in (a) represents the high resolution lateral force image to measure the periodicity of 1.1nm on a flat region of the 3D topmost structure and showed in the profile (b). Periodicities

3.2 Self-Assembled Monolayers and Crystalline Structure of MMTA on Au(111)

on the 3D structure corresponds to a dimension of a unit cell of the $(2\sqrt{3} \times \sqrt{3})$R30° structure already described for low and bilayer islands with different solvents. Although most of the samples were under the thermal process, we did not find fundamentals differences in results by using the furnace in air or controlling the environment with a nitrogen stream.
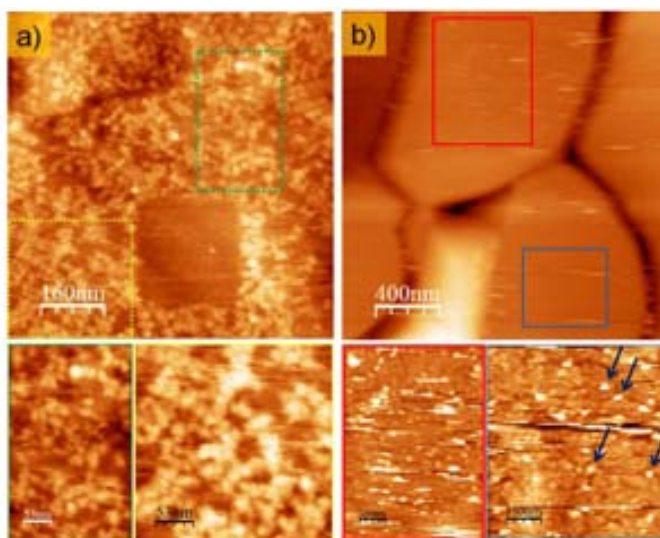
Figure 3.42. SFM images showing the Au(111) surface after immersing in a 2μM ethanolic solution of MMTA for (a) 270 minutes prior to annealing and (b) after 8 hours at 200°C under controlled N_2 environment (b). Topographic (a, b) images with magnified areas with dashed and continuous lines are shown.

Figure 3.42 compares the topographic images of Au(111) after immersing in a 2μM ethanolic solution of MMTA for 270 minutes prior to (a) and after annealing (b). Blue arrows in topographic image (b, down) show some tall islands formation. High adhesion values and difficulties to get topographic images were a common characteristic with theses samples by using high annealing rates. The annealing process was performed under controlled environment with an annealing rate of $200°C \cdot h^{-1}$ using the second program described in section 2.3.3. Samples obtained from 2μM in ethanolic solutions of MMTA required high immersion times to observe islands formation, clustering or coalescence of the molecular islands; however, the thermal process performed with these
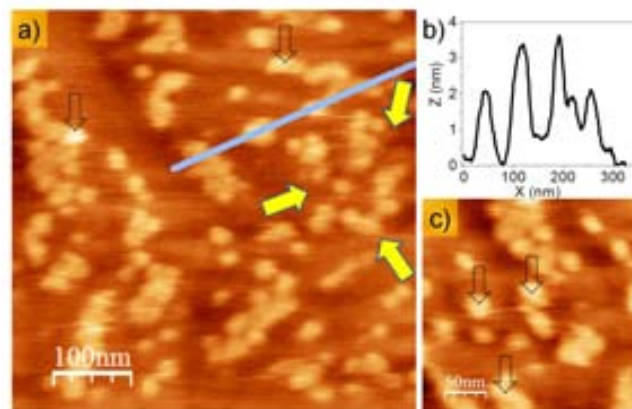
Figure 3.43. SFM topographic images (a, c) showing the Au(111) surface after immersing in a 100μM ethanolic + acetic acid (10%) solution of MMTA for 16 hours annealing the solution at 30°C. Profile (b) taken along the line in (a) reveals heights for both low and tall islands formation. Yellow arrows in (a) show clusters of islands, whereas black dashed arrows in (c) show some tall islands.

preparations by using both programs with annealing rates of $200°C \cdot h^{-1}$ and $120°C \cdot h^{-1}$ were not successful to get well packed molecular layers.

By immersing the Au(111) substrates in ethanol plus acetic acid solutions of MM-TA within a thermal bath controlling the temperature, interesting morphologies and specially the clustering of MMTA molecular islands were observed. Figure 3.43 shows topographic images (a, c) and profile taken on the low and tall islands on Au(111) on glass by using a mixture of ethanol and acetic acid (10%). Despite the longer immersion time ($\approx$ 16 hours) and annealing the solution within a thermal bath at 30°C, we did not observe 3D structures. Interestingly, the clustering was observed as shown by the yellow arrows in (a). The black dashed lines show islands with heights around of 3.2nm, indicating bilayer formation. Following this protocol for higher temperatures (90°C.) we observed only high coverage with height corresponding to a single molecular film.

Clusters of islands are formed by coalescence in 2μM solutions of MMTA using a thermal bath for several samples between a temperature range from $30°C$ to $80°C$. This fact indicates that the low and tall islands already described in acetic solutions of MMTA after annealing are formed in a temperature range from $80°C$ to $120°C$, in agreement with islands formation observed in general after annealing of about $100°C$.

3.2 Self-Assembled Monolayers and Crystalline Structure of MMTA on Au(111)
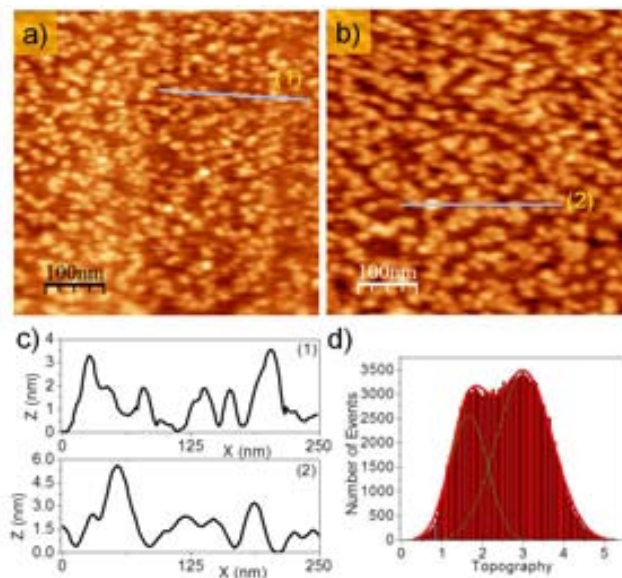
Figure 3.44. SFM images of Au(111) after immersing in a 2μM ethanolic solution of MMTA. Topographic (a, b) images for 90 minutes and 270 minutes annealing the solution at $50°$C. Profiles (1, 2) in (c) were taken along the lines in (a, b) for both 90 minutes and 270 minutes. The Histogram (d) was acquired for the whole image (b). Total z-scale: (a, b) 0-6nm.

The SFM images obtained in the stage of growth prior to island coalescence are shown in Figure 3.44 after immersing Au(111) on glass for 90 minutes and 270 minutes annealing the solution at $50°$C. Topographic image (a) shows low islands with lateral dimensions $\approx$15nm for the case of 90 minutes of immersion time and simultaneously annealing the solution in a thermal bath. Numbered profiles (1, 2) taken on the molecular islands reveal the corresponding molecular lengths for both low and tall islands for both cases. Brighter spots in both topographic images (a, b) are approximately 3.2nm, in agreement with the molecular length for bilayers; the coalescence was more evident in the topographic image (b), due to the larger lateral dimension of the islands ($\approx$ 50nm). Profiles in (c) as well as the histogram in (d) show the height distributions found for both sample preparations.

3D structures were not observed in 2μM (ethanol+acetic acid) solution of MMTA annealing the solutions in a thermal bath for a wide range of temperature (from $25°C$

to 90°C).

3.2.4.4 Morphologies from Toluene Solutions of MM-TA

Figure 3.45 shows SFM images of the MMTA islands on Au(111) after immersing in 100μM toluene solution of MMTA for 20 hours and after annealing at 120°C for 24 hours. We found areas of low islands with heights of 1.6±0.2 nm as shown the numbered profiles (1, 2) in (a) and clustered bilayers of 3.4±0.2 nm (3, 4), as a result of the thermal process. The lateral dimensions of the tall islands were observed in the range (≈100nm), the 3D structures were not observed by using solutions with this solvent. As previous measurements performed on samples thermally treated, the friction response on the bilayer islands follows similar characteristics, lower lateral force signal in forward than backward scan directions (b, c). Au(111) substrates after immersing in
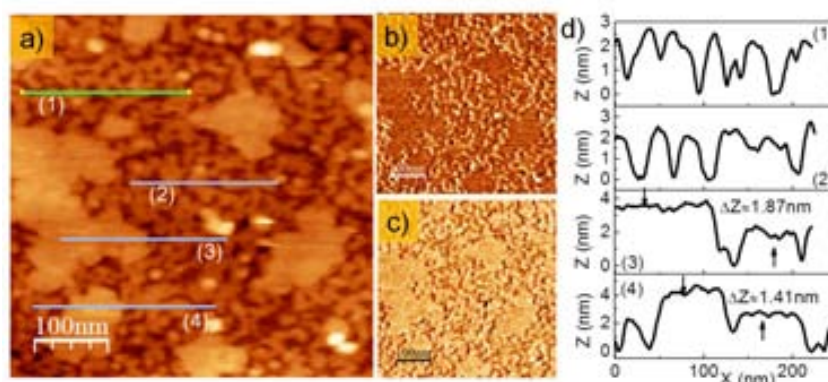
Figure 3.45. SFM images of Au(111) on mica after immersing in a 100μM toluene solution of MMTA for 20 hours and after annealing at 120°C for 24 hours. Topography (a) and lateral force images (Fw&Bw) (b, c) are displayed. Topographic profiles (d) confirm the heights of the a single molecular and bilayer length.

100μM solutions of MMTA for longer immersion times and thermal process reproduce the same morphologies of the islands. Some samples were measured one month later and revealed a clear contrast in friction measurements between both morphologies.

3.2 Self-Assembled Monolayers and Crystalline Structure of MMTA on Au(111)

For ethanolic solutions of MMTA and similar concentrations and immersion times, high coverages were observed as well as multilayers structures. Interestingly, samples obtained in 100μM THF solution of MMTA and high immersion times after annealing, islands at submonolayer scale and few tall islands (bilayer) were observed. Samples obtained in 2μM (ethanolic+acetic acid) solutions of MMTA required at least 6 hours of immersion annealing the solution at $50°$C to observe isolated islands with lateral dimensions ($\approx$ 15nm) and coalescence between them over the Au(111) surface.

3.2.5 Patterned Gold Surface with the MMTA Aromatic Thiol by using μCP
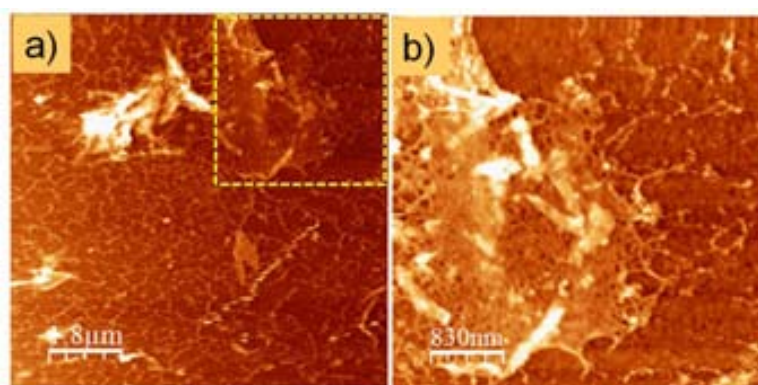
Figure 3.46. Topographic images (a, b) show the molecular material in 100μM (ethanol + acetic acid) solution of MMTA transferred from untreated stamp on the gold surface, magnified area (b) and marked in (a) shows unsuccessfully patterned zones. A square motif stamp of $(3\times3)\mu m^2$ was used. Total z-scale: (a) 0-183nm; (b) 0-72nm

Figure 3.46 shows topographic images of MMTA molecules transferred from PDMS untreated stamp on granular gold surface. For all untreated stamps similar morphologies were obtained by using different concentrations and solvents such as ethanol, toluene or acetic acid. The difficulty of molecular diffusion of the polar substance onto the hydrophobic surface and then to transfer the patterned relief of the stamp was evident. Patterned regions on the substrate with treated PDMS stamps were sometimes difficult to identify with only topographic images. Lateral force, phase or excitation frequency and surface potential images were necessary to verify the successful transferring of

molecular material onto the gold surface. Once identified the stamping on the surface by measuring in contact or tapping mode, functional studies of the surface were carried out.
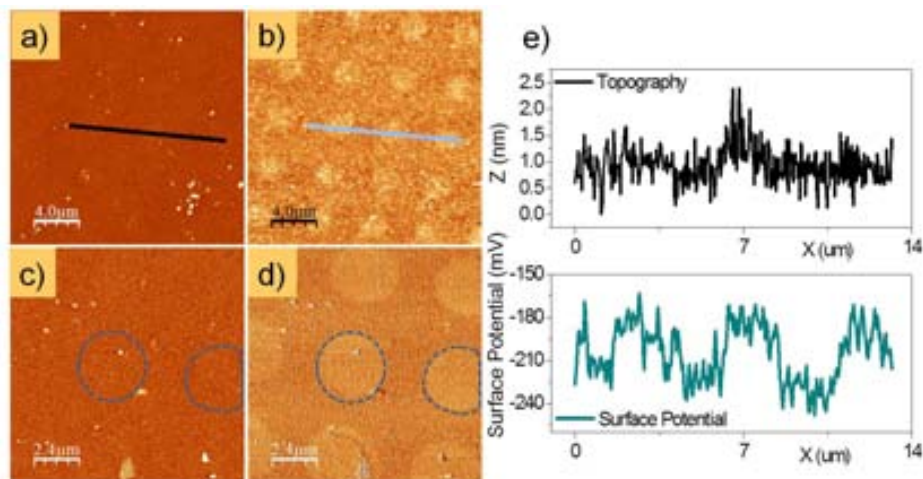
Figure 3.47. Topography (a, c), surface potential (b) and excitation frequency (d) images to identify MMTA patterned regions on the gold surface recorded in dynamic mode at $RH < 5\%$. Simultaneous profiles (e) taken along the lines in (a, b) are shown.

Figure 3.47 shows successfully the transferring and patterning of the gold surface by correlating the topography (a) and surface potential (b) images by means of simultaneous profiles (e) taken along the lines in (a, b) and *a priori* bare gold, in this case, using 2μM ethanolic solution of MMTA. Both profiles show a correlation between the patterned area with and without using MMTA molecules and their surface potential difference around of 50mV. The dynamic modes allow deciphering different chemical patterned regions by means of channels such as phase or excitation frequency that, sometimes the topographic images recorded in contact mode are impossible of detecting in marked regions as shown in (c, d).

Molecular heights between 1nm and 3nm were found for the samples obtained from ethanolic solutions of MMTA by using gold surfaces (RMS roughness $\approx$1nm). Interestingly, patterned gold surfaces have shown regions with low and high density molecular which allows studying surface properties such as friction and surface potential.

3.2 Self-Assembled Monolayers and Crystalline Structure of MMTA on Au(111)

In Figure 3.48, the morphology of the molecular film on gold surface revealed a different way of transferring the aromatic thiol onto the surface (a). This case showed that the molecular transferring occurred from regions without the intimate contact between the relief of the stamp and the gold surface (B regions). This can be explained by means of different diffusion pathways for the molecules described by Delamarche et al. [99] and [100] in alkanethiols. For instance, the ink might simply spread across the substrate on contact between the PDMS stamp and the gold surface (paths 1 and 2) in the model (c). The PDMS stamp might be considered a sponge impregnated with the solution that, in the worse case, is displaced and spreads across the surface (numbered paths 1, 2, 3 and 4) or the possibility of transferring molecules from the stamp to the substrate in non-contacting areas by the vapor phase (molecules having a high vapor pressure).
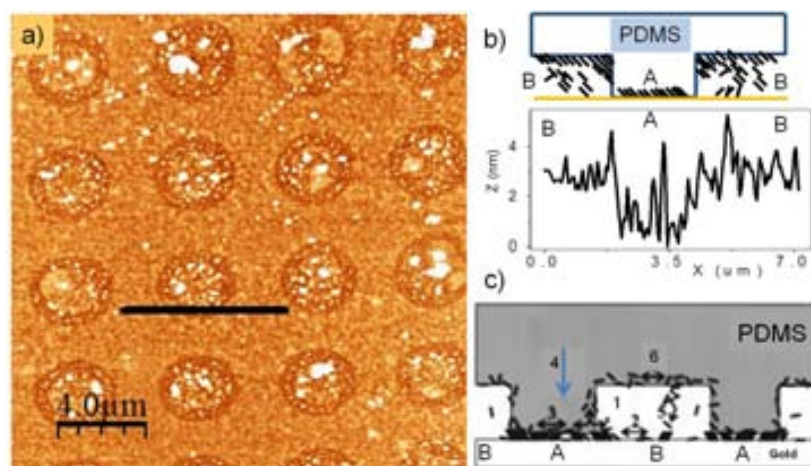
Figure 3.48. Topographic image (a) and the profile (b) taken along the line in (a) after pattering the gold substrate are shown. Model proposed (c) to explain the patterning of the gold surface for several pathways (adapted from [99]). The cartoon (inset in b) shows the intimate contact (A) and the non-contact (B) areas between the relief of the stamp and the gold surface. Total z-scale:(a)0-125nm

In agreement with the morphology observed in Figure 3.48 and the topographic profile taken along the line in (a), we suggest that during the poured of the solution on the PDMS patterned surface, the solution is not completely evaporated and by

capillarity effects is maintained in the non-contacting areas (B regions) as a molecular reservoir and transferred in major amount onto the surface. This fact could explain the regions with high density after stamping process where single and bilayer lengths can be formed while are transferred from the PDMS stamp. SAMs prepared from saturated solutions of about 50μM by using THF or ethanol as solvents, bilayers of MMTA can be formed by hydrogen bonds between the carboxylic groups [75, 77] on flat Au(111) substrates.

3.3 Conclusions

We have shown morphologies of the MMTA molecular films on Au(111) substrates obtained from 2μM and 100μM solutions of MMTA after annealing. In 100μM toluene and acetic acid solutions of MMTA and after annealing, we found morphologies corresponding to a single molecular layer, here called low islands, like percolated between them as well as tall islands (bilayer) formed by hydrogen bridges between the carboxylic groups.

Clustering was observed in 2μM ethanolic solutions of MMTA for longer immersion times with and without annealing at 80°C, whereas 3D structures or multilayers with heights of 30nm and high coverage were found at 100μM with immersions of up to 6 hours. We observed monolayers on Au(111) by using 100μM THF solutions of MMTA without annealing. Molecular islands of MMTA at submonolayer scale were obtained in samples thermally treated, few tall islands were observed. Two different morphologies were observed by using THF, acetic acid, ethanol and toluene solutions of MMTA after annealing. Interestingly, with the annealing process we can differentiate both chemical terminations (-COOH) and (-SH) of the nanostrutured surface by means of the lateral force microscopy.

From coverage studies performed with samples obtained in 100μM acetic acid solution of MMTA for 30 minutes and 18 hours at ≈ 100°C, we observed that these islands are $\approx 25\%$ wider for 18 hours. We did not observe large areas of bare gold when the thermal treatment is performed. Since this increase in size is not accompanied of a difference in bare gold areas, we suggest a coarsening of the initial islands.

A $(2\sqrt{3} \times \sqrt{3})$R30° structure on the Au(111) substrate was determined for samples obtained in a 100μM acetic acid solution of MMTA for 30 minutes of immersion

time. Despite the difficulty to determine the structural order on the 3D structures, we observed stripe periodicities of 1.15nm on their topmost surface which could correspond to a unit cell with dimensions $2\sqrt{3}$ in one direction.

By using the 3D modes on the low and tall islands, we deduced the presence of a thin contaminant film of 0.30±0.05nm on both (-COOH and -SH) end groups. Indentation as a function of the applied force revealed jumps within a range of force which we associated to a penetrating length of the tip on the contamination layer. Once achieved an applied force of $\approx$ 2.5nN, the thin film of contamination is removed and the real contact between the tip and molecular arrangements is done, at higher force $\approx$5nN an average tilt angle of 50° is suggested prior to a total compression or damage at forces around of 10nN. In some low islands (lateral dimension less than 10nm), even the smallest applied force was sufficient to tilt and compress the molecules so that the constant value in δ is not observed.

We have shown that the PDMS elastomeric stamp can be used for patterning of gold surfaces with polar MMTA molecules pouring a drop on the relief of stamp surface. Two ways to pattern the surface were observed: the first one, the MMTA molecules are transferred onto substrate only in areas where the contours of the stamp allow contact with the gold surface, thus reproducing the pattern of the stamp on the substrate. The second one, is referred as the transferring from areas that are not in conformal contact between stamp and surface. Despite the transferring and printing of the gold substrate with MMTA aromatic thiol, ambiguous results obtained in our case suggest that the methodology employed has not been completely optimized.

CHAPTER 4

TRIBOLOGICAL PROPERTIES OF FUNCTIONAL SURFACE MODELS

Understanding the different mechanisms underlying the interactions that appear when two materials are brought together, rubbed each other and separated are fundamentally important to many applications in nanotechnology that require an understanding of tribological process such as adhesion, friction, lubrication and wear at nanoscale. Friction is a common phenomenon at macroscopic and microscopic level, which is governed by the process prevailing on the surface layers of sliding bodies. In Friction Force Microscopy (FFM), the apex of a sharp tip is brought into contact with a sample surface, and the lateral forces are recorded while tip and surface slide relative to each other. Early works based in FFM studies of SAMs, for both monolayers of alkanethiols on gold and alkylsilane monolayers [101, 102], have been used to investigate the effect of a range of parameters such as the molecular organization, end-group functionality, interfacial interactions [103, 104] and scan sped [105] on friction behavior.

In our research group, FFM has been employed to study organic as well inorganic systems. For instance, a study of the changes of molecular packing in SAMs of islands of alkanethiols partially covering the gold surface induced by external pressure as well as a comparative study of the frictional and structural properties of alkanethiols ($C_nH_{2n+1}SH$, n =12, 16) and mixed films were described by Barrena et al. [106]. They found that for single components films, the film height decreases in a stepwise manner as a function of the load applied as well a stepwise increases in friction force, whereas mixed films exhibit two friction regimes: an initial stage where the friction increases rapidly and a second stage whit similar slope to obtained for single component films. Recently, Munuera et al. [95] used high resolution and high sensitivity FFM to distinguish different crystallographic domains within alkanethiols islands self-assembled

on Au(111). BP$_4$ monolayers on Au(111) containing α and β phase domains were studied by Paradinas et al. [107] by means of combined STM, FFM and adhesion force measurements. Their results have shown that structurally identical but differently orientated BP$_4$ domains give rise to a variation in friction measurements, in particular in the β phase for which the separate analysis of forward and backward scans is employed to differentiate domains rotated 180°.

In the present chapter, we show different measurements performed for molecular films of carboxylic acid (-COOH) and thiol group (-SH) terminated of nanostructures at submonolayer obtained after annealing process. We compare the frictional response between tall and low islands, the latter exhibiting the structure $(2\sqrt{3} \times \sqrt{3})$R30°.

Though a general analytical theory of friction can hardly be developed because of the many process involved, an analysis of the microscopic tribological properties of monolayers systems has been focused on the dependences of the friction force on applied load being functionally described by the Amontons´ law (see equation 4.1) [108] for the friction force,

$$F_r = \alpha F_N + F_0 \tag{4.1}$$

where α is the friction coefficient, F$_N$ the normal force (applied load) and F_0 the friction force when $F_N = 0$. This type of dependence has been successfully used to characterize different systems [109, 110].

4.1   Contact Mechanic Fundamentals Aspects

In 1882, Heinrich Hertz determined that the contact between a flat plane and a sphere of radius R pressed together with a normal load P occurred within a circular contact area with contact radius a following the equation,

$$a = \left(\frac{PR}{K}\right)^{1/3} \tag{4.2}$$

being $K = \frac{4}{3}\left(\frac{1-\nu_i^2}{E_i} + \frac{1-\nu_j^2}{E_j}\right)^{-1}$ the elastic constant, E the Young´s modulus *(i, j)* for the sphere and the flat plane, ν *(i, j)* are the sphere and flat plane Poisson ratios. To describe the adhesion contact between two surfaces, several models have been proposed. The Johnson-Kendall-Roberts (JKR) model based on the assumption on an infinitely small radius of effect of surface forces, i.e. interactions occur only within the

contact area [111] and Derjaguin-Muller-Toporov model [112] based on two assumptions: surface forces do not change the deformed profile of the sphere that remains Hertzian; the attraction force acts outside the contact perimeter pressing the bodies together with the contact zone being under compression by the stresses distributed according to Hertz Model. When two rough surfaces approach each other their opposing asperities with the maximum heights come into contact randomly distributed in space over the area of apparent contact. The total area of these zones is known as the real contact area. The formula for calculating the radius of adhesive contact is,

$$a^3 = \frac{R}{K}\left(P + 3\pi R\gamma + \sqrt[2]{6\pi RP\gamma + (3\pi R\gamma)^2}\right) \tag{4.3}$$

Therefore, in absence of adhesion force (γ=0) the Hertz equation is obtained while if $\gamma > 0$ the contact radius always exceeds that of the Hertzian contact area under the same normal load P. Moreover, when the contact is fully unload (P=0) it does not disappear but remains finite with the radius,

$$a = \left(\frac{6\pi R^2\gamma}{K}\right)^{1/3} \tag{4.4}$$

once defined the contact radius, the contact area can be written as,

$$A = \pi\left[\frac{R}{K}\left(P + 3\pi R\gamma + \sqrt[2]{6\pi RP\gamma + (3\pi R\gamma)^2}\right)\right]^{2/3} \tag{4.5}$$

or being proportional to the external applied force and the adhesion force,

$$A \propto (F_{ext} + F_{adh})^{2/3}$$
$$A \propto F^{0.67} \tag{4.6}$$

In chapter 5 we will presents electronic transport measurements through of the molecular film where the contact resistance could dependent with the contact area.

4.2 Dependence of friction response with the applied load on surfaces with MMTA

We were interested on studying the frictional properties on samples of MMTA prepared at low and high immersion times using different solvents, such as THF, ethanol, toluene and acetic acid. Solutions of MMTA were obtained following the protocols in chapter 2 for 30 minutes and after several days of immersion and thermal treatment

for 16 hours or more. The experiments were performed under a controlled Relative Humidity $(RH) \approx 5\%$. We used different types of cantilevers, from Veeco Probes, Budgetsensors and Nanosensors™ with nominal force constants of $k = 0.5 \ N \cdot m^{-1}$, $k = 0.38 \ N \cdot m^{-1}$, $k = 0.1 \ N \cdot m^{-1}$, and rectangular conductive diamond and chromium/platinum coated cantilevers of $k = 0.2 \ N \cdot m^{-1}$. Small size images revealed irregularities on top surface of the tall islands. This fact is also reflected on the friction map. The molecular packing, the terminal group and the measurements conditions will have an important effect on the tip-sample interaction. J. te Riet et al. [113] have used the nanografting method to construct well-defined nanoscale patches of thiols with functionalized end groups (-COOH, -NH$_2$, -SH, -OH, -CF$_3$) in a SAM matrix on a gold surface Au(111) showing the following friction hierarchy CH$_3 \leq$ CF$_3 <$ OH $\leq$ SH $<$ COOH $\leq$ NH$_2$. Depending on the end group type, these nanografted patches exhibited considerable differences in lateral friction force offering the possibility to use the friction response as a molecular recognition tool.

In agreement with the model exposed in chapter 3 [75], we expected the COOH and SH end groups for low and tall islands of MMTA, respectively, for which have been self-assembled and nanostructured after annealing.

4.2.1   Without Thermal Treatment

In this section, we show simultaneous topographic and friction images to map chemically distinct domains at nanoscale using frictional force microscopy (FFM). The basis of the following results is the dependence of the frictional interactions to identify chemical functional groups such as (-SH) and (-COOH) at the outermost of microscopic contacting areas. In agreement with the previous chapter, low islands with a (-COOH) end group and bilayers with a (-SH) end group were characterized using tetrahydrofuran or toluene solutions of MMTA for different immersions times, whereas ethanolic solutions of MMTA showed multilayers formation or cluster of islands in low concentrations and high immersion times without annealing.

4.2.1.1   Friction at low coverages from THF solutions of MMTA

Figure 4.1 shows the topographic image (a) and the friction map (b) of the MMTA molecular film after immersing in a 100μM THF solution of MMTA for 30 minutes. By using THF solutions, few bilayers were observed that allowed identifying the (-COOH)termination and its molecular length around of 1.5 ± 0.1nm by means of scratching experiment. Simultaneous profiles taken on both topographic and friction images revealed a friction difference value of 12 ± 2mV between the (-COOH) termination and the gold substrate by applying 0.5nN.
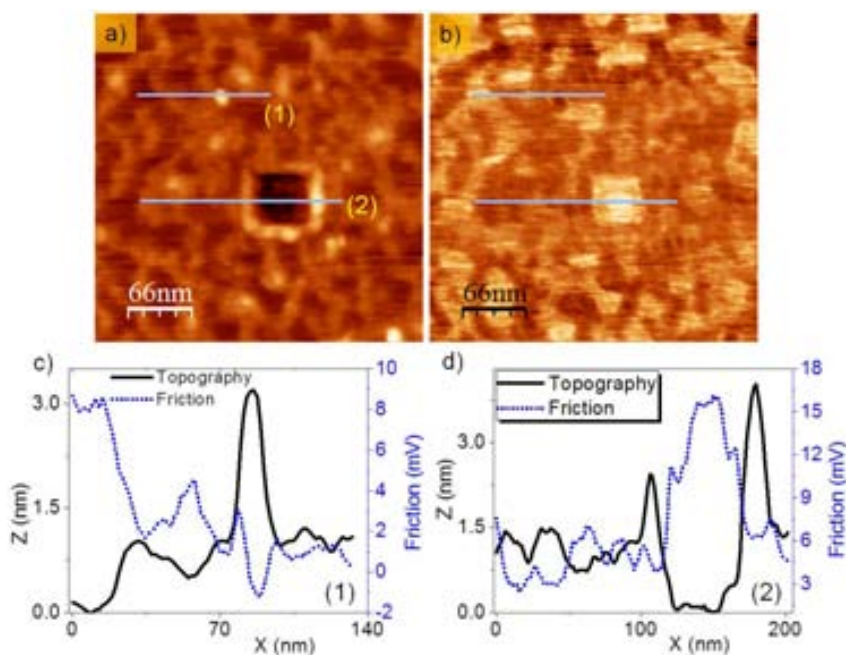
Figure 4.1. Topographic (a) and friction map (b) of MMTA on Au(111) after immersing in a 100μM THF solution of MMTA for 30 minutes. Numbered profiles (1, 2) taken along the lines in topography and friction map are shown in (c and d), respectively. Brighter regions on the friction map correspond to bare gold substrate. The brighter spots in topography correspond to tall islands. Adhesion force: -3.8nN; Applied force: 0.5nN. Total z-scale: (a) 0-5nm; (b)-15mV to 48mV.

Profiles are taken along the low islands as well as an incipient formation of tall islands with lateral dimensions of about 30nm respect to bare gold as reference. Num-

bered profile "1" shows a friction difference of about 9±2mV between the brighter spot (tall island) and substrate. Similar value is shown for the numbered profile "2" between the low islands of MMTA and the substrate. Scratching experiment was performed to obtain a region of bare gold to compare the friction. From results, we observe that the molecular film reduces the friction response of the substrate of about 60%-85%, then the lubricant character of the organic film is manifested.

4.2.1.2   Deciphering multilayers composition of 3D structures

Figure 4.2 shows topographic (a) image, friction map (b) (described in section 2.2), simultaneous topographic and friction profiles (c) taken along the lines in (a, b). Lateral force images (Forward and backward) are shown in (d, e), respectively, and simultaneous profiles are sown in (f). The topographic image shows several layers of the three-dimensional structure. Some are non-homogeneous, as will be suggested later might be related to a different chemical termination since the difference in height is ≈ 1.5nm. Topographic image reveals three levels of the 3D structure. From simultaneous topographic and frictional profiles taken along the line in (a, b) we observe a similar friction value between second and third level with a difference in height of about 8.4nm (5 single molecular lengths of 1.68nm), meaning they present the same terminal group. First and second level of the 3D structure shows similar height difference of about 8.4nm with a friction difference of 15mV between them. By comparing friction values between the first level and inhomogeneous regions of the second level, the friction difference between them is hardly detected (profiles not shown).

Taking into account the hydrophilic character and reactive of the molecular surface, the lateral forces images can be used to get insight about the chemical composition or structural order due to dissipation on the explored surface and measured by the torsion of the cantilever. Larger lateral forces in the forward scan are represented as bright colors, whereas a dark color is visualized in backward direction. Figure 4.3 was obtained by zooming in the 3D structure. Topographic image (a) and friction map show some details on the second level as reveals the simultaneous profile in (c).

A height difference of 1.5±0.1nm and friction difference of 15±2mV, quantified to be about 13% higher at the flat region than at depression marked with a dashed curve on
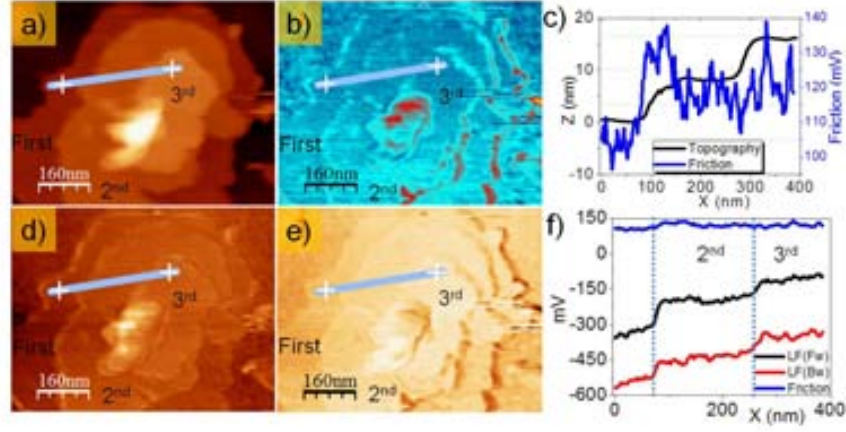
Figure 4.2. Topography (a), friction map (b) and cross-sectional profiles (c, f) taken along the lines in (a, b, d, e) images. Lateral forces and friction profiles in (f) are calculated from profiles taken along the lines in lateral force images (d, e) and friction map in (b). The levels of the 3D structure have been denoted as first, 2nd and 3rd in images and profiles. Total z-scale: (a)0-54nm; (b)-0.11V to 0.8V.
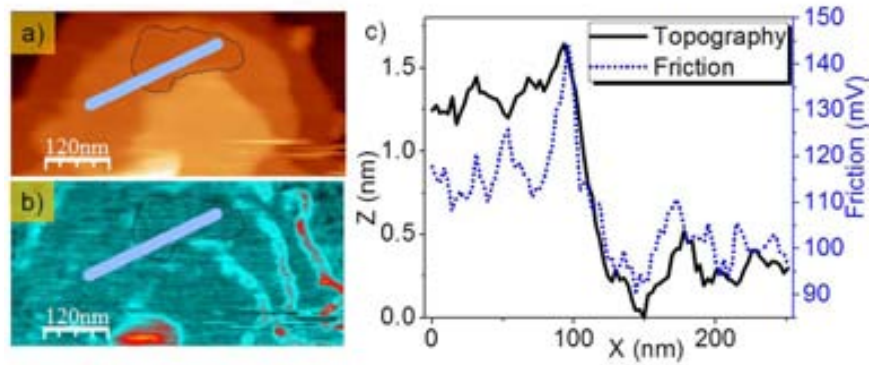
Figure 4.3. Topographic image (a), friction map (b) and simultaneous topographic and friction profiles taken along the line in (a, c) on the second level of the 3D structure are shown in (c). Dashed lines in (a, b) indicates the inhomogeneous region on the second level. Total z-scale: (a)0-54nm; (b) 4mV to 624mV.

the second level are shown. This inhomogeneous layer is observed in topographic image as a small dark region on the second level, as well as a contrast in friction image between

4.2 Dependence of friction response with the applied load on surfaces with MMTA

these regions. From these results, we deduce the presence of both chemical terminations in agreement to multilayer formation by hydrogen bridges and electrostatic interactions between bilayers within the stacking. Taking the first level of the 3D structure as a reference, lateral force profiles show that the second level appear brighter than the first level in both scan directions. Same friction value beteween the second and third level can be associated to same chemical termination or a result of friction asymmetry? or different friction observed between the first and second or third level can be due to the friction anisotropy? Can both friction asymmetry and friction anisotropy be present?

Both friction anisotropy and friction asymmetry are related to the dependence of the mechanical response on the sliding direction. The term friction anisotropy, on the one hand, refers to the variation of the friction coefficient (μ) with the relative orientation of sliding surfaces and is commonly correlated with the azimuthal orientation of a crystalline surface. On the other hand, friction asymmetry arises from a direction dependent (asymmetric) surface potential and has been also called directional dependence of friction (see nanotribological studies performed by Paradinas et al [107]).

FFM has been found to be sensitive to the tilt of molecules in two-dimensional molecular arrangement at surfaces [114] and employed to discriminate ordered configurations presenting different friction coefficients or different packing [95], as well as to identify highly dissipative transient molecular configurations [115] or tilt of carbonate ions at surface of calcite ($CaCO_3$) to explain frictional asymmetry [116]. Segura et al. [117] observed on freshly cleaved (011) surface of L-alanine in terraces or islands a relevant friction asymmetry. Both terraces and islands exhibit the same nature and crystallographic structure but a 180° rotated orientations.

Some nanostructures have shown several hundreds of mV in lateral force for both scan directions. Figure 4.4 presents the topography (a), the friction map (b) and lateral force images (Fw&Bw) (d, e) of a 3D structure. Simultaneous profiles taken along the line in all images are shown in (c, top profile) and (f, down profile). We observe a difference in height of about 6.3nm for the island (4 single molecular lengths of 1.6nm). Both profiles revealed less dissipation at the island than at the outside film. The top profile crossing the 3D structure was normalized to enhance and visualize this behavior. The down profile taken along the line between the outside film and part of the 3D
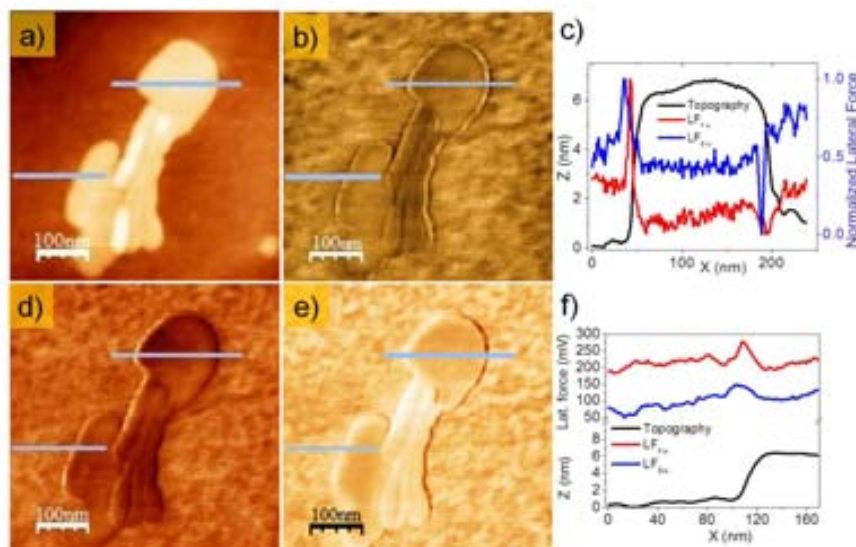
Figure 4.4. Topographic (a), friction map (b) and lateral force (Fw&Bw) (d, e) images. Nanostructures were obtained by drop-casting method from 2μM ethanolic solution of MMTA revealing friction asymmetry. Simultaneous topographic and lateral force are shown in (c, f). Normalized values for the lateral force are shown in (c). Total z-scale: (a) 0-13nm; (b) -0.345V to 0.415V.

structure shows the same trend for both scan directions. Interestingly, the friction map shows similar contrast between the outside film and regions within the 3D structure. A possibility of friction asymmetry is studied on molecular domains of these structures.

High resolution lateral force imaging allows observing small oriented molecular domains of $\approx 15nm^2$ on top of the 3D structure, as shown in section 3.2. Figure 4.5 shows topographic and high resolution lateral force images (a) recorded on top of the 3D structure from Figure 4.4. Small molecular domains were observed by zooming in high resolution images (a, down). By tracing a line along theses domains as shown in high resolution image (a, top) for forward and backward scan, we observed a behavior of friction asymmetry, as depicted in (b, down). A cartoon is depicted in (b, top) to explain this behavior during scan for both directions (Fw&Bw). In forward (the tip moves from left to right) and backward scan (the tip moves from right to left) across domains named a and b. When the tip moves on the a domain, the cantilever experiments higher torsion than on the b domain, this fact can be explained if molecules

in b are rotated 180°. Similar explanation is deduced in backward scan, the cantilever experiments higher torsion in a' than b'.

Despite the friction asymmetry, a contrast in LFM images between domains were not clearly observed. On the upper island surface a roughness of 0.18nm was estimated, i.e. an homogeneous chemical composition can be assumed, but an asymmetric response of the friction along the scan direction was detected, which is related to equivalent rotated domains.
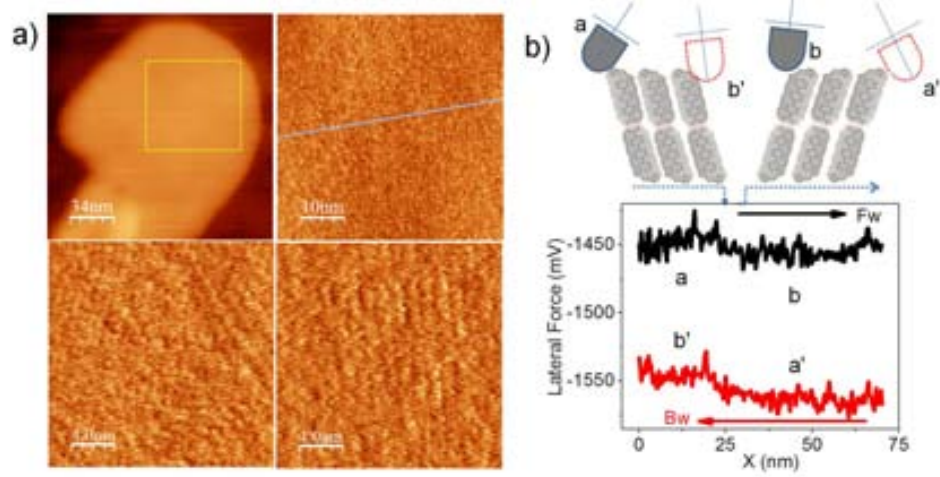
Figure 4.5. Topographic image of a 3D structure and high resolution images recorded on marked with yellow dashed line are shown in (a). High resolution lateral force images show small domains found on the nanostructures. Cartoon showing the friction asymmetry and correlating with the profile taken along the line in high resolution image is depicted in (b). Regions (a, b) and (a', b') are associated to molecular domains on the 3D structure during forward (black) and backward (red) scans, respectively.

From experimental data obtained for lateral force in (b) and summarized in table 4.1, we measured the absolute value of the friction difference for the positions labeled $\Delta |ba'|$=104mV and $\Delta |ab'|$=98mV. The discrepancy of the friction difference estimated above is, however, within the experimental error (5%). Bluhm et al. [118] have illustrated by a saw-tooth-like potential the possible friction asymmetry origin of organic ferroelectric crystals which ascribed to domains with the same structure but opposite molecular tilt directions. But, not all the 3D structures obtained by drop-casting me-

Lateral Force (mV)					
a	b	a'	b'	$\Delta\,|ab'|$	$\Delta\,|ba'|$
-1447.1	-1457	-1561	-1546	98	104

Table 4.1. Experimental data of friction asymmetry of small domains on 3D nano-structures. The *a, b* and *a', b'* values were calculated based on raw data average for each zone.
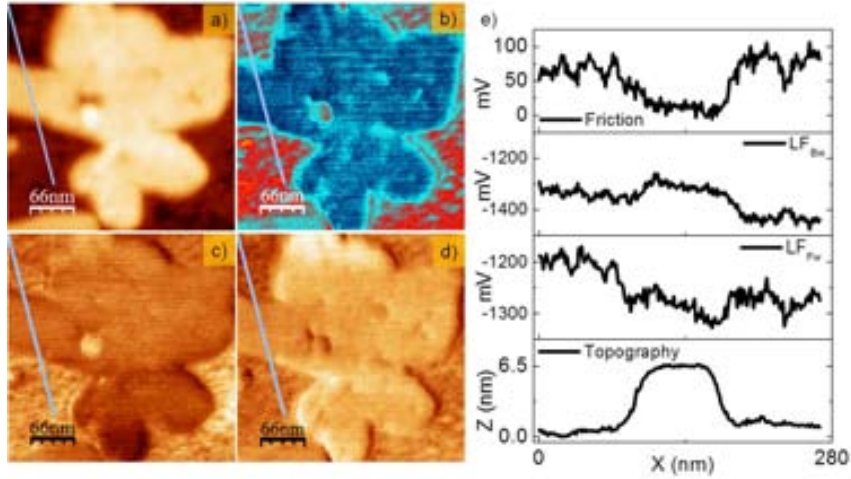
Figure 4.6. Topographic (a), friction map (b) and lateral force images (Fw&Bw)(c, d) on the 3D nanostructure obtained by drop-casting using a 2μM ethanolic solution of MMTA. Total z-scale: (a)0-9.5nm; (b) -0.02V to 0.152V.

thod have revealed friction asymmetry. For conventional LFM measurements, friction contrast within molecular domains occurs due to differences in the chemical composition of the surface which modify the surface potential. For homogeneous surfaces and surface potential symmetric along of a scan line, the lateral force contrast is reversed for opposite scan directions, and the observed lateral forces are independent of the relative orientation of tip movement with respect to the molecular surface.

Figure 4.6 shows topographic (a), friction map (b) and lateral force images (Fw&Bw)(c,

4.2 Dependence of friction response with the applied load on surfaces with MMTA

d) of a 3D structure formed on the Au(111) substrate by drop-casting . Simultaneous profile taken along the line in all images are shown in (e). Cross-sectional profiles obtained from topographic and friction images show a clear difference of friction of 50±10mV between the nanostructure and the background surface. The profile taken on the 3D structure reveal a height of 6.2±0.3 nm (double bilayer, 2L) showing lower lateral force than on the background surface in forward direction with similar behavior for the bilayer case. This fact suggests that for 2L values a (-SH) end group will be exposed on topmost surface.

4.2.1.3 Friction Response of the Bilayer
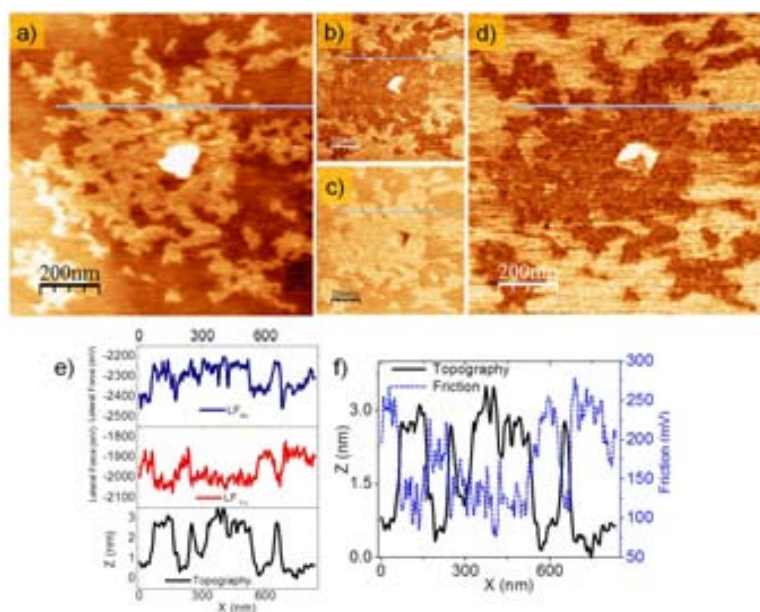
Figure 4.7. SFM images of Au(111) on mica after immersing in a 100μM toluene solution of MMTA for 20 hours. Topographic (a), lateral force (Fw&Bw) (b, c) images and friction map (d) with simultaneous profiles taken on the tall islands (bilayer). Total z-scale: (a) 0-27nm; (d) 23mV to 900mV. Adhesion Force: -1.5nN; applied force -0.2nN.

Figure 4.7 shows the topographic image of cluster of MMTA islands formed after 20 hours from 100μM toluene solution of MMTA. Bilayers of 3.1±0.1 nm are observed

respect to the gold surface. In lateral force (Fw) less dissipation is observed at the bilayer that at the substrate, by taking the simultaneous profile on topographic image and friction map we measured a friction difference between the thiol group (-SH) and the gold surface of about 120±10mV, having higher dissipation values on the substrate. The apparent inhomogeneous friction within the cluster islands in (d) is due to the small lateral dimensions and the roughness of the bilayer island top.
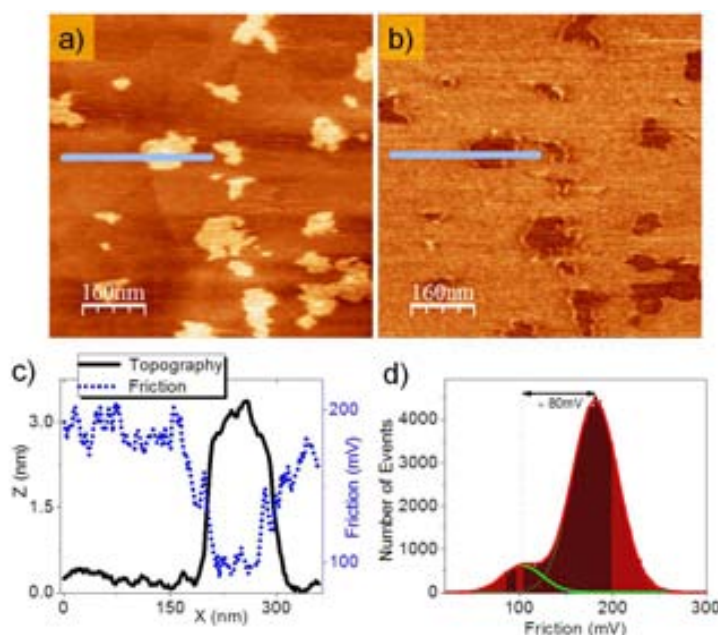
Figure 4.8. SFM images of Au(111) on mica after immersing in a 100μM toluene solution of MMTA for 20 hours. Topographic(a), and friction map(b) the simultaneous profiles taken on the tall island (bilayer) and depicted in (c). The histogram in (d) shows the friction value for the substrate and the bilayer. Total z-scale: (a) 0-6nm; (b) 13mV to 390mV.

Unlike the nanostructure showed for ethanolic solution in Figure 4.6 where the bare gold is no clearly defined and by which a friction difference of 50±10mV was measured, the Figure 4.8 reveals bilayer clusters and the gold surface as reference. Bilayer islands of 3.2±0.1nm in height are shown in topography image (a) with lower friction response than to the bare gold as shown the friction map in (b) and the difference of about 80mV as shown the histogram in (d) for the whole friction image. We have suggested a (-SH)

termination for bilayer and double layers, then we will expect a similar friction response for both cases if the friction response is given for type of chemical termination, however a discrepancy of at least 20mV exist. This possible discrepancy can be explained if some molecules with (-COOH) termination on the gold surface or lying-down phase are presents, in addition of any lose molecules that are not removed due to the low applied force. The most plausible explanation can be ascribed to single molecules within an intermediate phase lying down - standing up that reduces the friction value. The simultaneous profiles in (c), topographic and friction, show that friction values at border of the bilayers appear softer than the abrupt behavior in the topographic profile due to the poor molecular packing. The adhesion force of -1.5nN at the background surface was measured for several force distance curves. The images were recorded at -0.2nN normal force.

4.2.2 Tribological Studies After Annealing Treatment

Structural and morphological changes as a function of annealing time, immersion time and solvents were presented in previous chapters. We show in this section, the friction and adhesion response of the MMTA islands after annealing. Each set of samples under their respective preparation protocol were annealed in an appropriate furnace in air. The temperature was fixed at $(110\pm10)°C$ and kept constant to compare results.

4.2.2.1 Low Islands and Friction Map

In spite of the difficulty to elucidate the friction difference between tall and small islands for the samples obtained from THF solutions of MMTA (see Figure 4.9), as it will be seen later on this section, small difference of ($\approx$ 8mV) are obtained. The high coverage on the surface due to the high immersion times and concentrations used suggests to use the 3D modes for friction measurements simultaneous on both low and tall islands. Topographic image (a) reveal low islands connected between them and few tall islands to establish a clear friction difference as shown simultaneous topographic and friction profiles in (c).
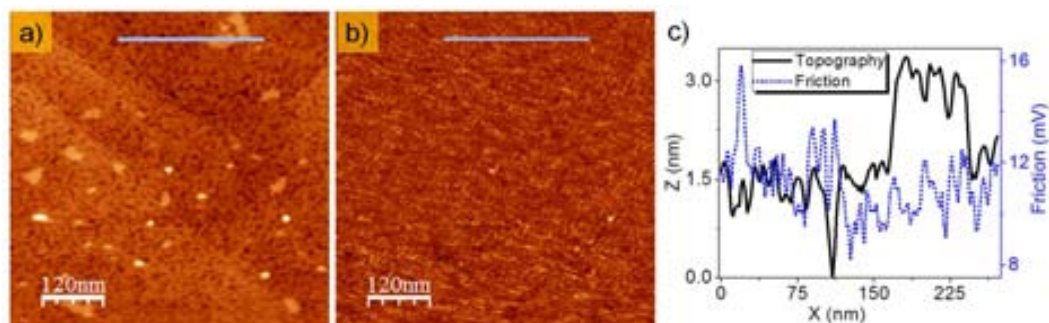
Figure 4.9. Topographic (a) and friction map (b) of Au(111) substrate after immersing in a 100μM THF solution of MMTA for 16 hours and post-annealing at 120°C for 16 hours. Total z-scale: (a) 0-7nm; (b)-2mV to 40mV. Adhesion force: -1.8nN; applied force: -0.1nN.

4.2.2.2 Friction and Adhesion Measurements between Low and Tall Molecular Islands

Samples obtained from acetic acid solutions of MMTA after immersing the Au(111) substrates in 100μM for 30 minutes and longer periods of immersion and annealing are presented.
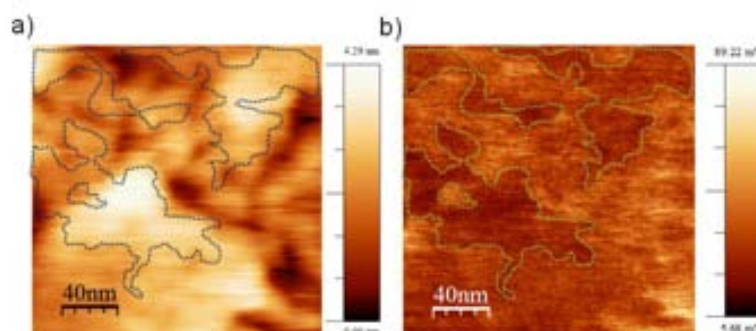
Figure 4.10. Topographic (a) and friction (b) images of Au(111) after immersing in a 100μM acetic acid solution of MMTA for 30 minutes and post-annealing at 100°C for 16 hours.

Figure 4.10 shows the morphologies described as low and tall islands. Topographic image (a) and friction map (b) reveal similar friction contrast for the surface of the low and tall islands, this observation is clearer for the delimited regions in topography

and friction map. By correlating topographic and friction profiles for tall islands, we observed a height difference of 5Å on the topmost surface. The COOH and SH end groups are associated with high reactivity with the environment and this height difference can be related with adsorbed contaminants and wetting layer even in low relative humidity conditions.
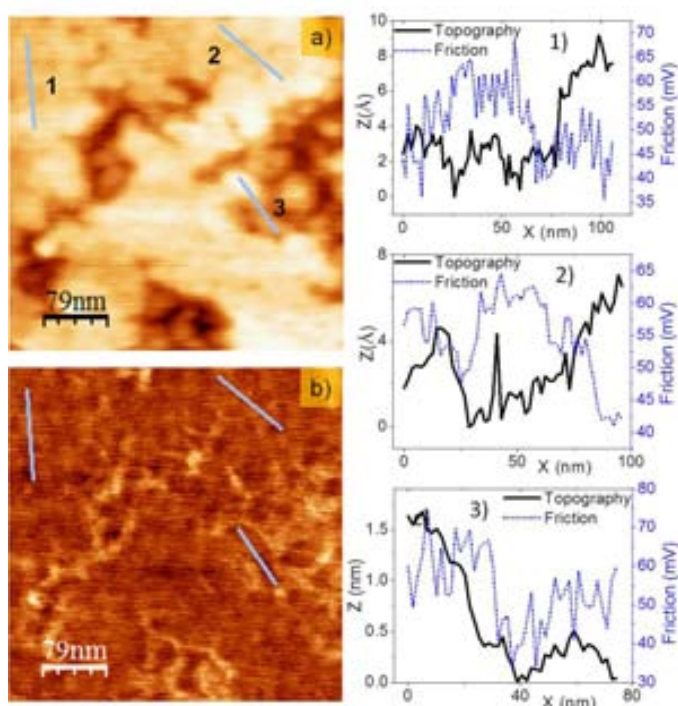
Figure 4.11. Topographic (a) and friction map (b) of the Au(111) substrate after immersing in a 100μM acetic acid solution of MMTA for 17 hours and annealing at 100°C for 16 hours. Simultaneous profiles on the topmost surface of tall islands (1, 2) and tall with low island (3) are shown on the right panel.

Once obtained the morphological characterization of samples prepared for 17 hours in 100μM acetic acid solution of MMTA, those were thermally treated. To compare morphological or structural changes with the samples prepared for 30 minutes of immersion times we fixed a common post-annealing time and temperature (105±5)°C. Figure 4.11 (a, b) presents the topography and the friction map for the surface of the tall islands.

Numbered profiles (1, 2, 3) taken along the lines in (a, b) are shown on the right panel. Numbered profiles (1, 2) taken on the bilayer surface revealed a difference in height of about 0.35Å and friction difference of 8±2mV and ($\Delta z \approx 0.4$Å and $\Delta friction \approx$ 10mV), respectively. The profile (3) shows a difference in height equal to the molecular length between tall and low islands, 1.5±0.1nm, and a friction difference of 13±2mV.
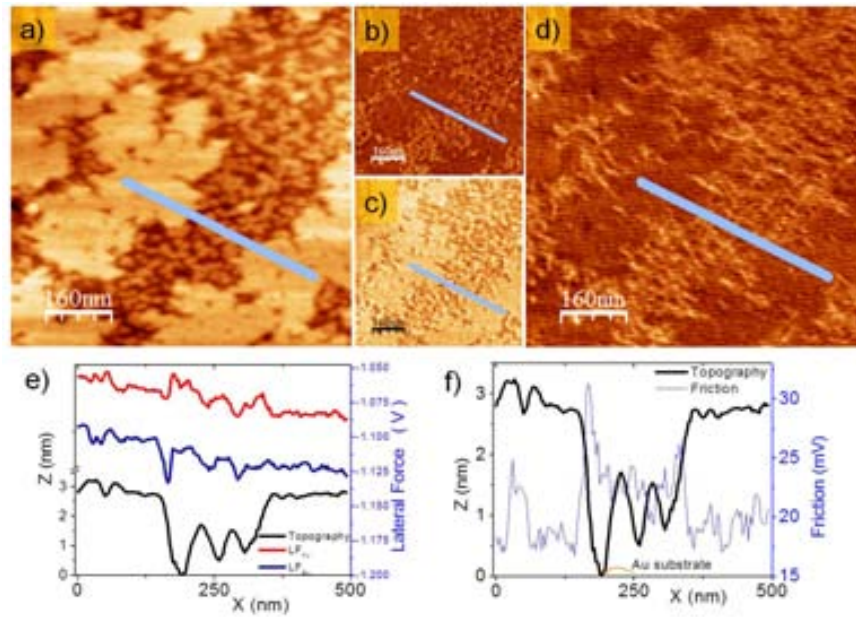
Figure 4.12. Topographic (a), lateral force (Fw&Bw) (b, c) and friction map (d) images of the MMTA morphologies after annealing at 100°C. Topographic profile shows islands with dimensions corresponding to low and tall islands. Cross-sectional profile on both morphologies and bare gold with the lateral force are displayed in (e). Friction map (d) reveals low friction values for the tall islands (bilayer) as displayed in profile (f). More detailed values can be observed with a contour map (not shown) of the friction map, where some tall islands show a friction contrast on the topmost surface. Total z-scale: (a) 0-6.5nm; (d) 2.3mV to 68mV.

Figure 4.12 shows the morphologies of low and tall islands described in chapter 3. From lateral force images we traced profiles across of these islands to define a friction value respect to each other. A friction difference of 5±2mV between low and tall island was measured; however, on the topmost surface of the tall island friction differences of about 3mV was also measured. A closer look of the friction map we can observe regions

with friction contrast for tall islands and differences in height that do not correspond to the MMTA molecular length. These observations would confirm the existence of two very reactive chemical terminations: a carboxylic group for low islands and a thiol group for the bilayer. Note that the friction of the bare gold is 1.5 times larger than the molecular film.
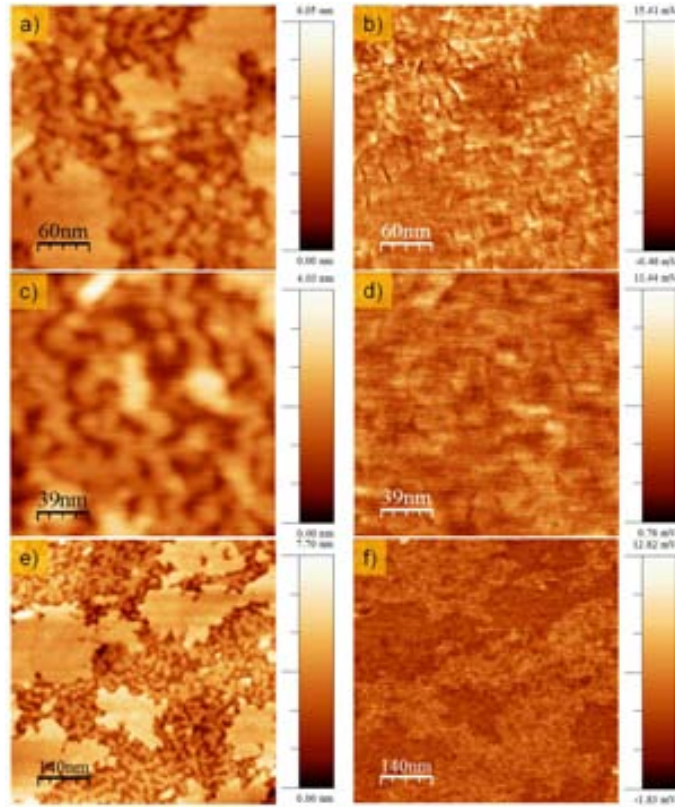
Figure 4.13. SFM images of low and tall islands of MMTA on Au(111) after immersing in 100μM acetic acid of MMTA for 16 hours and annealing at 110°C for 17 hours. Topographic (a, c, e) and friction map (b, d, f) are shown at RH 15%. Panel (e, f) corresponds to the same sample with 4 days old. Applied force: 2.5nN for (a, c) and 1.5nN for (e); Adhesion force (-2.5nN).

All presented measurements have been performed at low relative humidity conditions (RH≤ 5%). However, we obtained new samples to perform measurements at RH above 15%. Following the recipe for longer immersion times into acetic acid solution

and fixing the post-annealing time and temperature, we reproduced the morphologies previously observed. As show the friction maps (b, d) in Figure 4.13, both morphologies reveal inhomogeneities and hardly differences between them can be detected. Simultaneous profiles traced on several zones (not shown) revealed a small difference of 5±2mV for low and tall islands for images acquired in contact mode by applying 2.5nN. The same sample was observed 4 days later in air, and the friction map showed more detailed zones between both morphologies and bare gold, as shown in (e, f). Although the friction difference between low and tall islands was not above 10mV, we suppose that for longer times exposed to the environment, the low islands tend to increase their friction respect to the termination of the tall islands.

Alternatively, the 3D modes were also employed to evaluate the tribological properties of both low and tall islands described in section 2.2.3.2. By doing this, we obtained simultaneous images of the normal force and lateral force images for a selected area. When both tip and molecules are pressed against each other with an increasing load (F), the area of the contact increases in the manner predicted by continuum mechanic models basically the Hertz model and its modified versions (JKR, DMT) including short and long range adhesive interactions. By applying the Hertz model, the contact area of spherical bodies increases as $F^{2/3}$ assuming an elastic deformation by which we will expect the friction follow a $F^{2/3}$ dependence on load as long as the dissipation process do not change (see equation 4.6).

Figure 4.14 shows a typical acquisition using 3D modes for friction measurements with a selected line X in forward and backward scan direction across both types of islands. Normal force (F_n), friction map (b) calculated from simultaneous lateral force images are shown. Vertical and horizontal lines allow measuring the friction and the force values on the maps. Image in (c) is a 3D representation of normal force image. Experimental data with two polynomial functions are shown to explain the behavior of the friction within force ranges. The profile (d) taken on the tall island shows a smooth and almost linear behavior within a range force, where we have point out this threshold load of about 5nN. Depending on the island sizes, the threshold can be observed at different load values. The following graphs show how the friction between a gold substrate covered by tall and low islands of MMTA and the AFM silicon tip

4.2 Dependence of friction response with the applied load on surfaces with MMTA
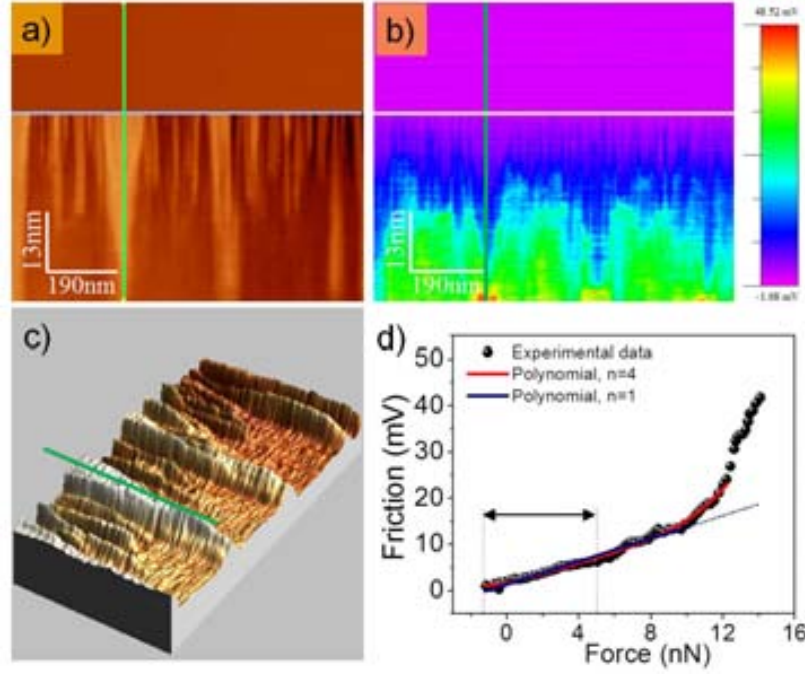
Figure 4.14. 3D modes for calculating friction on MMTA morphologies. Normal force F_n and friction map of MMTA islands obtained in 100μM acetic acid solution of MMTA for 16 hours and annealing at 100°C for 17 hours. Image (c) is a 3D representation to observe both low and tall molecular islands from (a). Profile in (c) reveal friction changes respect to the applied force in (d). Linear and non-linear models are suggested to fit the experimental data. Image (a) has been filtered only to enhance details, whereas (b) has been calculated subtracting the lateral force images.

evolves as the load is increased.

Figure 4.15 shows the normal force F_n (a) and friction map (b) with simultaneous numbered profiles taken along the tall islands. All profiles and the threshold load ($\approx$5nN) with vertical lines are shown in panel (c). Following a Hertzian contact and a normal force, $F_n = F_{load} + F_{adh}$, the frictional force per unit area can be interpreted as the shear strength of the tip-molecule junction. If this shear strength is assumed constant, friction force is determined by the contact area. The dependence of the friction with the normal force is modeled by means of polynomial functions, at low loads. We will analyze the contribution to the friction of the function $Y = \alpha F^{2/3} + \beta F$ at low force, being the first term proportional to the contact area, while the second one proportional
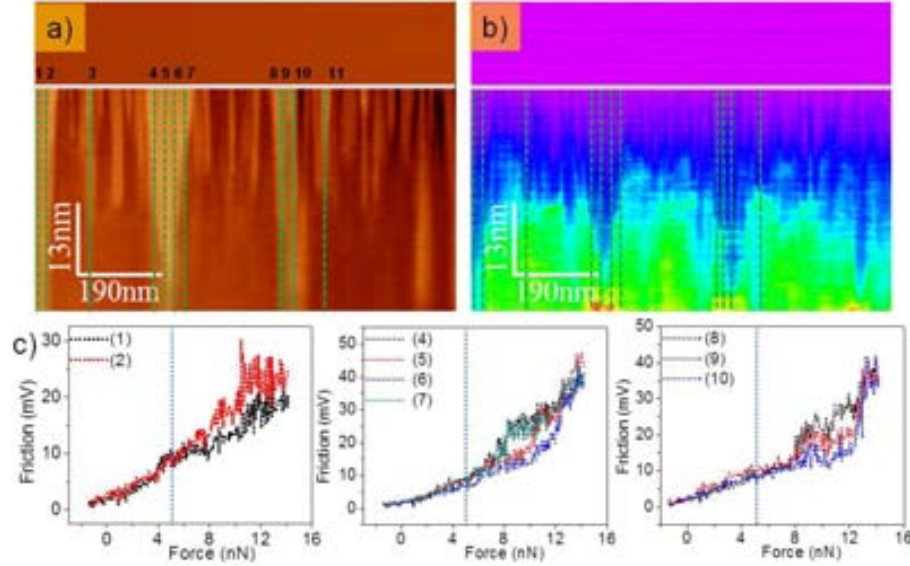
Figure 4.15. (a) Normal force F_n and (b) friction map of MMTA islands obtained in $100\mu M$ acetic acid solution of MMTA for 16 hours and annealing at $100°C$ for 17 hours. (c) Profiles were taken on MMTA tall islands to determine the friction value at different loads.

to normal force.

At low applied forces ($\approx$1nN), friction differences between low an tall islands can hardly be measured (see color contrast in friction map Figure 4.15); however by increasing the load friction is higher for the low than tall islands.

A close inspection to the friction curves at low forces we observe a linear behavior for both $Y = C + ... + Bx^{n-1} + x^n$ and $Y = B + Cx$ functions employed, as shown in Figure 4.14(d). With the Hertz theory, assuming a single asperity contact, a two-thirds power law is expected of the relation between the friction force and the normal force, F_n. However, by increasing the asperity contacts, a linear dependence is more likely, because asperities are elastically flattened to give a single point contact even at low loads. In table 4.2 we have summarized the results of some regressions performed on the labeled profiles by which both models suggest a linear friction dependence with the applied load within a low force range from all curves shown in Figure 4.16. From non-linear regressions, the exponent value n is close to 1, except profiles (8) and (9) where the friction response follows an approximated Hertzian behavior. The dependence

4.2 Dependence of friction response with the applied load on surfaces with MMTA
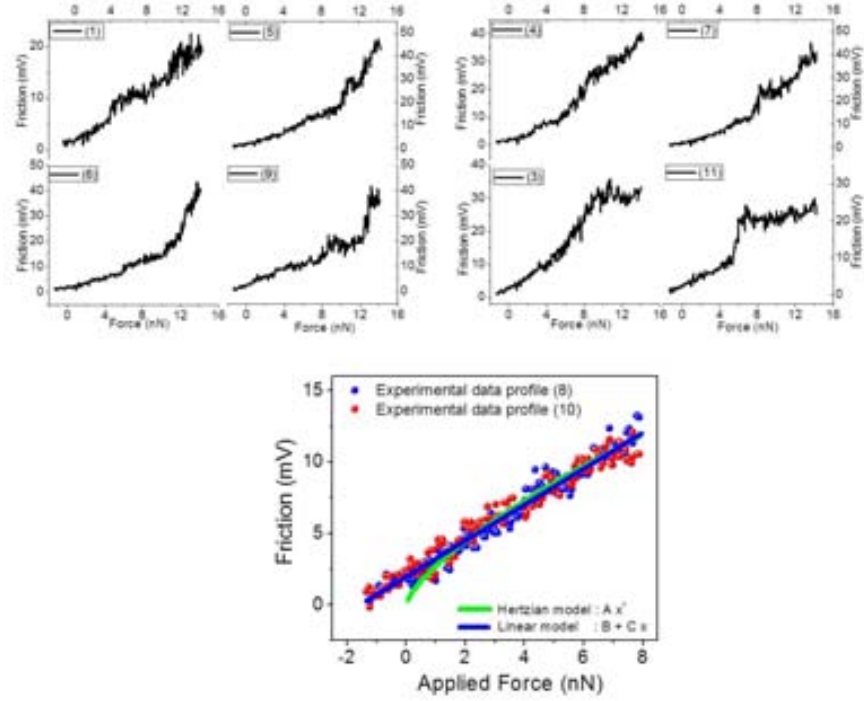
Figure 4.16. Profiles taken on the tall islands by means of the 3D modes. Top: Panels show more detailed profiles of friction versus load on MMTA islands. Bottom: at low range of applied force a Hertzian and linear model are fitting the experimental data.

of the friction force with the normal force, comes mainly from the term βF, as described before, being a characteristic behavior of complete monolayers.

Profile	A $\cdot x^n$		B+C$\cdot x$		Ratio
	A	n	B	C	A /C
3	2.80	0.97	2.10	2.30	1.20
5	2.01	0.94	1.46	1.57	1.28
6	1.70	0.93	1.38	1.22	1.39
7	1.79	1.00	1.30	1.54	1.16
8	2.70	0.71	2.87	1.19	2.26
9	4.50	0.49	3.06	1.31	3.40

Table 4.2. Friction dependence with the contact area and linear dependence with the applied force of tall islands.

Tall islands with lateral dimensions above 50nm present less lateral reduction when the applied force is increased, as shown numbered profiles (4, 7, 8, 10). This observation is also supported by some regions with step or plateau frictions corresponding to a specific force range (above 4nN). We suggested that tall islands are more stables and compactness and higher applied force are required to totally compress prior to damage of the islands. The higher cohesive energy of the tall islands yields mechanically more robust layer, in which compression and creation of conformational defects is hindered, and thus the number of deformation modes that can absorb energy from the probe is reduced, leading to a lower friction force.
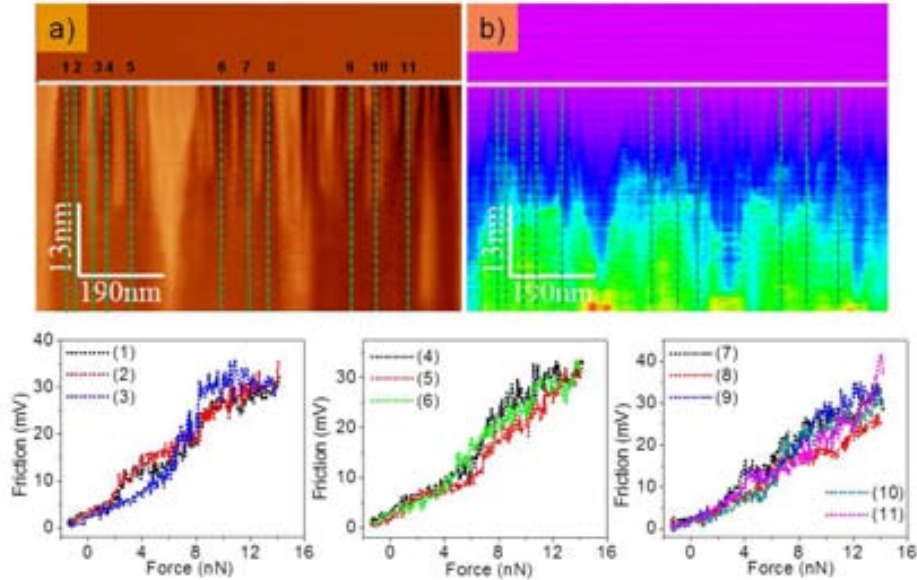
Figure 4.17. Normal force F_n and friction map of MMTA islands obtained in 100μM acetic acid solution for 16 hours after annealing at 100°C for 17 hours. Profiles were taken on MMTA low islands with lateral dimensions less than 20nm to determine the friction at different loads.

Profiles on low islands with lateral dimensions below 20nm were also drawn to estimate the friction as a function of the load (see Figure 4.17). Normal force F_n (a) and friction map (b) with simultaneous profile taken along the low islands are depicted. Some characteristics were observed in selected profiles, as shown in Figure 4.18. Profile (1) shows steps in the friction values at 2nN, 6nN and 8nN. When scanning at an

applied load above ≈7nN, the energy provided by the probe is enough to disturb the molecular packing of the low islands prior to irreversible damage. Similar values of applied force were measured for profiles (5, 2, 8). Each jump in the friction value was correlated with jumps in force distance curves in repulsive regime recorded during friction measurements and electrical characterization to study a possible molecular tilt angle as a function of the load. Unlike the friction curves obtained on tall islands, for low islands was not evident at low loads a behavior smooth of the curve. This is due to the successive turning on of new energy loss mechanism that are related to the deformation of the molecular assembly, vacancies or defects and size of the islands. Moreover, depending of the island size, the threshold force prior to damage can be observed even at 0nN normal force (curves not shown).
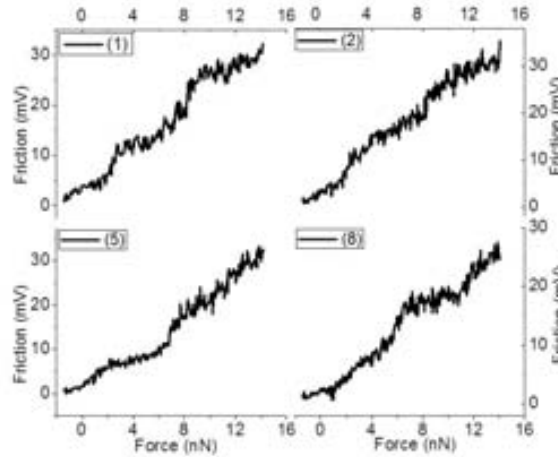
Figure 4.18. Profiles taken on the low islands and lateral dimension below 20nm. Panel shows detailed profiles of friction versus load by means of the 3D modes. Jump of the friction values are observed each 2nN in the repulsive regime.

As described Munuera [91], to tilt the molecular assembly a small separation between chains must exist (vacancies, defects,due to the penetration of the tip), to allow chain disengagement. Once separated, the chains are able to slide and arrange with a different tilt angle. The increase in friction is due to the energy absorbed from the the probe to overcome the activation barrier of the tilting process

Several topographic and lateral force images were also recorded in the same zone, 0.5×0.5 μm^2, at different loads. By taking the friction values in simultaneous positions for both topographic and friction images, a friction versus load curve is obtained. This method is convenient if the sample has large inhomogeneous domains. By using this method, a small area on the tall island is assumed homogeneous and taking both lateral force images (Fw&Bw) while the loading force is increased for each acquisition image we obtain the friction as $1/2(LF_{Fw} - LF_{Bw})$ for the whole image. For a range of force, we observed completely removed the molecular film leading to observe the bare gold and some monoatomic steps, as shown in Figure 4.19. Topographic images of Au(111) substrate after immersing in a 100μM acetic acid solution of MMTA for 16 hours and annealing at $115°$C for 16 hours is shown in (a). After loading experiment, all islands are removed leading to observe the bare gold substrate and monoatomic steps, as shown in (b). Topographic and friction values can be calculated of each recorded image at different load, as shown simultaneous profiles in (c). In this case, we have chosen a tall island to compare the behavior of the friction with previous 3D measurements.
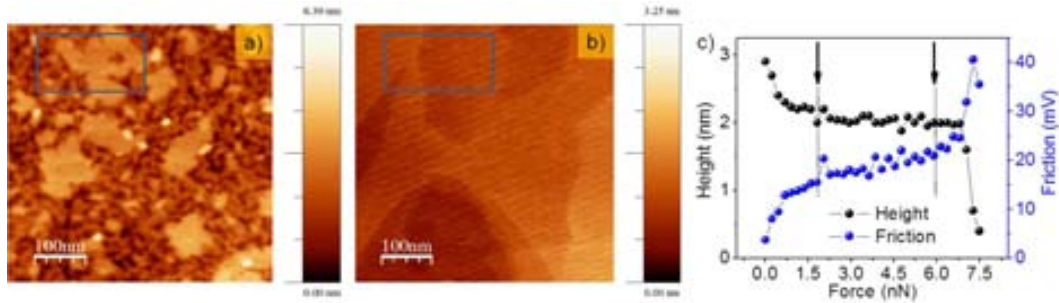
Figure 4.19. Topography image of Au(111) substrate after immersing in a 100μM acetic acid solution of MMTA for 16 hours and annealing at $115°$C for 16 hours is shown in (a). Bare gold substrate and monoatomic steps are observed after loading experiment in (b). Simultaneous friction and height versus applied load curves on the tall island for the marked region in (a) are shown (c). The molecular islands are removed by applying $\approx$ 8nN.

We observed also the stepwise behavior on tall islands by acquiring simultaneous topographic and friction images of a small selected area. It can be seen that every jump

in height at 2nN, 3.5nN and 4.5nN of applied force is accompanied with a restoring effect. As the load increases, the tip tilts the molecules under it while the molecules in the trailing part restore after passing of the tip. In addition, a 30% of the total height of the bilayer was reduced for loads between 2nN and 6.5nN as shown the black arrows in (c) prior to total compresing. Interestingly, for the range force between 0.5nN and 5nN, the friction curve reproduces the behavior of the friction curves measured by means of the 3D modes on the tall islands in Figure 4.15.
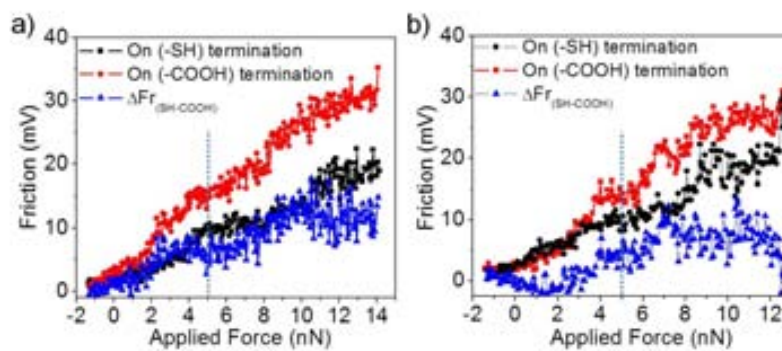
Figure 4.20. Simultaneous friction curves from 3D measurements for tall and low islands. Friction difference $\Delta \mathrm{Fr}_{SH-COOH}$ taken on low and tall islands by taking profiles (7, 9) and (2, 1) are shown in (a) and (b), respectively.

As described before, for a range of force from 0.5nN to 5nN the friction behavior is almost monotonous linear and related to the increase in contact area with applied load for tall islands with lateral dimensions of $\approx$ 50nm, in agreement with the load dependent model. However, for low islands with lateral dimensions of about 20nm within of this range o force a stepwise behavior was observed. At low force (below 1nN) differences in friction was not measured between tall and low islands with similar lateral dimensions. In spite the constraints, we tried deduce a friction difference between the carboxylic group (-COOH) of the low and thiol group (-SH) for tall islands.

Figure 4.20 shows two examples of the trend of the friction for small and tall islands when the load increases. For all measurements, the (-COOH) end group revealed higher friction than the (-SH) end group. Panel (a) shows friction curves for the thiol (-SH) and carboxylic (-COOH) end groups from low (profile 7) and tall (profile 9) islands, from

Figures 4.17 and 4.15, respectively. The friction difference between them is expressed as ($\Delta Fr = Fr_{small} - Fr_{tall}$). Panel (b) shows similar analysis between profiles taken from 3D modes for low (profile 2) and tall (1) islands.

From these results, the friction difference at low force (below 3nN) corresponds to low values ($\approx$3mV), however this difference is increased up to 15$\pm$3mV when the applied force is about 9nN. From F_n images one can deduce that by applying forces of about 6nN the low islands with reduced lateral dimensions can be completely crushed. Taking into account this fact, we suggest that a correct and comparatively friction difference between both (-COOH) and (-SH) terminations for similar lateral dimensions of the islands (above 20nm) is of the order of 8$\pm$3mV at RH $< 5\%$ conditions, within a force range from 2.5nN to 6nN.

Surface properties such as the adhesion can also be used to differentiate the chemical compositions of the explored surface. Because most samples obtained after annealing have shown two morphologies that correspond to a low islands with COOH-termination and tall islands with SH-termination, we performed studies of adhesion force on both terminations. A typical method employed for most SFM equipments is the so-called Force Volume Imaging, where the deflection of the cantilever is recorded as the tip approaches, contacts and retracts from the surface. A force volume contains an array of these force curves measured at a unique position over the entire explored area. Force curves from an array of points are combined into a three dimensional volume of force data.

Figure 4.21 shows topographic and adhesion maps acquired with force volume imaging. At low relative humidity (RH$< 5\%$) the adhesion force difference of 80$\pm$10 pN between low and tall islands can hardly be detected. However, by increasing the RH at 25% and 35%, the adhesion of tall islands increased respect to that of the low islands. By correlating topographic and adhesion maps, one can observe that higher adhesion values correspond to the bare gold substrate. Adhesion force differences of 110$\pm$10pN and 200$\pm$20 pN at RH$\approx$25% and RH$\approx$35%,respectively, were obtained between the low and tall islands.

We present in Figure 4.22 the adhesion force difference measured between small and tall islands for several samples at RH (5%, 25% and 35%). To keep a RH ($< 5\%$)

4.2 Dependence of friction response with the applied load on surfaces with MMTA
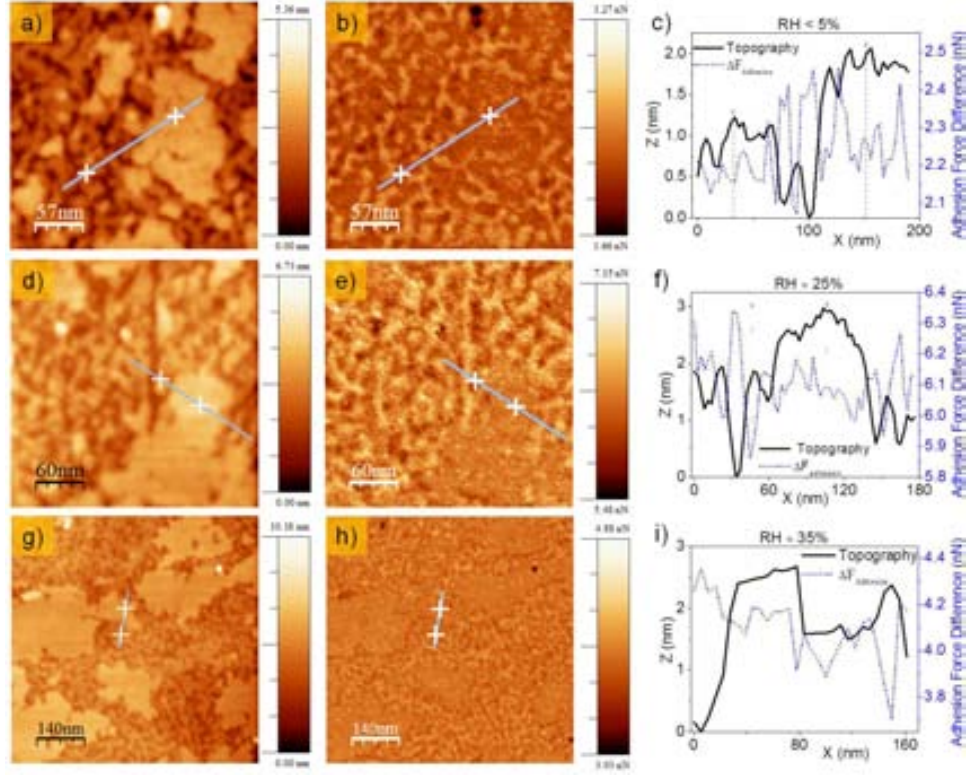
Figure 4.21. SFM images of MMTA islands on Au(111) surface after immersing in a 100μM acetic acid solution of MMTA for 16 hours and post-annealing at 110°C for 17 hours. Topographic (a, d, g) and adhesion maps (b, e, h) were obtained by using the force volume imaging for 5%, 25% and 35% of relative humidity, respectively. Simultaneous profiles taken along the lines in topographic and adhesion maps are shown in (c, f, i).

a nitrogen stream was always mantained for several hours, whereas intermediate RH values were obtained after turn off the stream nitrogen and maintaining the hood of the microscope head. For RH > 30% conditions the measurements were carrried out in air.

According to the different models in contact mechanics such as Hertzian model, JKR or DMT the work of adhesion per unit area (γ) can be obtained from experimental data using the equations 2.3 and 2.4. Force volume imaging allowed acquiring topographic image and adhesion map simultaneously to correlate each other and to obtain the specific regions of COOH and SH terminations on the sample. An estimation of the
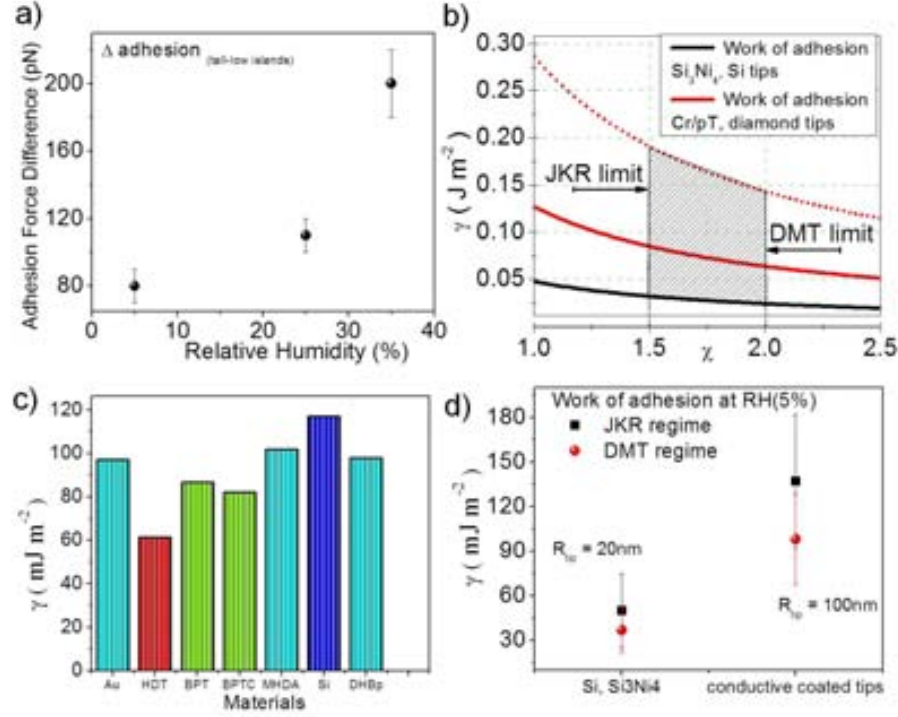
Figure 4.22. (a) Evolution of the adhesion force difference between low and tall islands of MMTA as a function of the relative humidity (RH). Small differences of the adhesion force were measured at low RH ($< 5\%$), whereas important changes were observed at higher RH values. Error bar correspond at (5%) of the obtained values for a series of samples. (b) Work of adhesion calculated within the limits given by JKR and DMT models for silicon nitride and ultrasharp tips as well as for coated conductive tips at low RH $< 5\%$. (c) Work of adhesion obtained for some materials by using contact angle adapted from [119]. Work of adhesion estimated from JKR and DMT regimes using silicon and coated conductive tips with radius 20nm and 100nm, respectively, at low RH(5%).

work of adhesion depends upon the appropriate contact regime (JKR$\rightarrow$ DMT). By using the generalized equation,

$$\gamma = -\frac{F_{pull-off}}{\chi \pi R} \tag{4.7}$$

where χ varies monotonically from 1.5 for the JKR limit to 2 for DMT limit, R the effective radius of the tip, and $F_{pull-off}$ experimental. The estimated work of adhesion is shown in Figure 4.22 (b) within limits given by χ . Adhesion values at low relative

4.2 Dependence of friction response with the applied load on surfaces with MMTA

humidity (RH< 5%)(black curve) on low islands (-COOH end group) ranged from -2nN to -8nN of force using silicon nitride or ultrasharp silicon tips during experiments, whereas higher adhesion values during electrical experiments (-25nN to -100nN) at low relative humidity using conductive diamond or Cr/Pt tips were measured (red curve at -40nN and dashed curve at -90nN). Details are summarized in table 4.3.

$F_{pull-off}$ nN	R nm	γ_{JKR} (J·m^{-2})	γ_{DMT} (J·m^{-2})
-2	20	0.021	0.015
-5	20	0.053	0.037
-8	20	0.084	0.060
-40	100	0.084	0.060
-90	100	0.190	0.136

Table 4.3. Work of adhesion estimated by applying JKR and DMT models on the low islands (-COOH) end group at low RH(5%). Silicon and coated conductive tips of nominal radius of 20 and 100nm, respectively, were employed.

Work of adhesion of some materials such as Si(111), Au (111) and Hexadecanethiol (HDT), Biphenylthiol (BPT), Cross-linked Biphenylthiol (BPTC) and Mercaptohexadecanoic acid (MHDA) and dihydroxybiphenyl (DHBp) SAMs on Au(111) were obtained by means of the contact angle technique [119], whereas the work of adhesion of MMTA islands (-COOH) end group was estimated by our SFM measurements. MHA and DHBp SAMs which have polar surface terminal groups (-COOH and -OH) lead to larger γ values. From experimental results in Figure 4.22(c) we observe that the work of adhesion of the MMTA low islands (with polar group COOH) at low RH values is less than other SAMs with polar groups. This behavior is observed in JKR and DMT models for tip radius of 20nm. However, using coated conductive tips the work of adhesion is similar to that of the other SAMs. As mentioned in chapter 2, the adhesion force consist of physical interactions such as electrostatic, van der Waals and chemical bonding and capillary forces even at low RH. Capillarity effects, contact area, particle shape and size, chemical property of the surface or molecular packing can be factors

that affect the adhesion measurements and contribute to increase or reduces the work of adhesion on the low islands.

4.2.2.3   Friction on Clustered islands
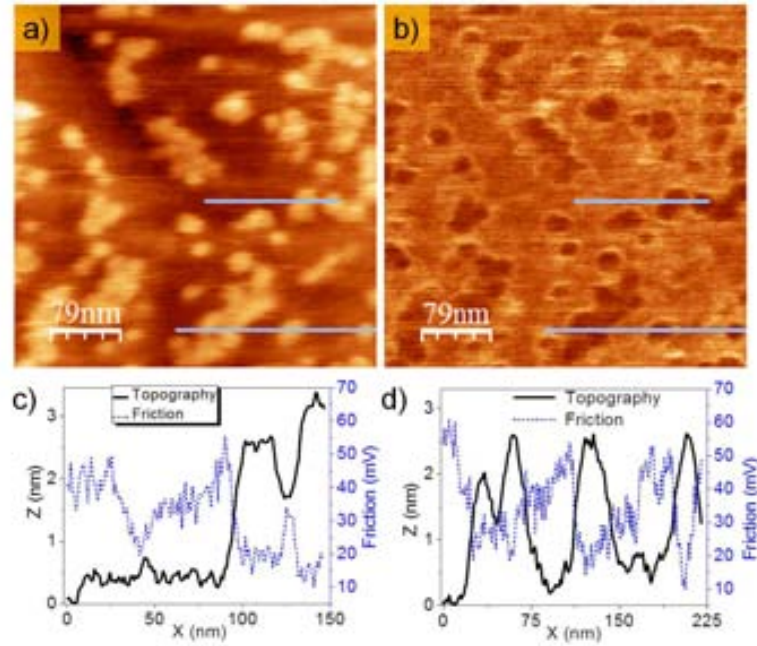
Figure 4.23. SFM topographic (a) and friction map (b) of MMTA islands on Au(111) after immersing in 100μM ethanolic + acetic acid (10%) solution of MMTA for 16 hours annealing the solution at 30°C. Simultaneosu topographic and friction profiles are shown in (c, d) along the short and long lines in (a, b). Total z-sale:(a)0-6nm; (b)-5mV to 98mV.

After immersing the Au(111) substrates using a percentage of acetic acid (10%) in 100μM ethanolic solutions of MMTA at 30°C [1], we observed the coalescence of some islands with lateral domains of 50nm. Figure 4.23 shows the corresponding topographic (a) and friction map (a). Small islands clusters reveal a friction difference respect to the bare gold substrate of 30±5mV for the tall islands and 25±5mV for low islands. The difference between both tall and low islands was measured to be about 8±3mV,

---

[1]A hot plate was used to heat the solution controlling the temperature for several hours.

4.2 Dependence of friction response with the applied load on surfaces with MMTA

as shown simultaneous profiles in (c, d) taken along the lines in (a, b). As previous measurements for acetic acid solutions of MMTA, the friction of the bare gold substrate is 3 times larger than for the molecular islands and the friction difference between low and tall islands can hardly be detected. Clustered islands (low and tall) reveal less friction than the bare gold substrate, as previous measurements at higher annealing temperature using different solvents.

4.2.2.4   Aging Time Effect on the Frictional Response
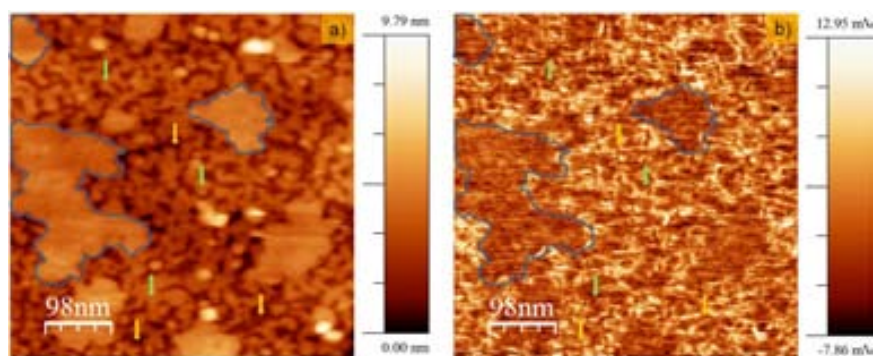
Figure 4.24. SFM images showing the Au(111) surface after immersing in a 100μM toluene solution of MMTA for 20 hours and annealing at $120°$C for 24 hours. Topography (a) and friction map(b) are shown. Some yellow and green arrows indicate the bare gold and the low islands. Applied force : -0.5nN; Adhesion force :-2.5nN.

Figure 4.24 shows the topography (a) and the friction map (b) of MMTA on Au(111) after immersing in 100μM toluene solution of MMTA for 20 hours and annealing at $120°$C for 24 hours. Low and tall islands were also observed for toluene solutions of MMTA for longer immersion times after annealing. Small friction differences ($\approx$8mV) between both types of islands for different preparations and higher friction for the bare gold substrate than the molecular film have been measured, at low RH (5%).

Yellow arrows indicate the bare gold areas in topography (a) and higher friction values (brightness) on the friction map. The friction map revealed similar values for low and tall islands for applied forces in the adhesion range, in this case the applied load is -0.5nN and the adhesion force is -2.5nN.
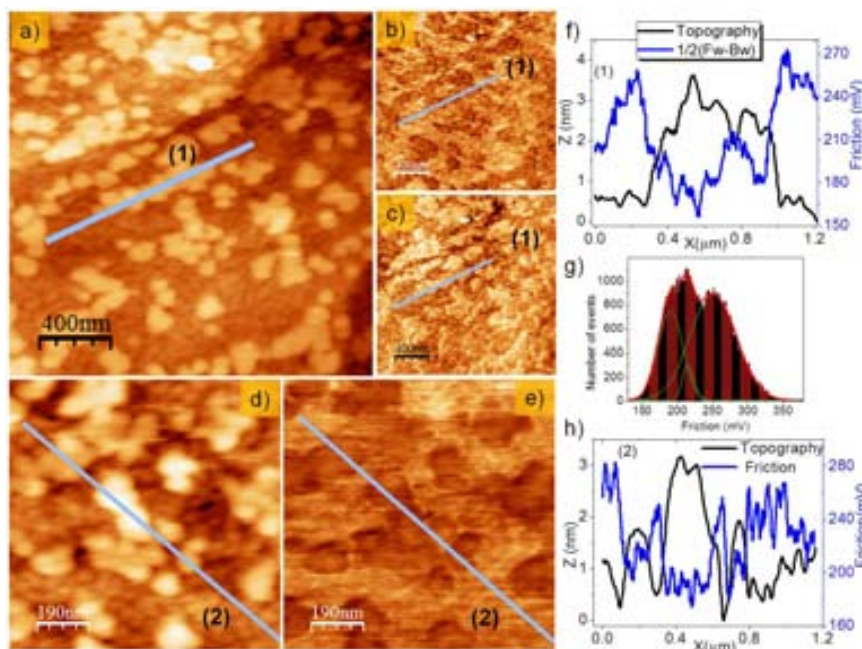
Figure 4.25. SFM images of the sample immersed in a $100\mu M$ toluene solution for 20 hours and post annealing at $120°C$ for 24 hours and observed one month later. Topographic (a) and lateral force images (Fw&Bw) show simultaneous profiles to compare the friction between low and tall islands in panel (f). Panel (d, e) shows the topography and friction map of the center part of image in (a) with simultaneous profiles shown in panel (h). Histogram in (g) obtained of the image (e) between low and tall islands. Total z-scale:(a) 0-8nm; (b) -0.790V to 0.422mV; (c) -1.27V to 0.02V; (d)0-4nm; (e)0.1V to 0.4V

Figure 4.25 shows the same sample measured one month after preparation to observe any possible morphological or tribological changes. The lateral force images revealed more energy dissipation on the low islands (i.e. more friction respect to tall islands) and the friction difference between both increased 10 times respect to the fresh sample as shown the numbered profiles (f, h) and histogram (g) for whole the image (50 ± 5mV). Note that the bare gold is not visible as before (fresh sample). The COOH-termination of the low islands presents more reactivity with the environment than the SH terminated. This behavior was also as observed in samples from acetic acid solution of MMTA after 4 days of aging (see Figure 4.13).

In addition to factors related to the substrate and solution, the quality of the

molecular film is sensitive to factors such as adsorption temperature, immersion time, annealing and aging time reflected on the molecular packing order and packing density that can have some influence on the resulting friction value and cannot be neglected.

4.3   Friction Response of Patterned MMTA SAMs
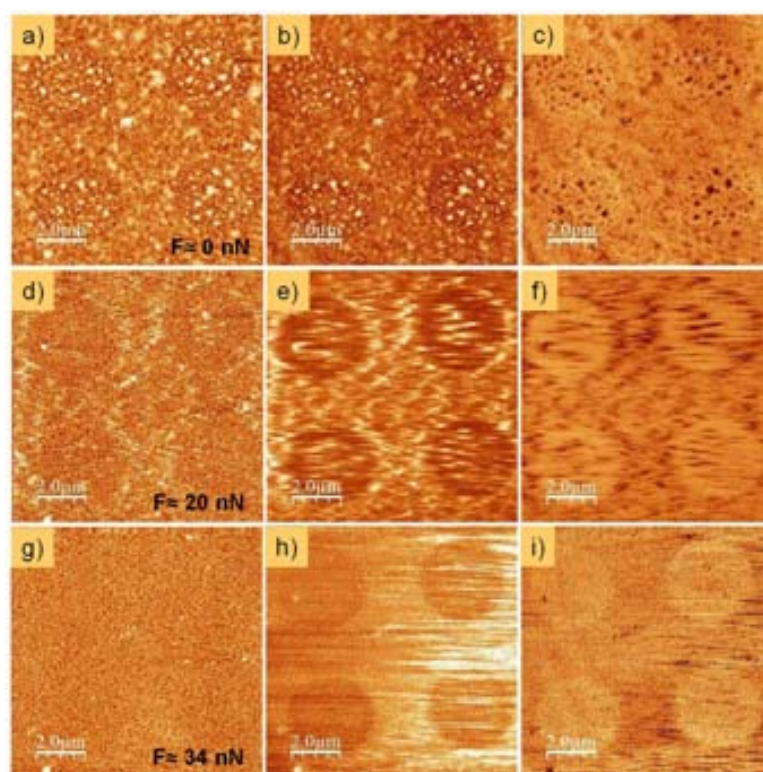
Figure 4.26. Topography(a, d , g) and lateral force forward (b, e, h) and backward(c, f, i) images for different values of applied force from load movie. Total z-scale: (a) 0 - 46nm; (b) -22.1mV to 244mV; (c) -83.6mV to 21.9mV; (d) 0 - 42nm; (e)75.3mV to 562mV; (f) -203.8mV to 90mV; (g) 0 - 21nm;(h) 168mV to 574mV; (i) -120mV to 174.8mV.

Microcontact printing μCP seems to be an alternative method for forming patterns on gold surfaces using polar aromatic thiols. In this section, we present friction measurements performed on the patterned SAMs of MMTA. For this purpose, we used

sharpened V-shaped silicon cantilever with nominal force constant of k = 0.57 N· m^{-1} at low relative humidity (5%), the adhesion force was -2nN.

Scratching or mechanical removing of material can be seen as a way of modifying surfaces, and from this point of view nanostructured materials can be also built. We have observed that the single molecular film or bilayer on flat Au(111) can be easily removed by applying forces around 15nN, whereas the same molecular film with similar heights requires more applied force ($\approx 30nN$) to be completely removed when rough gold surfaces were employed.

Figure 4.26 shows SFM images for patterned SAMs on the gold surface (roughness $\approx$ 1nm) during a load movie for 3 hours. Each topographic (a, d, g) and lateral force (Forward: b, e and h) and (backward: c, f, and i) images corresponds to a sequence of the movie obtained by scanning the same area at different forces (0nN, 20nN and 34nN), respectively. We observed morphological changes when the applied force is about 20nN, as shown in topographic image in (d). For higher forces the molecular film deposited on the surface was removed. The bare gold substrate was observed and the molecular film removed at 34nN, as shown in (g). Despite the molecular film was removed, lateral force images reveals that some molecules remain on the scratched surface after loading.

Figure 4.27 shows the scratched area after finishing the experiment. The applied force was kept constant at 0nN to avoid the possible damages or modifications of the tip during the scans. Topographic (a), friction map (c) and numbered profiles taken along the lines for both images are shown in (b, d). A molecular film of 2.2nm was estimated from topographic profiles.

A closer look at the scratched area is shown in Figure 4.28. By avoiding in both topography (a) and friction map (b) the higher signal at the scratch border, a friction difference of about 6±3 mV is measured between the bare gold and homogeneous molecular as shown in (a, b) and profiles in (c, d). In contrast to previous measurements, the scratched area reveals less or similar friction than the molecular film. This fact suggests that the film was not completely removed or that during the scans some molecules are moved into the scratched area again.

Although the characterization of alkanethiol systems is outside the scope of this work, we used some such as n-hexadecanethiol (C16) and n-octadecanethiol (C18)
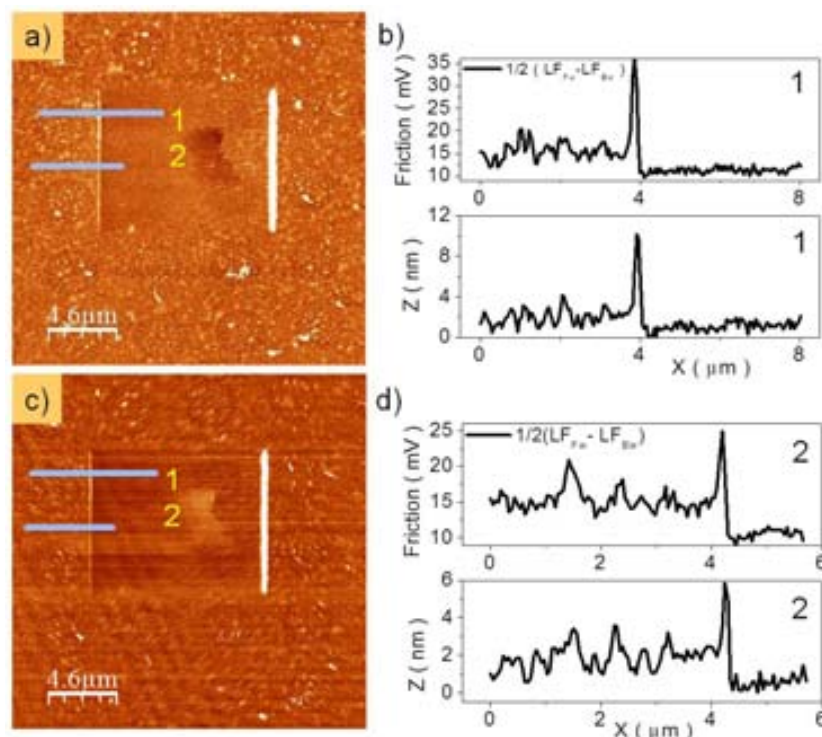
Figure 4.27. Topographic image shows the appearance (a) after loading experiment. Profiles show a height of about 2nm between the molecular film and the background of the scratched region. A friction map defined as $\frac{1}{2}$(lateral force Fw-lateral force Bw) for the whole image is displayed in (c). Numbered profiles taken along the lines in (a, c) are shown in (b, d).

as the ink molecules to be transferred into the gold surface by means of the μCP technique. Once adsorbates have been placed on the surface at submonolayer coverage, the remaining bare area can be backfilled with a new adsorbate.

For alkanethiols patterned gold substrates, PDMS stamps with chessboard and square reliefs were employed. After inking with a 100μM ethanolic solution of C16 the stamp was allowed to dry for few minutes and was then contacted to the gold surface. Afterwards, several SFM were acquired to verify the quality of the printing. Lateral forces images were recorded to distinguish between adsorbates and bare gold surface. Once done this, the patterned substrates were immersed in a 2μM ethanolic solution of MMTA for 24 hours. Low concentration was chosen to avoid high coverages
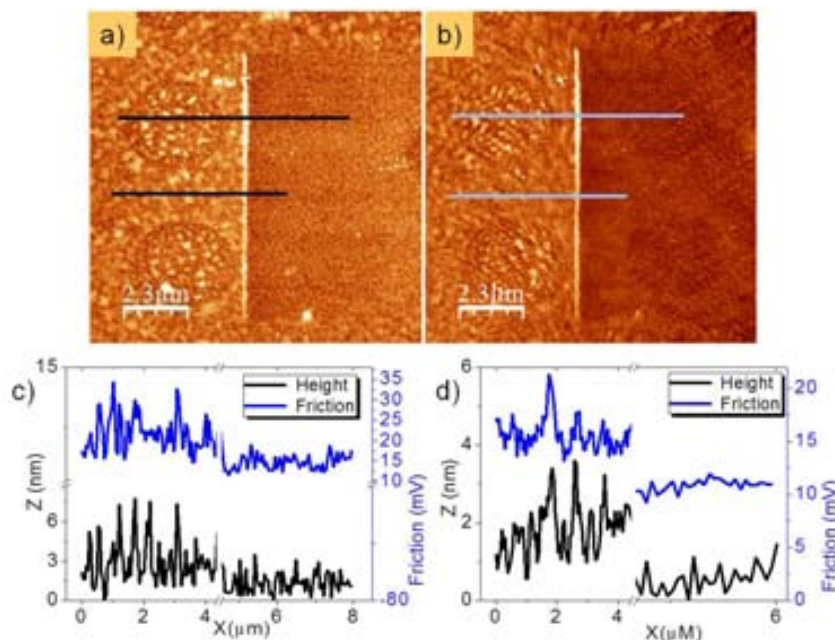
Figure 4.28. Topography (a) and friction map (b) were obtained by zooming in the scratched area. Total z-scale (a)0-30nm; (b)-9mV to 86mV.

and 3D structures on the patterned surface.

Figure 4.29 shows topographic (a), friction map (b) and lateral force images (Fw&Bw) (d, e), respectively, of the patterned gold surface. Simultaneous profiles taken along the lines in (a, b) are shown in (c), whereas lateral force profiles taken along the lines in (d, e) are displayed in (f). Topographic profiles revealed a difference in height of 5Å between C16 and MMTA regions,

whereas the friction map showed higher friction for MMTA than C16 following the hierarchy (COOH > CH$_3$), in agreement to early reports [120, 121, 122]. Lateral force images (d, e) show the patterned gold surface as well as material on the MMTA domain being removed during the scanning. Note that the friction profile has smoothest borders between MMTA and C16 than the corresponding topographic profile (see simultaneous profiles in c). This fact is most likely due to different packing at the pattern border, though an intermixing of MMTA and C16 in these regions cannot be excluded.

Structural studies at submonolayer coverages performed by Munuera [91], in parti-
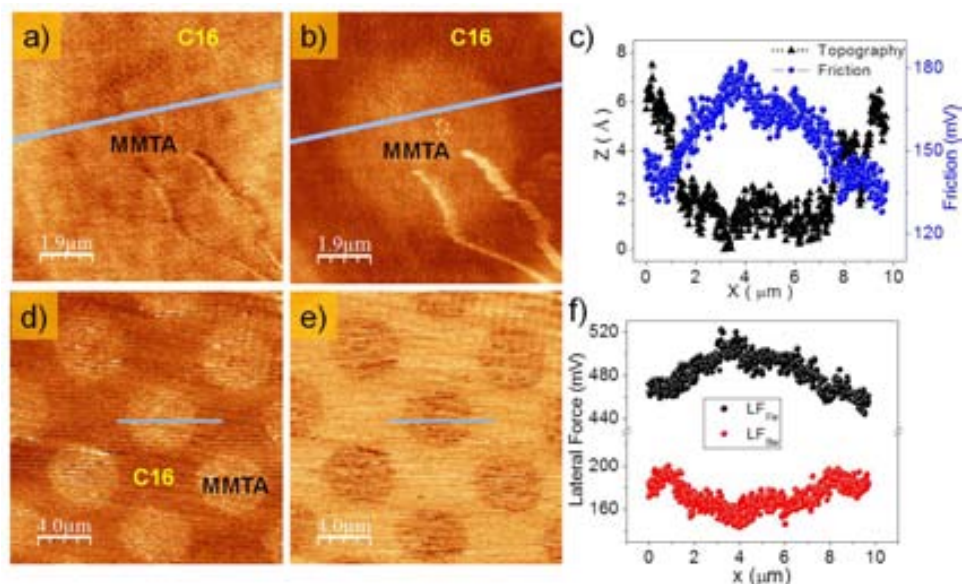
Figure 4.29. SFM images of alkane (C16) and aromatic (MMTA) thiols printed obtained by transferring the alkanethiol from PDMS stamp to the bare gold substrate and then by immersing in a 2μM MMTA ethanolic solution for 24 hours. Topography (a), friction map (b) and lateral force images (Fw&Bw) are shown (d, e). Simultaneous topographic and friction profiles taken along the lines in (a, b) are displayed in (c). Simultaneous lateral profiles taken along the lines in (d, e) are shown in (f).

cular (C16), showed island's height of 20.1±0.8Å . A difference in topography of ≈5Å between C16 and MMTA is in agreement with their difference in molecular length for assigned tilt angles of 30° for both C16 and MMTA. The difference in height between C16 and MMTA will correspond to experimental lengths as well as the theoretical (C16 > MMTA).

4.4   Conclusions

Islands of a single molecular thickness as well as bilayer have been observed to coalesce into larger clusters of islands. However, samples prepared with THF solvent at low immersion times and without annealing have shown few bilayer formations and domains with lateral dimensions too small (below 50nm) that make difficult to measure a friction value between chemical terminations and the substrate. In spite of this difficulty, by performing scratching on the molecular surface it was possible

to obtain the bare gold as a reference that allowed measuring a friction difference of 12±2mV between a (-COOH) terminal group and the gold surface by applying 0.5nN. However, after annealing a friction difference of $\approx$ 8mV between terminations (COOH > SH) was observed.

3D nanostructures revealed also a friction difference around 15mV between layers separated by 1.5nm, precisely the single molecular length of the MMTA.

Interestingly, small domains of $\approx$ 20×20 nm^2 were observed in agreement with the structure found in chapter 3 showing friction asymmetry.

For bilayers and double bilayers, i.e., with (-SH) thiol groups exposed, at the surface a friction difference of 50±10mV with respect to the bare gold was found using ethanolic solutions of MMTA, whereas bilayers obtained from toluene solutions of MMTA showed a friction difference around 85mV for samples without annealing.

Samples prepared from toluene solutions of MMTA after one month of aging revealed a friction difference of 50±5mV between the (SH) and (COOH) terminal groups (COOH>SH), a value almost 10 times larger than for other measurements on both terminations, similar results were observed after 4 days of aging for the samples prepared in acetic acid solutions of MMTA.

By mixing ethanol and acetic acid solvents it was possible to obtain low island clusters with both thicknesses (single and bilayer) in 100μM solutions. In this case, differences between (-SH) thiol group and Au or (-COOH) carboxylic acid and Au were hardly differentiated at low forces.

Large areas with bilayer height were obtained coexisting with single layer islands using acetic acid solvent plus a post-annealing, thus allowing differentiating the two cases. By using the 3D modes or by varying the force for each image (load movie) we found the following friction hierarchy Au > COOH > SH within the repulsive range (from 2nN to 6nN). At low forces, friction values are similar for SH and COOH terminations, but by applying a intermediate force ($\approx$4nN) the friction value for COOH was always larger than for SH prior to the damage of the islands. Bilayer islands with lateral dimensions of about 50nm showed a linear behavior respect to the applied force within the range of force from 1nN to 6nN, whereas low islands with lateral dimensions of 20nm revealed a stepwise behavior in the same range of force. Low islands with lateral

dimensions below 20nm were crushed even at low forces. SFM topographic images revealed that the the tall islands were reduced to 30% of its original height due to the pressure exerced by the tip, within a range of force from 3nN to 7nN.

Unlike the case of single molecular lengths, where indentations measurements have shown a stepwise behavior on the friction at low applied forces, for bilayers this behavior was not clearly defined. From topographic profiles the bilayer length was around 3.0±0.1nm. A tilt angle respect to the normal surface of $(18±2)°$ could be estimated, but with a reduced height of 30%, the new tilt angle would be around 50°. This new tilt angle can be facilited by the type of bond presents: the head group (SH) with the gold surface $(\approx 189 kJ \cdot mol^{-1})$ and the hydrogen bond strenght $(\approx 21 kJ \cdot mol^{-1})$.

Adhesion measurements at low relative humidity ($\approx$ 5%), revealed differences of 80±10 pN between both terminations, SH COOH, but increasing the relative humidity at 35% or in air measurements this difference was increased up to 200±15pN revealing that (-SH) thiol group had a more adhesive response.

Typical values of adhesion for (-SH) as well as (-COOH) were always less than 5nN in pull-off when silicon nitride or ultrasharp silicon tips were employed. However, for conductive diamond tips or Cr/pt after electrical experiments the adhesion was increased about 10 times. The adhesion force under a humid atmosphere is controlled mainly by the capillary force which is produced by condensing water vapor in the tip-sample gap, therefore it is dependent on the relative humidity. Interestingly, high friction values on (-COOH) end group did not imply high adhesion values.

Forces around 30nN were necessary to remove the MMTA pattern with a single molecular thickness on rough gold surfaces ($\approx 1nm$). However, the friction difference between the scratched area and the molecular film was almost the same, in contrast with other measurements where all lateral force images and friction maps showed always high friction on the bare gold substrate. This fact is likely due to adsorbed molecules or deposited by the tip again during scanning.

CHAPTER 5

ELECTRICAL CHARACTERIZATION

Molecules with excellent conductive properties are described as those that contain groups with their energy levels Highest Occupied Molecular Orbital (HOMO) and Lowest Unoccupied Molecular Orbital (LUMO) separated by a reduced energy gap, typically between 1 to 4 eV, such as organic semiconductors. Molecular systems based on double, triple carbon bond or aromatic rings have been extensively studied; in particular, conjugated molecules due to extended π-system or methylene groups in the alkane spacer of conjugated molecules and the effect on the electrical conduction of SAMs [123, 76, 124].

5.1 Introduction

For alkanethiols the transport mechanism is expected to be of tunneling nature along the tilted molecular chain due to alignment between the Fermi level of the metallic contact and the gap (HOMO-LUMO) in the low voltage range. For a wide range of temperatures (300-80)K, measurements of transport across alakenthiol monolayers were carried out by Wang and co-workers [125] to elucidate the type of electronic conduction mechanism, concluding that the conduction mechanism through alkanethiol is tunneling.

Conjugated molecules have shown a reduced energetic gap (3-5)eV comparatively with those found in alkanethiols ($\approx$ 8eV), this reduced gap can provoke the activation of other mechanism of transport such as hopping or thermally activated process. Hopping and thermoionic transport mechanism have been reported for 4-thioacetylbiphenyl [126] and 1,4-phenylene diisocyanide [127] SAMs for variable temperature conductance measurements, in which these conjugated molecules were placed between top and bottom metallic contacts. Conjugated oligonaphthalenefluoreneimine (ONI) wires were

studied by using (C-AFM) by Choi et al.[128], they observed a transition from tunneling to hopping in transport measurements, whereas Beebe J. et al. [129] reported a change from direct tunneling to field emission across of π-conjugated thiols by analyzing IV curves from electrical measurements at moderate bias voltages ($\leq$ 1 V). Selzer et al. [130] studied the importance of the presence or absence of neighboring molecules in the conduction mechanism by means of two types of junctions based on isolated individual molecules and SAMs of 1-nitro-2,5-di(phenylethynyl-4´-mercapto) benzene. They found a transition from coherent conduction at low temperatures (T$\leq$100K) to thermally activated hopping mechanism for higher temperatures (T$\geq$ 100K) in isolated individual molecule junctions. In contrast, $IV(T)$ measurements carried out in-wire SAM junction revealed a temperature independent behavior of coherent tunneling. Taking into account that a direct tunneling is a dominant conduction mechanism for alkanethiol and π-conjugated systems, the Simmons model [131, 132, 133] is an approximation that can be used to understand the behavior of a molecular junction across of arbitrary tunnel barrier.

Hong et al. [134] have studied by means of STM in UHV conjugated molecules containing from one to three phenyl rings and having both thiol (-SH) and isocyanide(-NC) end groups. They reported a shift in Fermi level of the isocyanide molecules as a function of phenyl rings number opposite to that observed for the thiol-terminated molecules. The overall trend for the thiol molecules follows a conventional physical chemical model. As the number of phenyl rings in the thiol molecules increases, the density of bonding π and antibonding π^* levels also increases. This causes the HOMO energy to increase while decreasing the LUMO energy. As a result, the HOMO-LUMO gap decreases as the number of phenyl rings increases. Thus, as the number of phenyl rings increases, the HOMO moves closer to E_f and $E_f - E_H$ decreases.

5.2   Background

The Conductive-AFM (C-AFM) is basically a conductive AFM tip connected to a current pre-amplifier during conventional contac-mode AFM, employing the cantilever deflection as the feedback signal to regulate the tip-sample distance. When a bias voltage is applied between both tip and sample, the current signal is obtained allowing

probing and mapping the surface. C-AFM and break-junction experiments are tools for studying the conduction properties of organic monolayers as well as inorganic systems [135, 136, 137, 138]. In most tip-SAMs-metal junctions of C-AFM, the self-assembled monolayer simply acts as a tunneling barrier, albeit with a reduced barrier compared to a vacuum gap of similar thickness. This is because the HOMO-LUMO molecular levels assist electron transfer by non-resonant tunneling through the molecular layer.

The control of the electric properties of SAMs or molecular nanostructures is of special relevance from the viewpoint of constructing future nanodevices. Kelvin Probe Force Microscopy (KPFM) is a technique for such a purpose and is frequently employed to investigate electric properties of surfaces and mapping surface potential distributions on many materials such as organic molecular films on metal or semiconductor substrates [139, 140, 141, 142, 143, 144, 145].

The conventional Kelvin method is a well-established technique for measuring the contact potential differences (CPD) between a reference electrode and a surface. The CPD for clean metal surfaces is given by the difference in the work functions of the two materials by using the vibrating capacitor method. The Kelvin method is based in detecting the zero point of current function $i(t)$ while the additional bias voltage is supplied between the two plates until the electric field in between disappears, then the contact potential difference $V_{CPD} = -V_{bias}$ can be obtained. The KPFM principle is similar to that of the Kelvin method, except that forces instead of currents are measured. From equation 2.18 the CPD or V_S(x, y, z) can be determined by two methods: the spectroscopic method and the second feedback loop technique.

Rusu et al. [143] studied the dipole formation at the surface formed by (-CH$_3$) and (-CF$_3$) terminated short-chain alkylthiolate monolayers on Au(111) using density functional theory calculations. Their experiments suggested that the direction of dipole moment of alkylthiolate molecules lowers the work function as compared to the clean Au(111) substrate, whereas SAMs of fluorinated alkylthiolates decrease it. Sushko et al.[146] have studied the influence of electrostatic interactions due to the presence of permanent dipole moments on the structure of the COOH-terminated SAMs. They showed some results of the dipole moments and the barriers for rotation of the tail-groups for SH(CH$_2$)$_{n-1}$X, where X=COOH and CH$_3$ by means of density functional (DFT).

The chain-length dependence of the dipole moment of COOH-terminated monolayers revealed three regions with different dipole moments corresponding to (n = 2-4) and (n > 14) chains within a dipole range of 0.6D to 5D. On the basis of an idealized model of a monolayer, they estimated the increase in surface potential of 7mV per carbon atom in the aliphatic chain, which is in close agreement with the average value of 9mV per carbon estimated from early Kelvin probe experiments [147].

Based on alkanethiols SAMs to be a dipole sheet in which the total dipole moment arises from two internal dipoles stacked on top of each other, it is possible to model a SAM as a first effective dipole formed by the metal-sulfur interaction, and the second effective dipole determined by the monolayer itself. The potential drop caused by the dipole can be estimated from the integral of the electric fields across the parallel sheets and the change in work function obtained as,

$$\Delta\Phi_{Vacuum}(eV) = e \cdot \sum \mu_\perp = -e \cdot N \left[\frac{\mu_\perp}{\epsilon_{SAM}\epsilon_0} + \frac{\mu_{m-s}}{\epsilon_{m-s}\epsilon_0} \right] \tag{5.1}$$

where e is the electronic charge, $\mu_\perp$ is the dipole moment of the SAM (perpendicular to the surface), μ_{m-s} is the dipole moment of the metal-thiolate bond, ϵ_0 is the permittivity of free space, ϵ_{SAM} and ϵ_{m-s} are the dielectric constants of the self-assembled monolayer and the metal-thiolate bond, respectively, N is the number of molecules per area.

5.3 Electronic Transport and Surface Properties of MMTA Islands

For electronic transport measurements across of the π-conjugated molecular system MMTA, we modeled the current-voltage behavior of the molecular junction by using Simmons model within regime of $V < \frac{\Phi_B}{e}$,

$$
\begin{aligned}
I = \frac{e\,A}{4\pi^2\hbar\,d^2} &\left\{ \left(\Phi_B - \frac{eV}{2} \right) \exp\left(-\frac{2d\alpha\sqrt{2m_e}}{\hbar} \sqrt{\Phi_B - \frac{eV}{2}} \right) \right. \\
&\left. - \left(\Phi_B + \frac{eV}{2} \right) \exp\left(-\frac{2d\alpha\sqrt{2m_e}}{\hbar} \sqrt{\Phi_B + \frac{eV}{2}} \right) \right\}
\end{aligned}
\tag{5.2}
$$

being A the junction area, d the barrier width, m_e the electron effective mass, Φ_B the barrier height, e the electronic charge and α the adimensional parameter introduced by

Holmlin et al. [148] to provide a way of relating nonrectangular barrier to a functional form for rectangular ones and by Wang et al. [125] as an adjustment to account for the effective mass (m^*) of the tunneling electrons through of a barrier. The equation 5.2 describes a trapezoidal barrier when the applied bias voltage $V < \frac{\Phi_B}{e}$. At low voltage range, the barrier is rectangular and the equation 5.2 can be approximated as,

$$I = \frac{e^2 \alpha\, A\, \sqrt{2m_e \Phi_B}}{d\, h^2} \cdot V \cdot \exp\left(-\frac{2d\alpha\sqrt{2m_e\, \Phi_B}}{\hbar}\right) \tag{5.3}$$

for this voltage regime the tunneling current is dependent on the barrier width d as $I \propto \frac{1}{d}\exp(-\beta d)$ allowing obtaining the bias-independent tunneling decay coefficient β,

$$\beta = \frac{2\,\alpha\,\sqrt{2m_e \Phi_B}}{\hbar} \tag{5.4}$$

Though the Simmons model directly gives access to obtain both tunneling barrier height and width, their prediction is for symmetrical IV behaviour. In order to study the dependence of the conductance respect to the applied force, the molecular assembly is confined between the AFM tip and the gold substrate. We have restricted the bias voltage at ± 0.35V for the non-linear fitting analysis, although the asymmetric behavior of the IV curves can be discussed in agreement to some modified models [149, 150].

Owing to their chemical tunability or mechanical flexibility, organic molecules have been object of studying within promising field of organic electronic in the single molecular case as well as molecular assemblies. Several strategies have been employed to this end, molecules in a metal break-junction [151, 152], STM as a two-layer tunnel junction model [153] or by means of the so-called three-dimensional (3D) operation mode in Scanning Force Microscopy [39, 40, 154]. In the present chapter, we will show the behavior of the electronic transport and the surface potential of the MMTA islands obtained at low and high immersion times without and with post-annealing.

5.3.1 Barrier height (Φ), Decay Factor (β) and Resistance of Contact (R): samples without thermal process

In agreement with the preparation protocols previously described, different samples were prepared by immersing the Au(111) substrates in 100μM tetrahydrofuran (THF) solution of MMTA for 30 minutes and 17 hours, whereas ethanolic solutions were more

dilute to avoid high coverages of the surface. All measurements were carried out at RH <5% conditions.

5.3.1.1 At Low Immersion Times: from THF solutions

To investigate the electrical response of the MMTA molecular film we carried out controlled experiments by means of the so-called 3D operation modes. As it was described in section 2.2.3.2, these modes allow measuring a given magnitude as a function of two other magnitudes, $F_n(X_1, X_2)$. The magnitudes of interest in our case are the applied normal force ($F_1 = F$) and the electronic current ($F_2 = I$) flowing between the conductive tip and sample, being the independent parameters the applied voltage ($X_1 = V$) and vertical piezo displacement ($X_2 = z$).

Figure 5.1 shows the electrical transport measurements performed on selected low islands of MMTA on Au(111) from Figure 3.8, obtained by immersion in a 100μM THF solution for 30 minutes. Current (a) and normal force (b) are images simultaneously recorded as a function of bias voltage (V) and tip-surface distance (z), whereas (c) represents the force-distance curve showing a stepwise behavior within a range of forces marked by dashed lines. A set of *IV* curves from horizontal profiles (a) were extracted in (d, e). Some jumps on the force-distance curve at 2.5nN, 4.1nN and 6.9nN were observed and used to classify three ranges of forces for our analysis. In agreement to morphological and mechanical measurements described in chapter 3, a thin contaminant layer can be adsorbed on the molecular surface after their process of preparation as observed for several acquisitions at low applied forces. We classify the first range below 2.5nN where the force is not enough to establish a real contact with the molecular film; the second one, by applying forces between 2.5nN and 4nN the real contact between the tip and the molecule is performed. Lastly, forces from 4nN up to 7nN reveals a possible new molecular tilt angle before penetrating the molecular film. The adhesion force was around -8nN during the experiments under controlled conditions of relative humidity ($RH < 5\%$).

From equation 5.2 by adjusting the parameters Φ_B and α, a nonlinear square fitting has been performed to the data within $\pm$ 0.45V voltage range and the contact area[1] of

---

[1]Considering a contact between a spherical tip and an elastic half-space, $E_{diamondtip}$=1140GPa and
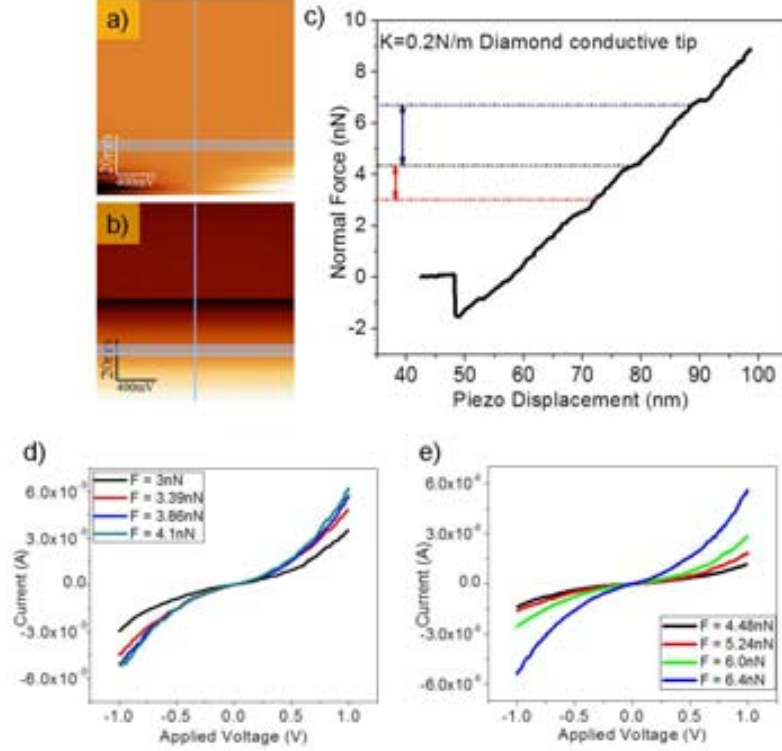
Figure 5.1. (a) Current I(V, z) and (b) normal force F_n(V, Z) images simultaneously recorded on molecular film by applying the 3D modes; current vs applied voltage curves (d, e) were acquired from horizontal profiles in the current image. Force vs piezo displacement curve (c) taken along the vertical profile in (b) shows the force ranges applied for IV curves (d, e).

order of $10^{-17}m^2$; as well as the molecular lengths obtained from topographic images and thicknesses from the Table 3.3 were taken into account. Once obtained the barrier height Φ_B and the α parameter from fitting, the decay coefficient β can be estimated by using equation 5.4. IV curves illustrate that using $\alpha = 1$ a best fit at low voltage is obtained, that is, limited regions of the IV curve for $V < 0.5V$. Considering that, if the parameter $\alpha = 1$, the approximation of an electron tunneling through a rectangular

---

E$_{SAM}$=9GPa the Young´s modulus of indenter tip and Polymers, respectively, $\nu_{diamondtip}$=0.07 and ν_{SAM}=0.3, the Poisson´s ratios of the tip and sample. Nominal tip radius from 20nm and 100nm were used to estimate the contact area by means of the JKR model.

barrier applies; however for $\alpha \neq 1$ the barrier shape is assumed nonrectangular with an effective mass for the tunneling electrons through organic layer as $m^* = m_e\alpha^2$. By applying equation 5.3 and 5.4 at low bias voltage range, the resistance R of the junction defined as the inverse slope of the linear region (± 0.35V) and the β decay coefficient of the IV experimental curves can be extracted, respectively.

Decay coefficients β reported for SAMs of thiols with redox center pyRu(NH$_3^{2+/3+}$)$_5$ on the surface of metal electrodes have been obtained by means of electrochemical experiments [155] across of the electroactive monolayer and C-AFM [156] by contacting Au-supported alkyl or benzyl thiol SAMs. The range of β values reported for alkanes is from 0.6Å^{-1} to 1.2Å^{-1} [155, 157, 158], whereas β=0.32Å^{-1} to 0.662Å^{-1} for oligophenylene and β= 0.06Å^{-1} to 0.5Å^{-1} for oligo-(phenyleneethylenes) (OPEs) and oligo(phenylenevinylene)(OPVs) [159, 2, 160] have been reported. The lower β values for oligophenylenes can be explained by the total barrier height of the system conductive tip-molecule-gold substrate comparatively whith whose found for akanethiols [161, 162, 163, 164, 165].

Figures 5.2 and 5.3 show IV curves obtained within the applied force range (from 3nN to 4nN) and (from 4nN to 6.4nN) for the positions labeled as REF A and REF B, respectively. Current-Voltage curves recorded at lower force (adhesion regime) have shown a characteristic sigmoide shape attributed at electron tunneling across of the organic layer. Keeping in mind that the MMTA has a methyl group between the thiol group and the aromatic rings and a carboxylic polar group at the end, these systems can be considered as a dielectric film. By performing individual fitting on each IV curve, using a contact area of about $(2.5\pm 0.5)\times 10^{-17}m^2$, the decay tunneling β, the barrier height Φ_B, the α parameter and the contact resistance R are obtained (see Table 5.1). From fitting results, we observe that decay coefficient β remains almost constant (0.96$\pm$0.01) for the first force range (from 3nN to 4nN) and softly reduced (0.93$\pm$0.01) in the second range of force (from 4nN to 6.4nN).

Tunneling coefficient β for tunneling through MMTA low islands trapped in the tip-gold substrate junctions was almost similar for a range of forces from 2nN to 5.5nN. Barrier heights of $\approx$1.1eV calculated from IV curves were agreement with reported in literature for π-conjugated systems and considerably smaller than the reported for
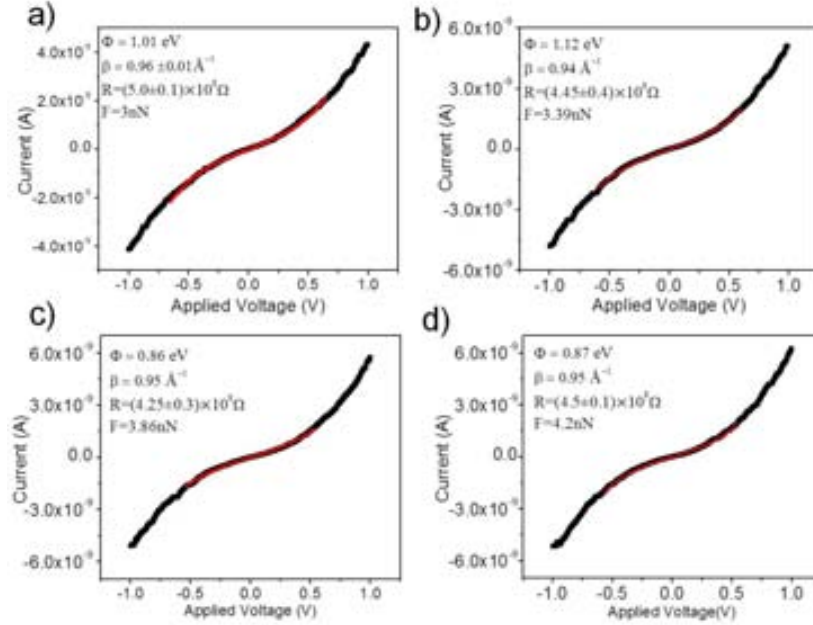
Figure 5.2. Current-voltage *(IV)* curves on the molecular film for several force values for the range from 3nN to 4.1nN. Immersion time for 30 minutes in 100μM THF solution of MMTA.

Force	β	Φ		α	Resistance
nN	Å^{-1}	J $(\times 10^{19})$	eV		$(\times 10^{8}\Omega)$
3	0.96	1.62	1.01	0.95	5.01 $\pm$0.10
3.39	0.94	1.79	1.12	0.87	4.45 $\pm$0.40
3.86	0.95	1.37	0.86	1.0	4.25 $\pm$0.30
4.18	0.95	1.40	0.87	1.0	4.50 $\pm$0.10
4.48	0.94	1.36	0.85	1.0	2.40 $\pm$0.17
5.24	0.94	1.41	0.87	0.98	1.65 $\pm$0.15
6.0	0.92	1.31	0.81	1.0	0.785$\pm$0.02
6.4	0.93	1.34	0.83	1.0	0.46 $\pm$0.03

Table 5.1. Decay coefficient, β, barrier height Φ, parameter α and resistance R are obtained from experimental *IV* curves.

alkanethiols. The contact resistance calculated for labeled position as "REF A" was less than 1 GΩ, whereas in "REF B" position was an order of magnitude lower.

Figure 5.4 (a) shows the plot of the decay coefficient β of the MMTA molecular film
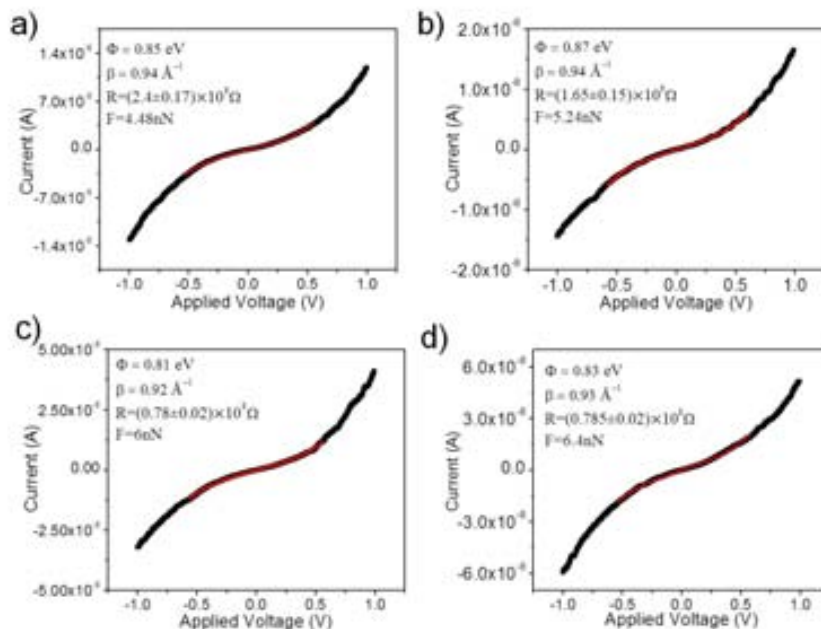
Figure 5.3. Current-voltage *(I-V)* curves on the molecular film for several force values ranging from 4.48 to 6.4nN. Immersion time for 30 minutes in 100μM THF solution of MMTA.
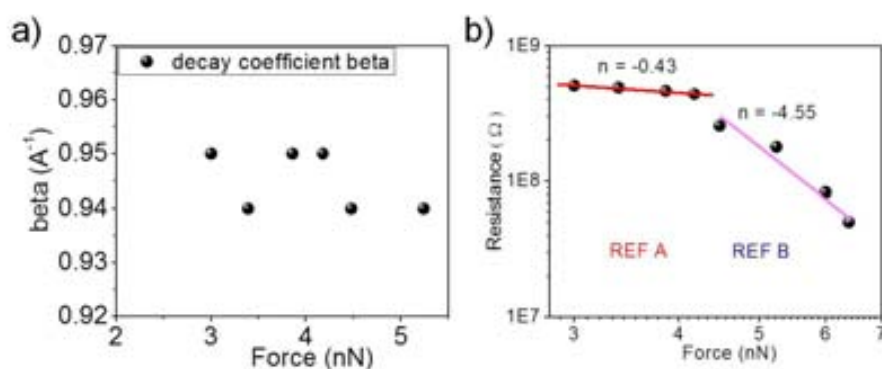
Figure 5.4. β-decay coefficient and contact resistance dependence on the applied force of the molecular film (a). Log-Log plot of the junction contact resistance versus the applied force for "REF A" and "REF B" positions show two power law scaling regimes (b).

versus load from Table 5.1, log(R) vs log(load) plot with a linear fit for "REF A" and "REF B" are displayed in (b). According to equations 4.3 and 4.6 from JKR model, the resistance should be proportional to load $(F_{ext} + F_{adh})^{-2/3}$ if there is not deformation or penetration of the molecular film. Two different power law regimes (i.e., R-load^n) are observed in log-log plot shown in (b). At low forces (from 3 to 4.1nN), for the "REF A" position, n=-0.43 and for "REF B" position, ranging from 4.2 to 6.4nN, the exponent n increases to -4.5. The power law exponent, n=-0.43, in the low load regime is close to the expected factor n=-0.67 based on the Hertzian Contact model, which predicts that the contact area scale as load$^{0.67}$, and resistance being inversely proportional to the contact area, could be expected to scale as load$^{-0.67}$. For the force range above 4nN, we hypothesize that increased pressure produced disorder of the molecular assembly (i.e., penetration of the tip, tilting and compression) as shown indentation experiments in previous chapter. Similar observations were early reported by Wold et al. [156] for *IV* curves obtained with dodecanethiol SAMs as a function of applied load, over a range of force up to 200nN.

5.3.1.2 Transition from Tunneling to Field Emission: 3D-structure crystallites

By employing the drop-casting method and using 2μM ethanolic solutions of MMTA we obtained 3D crystallites with lateral sizes in the micrometer range and heights of $\approx$20nm . To get insight on the transport properties of such 3D nanostructures we choose a point on the surface of the molecular crystallite ($\Delta z \approx$ 16nm) as shown in Figure 5.5 to perform current versus voltage and applied force measurements. A set of I(V) curves of the 3D-representation in (b) were extracted for a wide range of applied forces (from -4.5nN to 40nN) within an applied voltage range of $\pm$ 1.5V, as shown in (c).

At low force (i.e., negative values, the adhesion force regime), where the contact between tip and film is established by attractive forces, the measured current intensity at low bias voltage range ($\pm$ 0.5V) was an order of magnitude lower than those obtained close to F$\approx$ 0nN, on the other hand, in repulsive regime (from 0.3nN to 40nN) the measured intensity current was higher by 3 orders of magnitude. These results are shown in the log(I) versus voltage plot in (d) for V=$\pm$0.5V and Figure 5.6(a) for V=$\pm$1V and selected force values. As can be seen in the log$|(I)|$ vs V plots, all curves
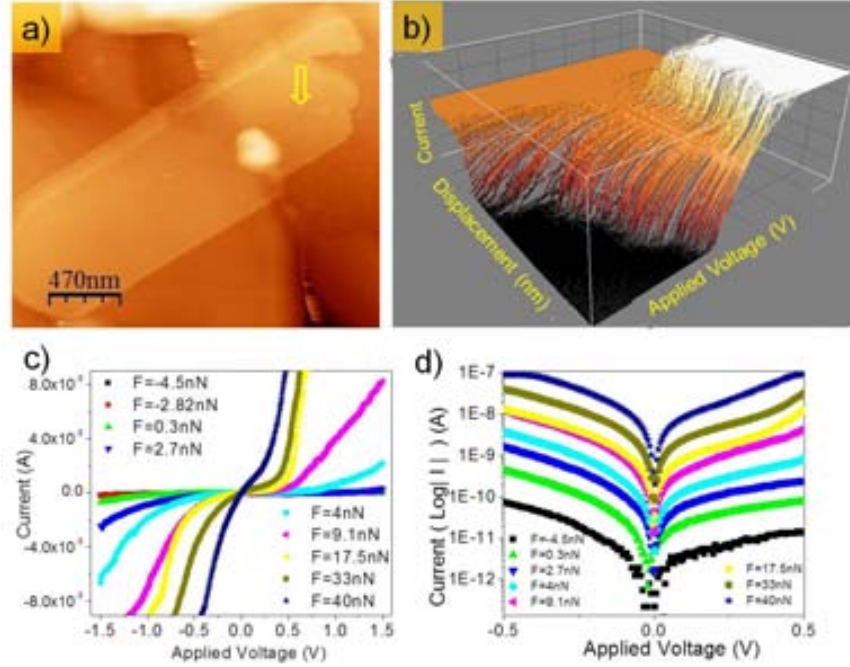
Figure 5.5. Topographic image of a 3D crystallite recorded from the dynamic mode (a). Three-dimensional representation of the I(V, z) image (b) taken on the single point (marked by an arrow in topographic image). Selected *IV* curves as a function of the applied load extracted from the I(V, z) are shown in (c). Log|(*I*)|-V plot for selected forces is shown in (d).

present a certain asymmetry. Interestingly this asymmetry is dependent on the force and applied voltage ranges.

Two observations can be drawn from Figure 5.5, (i) the asymmetric shape of the *IV* curves for the applied forces within the voltage range $\pm$ 0.5V showed more charge injection for negative than positive bias voltages, (ii) for bias voltage close to +0.3 V, the current intensity increases faster to force applied close to 9nN. The larger current for negative voltages and low forces is typical of n-type junctions or an asymmetric barrier in which conduction is dominated by electron transport. On the other hand, as will be seen in the following for large forces a quite marked change in the slope of this logarithmic plots is observed if increasing the applied voltage range. The change in behavior seems to occur at about 9nN where a rather linear *IV* is observed in the positive branch of the curve (pink symbols in Figure 5.5(c)). From this force on, a

steep IV curve at positive voltage values indicates an increase of the electron transport towards the tip (p-type junction).
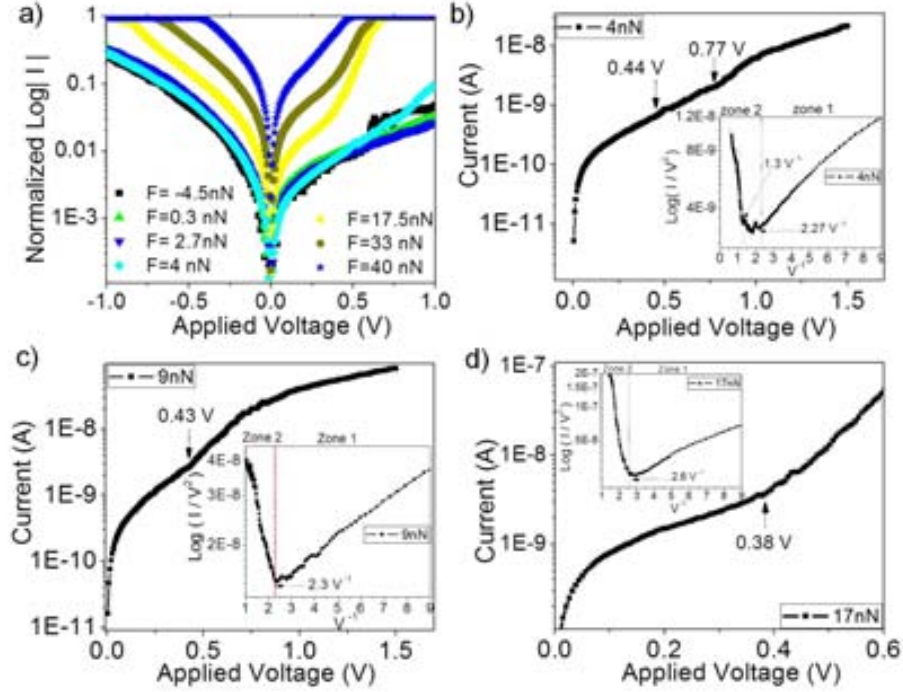
Figure 5.6. IV curves normalized (a) for low and high applied forces on the 3D nanostructure. Positive branch of selected IV curves show the change of the slope (b, c, d). Insets of $Log(I/V^2)$ versus V^{-1} reveal the voltage value where the change occurs and the transition from tunneling to field emission regimen.

The Figure 5.6 shows selected normalized[2] IV curves (a) in a larger applied voltage range ($\pm 1V$). We have independently plotted the positive branches of IV curves at 4nN (b), 9nN (c) and 17nN (d) to show the exponential trend of the current within limits of the Simmons theory at low voltages ($\pm 0.5V$) and the change to field emission regime of about 0.4V, at different loads. In order to that we employ the Fowler-Nordheim representation (see equation 5.5) to more clearly observe the possible transition value

---

[2]The normalized plot was performed by using the algorithm from Origin Pro8 as: $\frac{Y-Y_{min}}{Y_{max}-Y_{min}}$ where Y is the y value of input curve.

between both regimes. These plots are shown in the insets in (b, c, d). When the applied bias voltage exceeds the barrier height, the barrier transitions from trapezoidal to triangular, the current-voltage dependence can be described as,

$$\ln\left(\frac{I}{V^2}\right) \propto -\frac{4d\sqrt{2m_e\Phi^3}}{3\hbar q}\frac{1}{V} \tag{5.5}$$

The change in mechanism to field emission for the 3D structures of MMTA can be observed in the corresponding approximation Fowler-Nordheim plots by comparing the low and high voltage regimes. At low voltages (zone 1), the logarithmic behavior of the current with $\frac{1}{V}$ and a rectangular barrier is expected, as predicted the equation 5.3. Above transition voltage ($\approx$0.4V), in zone 2, a decreasing linear behavior of the current respect to $\frac{1}{V}$ is observed as well as a change from trapezoidal to triangular barrier, as predicted the equation 5.5. A close look in (b, zone 2), we observed different behaviors. The first one, a plateau region associated likely to the presence of both transport mechanisms (tunneling and field emission). Other authors have suggested this conduction regime as a space charge limited conduction (SCLC) (see details in [128]). The second region associated to field emission regime due to their negative slope and lastly, a region close to 0.77V (1.3 V^{-1}) with a light slope change likely due to the activation of other transport mechanism. Similar observations can be deduced, insets in (c, d), within the zone 2 for the field emission regime.

Figure 5.7 shows the regimes described using log-log plots of IV curves. Different linear fits were performed revealing different slopes for each regime: at low voltage (tunneling regime) a slope of 0.89±0.02 is common for IV curves (4nN, 9nN and 17nN). Close to the transition voltages, a second regime is observed with a slope of 1.47±0.03 and detected hardly at 17nN, which is ascribed to a SCLC. At field emission regime, we observed two slopes (3.2 and 2.8) and (3.6 and 1.8) for IV curves acquired at 4nN and 9nN, respectively. Interestingly, only a high slope of 6.7 is obtained for the IV curve at 17nN. At this point it is interesting to note that the investigated the 3D crystallites ($\Delta z\approx$ 16nm) of MMTA have shown similar behavior to that oligonaphthalenefluoreneimine (ONI) wires with lengths up to 10 nm. Based on the slopes of 1.47 in our 3D-nanostructure and of 1.9 in ONI wires, we suggest that a SCLC regime occurs at voltages close to 0.4V prior to the field emission regime.
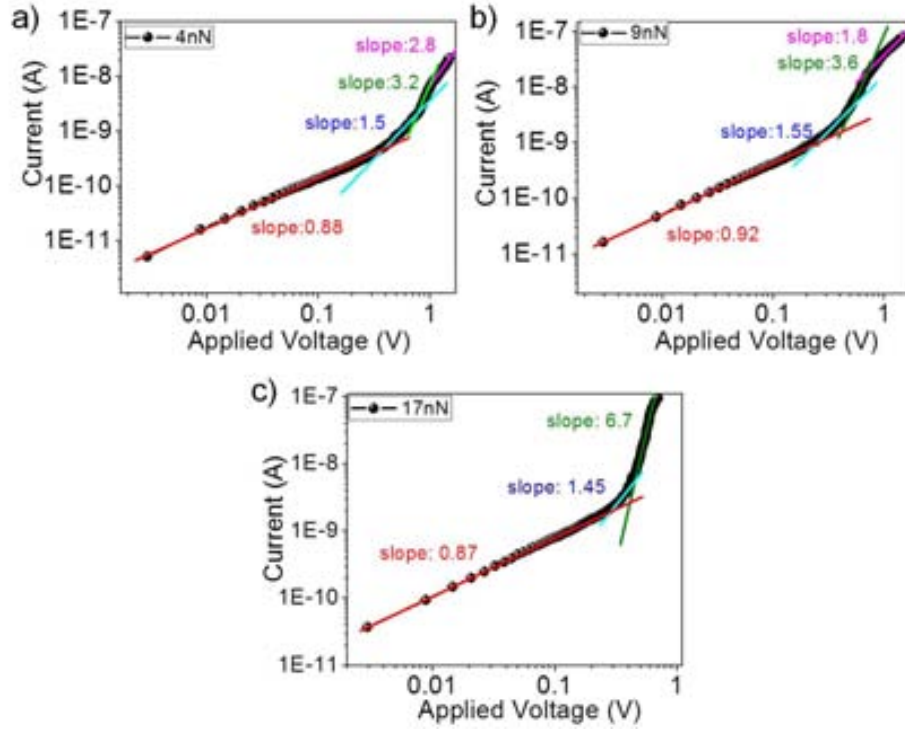
Figure 5.7. Log-Log plot scale of *IV* curves at (a) 4nN, (b) 9nN and (c) 17nN. Linear fits for each region along the curves with their slope value are shown to describe the different transport regimes.

Transition between different transport mechanisms have been observed for conjugated molecular systems with reduced HUMO-LUMO gap. In this sense, we show the transition regime from direct tunneling to field emission at moderate bias voltage (≈ 0.4V) on the 3D-nanostructure formed at least by 5 bilayers. Interestingly, Beebe et al. [129] showed transition voltages for transport mechanism from direct tunneling to field emission of π-conjugated thiols monolayers by using C-AFM and Ultraviolet Photoelectron Spectroscopy (UPS). Their results have shown the transition voltages for phenyl-thiol (Ph-SH, 0.95 V), Naphtalene-thiol (Naph-SH, 0.76V), Antracene-thiol (Ant-SH, 0.62V, -0.85V), Biphenyl-thiol (BP-SH, 0.82V) and Terphenyl-thiol(TP-SH, 0.67V, -0.82V).

5.3.2 Post-Annealing Treatment

In order to investigate the influence of post-annealing, samples prepared for 30 minutes and 17 hours were annealed at $(110 \pm 10)°C$ for 17 hours using a furnace in air. Au(111) substrates were immersed in $100\mu M$ THF and acetic acid solutions of MMTA.

5.3.2.1 Barrier height Φ, decay coefficient β and Resistance: low islands
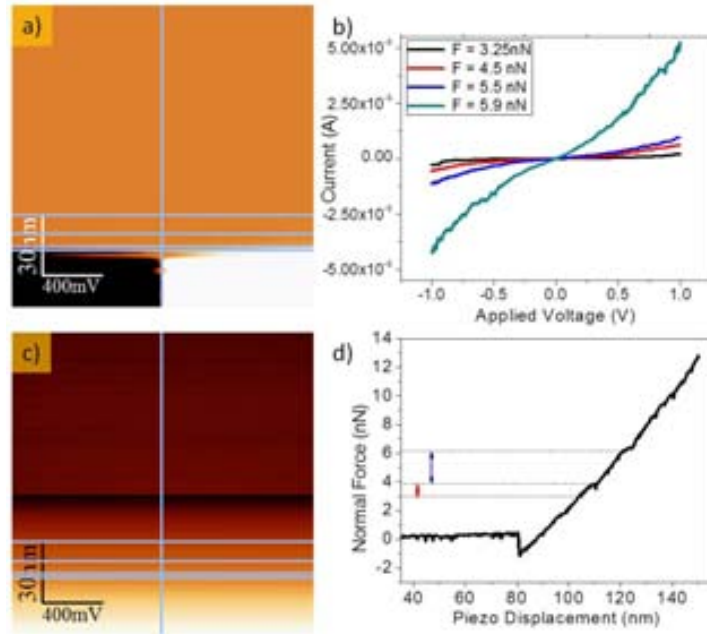
Figure 5.8. (a) Current I(V,z) and (c) normal force F_n(v, z) downloading images simultaneously recorded on the molecular film by using the 3D modes, current vs applied voltage curves (b) were obtained from horizontal profiles in the current image. Force vs piezo displacement curve (d) taken from the vertical profile in (c) shows the corresponding applied force for the *IV* curve. Nominal constant force k = 0.2 N· m^{-1} conductive diamond tip; RH< 5%.

The electrical characterization was carried out to compare possible differences in parameters, i.e., the decay coefficient β, the barrier height Φ of the system. From simulations, we assumed a contact area of order of $10^{-17}m^2$, according with Hertzian and JKR models described before. Lateral dimensions of low islands (below 30nm) and

of $\approx$ 1.6nm in height are the main characteristics of these samples, as mentioned in chapter 3.

From simultaneous F(V, z) (c) and I(V, z) (a) images recorded by using the 3D modes, the loading effect on the junction properties of the film with post-annealing can be studied. Figure 5.8 shows IV curves for every applied force in the voltage range of $\pm$ 1V. The force-distance curve revealed also the stepwise behaviour between 2nN and 6nN, being this range of force similar to those already described as "REF A" and "REF B". Each experimental IV curve was fitted by means of the Simmons model at low range voltage ($\pm$0.5V).

By performing individual fitting on each IV curve where the red line represents the best non-linear fit of the current data using a contact area of $(2.5\pm 0.5)\times10^{-17}m^2$, the energy barrier ($\Phi$), the decay coefficient (β), the contact resistance (R) and the applied force (F) were obtained of the MMTA molecular film obtained after immersing the Au(111) substrates in a 100μM THF solution for 30 minutes and post-annealing, as shown in Figure 5.9 and summarized in Table 5.2. Taking into account the tunneling coefficient β calculated from samples untreated thermally, we observed that values of β for samples thermally treated show a surprising force dependence.

Force	β	Φ		α	Resistance
nN	Å^{-1}	J ($\times10^{19}$)	eV		($\times10^9\Omega$)
3.10	1.0	1.65	1.02	0.95	2.75 $\pm$0.75
3.25	0.98	1.63	1.01	0.95	2.76 $\pm$0.50
3.70	1.0	1.66	1.03	1.0	2.50 $\pm$0.01
4.10	0.97	1.45	0.90	1.0	0.66 $\pm$0.02
4.50	0.96	1.58	0.99	0.95	0.47 $\pm$0.02
4.60	0.86	1.49	0.93	0.90	0.49 $\pm$0.01
5.50	0.94	1.51	1.04	0.90	0.20 $\pm$0.01
5.90	0.91	1.57	0.98	0.90	0.40 $\pm$0.01

Table 5.2. Experimental data extracted from IV curves of samples with post-anneaaling.

The different values of β for the low islands (untreated and treated thermally) suggest that the transport efficiency of both junctions is different. A representative plot
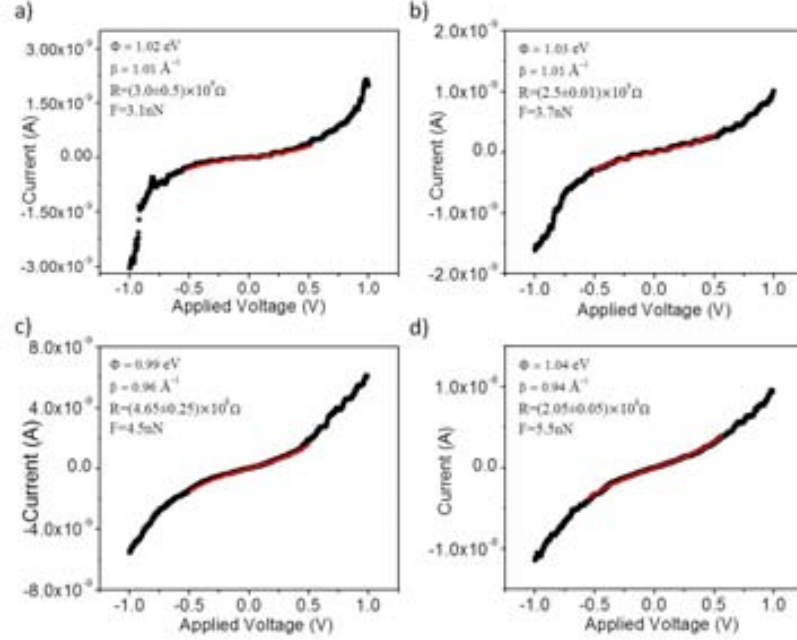
Figure 5.9. Current-voltage IV curves by using the 3D modes for MMTA molecular film thermally treated. Red line represents a nonlinear fit to the experimental current data.

of the decay coefficient β and the contact resistance (R) versus the applied force (F) is showed in Figure 5.10. Over the range of 6nN of applied force, the decay coefficient β decreases as the applied force increases; the barrier height is around 1.0 ± 0.1 eV. The resistance R of the junction can be determined as the inverse slope of the linear region (± 0.35V) of each IV curve; it is observed that decreases as the applied force is increased. This fact is expected, because the contact area increases and the thickness of the film is reduced making more efficiently the electronic transport. Unlike the previous measurements without post-annealing, distinct power law regimes were not observed over the range of force 6nN. From the linear fit to the data of log-log plot R versus F (b), was obtained the power law exponent, n = -6.4. Due to that in the Hertzian and JKR models the relation between the contact area and the applied force scales as A $\propto (F)^{0.67}$ and the contact resistance is inversely proportional to the contact area, $R \propto A^{-1}$, the deviation between the power law exponents (n = -0.67 and n = -6.4)

suggests that not only the increasing of the contact area is responsible in the reduction of the resistance, as described before (untreated thermally). Interestingly, for the same range of forces, the resistance obtained in post-annealed samples was similar that those without post-annealing, (see Figure 5.4).
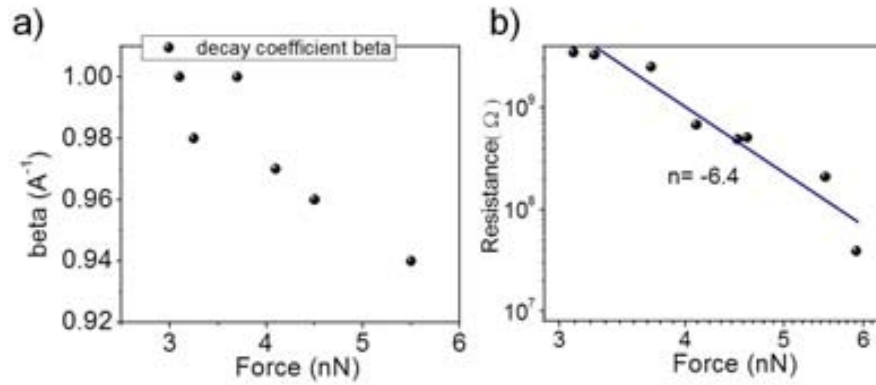
Figure 5.10. Decay coefficient and resistance of the junction as a function of applied force. (b) log-log plot of the junction resistance vs. the applied force.

5.3.2.2 Current differences, Resistance and Surface Potential: low and tall islands

Samples with both morphologies low and tall islands were obtained after immersing Au(111) substrates in 100μM acetic acid solutions of MMTA plus annealing. A strategy to define the reference level and measure the island heights has been carrying out current maps on areas with both morphologies, low and tall islands. By observing the current intensity given by the contact between the conductive tip and the bare gold substrate, the higher current signal (brightness in current image) will correspond at lower value in topographic profiles (dark in topographic image). We considered low applied forces of 3 ± 1nN during the different electrical measurements.

Figure 5.11 shows the topographic (a) and current maps (b) at a force of 4nN and applied voltage of 2.5V. Each image corresponds to a sequence of a SFM movie for MMTA obtained scanning the same region at several bias voltages (from 1.5V to 3V).
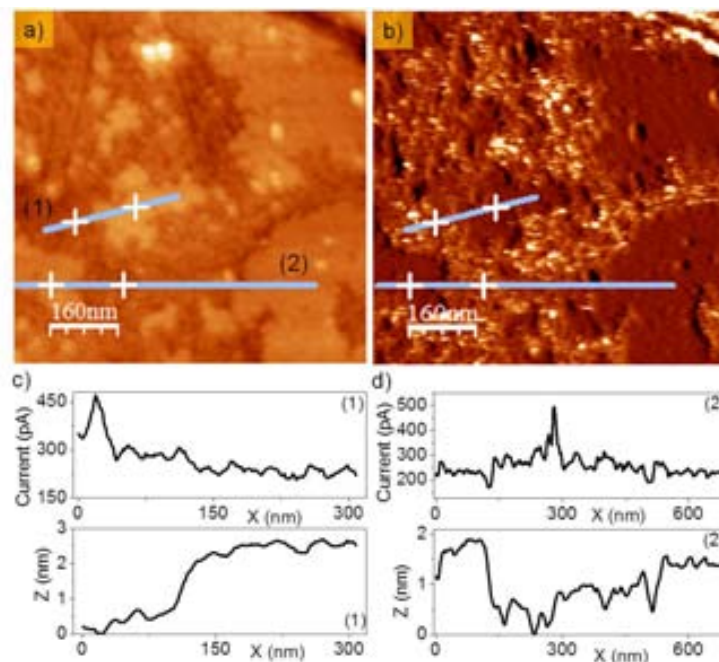
Figure 5.11. SFM images showing the Au(111) surface after immersing in a 100μM acetic acid solution of MMTA for 16 hours and post-annealing at $110°$C for 17 hours. Simultaneous topographic (a) and current map (b) recorded at low RH $< 5\%$ are shown. Cross-sectional profiles taken along the lines in (a, b) between low and tall islands are displayed in (c, d) revealing a current difference of 50 ± 10pA. Total z-scale: (a) 0-9nm; (b) 0-60nA. Adhesion Force: -6.5nN; Applied Force: 4nN; Applied Voltage: 2.5V.

Applying bias voltages above 2V was possible to determine a current difference $\Delta I \approx 50\pm10$pA between low and tall islands.

We compare some current-voltage (IV) curves performed on both morphologies in the range of -1nN to 4nN showing current intensities very low for the bilayer case. By observing the asymmetrical behavior of the IV curves obtained for a single molecular thickness as well as bilayers, this fact can suggest that the applied voltage will not lead to an equal shift of Fermi levels on both the conductive diamond/CrPt tip and the gold electrode due to the different contact between them. The molecular bilayer of MMTA can seem like a symmetric system trapped between the tip-gold substrate junction.

Figure 5.12 shows comparatively IV curves performed on tall (a, b) and low islands (c, d) at low forces. The high voltage range applied to obtain current signal on tall
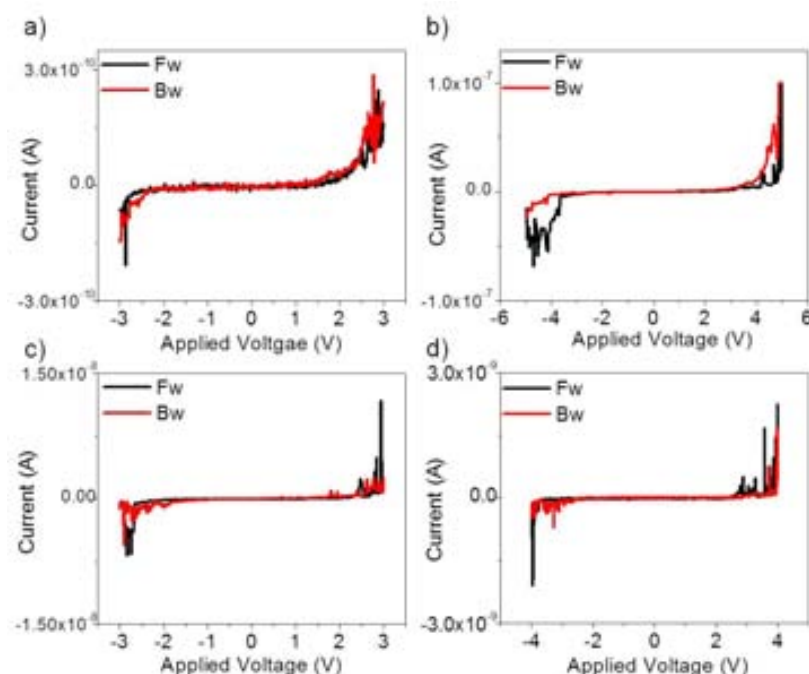
Figure 5.12. Current-Voltage *(IV)* curves on tall (a, b) and low (c, d) MMTA islands on Au(111) after immersing in a 100μM acetic acid solution of MMTA for 30 minutes and post-annealing at $100°$C for 16 hours. Applied Force: 1nN in (a, b); 3nN in (c, d).

islands produce damage on the molecular surface. In panel (a, b) shows two voltages ranges where the intensity is increased almost in the limit prior to mechanical damage of the surface, as possibly occurs around $\approx \pm 4$V. Panel (c, d) shows *IV* curves carried out on low islands by applying similar voltages. Mechanical damage on the molecular film occurred when high voltages were applied ($> \pm 3.8V$) on the surface of the islands as well as the adhesion force increased up to -85nN after several spectroscopic measurements. Molecular junction studies have shown the voltage dropped across of the SAMs produces fields of $\approx 10^9$V$\cdot$m^{-1} in magnitude, but high fields are sufficient to lead to dielectric breakdown of the molecular layer.

IV curves performed in contact mode on samples prepared for longer immersion times and post-annealing are presented in Figure 5.13 for a wide range of applied voltage. Forward curves (Fw) are recorded starting from negative voltages until to arise the maximum positive value and the backward (Bw) curve from this value until
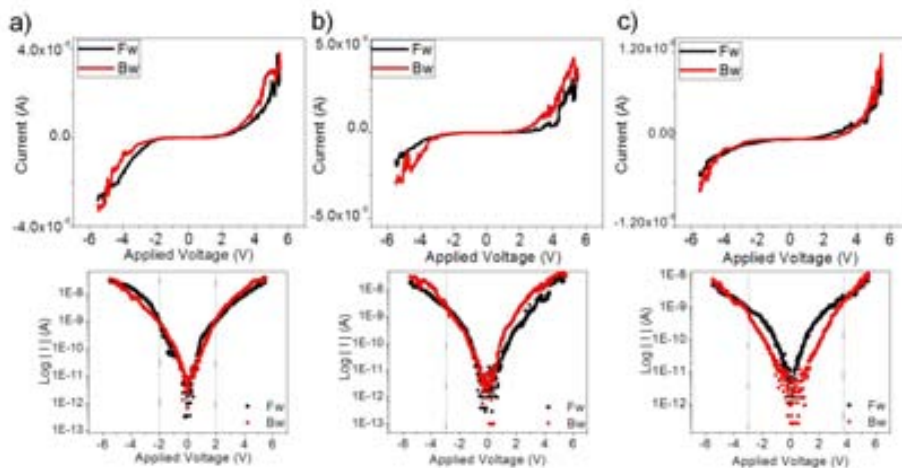
Figure 5.13. Current-Voltage (IV) curves (a, b, c) on low MMTA islands on Au(111) after immersing in a 100μM acetic acid solution of MMTA for 17 hours and post-annealing at 100°C for 16 hours and log$|I|$-bias voltage plots are shown. Vertical lines are showing the paths cross-over between forward and backward curves at bias voltages $\pm$2V and $\pm$3V. Applied Force: 3nN; Initial adhesion force of -20nN and -63nN at the end of the experiment.

the start point negative value to close the loop curve. For both Fw and Bw, the current curves do not follow the same way as well as their paths cross each over close to $\pm$ 2V or higher, as shown the log (I)-voltage(V) curves in (a, b, c). On the other hand, at low range voltage ($\pm$ 0.5V) the current intensity order is below nA, as shown the log-scale plots.

To compare the electronic transport response across the molecular layer, we performed IV curves by means of the 3D modes on the low islands. Taking into account the applied force range to establish a real contact between the tip and molecules, the intensity of current measured even by applying 3.5nN was considerably low in the applied voltage range $\pm$0.5V.

We performed systematic experiments using the 3D modes on a selected point of the low islands. Series of IV curves with current intensities of order of 10^{-12}A at $\pm$ 0.5V in repulsive regime (F$\approx$1nN) were measured. Figure 5.14 shows some IV curves recorded at different forces from adhesion regime until the conductive tip contacts the gold substrate to 9.6nN (a) and log$|I|$-bias voltage plot of selected curves at low applied
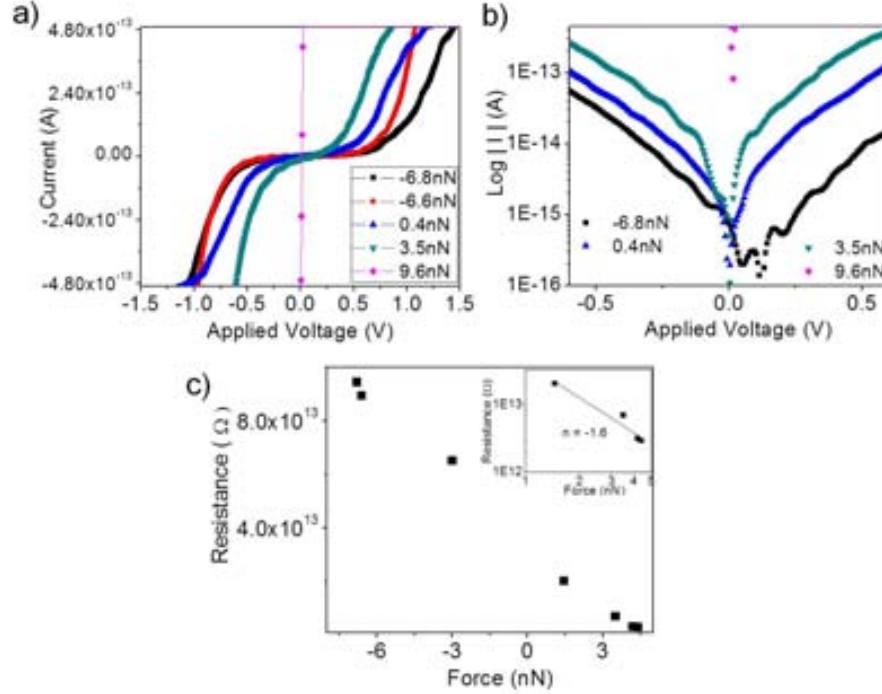
Figure 5.14. Current-Voltage (IV) curves (a) on low MMTA islands on Au(111) after immersing in 100μM acetic acid solution of MMTA for 17 hours and post-annealing at $100°$C for 16 hours with their respective Log$|I|$ versus bias voltage plots (b). Plot (c) shows the contact resistance in linear scale, whereas inset shows the Log (I) versus Log (Force) fitting with n=-1.6.

voltage range. In the adhesion regime, instabilities on the current curve is observed, which we associated to a poor contact between tip and sample, whereas at forces of 0.4nN and 3.5nN a stepwise behavior is observed on both branches of the curves. This latter behavior, can be interpreted as a Coulomb staircase effect, by assuming that the capacitance of the low island is small enough that adding electrons to it will increase its potential, in this way, the low island potential is higher than the bias voltage applied. This effect shows that tunneling is blocked for as long as the applied voltage is not large enough to overcome the Coulomb blocked with n electron residing in the electronic states of the island. As before, the contact resistance (R) decreases as the force increases, as shown in (c). Following the Hertzian or JKR models with the relation $R \propto F^n$ by performing log-log plot linear fit from IVs in the force range from 1.5nN to

4.5nN we obtained the power law exponent, n =-1.6.

IV curves performed on tall islands (bilayer) have shown a considerable voltage gap by applying 4nN for a wide range of bias voltage as shown both *IV* curves and log-current scale in Figure 5.15 (a, b, c). Although the curves show an apparent rectifying behaviour $\left(\frac{I_{+3V}}{I_{-3V}}\right) \neq 1$ between the intensities of current obtained in the voltage range $\pm$ 4V, the origin of this asymmetry is not yet clear.
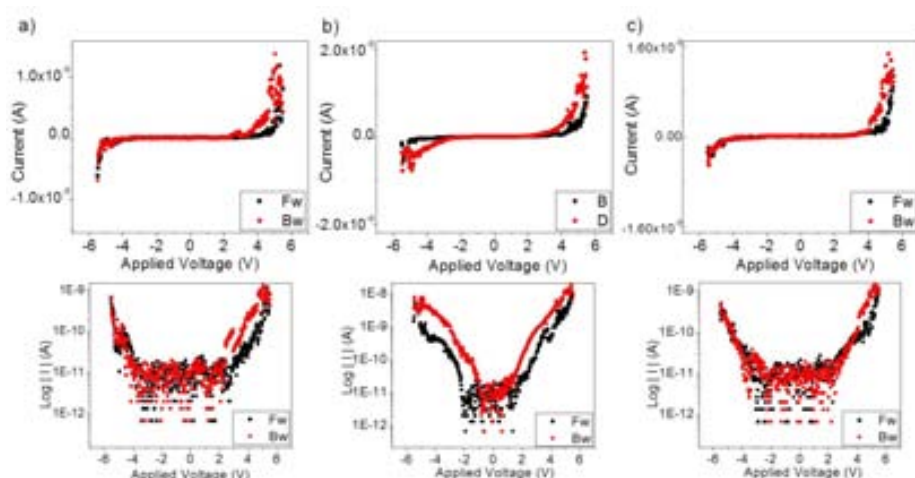
Figure 5.15. Current-Voltage (IV) curves (a, b, c) on tall MMTA islands on Au(111) after immersing in 100μM acetic acid solution of MMTA for 17 hours and post-annealing at 100°C for 16 hours. Bottom panels correspond to their respective log$|I|$-bias voltage plots. Applied Force: 4nN; Adhesion force: -17nN.

As can be seen in Figures 5.13 and 5.15, the current intensities measured for bilayers (of order of 10^{-9}A) are obtained for voltages close to ($\pm$4V) or higher. This is a surprising result since the expected high current due to their strongly π-conjugated system is lower than current intensities measured in low islands. The poor efficiency in the tunneling pathway through a bilayer of the MMTA islands is due to likely the hydrogen bonds at the single molecular/single molecular interface.

To explore the possible changes in surface work function or effect of surface dipoles, we carried out measurements at low relative humidity for determining the surface potential of the molecular film on the gold substrate. Samples with post-annealing treatment were studied immediately at low RH< 5% conditions. Figure 5.16 revealed a

surface potential difference $\Delta SP = SP_{SH}$-$SP_{COOH} = 50\pm5$mV bewtween bilayer and single molecular layer.

Mapping of the surface potential was performed in the so-called *lift mode*. Several measurements were carried out simultaneously with the topography scan in the tapping mode, using an electrically conducting tip. After each line of topography scan was completed, the feedback loop controlling the vertical piezo was turned off, and the tip was lifted from the surface and traced over the same topography at constant distance. Oscillating amplitudes from 8nm to 12nm were employed during experiments.

The surface potential (SP) values were constants up to 10nm in *z-lift mode*, but higher values did not allow measuring appropriately. Interestingly, we will expect the vanishing the surface potential for tall islands due to their symmetrical shape and a priori to the nullifying the total moment dipole, but the surface potential measured on the tall islands was always higher than the low islands.
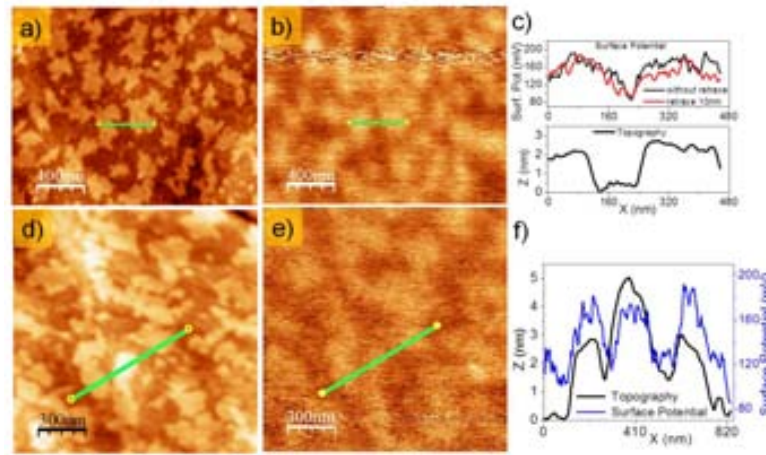
Figure 5.16. SFM images of MMTA islands on Au(111) surface after immersing in 100μM acetic acid solution of MMTA for 16 hours and post-annealing at $110°$C for 17 hours. Topographic (a, d) and surface potential (b, e) images at RH < 5%. Simultaneous profiles taken on tall and low islands are presented in (c, f).

Figure 5.17 shows the morphologies for tall and low islands with the respective surface potential image recorded in air (RH≈35%). We estimated a surface potential difference of 80 ± 5mV between tall and low islands by means of several cross-sectional

profiles and 75±10mV by performing a histogram on the whole surface potential image. On tall islands the surface potential is higher than low islands and these values were also constants for measuring in z-lift mode up to 10nm. Clearly, we observed a dependence of the surface potential with the relative humidity for both carboxylic acid and thiol end groups where the difference was increased at least 60%. When increasing RH from 5% to 35% suggests that water molecules adsorbed on each termination produce a different effect (i.e., screening.)
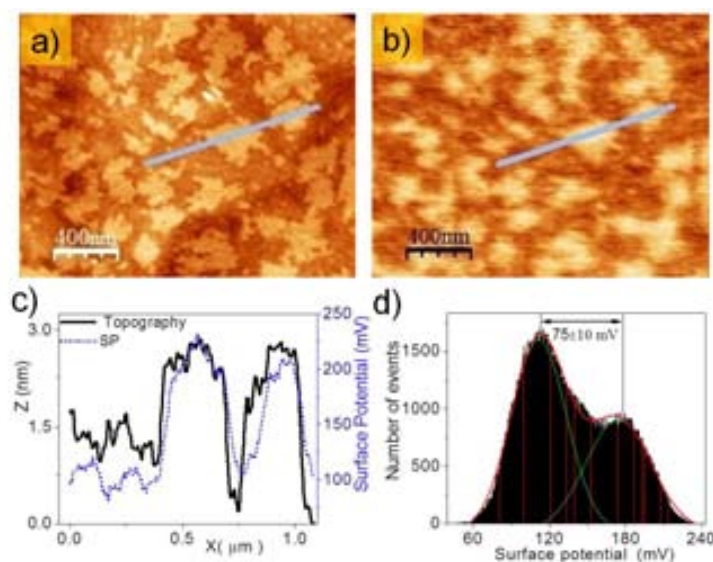
Figure 5.17. SFM images of MMTA islands on Au(111) surface after immersing in a $100\mu M$ acetic acid solution of MMTA for 16 hours and post-annealing at 110°C for 17 hours. Topographic (a) and surface potential (b) images were recorded in air (RH≈35%). The corresponding profiles taken crossing both tall and low islands are presented in (c), whereas the histogram of the whole surface potential image is showed in (d).

For SAMs of aromatic oligomers bearing a thiol end group (-SH), the molecular dipole is oriented towards the surface. Due to this, a reduction in the surface potential distribution between the bare substrate and the SAM-covered gold substrate is observed. The delocalization of the π-electron orbitals is higher than in alkanethiols, and thus decrease in surface potential, proportional to the molecule length (phenyl, biphenyl or triphenyl thiol molecules) [166]. To understand the surface potential difference measured

between both tall (-SH end group) and low (-COOH end group) islands, the equation 5.6 can be used as a good approximation by assuming two different SAMs [141],

$$\Delta V_{SH-COOH} = \left[\frac{\mu_{SH}}{\epsilon_0 \epsilon_{SH} \cdot A_{SH}} - \frac{\mu_{COOH}}{\epsilon_0 \epsilon_{COOH} \cdot A_{COOH}} \right] \qquad (5.6)$$

μ is the molecular dipole moment normal to the substrate, A the area per molecule, ϵ the dielectric constant, ϵ_0 the permittivity of free space.

5.3.2.3 Low Islands and Multilayers from Ethanolic Solutions: tunneling and field emission regimes

Samples prepared at low concentration in ethanolic solution of MMTA and immersion times below 1 hour have shown a partial coverage on the surface allowing to observe the coalescence of the low islands when the solution was heated. In Figure 5.18 we show the molecular film after immersing the gold substrate in ethanolic solution.
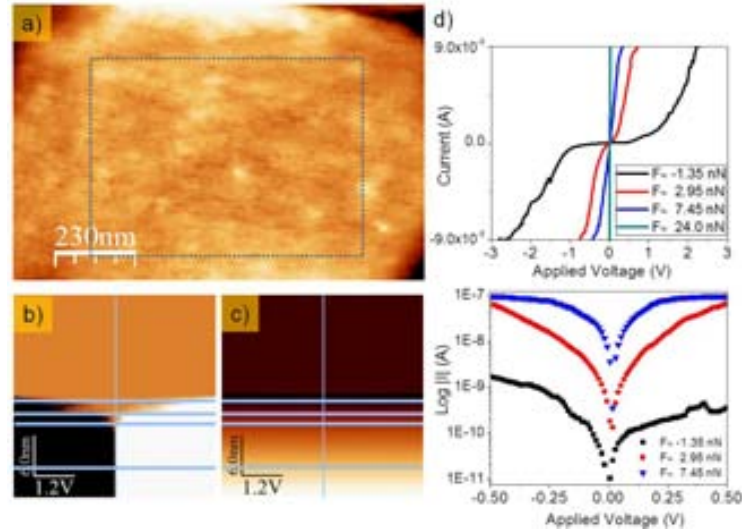
Figure 5.18. (a) Topographic, (b) current I(V, z) and (c) normal force F_N(V, z) images are displayed. In (d) extracted IV curves and their log(I)-voltage plot are shown. Au(111) substrate immersed in 2μM ethanolic solution of MMTA for 1 hour and annealing the solution at 80°C.

The temperature was fixed at 80°C for 1 hour. Low islands form clusters and a RMS roughness of 0.5nm was estimated for the area marked of the topographic image.

5.3 Electronic Transport and Surface Properties of MMTA Islands

By using the 3D modes over a particular point of the surface we obtained the current across the molecular film for different loads. By comparison between the IV curves recorded at low forces (i.e. in the adhesion force range) and forces in repulsive range we observed differences of 2 orders of magnitude in the current range, this fact is shown in $\log|I|$ versus applied voltage in the range ±0.5V.

Figure 5.19 shows high coverage gold surface where several IV curves were performed. Prior to the electrical experiments, a small area of the surface was scratched to know the thickness of the molecular growth which which resulted to be 10nm (3 bilayers). As in the case of the 3D-nanostructure in Figure 5.5, IVs curves on the marked region show an asymmetric behaviour and regimes with changes in the slope of the IV curve at voltages below 1V. Multilayers of MMTA obtained on high coverage
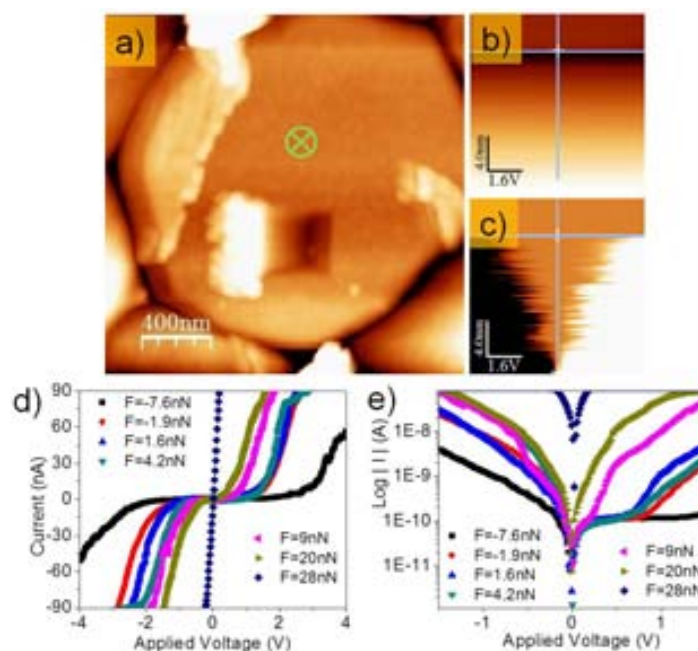
Figure 5.19. SFM images of Au(111) after immersing in 100μM ethanolic solution of MMTA for 20 hours and post-annealing at 110°C for 24 hours. Topography (a) , normal force F(V, z) and current I (V, z) images recorded by means of the 3D modes. Current versus applied voltage curves on the mark in (a) and log plot are shown (d, e). Scratching on the surface was performed to know the thickness of the molecular layer.

surfaces revealed that the current intensity within voltage range $\pm$ 0.5V was two orders of magnitude higher than for the 3D-nanostructures. Both the 3D-nanostructures and covered surface by multilayers showed clearly a transition voltage in which the transport mechanism changes from direct tunneling to field emission. This change of regime is particularly noticed in the repulsive force range, as shown log plot in (e) from 1.6nN to 20nN. This occurs at moderate voltages below $\pm$ 1V.

5.4 Electronic Transport on Patterned Gold Surfaces

Ethanolic and toluene thiols solutions were prepared following the protocols described in chapter 2. A drop of the aromatic thiol solution (ink) was placed on the structured side of the stamp using a dropper. After some seconds the solution was dried under a stream of nitrogen, then the stamp was placed by hand on the gold substrate (roughness $\approx$ 1.5nm) and a softly pressed. In order to compare and discuss the response of the surface potential of chemically modified surfaces, we patterned surfaces with alkanethiols such as the mercapto hexadecanoic acid (MHDA) and hexadecanethiol (C16) on the gold surface, as well as the biphenyl derivative (aromatic thiol BP4) on Au(111).

5.4.1 Current Maps and Surface Potential: patterned surface

In a first stage, current maps were performed on the patterned surface. Figure 5.20 shows an example of the morphological changes during the scanning for positive tip voltages. Each couple of images in the figure corresponds to selected sequences of the respective complete topographic (a, d, g) and current (b, e, h) movies obtained at constant voltage intervals of ΔV_{tip}=0.05V ranging from 0.3 to 1V.

Topographic and current profiles taken along the lines in each couple of images are shown in (c, f, i). By correlating the current maps and the topography images, it is possible to deduce that the gold surface correspond to the lower level in topographic profile and the highest signal in current (brightness). After applying a voltage of 0.3V, the process of morphological disruption of the molecular film increases (high roughness) for applied voltages up to 1V, as shown in (d, g). At low voltages (below 0.1V) the current intensity is less than 20nA on the bare gold arising the maximum value after applying above 0.3V. This morphological change seems to have a voltage dependence,
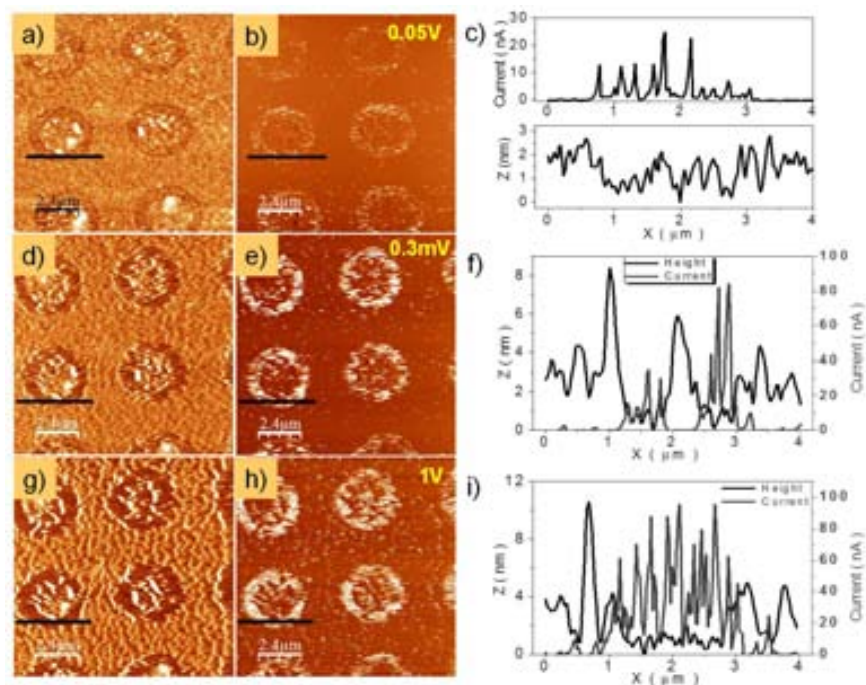
Figure 5.20. Topography (a, d, g) and current maps(b, e, h) by applying different bias voltages (0.05V, 0.3mV and 1.0V), respectively. Applied Force: 2nN. Adhesion Force: -30nN. Total z-scale: (a) 0-45nm; (d, g) 0-32nm

because the applied force was of 2nN during acquisition. Figure 5.21 shows regions with high molecular transferring from PDMS stamps, heights up to 6nm were measured, whereas a surface potential difference between two reference points marked with dashed lines in (c) revealed a value of 140mV using the *z-lift mode* or retrace at 80nm. From current images, the bare gold substrate provided a reference point to measure the surface potential for several levels of the film. In this sense, it is possible to observe that the surface potential difference increases with the thickness of the molecular layer. This fact can be observed in Figure 5.21 (d, e) and profiles in (f).

Simultaneous profiles of surface potential and topographic images at zones with double bilayer (average height of 6nm) revealed a $\Delta SP \approx 140mV$ as shown in Figure 5.22(a). By correlating the current maps, the topographic and the surface potential images the reference of the gold substrate was pointed out with the black arrows (inset in a), where a small difference in the surface potential on the background of $\approx 15mV$.
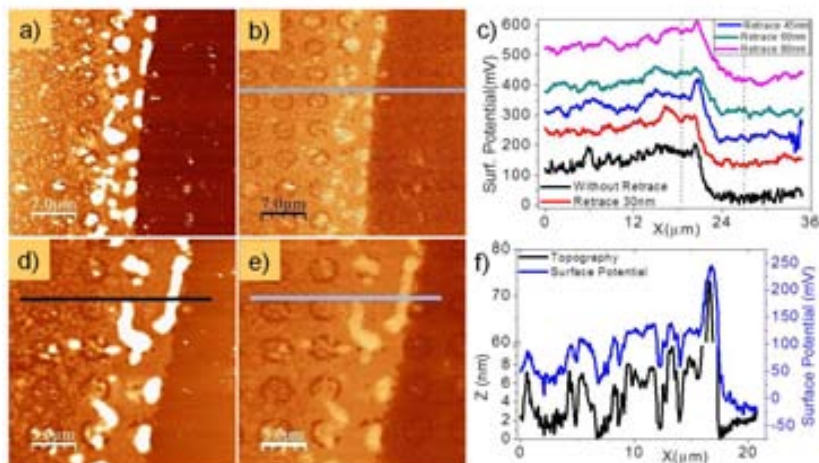
Figure 5.21. Topography (a, d) and surface potential (b, e) images simultaneously obtained showing different levels of MMTA on the gold surface. Surface potential profiles taken on the same area in (a, b) are shown in (c) using the *z-lift* mode. Simultaneous topographic and surface potential profiles taken along the lines in (d, e) are displayed in (f). Total z scale: (a)0-241nm; (b)-191mV to 860mV; (d)0-172nm; (e)-176mV to 478mV.

Due to the height difference is less than 0.7nm, we suggest the presence of molecules in the lying-down phase in agreement with the expected value of the surface potential for molecules with their dipole moment parallel to the metallic substrate.

Interestingly, the surface potential difference increased for bilayer and multilayers, this fact can be compared as a donor-acceptor behavior with different dipole moments between them. The bonding of sulfur and gold at atomic scale involves a sharing of electrons with polarization $Au_3^{+-}SR$, the sulfur atom obtains a negative charge from the π-bond delocalization of the electrons. This electron delocalization into the phenyl system result in net charge density at the ortho and para-positions. The presence of the polar group (-COOH) likely contributes to a new charge distribution for the molecular film with dipole moment $\mu_{single} < \mu_{bilayers}$ acting in opposite directions.

From non-contact regime (50nm apart from the surface) we performed *IV* curves using 3D modes over the patterned zones without multilayers and the excitation frequency image was used to define the regions of interest, as shown in Figure 5.23. Topographic (a) and excitation frequency (b) images were recorded previously to the
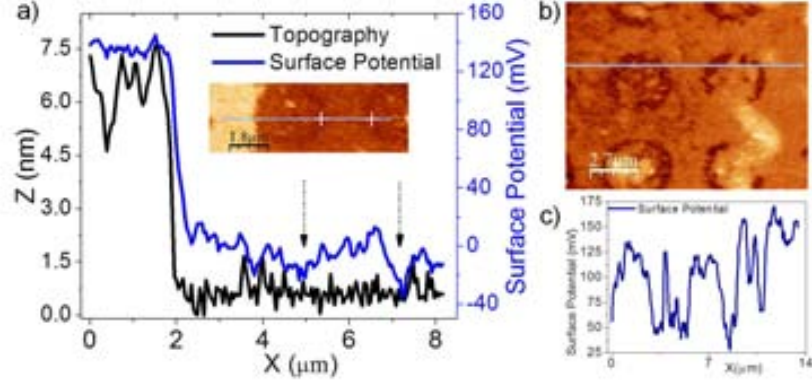
Figure 5.22. Topographic (inset in a) and surface potential (b) images for double bilayer of MMTA on the gold surface. Simultaneous topographic and surface potential profiles taken from surface potential (inset) and topographic images on the double bilayer and substrate (pointed out with arrows) are shown in (a). Surface potential profile in (c) was taken along the multilayer and the gold surface.

3D experiments. Inset in (a) is the I(V, Z) image showing horizontal profiles to extract several IV curves at different loads. Current-applied voltage are shown in (c), inset shown the direct contact between the conductive tip and substrate achieved by applying forces $\approx$ 10nN. Spectroscopic experiments performed on the patterned surface and the gold surface allow measuring the surface potential difference of about 55±5 mV between both regions, as shown in (d).

By doing this, the normal force F(V, d) and current I(V, d) images are recorded at a given position on the sample as a function of tip-sample voltage and tip-sample distance. Since each horizontal line F(V, z) depends quadratically on tip-sample voltage, the derivative of the total potential given by the molecular and electrostatic interactions $U_{tot}(V, z) = U_{VdW}(z) + U_{elec}(V, z)$ can be adjusted to a parabola of the form $A+B(x-C)^2$. The parameters A, B and C are describing the Van der Waals interaction by assuming the plane-sphere interaction potential, the capacitance and the surface potential, respectively, whereas the x is the applied voltage (see 2.19 (F_{dc})).

Surface potential values of the MMTA molecular film using both methods the spectroscopic and KPFM images showed similar values on the patterned region with thicknesses of single molecular layers on gold surface (roughness 1nm).
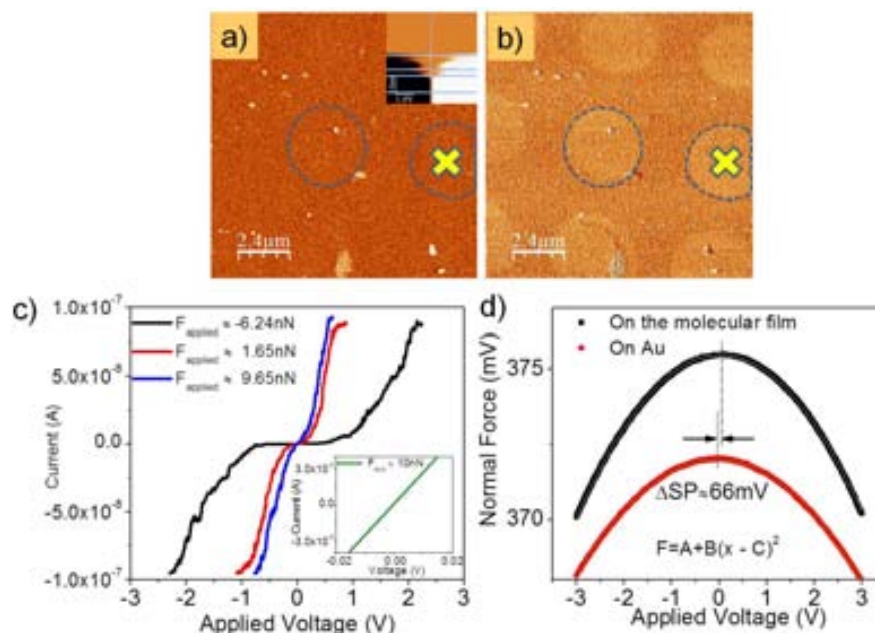
Figure 5.23. Topography (a), excitation frequency (b) images obtained from dynamic modes. Inset in (a) shows I(V, z) image recorded at the marked zone, whereas (c) show the *IV* curves as a function of applied load. Inset in (c) is the ohmic region of contact with the gold surface. Experimental data in both Au surface and molecular film are fitted to obtain the difference of surface potential (d).

5.4.2   Low Coverages: patterned surfaces

Patterned surfaces using 100μM toluene solution of MMTA were also prepared to get stamped regions on the gold substrate following the same procedure that for ethanolic solutions. PDMS stamps with a rounded pattern with diameter of 5μm were employed. Although we observed a poor molecular transferring, this fact, allows obtaining the surface potential difference between bare gold and an incomplete molecular layer. Figure 5.24 shows the topographic image (a), the surface potential (b), the excitation frequency on the patterned surface. Topographic and surface potential profiles taken along the lines in (a, b) are displayed in (d). Excitation frequency image allows identifying both regions the bare gold and patterned surface. From topographic, surface potential and excitation frequency profiles taken simultaneously, a difference of 1.3 ± 0.5nm in height between bare gold and the molecular film was measured,as shown in (d). The surface

potential difference was estimated around 55mV similar to previous values in ethanolic solutions of MMTA.
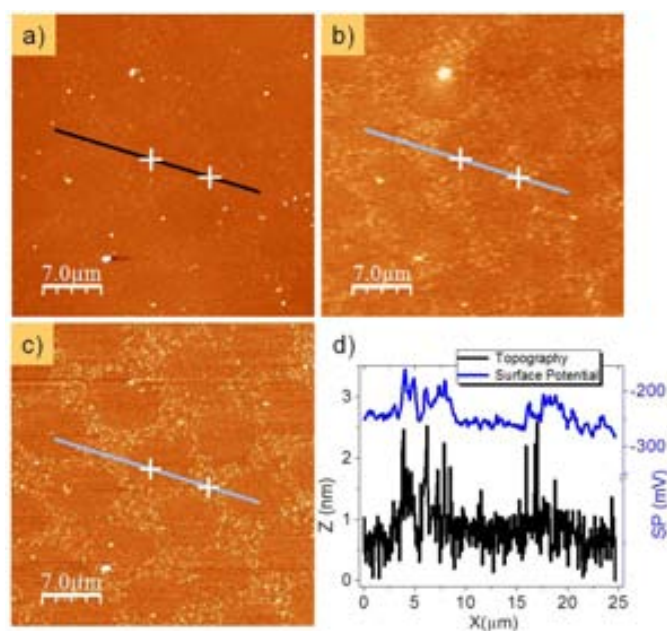
Figure 5.24. Topography (a), surface potential (b), excitation frequency images on a patterned zone of gold surface (c). Topographic and surface potential profiles taken a long the lines in (a, b) are displayed in (d). $100\mu M$ toluene solution was employed. Total z-scale: (a)0-310nm; (b)-467mV to 262mV and (c) 0-1kHz.

Patterned regions were obtained as previous measurements with other solvent, unlike ethanolic solutions we did not observe regions with high density of transferred material. Furthermore, the poor molecular transferring is observed in the current map, because the higher density of defects presents on the molecular layer facilitates the direct contact between tip and the gold surface. In contact mode we carried out the current maps to verify the reference of bare gold and the patterned region showed in Figure 5.25. Topographic (a) and current map (b) with their corresponding topographic and current profiles taken along the lines in (a, b) are shown in (c). To this end, we used diamond conductive tip by applying lowest load to avoid damage on the molecular film. Following the code color for current images presented, the color brightness (dark)

represents to higher(lower) current values. By performing current maps permitted us to be sure that the value of the surface potential difference between the molecular layer or small cluster of molecules and the bare gold must be around 50±5 mV within the experimental error. In this case, the round pattern is not covered with molecules (not conducting black dots).
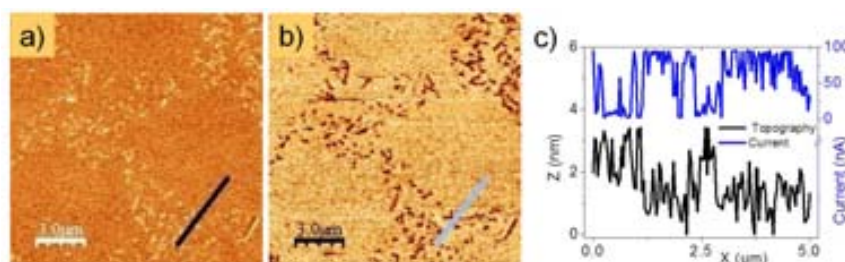
Figure 5.25. Topography (a) and current map (b) images have been obtained by using a conductive diamond tip k=2.8 N·m^{-1} under a nitrogen environment applying 10nN of force and bias voltage of 100mV. Total z-scale: (a) 0-30.4nm (b) 0-100nA.

As mentioned in chapters 3 and 4, the patterned surfaces obtained by μCP using the *ink* MMTA or island formations induced by thermal process showed from a single molecular thickness to multilayers of organic material. Using these strategies, it was possible to obtain a mixed surface containing zones of thiol-terminated (bilayers) and carboxylic-terminated molecular structures which allowed measuring of their surface potential difference. In order to compare and estimate with other molecular systems, we show in Figure 5.26 the topographic (a, d, g, j) and surface potential (b, e, h, k) results of two types of thiols (alkane and aromatic thiols) patterned on gold. For the μCP pattern in (a), higher square regions correspond to mercaptohexadecanoic acid (MHDA) molecules as shown the topographic profile. Clearly the contact potential of the substrate is modified with a difference of ≈ 270±10 mV due to this molecular film. For aromatic thiol (BP4), a surface potential difference of 210mV respect to the gold surface is measured. By combining, aromatic and alkanethiols as shown in (g, h , i) we observed lower surface potential for MMTA than C16. Even in this case, the quality of patterned topography is rather poor, due to the presence of a high density of

defects such as depressions, low coverage, domain boundaries or poor packing, SAMs of molecules with different end groups give work function changes.
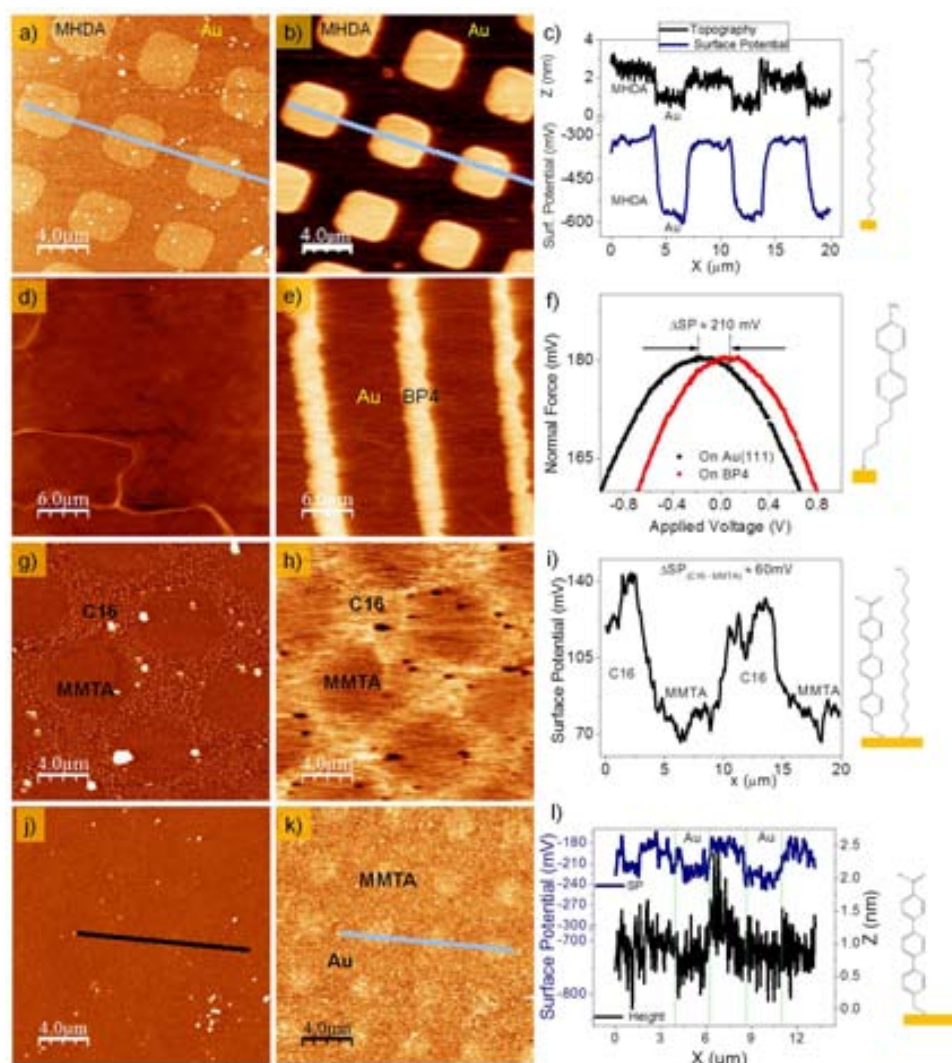
Figure 5.26. SFM images of alkanethiols and conjugated molecules printed pattern obtained by direct transfer from PDMS stamp to bare gold surface. Topographic (a) and surface potential (b) of mercapto hexadecanoic acid (MHDA) on gold surface. Topographic and surface potential for the CH_3-C_6H_4-C_6H_4-$(CH_2)_n$-SH , n=4 (BP4) (d, e) are shown. Topographic and surface potential of multicomponents C16 (hexadecanethiol) and the aromatic thiol MMTA are displayed (g, h). Topographic and surface potential for MMTA on Au substrate are displayed in (j, k). Panels (c, f, i, l) show the surface potential obtained between patterned regions.

Well-ordered dipolar monolayers have been modeled as dielectric films using the equation 5.1, where N is the areal density of modifiers[3] and $\mu\perp_{C16} \approx 1.6$D [167] with $\epsilon_{SAM} \approx 2.8$, the work function shift of hexadecanethiol is around -0.75eV [143, 167]. Table 5.3 shows some values reported by Alloway et al. [168, 169] using w-functionalized alkanethiols with the tail group varying electronegatively (i.e., -CH3, Ph, -Cl, -Br and -CF3) and characterized by UPS to monitor changes in effective work function of the gold surface. They suggested that the the vacuum level and the work function of a gold surface can be modified by means of functionalized alkyl chains with electron-donating or electron-withdrawing substituents.

Thiols	Shift in effec. vacuum level(eV)	Effec. Work function (eV)	$\mu\perp$ Calc. dipole(D)
C12	-1.13	3.9	1.32
C12Ph	-0.8	4.1	0.99/0.79
C12Cl	-0.24	4.7	-0.34
C12Br	-0.2	4.8	-0.42
$SH(CH_2)_9CH_3$	-1.27	3.83	1.4
$SH(CH_2)_{15}CH_3$	-1.35	3.75	1.5
$SH(CH_2)_{12}CF_3$	0.12	5.22	-0.7
$SH(CH_2)_{15}CF_3$	-0.12	4.98	-1.8
$SH(CH_2)_6(CF_2)_9CF_3$	0.46	5.56	-1.5

Table 5.3. Changes in effective work function of clean Au(111) as a function of the molecular dipole moment projected along the normal axis.

The main difference between CH_3 and COOH-SAMs is that molecules such as the C16 carry a single dipole moment due to its head-group (S-C bond), whereas others such as MHDA or MMTA molecules have dipole moments on both head and tail groups, in addition of the polarization effects caused by the aromatic rings within itself monolayer.

---

[3]Considering the area per molecule in the $(2\sqrt{3} \times \sqrt{3})R30°$ structure (21.6Å^2) and $(\sqrt{3} \times \sqrt{3})R30°$ structure (21.4Å^2), N values are typically ca. (3-5)×10^{18} molecules·m^{-2}.
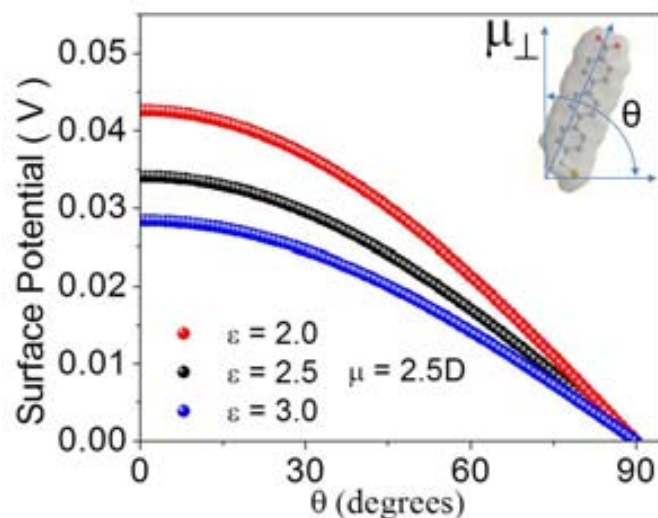
Figure 5.27. Surface potential versus the dipole moment angle along the molecular axis and the normal surface. Permittivity of the SAMs are taken from 2 to 3.0.

Taking into account the formula 5.1, we can estimate the surface potential (V) for the layer of MMTA of a single molecular length.

$$V = -\frac{(\Phi_{sample} - \Phi_{tip})}{e} + N\frac{\mu_\perp}{\epsilon\epsilon_0} \qquad (5.7)$$

The first term represents the Contact Potential Difference (CPD) from theoretical and experimental values of the clean substrate (5.25eV)[170, 171] and second one the surface potential calculated for the absorbed molecular layer on the substrate. The dipole moment along the isolated molecule was estimated as 2.8D, the dielectric constant ϵ=2.8 was used, $N = 9\times10^{16} molecules\cdot$m^{-2} from coverages analysis (35%) of low islands for high immersion and post-annealing times.

Figure 5.27 shows the expected surface potential for the single molecular thickness of the MMTA aromatic thiol, with the previous values. Low signal in surface potential corresponds to molecules in lying-down phase (90°), whereas at 30° a surface potential of $\approx$35mV, for ϵ=2.8 agrees with the expected value, from surface potential images using Au(111) substrates. Surface potential acquired by spectroscopic and and KPFM

using gold substrate (roughness 1nm) was 1.5 times larger than for surface potential values estimated using this approximation.

5.5   Discussion of Electrical Properties and Models

In this section we will discuss some results from the electrical characterization of the MMTA islands on Au(111) and gold surfaces (roughness 1nm). Tall and low islands were obtained after immersing Au(111) substrates in solutions of MMTA plus annealing. Both morphologies were observed as shown the side view of the illustration 5.28. A conductive AFM-tip (positive polarization) scans both morphologies allowing measuring a current difference of 50±10pA between tall and low islands. For low islands the electronic transport is more efficient than for tall islands. By performing the 3D modes, the molecular assembly is tilted as the load increases. Several transport pathways can exist across the molecular film by considering the different tunneling path of the electron coming from the AFM-tip, pathways (1) and (2). A first tunneling path is depicted from the tip into the gold electrode within low voltages (±0.5 V) across of the molecular backbone, the second path can exist by tunneling between neighbor molecules, for the "REF A" position. For "REF B" position, the molecular assembly has been tilted and the tunneling occurs more efficiently across the aromatic rings and the alkyl chain, between neighbor molecules by means of the strong intermolecular force and $\pi - \pi$ stacking.

In low islands with lateral dimensions below 20nm as well as 3D-nanostructure crystallites, the electron transport occurs perpendicular to the grown layers. In such structures quantum effects can occur at high bias ($\approx$1V) and room temperature, such as the Coulomb staircase behavior.

On the basis of Kelvin probe measurements and theoretical calculations, it is widely accepted that the chemisorbed SAMs form a dipole layer on metal substrates modifying the work function of the metal ($\Phi_{Au(111)} = 5.25$eV)[143]. We have used the ω-functionalized aromatic thiol where a single molecular thickness as well as bilayers forms a dipole layer to tune the effective work function of gold. The first interfacial S-Au dipole is as low as 0.02D being approximately 2 orders of magnitude lower than the value of the dipole moment of the molecules [172]. Figure 5.29 shows an illustration
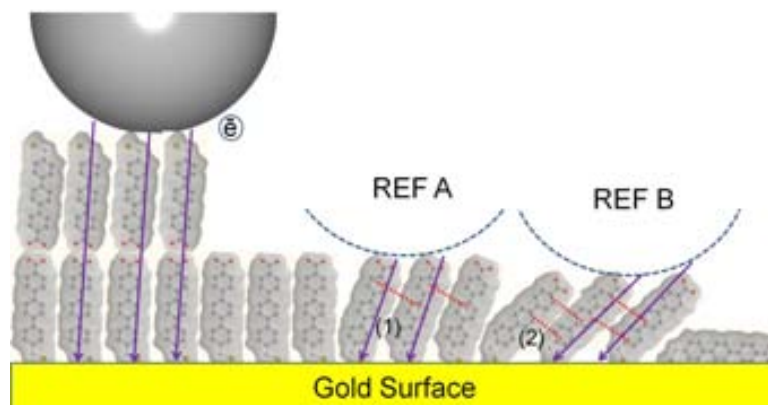
Figure 5.28. Illustration of bilayer and single molecular thickness for MMTA islands under a pressing of the AFM-tip. Two possible paths of transport are depicted en REF A and REF B for the molecular film, a tunneling mechanism across of the molecular backbone and interchain transport.

for alkanethiols and polar molecular films where the end group is represented by the carboxylic group. The interface dipole formed on the substrate for both single molecular thickness and bilayer reveals a difference of surface potential of about 50±10 mV.

Lying-down molecules with a dipole parallel to the gold substrate (roughness 1nm) were obtained by microcontact printing which allowed measuring a difference of surface potential of 15mV and standing-up molecules with a surface potential of 50±5mV from KPFM images and 60±5mV from spectroscopic measurements. Interestingly, for the molecular bilayer is twice the value obtained of single molecular thickness showing a clear dependence with the thickness of the molecular film. Though the surface potential for low islands respect to the bare gold were not clearly acquired during experiments due to their reduced lateral dimensions, the surface potential estimated from equation 5.7 of 35mV is a good approximation.

5.6 Conclusions

Samples prepared by immersing the Au(111) substrates in solutions of MMTA at low immersion times without annealing have revealed that the decay coefficient $\beta=0.94\pm0.01$ remains constant at low forces in the voltage regime described by Simmons theory. Contact resistance (R) of order of $10^8\Omega$ were calculated from IV curves at low
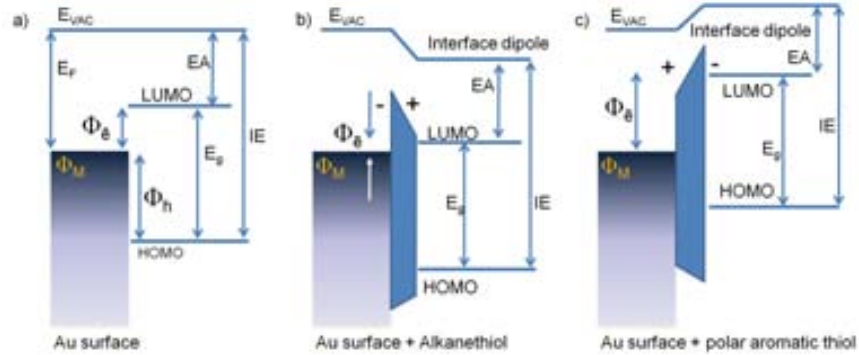
Figure 5.29. Schematic energy-levels diagrams of metal-organic interfaces. Electron injection barrier (Φ_e) and hole injection barrier (Φ_h) for an untreated interface are shown in (a). In (b) an alkanethiol impose an interface dipole that decrease (Φ_e) and increase (Φ_h), whereas a polar aromatic thiol impose an interface dipole that increased Φ_e and decrease Φ_h. E_F is the Fermi energy of Au; E_{vac} is the local vacuum energy level; IE represents the ionization energy and EA the electron affinity. Adapted from Boer et. al. [167].

voltage range (± 0.3V). Interestingly, the junction contact resistance analysis showed a power law exponent n=-0.43 respect close to n=-0.67 expected for the Hertzian model for the samples immersed for 30 minutes. For the reference "REF B", the resistance and force scale with a power law exponent n=-6.4 which indicate that other phenomena are involved in the reduction of the resistance likely due to the structural changes produced at high forces ($\approx$ 6nN).

For samples thermally treated, values for the decay coefficient β calculated for low islands showed a different behavior for the same force range. We assumed that the transport efficiency reflected for the decay coefficient is related with close packing and the efficient electronic coupling across strongly π-conjugated system. Linear fits performed in log(R)-log(Force) plots revealed a different behavior as expected in Hertz model and JKR for the law power n=-0.67. We assumed contact areas at minimum applied forces, however, the contact area is increased as increases load. This fact, suggests take into account the indenter geometry to estimate a contact area as a function of load, in the repulsive regime.

IV curves showed some asymmetry likely due to the non-uniformity of the electric

field between the tip-organic-Au substrate, and the nature of the contact between electrodes. However, asymmetric intrinsic transport characteristics may also exist based on the non-symmetric molecular arrangement across the film thickness. 3D crystallites (15nm) obtained from drop-casting method as well as for high coverage multilayers (thickness of 10nm) revealed an asymmetric behavior for ranges of forces from -4nN to 30nN at low voltages. The larger current for negative voltages and low forces is typical of n-type junctions or an asymmetric barrier in which conduction is dominated by electron transport, as observed in $\log|(I)|$-V plots. On the other hand, for large forces a quite marked change in the slope of these logarithmic plots is observed if increasing the applied voltage range. Forces at 9nN, a steep *IV* curve at positive voltage values indicates an increase of the electron transport towards the tip (p-type junction). Fowler-Nordheim representation was employed to observe the transition voltage ($\approx$0.4V) from tunneling to field emission.

In spite of the reduced lateral dimension of the low islands, the surface potential difference of 50±5mV between low and tall islands is measured in Au(111) substrate at low relative humidity ($\approx$5%). At higher relative himidity (above 35%), the surface potential difference was of 85±10mV between tall and low islands.

μCP technique was employed to pattern surfaces as well as gold (roughness 1nm) and Au(111) substrates. Current maps performed on topographic areas with both morphologies low and tall islands showed a current difference of $\approx$50±10pA after applying high voltages (2.5V). Electronic transport experiments and electrostatic characterization performed by using both types of substrates revealed its importance for the surface potential results of the adsorbed molecular film. Thickness dependent surface potential measurements were possible using these patterned surfaces. Though dipole cancellation was expected for multilayer films made out of bilayers, the surface potential resulted to increase with increasing film thickness. This result could be interpreted if cancellation exist within the intermediate layers but interface charge transfer and upper surface dipoles remain. The increased separation between this two contributions with thickness would lead to a larger effective or net dipole.

CHAPTER 6

COMPLEX OXIDES SURFACES

Low-dimensional structures of complex oxides with a wide range of functional properties, from ferroic to catalytic properties, hold the promise to lead to a new generation of materials with unrivalled properties compared to their bulk counterparts. This expectation is at the heart of the unprecedented development of oxide nanostructures. However, nanostructure fabrication of complex oxides is not as well established as these of metals or semiconductors, which is partly due to the complexity of lattices and the numerous chemical elements. Moreover, the long-range order is even more challenging.

In this chapter, we will describe some results obtained and published in collaboration with the Professor J. Fontcuberta Group, who prepared and growth thin films of oxides such as LSMO and BTO on the STO(001) and LSAT substrates. In addition, we present a possibility of using these chemically-patterned substrates for selective growth of others materials, organics in particular, addressed here to demonstrate that they can act as host platforms for nanostructuring organic-based monolayers.

6.1   Introduction

Most oxides are chemically inert to the common etchants, and thus the use of conventional photolithography techniques is very limited. Photolithography by focused ion beam can be used [173], but it is restricted to pattern only small areas [174]. For larger area production, nanoimprint or electron beam lithographies can be used to create patterns, on which an oxide nanostructure can be fabricated by low-temperature deposition methods. Unfortunately, the use of vapor deposition techniques is restricted because high temperatures are usually required [175, 176, 177].

As an alternative, ferroelectric nanostructures were straightforwardly grown through heat-resistant stencil masks as nanoporous anodic aluminum oxide [178, 179] or SiN, with deposition temperatures of 650 and 600°C, respectively [180]. In addition to these

top-down approaches, self-organized growth of nanostructures is the alternative cost-effective bottom-up approach to create nanostructures ordered over macroscopic areas. Indeed, self-organized growth of nanostructures has been achieved with different types of materials: organics [181], metals [182, 183], semiconductors [184] and oxides [185]. Bachelet et al. [186] reported a method to fabricate functional oxide nanostructures ordered that exploits the presence of two chemical terminations, TiO_2 and SRO, in the widely used $SrTiO_3(001)$ surfaces. Taking advantage of the self-organization of chemical terminations and of the termination-dependent nucleation of complex oxides, they have shown a simple procedure to obtain 1D ordered functional nanostructures. The cubic perovskite $SrTiO_3$ viewed in the $\langle 001 \rangle$ directions is made up from a stack of alternating neutral TiO_2 and SrO layers (spaced out half of one unit cell, i.e., (0.3905/2) nm). It is known that both terminations are randomly present on as-received substrates, and that SrO surface segregation can appear under annealing at high temperature and oxidizing conditions.

Controlling self-assembly of the SrO and TiO_2 chemical terminations, the single-crystals exhibit well-defined local chemical reactivity. This approach has been very recently expanded to other ABO_3 single-crystals, namely DyScO3 (DSO)[186, 12, 187]. Nanostructured $SrTiO_3$ (STO) and DSO substrates have been used as templates for instance to deposit $SrRuO_3$ (SRO) selectively on the BO_2termination [188]. The lattice parameters of STO, DSO, and SRO are similar favouring two-dimensional (2D) selective growth resulting in the formation of nanostripes. The strategy is addressed to increase the overall interfacial energy, ideally to promote three-dimensional (3D) selective growth of nanodots rather than the reported nanostripes. Progress in this direction requires the development of self-patterned substrates, as shown before for STO and DSO. $La_{0.18}Sr_{0.82}Al_{0.59}Ta_{0.41}O_3$ (LSAT), with cubic perovskite ABO_3 structure of smaller lattice parameter than STO and DSO and larger lattice mismatch with SRO (around 1.5%), appears to be a convenient candidate.

6.2   Background

Due to the miniaturization of the relevant electronic devices, investigations on electronic properties and structure of ABO_3 perovskite thin films are an object of

intense interest. The cubic perovskite oxides have three low-index surfaces (001), (110), and (111) and according to the classification given by Tasker (1979), only the (001) surface of perovskite crystals corresponds to the stable surface, since it exhibits no dipole moment perpendicular to the surface because of neutral cumulative charge in each layer, AO and BO_2, parallel to the surface. Perovskite-type ferroelectrics are generally denoted by ABO_3, where A is a mono or divalent cation represented by an alkali or rare-earth element, and B is correspondingly a penta or tetravalent cation of the transition metal series. The classic examples are $KNbO_3$ and $BaTiO_3$. The perovskites containing trivalent cations, i.e. $LaMnO_3$, are interesting due to the colossal magnetoresistance effect which is associated with a ferromagnetic-to-paramagnetic phase transition [189], and by presence of mixed ionic-electronic conductivity which makes them very attractive for use as cathodes in solid oxide fuel cells.

The STO(001) perovskite surfaces are quite stable at room temperature. The STO (100) surface structure and the electronic states of SrO and TiO_2-terminated STO haven been analyzed by means of Low Energy Electron Diffraction (LEED) by Bickel et al. [190] and Hikita et al. [191] by means of Reflection High Energy Electron Diffraction (RHEED), X-ray Photoelectron Spectroscopy (XPS) and Ultraviolet Photoelectron Spectroscopy (UPS). The surface relaxation and rumpling of TiO_2-terminated STO(001) surface have been explored by Ikeda et al. [192] by means of Medium Energy Ion Scattering (MEIS) and Charlton et al. [193] published results of examination of STO structure with both SrO and TiO_2 terminations by means of Surface X-ray Diffraction (SXRD). Other experimental studies on STO(001) have been obtained by van der Heide et al. [194] (XPS, LEED, Time-Of-Flight Scattering and Recoiling Spectrometry), and by Maus-Friedrichs et al. [195] (UPS and Metastable Impact Electron Spectroscopy (MIES)).

6.3 Morphological Studies on STO (001) Surfaces

STO has a ABO_3 perovskite structure, having either A (SrO) or B (TiO_2) terminating planes in the (001) direction (see Figure 6.1 (a)). As-received STO(001) substrates are flat with both Sr and TiO_2 chemical terminations random distributed on the surface. Due to the substrate cutting and mechanical polishing process afterwards the atomic

steps on the surface are not easily visible. However, under annealing an as-received STO (001) substrate, large terraces can be present with the average width limited only by the miscut angle, as shown the cartoon in (b).
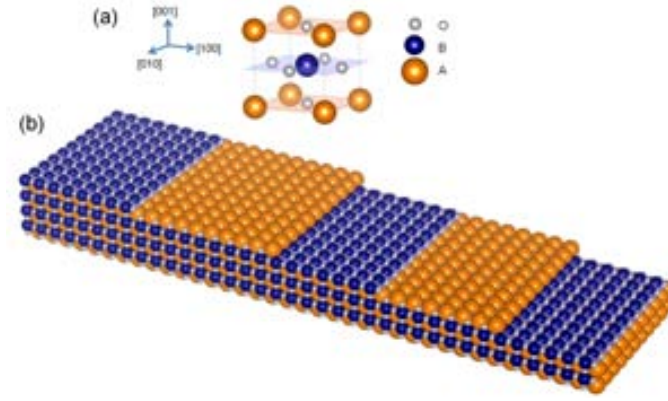
Figure 6.1. Space-filling model of $SrTiO_3(001)$ showing (a) crystallographic directions, unit cell with dimensions 3.905×3.095 $Å^2$ oxygen O and cations (A: Sr, Ba and B: Ti). (b) Sketch of SrO and TiO_2 terminated surfaces of STO(001).

6.3.1   Spatial Localization of Chemical Terminations STO(001)

The morphology of $SrTiO_3(001)$ surfaces can be observed in the amplitude modulation atomic force microscopy (AM-AFM) images, as shown in Figure 6.2. Left panels are topographic images, right panels are the corresponding phase-contrast images and central panels are the height profiles measured along the indicated lines on the corresponding topographic images. In the topographic image of the as-received substrate (a), distinguishable steps and terraces can be observed having very irregular step-edges. The height profile shown in the central panel of (a) reveals the existence of one unit-cell (u.c.) steps to which a fluctuating signal of amplitude larger than the level of noise is superimposed. This likely reflects the coexistence of random distribution of TiO_2 and SrO terminations that coexist in untreated substrates.

The effect of high-temperature annealing on the surface nanostructure of as-received substrates can be appreciated in (b), where the AFM images taken after thermal treatment under air (2 hours, 1100°C) of the very same crystal are shown.
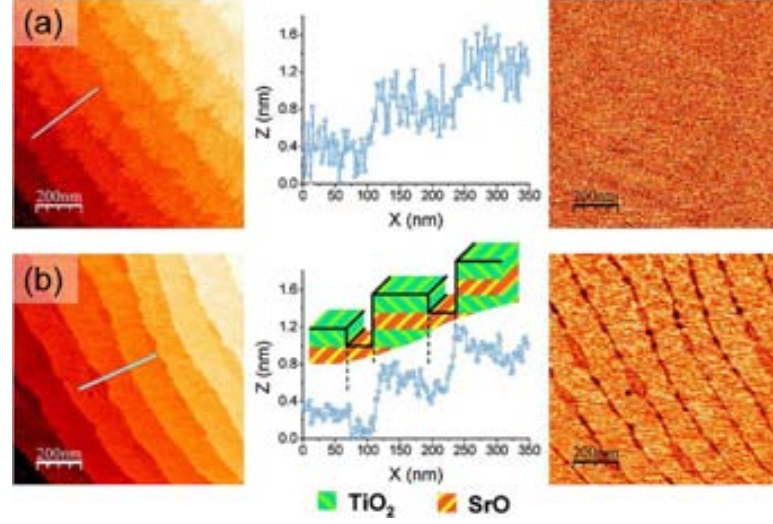
Figure 6.2. AM-AFM topographic (left panels) and simultaneous phase-contrast (right panels) images of (a) as-received and (b) (1100°C, 2 hours)-air-annealed $SrTiO_3(001)$ substrates. Central panels show the corresponding topographic profiles. A sketch of the deduced surface nanostructure has been placed correspondingly above the topographic profile. Taken from [186].

Inspection of the topographic image reveals that high-temperature annealing leads to a great smoothing of the virgin surface (a) with formation of smoother step-edges and flatter terraces (rms = 0.18 nm). However, detailed examination shows some darker (lower height) regions aligned along ascending step-edges. Indeed, the corresponding height profile (central panel) shows the existence of low-lying trenches adjacent to step-edges, up to ≈40 nm wide and depressed by $\frac{1}{2}$ u.c. below the neighboring descending terrace, sketch in (b) (central panel). Because of the alternating composition of $\frac{1}{2}$ u.c. stacked layers in $SrTiO_3(001)$, the $\frac{1}{2}$ u.c. height difference between exposed regions points to a possible difference in their chemical termination. This fact is verified by the corresponding phase lag image (right panel), which clearly shows a strong contrast at the trenches. Provided the phase shift signal in the amplitude modulation AFM operation mode changes with variation in the dissipated energy on different materials, the contrast between surface regions reveals their different nature.
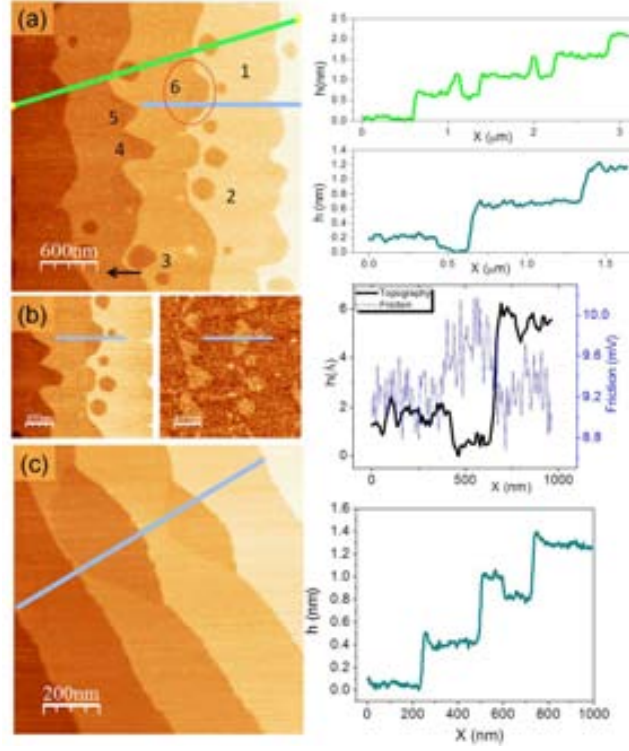
Figure 6.3. Topographic and friction data for the incipient state of the bi-chemical termination nanostructuring of a STO substrate thermally treated at $\approx 1100°C$ for 30 minutes (a, b) and for 2 hours (c). The number labelling in (a) is used to describe the dynamics of the vacancy islands until formation of SrO-terminated patches at the edges of steps separating TiO_2 terraces. Line profile panels taken in (a) cross different surface features (terraces, steps and vacancy islands), number 6 in the gray profile serve as reference to locate one complete leaf shaped structure ≈ 0.2 nm deep circled in (a), which is hardly seen in the topographic image due to a total vertical scale of 3 nm. A topographic profile as indicated in (b) is shown with the corresponding friction profile calculated as $\frac{1}{2}[FL(f) - FL(b)]$ from the profiles in the lateral force forward and backward images (not shown).

6.3.1.1   Nanostructuring the STO (001) Substrate

Figure 6.3 (a) shows an incipient state of the self-assembly of the chemical terminations. The expected stepped surface, i.e. flat TiO_2 terraces separated by ≈ 0.4 nm high steps (one u.c. in height) do present other remarkable surface features such as meandering step-edges and some rounded holes in the flat terraces (a, b). As-received STO substrates consist of terraces differing by 1 u.c. in height with disordered steps

and present coexistence of the two terminations (SrO and TiO_2), which differ by $\frac{1}{2}$ u.c. Therefore, the observed holes might originate from coalescence of much smaller ones pre-existing in the as-received substrates surface, which would not be visible because of the limited lateral resolution of SFM . However, their presence can be inferred from a substantial surface roughness on the terraces of untreated samples. As can be seen, the holes have different diameters (from tens of nm to a few hundred nm), are located in the terraces at diverse distances from the descending step edges but, remarkably, are all 1.5 u.c. ($\approx$0.6 nm) deep. Since SrO termination is a minority part of the (001) surface of untreated $SrTiO_3$ crystals, [196] these 1.5 u.c. deep holes should be vacancy islands with the appropriate depth to exhibit a SrO termination. This idea is further supported by the friction force measurements (right friction map, b) which are in agreement with previous assignment of the termination chemistry.

Holes of different sizes are the result of coalescence of smaller vacancy islands. Dynamics of the vacancy islands diffusion can be better appreciated by comparing the size and position of the holes. In (a, b) some holes have been labelled (from 1 to 6) at progressively shorter distances from the step edges. Thus, several stages of the vacancy islands diffusion to these locations can be seen as frozen frames of a time resolved surface evolution. Once a specific vacancy island is close enough to the step edge, the resulting neck is subsequently narrowed (3) until it is broken to minimize the island perimeter plus step border (4, 5). At this stage, the total ledge relaxation gives rise to leaf-shaped structures (6). In the topographic image (c), these structures have a $\frac{1}{2}$ u.c. and 1.5 u.c. depth with respect to the lower and upper terrace levels. All line profiles are consistent with the dynamical picture outlined above in which initially 1.5 u.c. deep holes formed at a given terrace, migrate to the descending step edges and are at the origin of SrO terminated regions ($\frac{1}{2}$ u.c. in depth) confined between terraces.

Resulting from this diffusion of holes which expose the SrO termination, one expects that if the surface treatment is prolonged, these leaf structures will still evolve and eventually give rise to the formation of SrO trenches, $\frac{1}{2}$ u.c deep with respect the lower terrace level. In fact, after longer annealing (2 hours) at the same temperature (1100 °C), step edges smoothen and the $\frac{1}{2}$ u.c. low-lying regions coalesce to form well-defined SrO-terminated regions running along the lower step edges in between TiO_2-terminated

terraces (c).

The mechanism of vacancy islands coalescence detailed above and observed in real time for metallic surfaces,[197, 198] has also been proposed to describe the dynamics of similar circular holes observed in low miss-cut STO substrates after chemical etching and annealing at 950 °C aiming to get single TiO_2 termination. However, in that case, the observed holes were only 1 u.c. deep as expected from the single terminated TiO_2 surface used in those experiments, i.e. the holes exhibited the same TiO_2 termination as the surface terraces [199].

6.3.1.2 LSMO and BTO//LSMO on Treated STO(001) Substrate

Replication has been observed by growing LSMO on (001)STO substrates with self-ordered AO and BO_2 terminations (see Figure 6.4). Few monolayers of LSMO were deposited subsequently by LBL as monitored by RHEED (a) on a (SrO/TiO_2)-patterned STO substrate prepared by thermal annealing at 1300°C for 4 hours in air. The oscillations are proof of layer-by-layer growth of the ultrathin LSMO film on STO (LSMO//STO). The resulting surface (b) shows terraces and $\approx(n + \frac{1}{2})$ u.c high steps (c). Two kinds of terraces can be recognized: some (labeled A) have rounded edges, and others (labeled B) have straight edges and 90°kinks (signaled by arrows). These distinct ledge shapes are similar to those ascribed to SrO- and TiO_2-terminated terraces, respectively, of treated STO substrates. The height differences between terraces (c) agree with their distinct chemical termination, indicating that growth of LSMO occurs on STO, as on LSAT, by successive stacking of complete perovskite unit cell layers whatever the starting interface is (AO or BO_2). The resulting topmost surface of LSMO is formed by regions of $(La_{2/3}Sr_{1/3})$- O≡ A´O and $MnO_2 \equiv B´O_2$ composition grown on the corresponding self-ordered $TiO_2 \equiv BO_2$ and SrO≡ AO terminations of the STO substrate. Outstandingly, the patterned termination phenomenon fostered by the LBL growth propagates not only through the first deposited film (LSMO) but even throughout ulterior LBL growth of a second heteroepitaxial layer, here chosen to be $BaTiO_3$. Image (d) shows the RHEED intensity oscillations corresponding to the growth of 4 ML of BTO on the chemically patterned surface of the LSMO film described above. The resulting BTO surface (e) consists of terraces and steps preserving
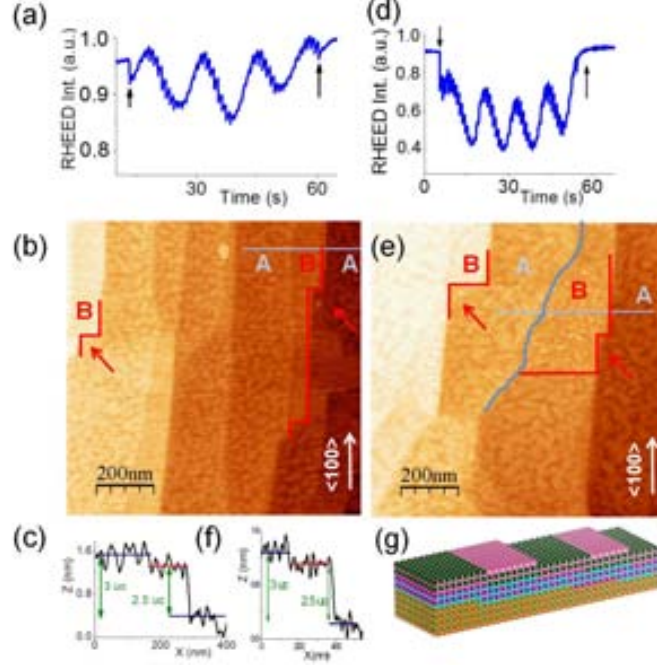
Figure 6.4. (a) RHEED specular oscillations during deposition of LSMO on a chemical termination patterned STO substrate with SrO (AO) and TiO_2 (BO_2) terminated regions. The black arrows indicate start and stop times of deposition. (d) RHEED oscillations during deposition of BTO on the LSMO//STO surface (BTO//LSMO//STO). (b) and (e) are the topographic images of the LSMO//STO and BTO//LSMO//STO surfaces, respectively. The wavy lined ledge and the different surface roughness can be used to spatially locate A regions (e). The different composition of terraces is also supported by the relief profiles in (c) and (f). The measured $n + \frac{1}{2}$ u.c height of descending steps corresponds to that expected for alternate planes of these perovskites (i.e. AO and BO_2). The sketch in (g) illustrates the BTO//LSMO//STO structure with patterned surface and interfaces. Taken from [200].

the morphological details (as highlighted by wavy and straight lines with right angles to guide the eye) of the chemical patterns of the buried LSMO and STO surfaces. This preservation allows spatially locating the two types of chemical terminations (BaO≡ A´´O and $TiO_2 \equiv B´´O_2$) for the BTO surface layer. In full agreement, the height profile in (f) confirms the presence of terraces and steps $\propto \frac{1}{2}$ u.c height. This result means that the $SrO\text{-}TiO_2$ surface termination pattern of the STO substrate replicates throughout perovskite layers, that is, at the top surface of LSMO//STO and

up to the BTO film surface of BTO//LSMO//STO by forming in all cases A´´O - B´´O_2 modulated surfaces, as sketched in (g). In both (b and e), two kinds of terraces presenting wavy or straight edges are marked as A or B to signal that they correspond to chemical terminations AO and BO_2 of the respective perovskite ultrathin film top layer. Some steps of a couple of the smoother B regions have been lined to illustrate that they lie parallel to the crystallographic ⟨100⟩ directions.

6.3.2 Tribological Response of the STO(001) Surface
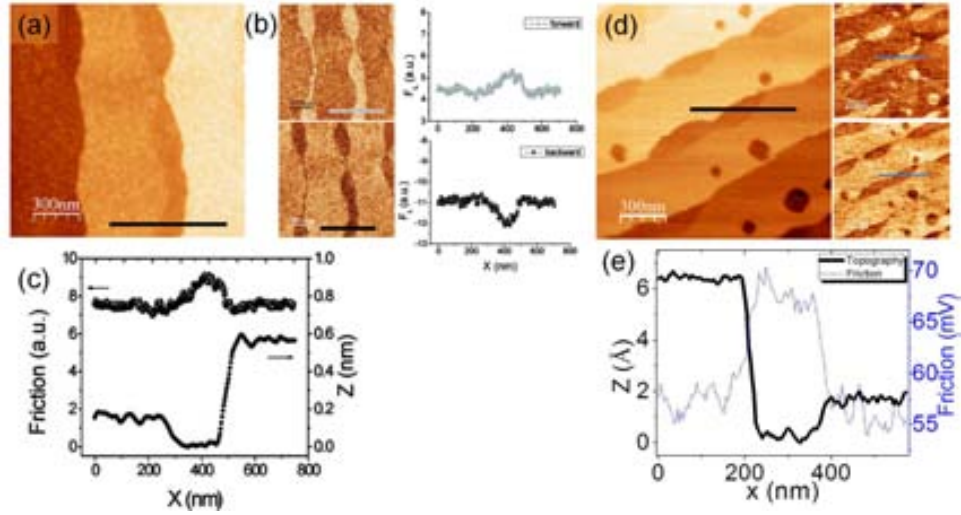
Figure 6.5. Topographic and friction data simultaneously acquired on 1100°C-annealed $SrTiO_3$(001) substrate are shown. (a) Topographic image; (b) lateral force images and the corresponding profiles, forward (top) and backward (down); (c) resulting friction force shown with the topographic profile. (d) Topographic and lateral forces images with the simultaneous profiles (e) showing the friction value increased on the SrO termination. The trenches (brighter regions in the forward scan) correspond to the higher-friction SrO regions. Adapted from [186].

To further verify the different chemical nature of flat terraces and trenches, we performed friction force microscopy maps (FFM). To quantify the difference between friction responses, we acquired simultaneous topographic and lateral force (forward and backward) images in low-humidity conditions (2% RH in a N_2 flux). In Figure 6.5 (a), the incipient formation of trenches along step-edges is well visible, with smooth

step-edges and flat terraces separated by 1/2 u.c. deep low-lying regions. The lateral force (F_L) images shown in (b) evidence a clear friction contrast between the flat terraces and the trenches, confirming differences in chemical-termination, in agreement with the AM-AFM phase-contrast images. The calculated resulting friction force is displayed with the corresponding height profile in (c). The friction is quantified to be about 15% higher at the trenches (brighter regions in the forward images) than at the terraces. This percentage reached values close to (35-40)% under higher humidity conditions, as shown (d, e), likely due to an enhanced water adsorption [201] on the more hydrophilic SrO termination.

6.3.3 Spatial Localization of Chemical Terminations LSAT

Treated LSAT(001) single-crystals can be used as nano-templates for the fabrication of functional 1D-arrays by exploiting the different properties of the AO and BO_2 stripes to selectively grow an active material on top. Here, we push further the capabilities of the self-organized AO-BO_2 terminated surfaces as templates by tuning the growth mechanisms to induce distinct oxide nanostructure both by lateral confinement and by enhanced epitaxial strain. The growth of an oxide film (A´B´O_3) on a substrate (ABO$_3$) with separated (AO/BO_2) chemical terminations will depend critically on the B´O_2/AO and A´O/BO_2 interfacial energies (γ) as well as on the difference between them. If γ(A´O/BO_2) and γ(B´O_2/AO) differ appreciably, selective adsorption and growth on one termination will be favored; the lower value of γ determining if the growth mechanism occurring in the confined region is 2D or 3D to form atomically flat stripes or dots, respectively.

Figure 6.6 shows topography (left panel) and phase images (right panel) of a LSAT single-crystal ($\approx$0.13°-miscut) after 2 hours of thermal treatment at different temperatures (1100°C, 1200°C and 1300°C). Step-and-terrace morphology can be distinguished at the surface after the treatment at 1100°C (a); this surface morphology is similar to that obtained with similar thermal treatments reported elsewhere. One can appreciate the existence of highly kinked steps, 2D islands, and vacancy islands. Although accurate measurements of step heights are difficult in these surfaces, with height variations within each terrace of $\pm$1Å (see the topographic profile), the step height between adjoining terraces is $\approx$4Å , similar to previous observations. The phase-shift image does not show
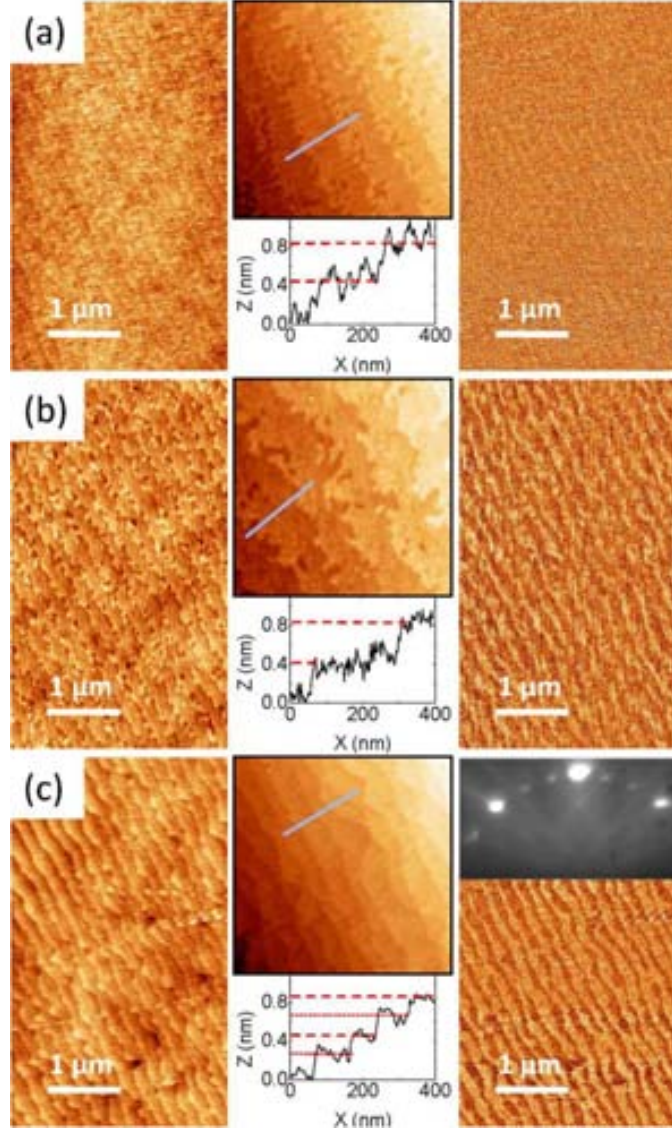
Figure 6.6. AFM topographic images (left panel) and the corresponding phase-shift images (right panel) after 2 hours treatments of a LSAT single-crystal at (a) 1100°C, (b) 1200°C, and (c) 1300°C. The same wafer was cut in three pieces and each piece suffered one of the single-treatments. The insets (center panel) are closer views (1×1 μm^2) of the topography with the corresponding height profiles. The additional inset in (c) is a RHEED pattern taken along the [100] direction of the 1300°C-treated substrate. Taken from [202].

appreciable contrast, suggesting that each terrace is formed by mixed AO and BO_2 chemical terminations, randomly distributed in small areas and thus not resolved within the standard lateral resolution of AFM. Interestingly, thermal treatment at a higher temperature (1200°C) leads to a clear contrast in the phase-shift image (b), right panel, revealing chemical separation by self-assembly of each termination, AO, and BO_2.

This chemical separation is accompanied by an increase in the local terrace width, which makes clearer the step-and-terrace morphology (b), left panel. At this temperature, an enhanced surface diffusion permits reducing the total step length: the edge meandering presents a longer wave-length and the 2D-vacancy islands areal density is lower by coalescence and healing at the step edges. After treatment at even higher temperature (1300°C), the surface reorganization leads to a neat step-and-terrace morphology with smooth edges, without islands, and with $\frac{1}{2}$ u.c steps separating regions that present sharp contrast in the phase-shift image (c). These observations indicate a good lateral ordering of the chemical terminations with a terrace-width period. The topography and the different chemical nature of the distinct terraces of treated LSAT crystals were further verified by FFM with simultaneous acquisition of topographic and lateral force images.

6.3.3.1   SRO on Treated LSAT Substrate

Figure 6.7 shows SFM images of SRO deposited on a treated ≈0.12°-miscut LSAT substrate exhibiting a good stripe-like chemical ordering (a). Images (b, c) show that effectively 3D-growth occurred and SRO dots nucleated exclusively on one of the terminations (simple topographic inspection does not permit determining on which one). Selective growth of SRO had been observed on the BO_2 termination of STO [186, 187] and DSO [188], but in both cases, confined growth occurred 2D resulting in quasi-1D nanostructures. In the case reported here, the 3D growth of SRO signals higher interfacial energies of SRO/ LSAT(001) (might be favored by the higher lattice mismatch: -1.5%, compared to -0.6% with STO and ≈0.03% with DSO).

The ordered 1D-arrays of SRO dots formed because the selective 3D-growth was guided by the self-ordered chemical- terminations. Remarkably, the intra-line profile of the self-correlation function indicates also certain order of the dots along the stripe, as attests the broad but evident maxima. The corresponding dot-dot mean distance
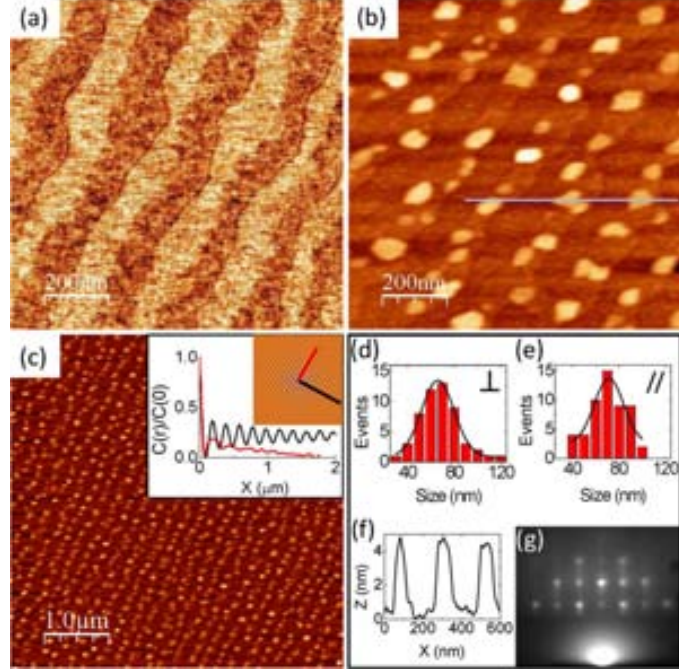
Figure 6.7. (a) AFM phase shift image of a LSAT single crystal treated at 1300°C for 2 hours. AFM topographic images (b) and (c) after growth of SRO. The inset in (c) is the self correlation of the topographic image with the corresponding profiles taken across (inter line correlation) and along (intra line correlation) the substrate steps direction. (d) and (e) Histograms of lateral sizes of the dots shown in (b), in the direction perpendicular and parallel to the steps, respectively. (f) Height profile along the line marked in (b). (g) RHEED pattern after SRO growth taken along the [100] direction. Taken from [202].

along the stripes is ≈180 nm. The maximum lateral size of the dots is dictated by lateral confinement, and thus, the array distribution mimics the chemical order of the underlying treated LSAT (see inset in (c)). The lateral sizes are close to 65±15 nm perpendicularly to the steps and 71±12 nm along the steps (d) and (e), respectively. The mean height is 3±1 nm (f). The resolution of the present experiments cannot exclude the possible existence of an extremely thin (1-2 uc thick) SRO wetting layer. Remarkably, the SRO dots are epitaxial with LSAT, as shown by the diffraction spots in the RHEED pattern taken along the in-plane [100] direction (g).

6.3.3.2   LSMO on Treated LSAT Substrate

Figure 6.8 shows the topographic image of a (001)LSAT single crystal after a thermal treatment at 1300°C for 2 hours. The surface consists of a step-and-terrace morphology with height differences of $\frac{1}{2}$ u.c between alternating atomically flat terraces (see height profile in (c)). This surface corresponds to a nanoscale self-patterning of AO and BO_2 terminations; according to Ohnishi et al.,[203] the majority surface termination is of BO_2 type. Lateral force imaging (b) shows a strong contrast between adjacent terraces, confirming their different chemical nature: AO and BO_2. The reflection high energy electron diffraction (RHEED) pattern of this surface is typical of an atomically flat single-crystal surface (inset in (a)). As inferred from these data, the thermally treated LSAT surface is sketched in (d) as a bimodal landscape.

The described surface constitutes the substrate where few ML of LSMO were grown by RHEED-assisted pulsed-laser deposition (PLD) expecting a layer-by-layer (LBL) growth. The features in the RHEED specular spot intensity (e) before the first maximum reflects differences on the first stages of growth on each substrate termination, whereas the regularity of subsequent oscillations and the postgrowth RHEED pattern (inset in (f)) are signatures of a LBL growth, in agreement with the presence of steps and terraces at the film surface (f). The step-height differences (h) are $\approx(n + \frac{1}{2})$ u.c (here, n = 0 or 1), indicating that an extra layer has developed on one of every two terraces; this is in accordance with an initially preferential growth on one surface termination before a steady LBL growth mode sets in. This description also agrees with the phase-shift contrast between neighboring terraces observed in amplitude modulated AFM (AM-AFM) (g) that confirms their distinct chemical termination, namely $(La_{2/3}Sr_{1/3})O$ and MnO_2, as illustrated in the sketch (i). The described topographic and chemical features (checked on other LSMO//LSAT samples) indicate that the terminations of the LSMO (A´O and B´O_2) replicate the spatial distribution of the LSAT terminations underneath (AO and BO_2, respectively).

6.4   Functional Properties of Thin Films Oxides on LSAT and STO

Once obtained the morphologies of the treated LSAT and STO substrates, we performed KPFM and C-AFM measurements on the terminations AO and BO_2 as
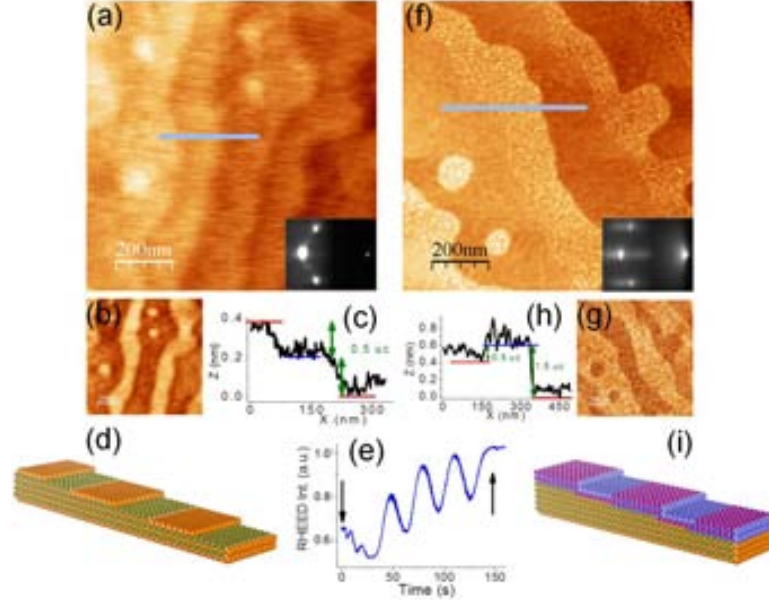
Figure 6.8. Topography of the treated LSAT substrate obtained in contact mode (a), and RHEED pattern (inset), lateral force image (b) and topographic profile (c) along the line in (a). The RHEED specular spot intensity oscillations typical of a layer-by-layer (LBL) growth mode in (e) correspond to the deposition of 4-5 ML of LSMO on the substrate shown in (a). Topography of the deposited LSMO film obtained in dynamic mode (f) with RHEED pattern of the film in the inset, phase-shift image (g) and topographic profile (h) along the line in (f). The schematics at the bottom panels illustrate the two chemical terminations (AO, BO_2 and A´O, B´O_2) for each surface: (d) LSAT substrate and (i) LSMO//LSAT film. Note the $n + \frac{1}{2}$ u.c (n = 0 and 1) differences in height between adjacent descending terraces in each case. Taken from [200].

well as thin films oxides grown on these substrates.

6.4.1   LSAT substrates

The well differentiated AO and BO_2 regions of LSAT in the topographic image (see Figure 6.9) (a) give rise to a noisy but modulated contrast in SP (b), more clearly seen in the corresponding line profile (c), which permits saying that on average SP(AO)-SP(BO_2)≈65mV. Visual inspection of the topographic image of the LSMO//LSAT surface (d) allows identifying higher stripes along the step edges. The well-defined modulated contrast in (e) indicates that SP(A´O) - SP(B´O_2)≈35mV (f). In Figure

Figure 6.9. Top panels: topographic image (a) and corresponding KPFM or contact potential difference, SP, map (b) of the treated LSAT substrate exhibiting AO (A) and BO_2 (B) terminated terraces. An SP profile along the line in (b) crossing AO and BO_2 terraces is presented in (c). The AO-terminated region delimited by hand drawn lines in the images is marked also in (c). Bottom panels: topographic image (d) and corresponding SP map (e) of the LSMO ultrathin film on LSAT (LSMO//LSAT) showing a clear modulation replica of the substrate characteristics. As before, one AO-terminated region is marked in the images and SP profile (f). Averaged hill to valley values are $\approx$65mV (c) and $\approx$35mV (f). Taken from [200].

(a-e), one AO(A´O) region has been delimited by fine hand-drawn lines and marked at the SP profiles to help visualizing the data.

Once the correspondence between terminations and their surface potential differences is established, the local conducting character of the thin LSMO film surface was investigated at the very same surface locations (see Figure 6.10), as confirmed with the help of the dashed rectangles in (a) and (c) and some fine details (signaled by arrows in all images). The current image (d) is a two levels map that reproduces the SP pattern (b), such that those regions with higher(lower) conductance correspond to regions of higher(lower) SP. We note that while the chemical differences may be at the origin of the different SP values, the fact of measuring nonhomogeneous conductivity is a striking observation provided the lateral continuity and conducting character of the LSMO film, which homogeneously covers the insulating substrate. Similar behavior has been found for a range of LSMO thicknesses between 2 and 10 ML.
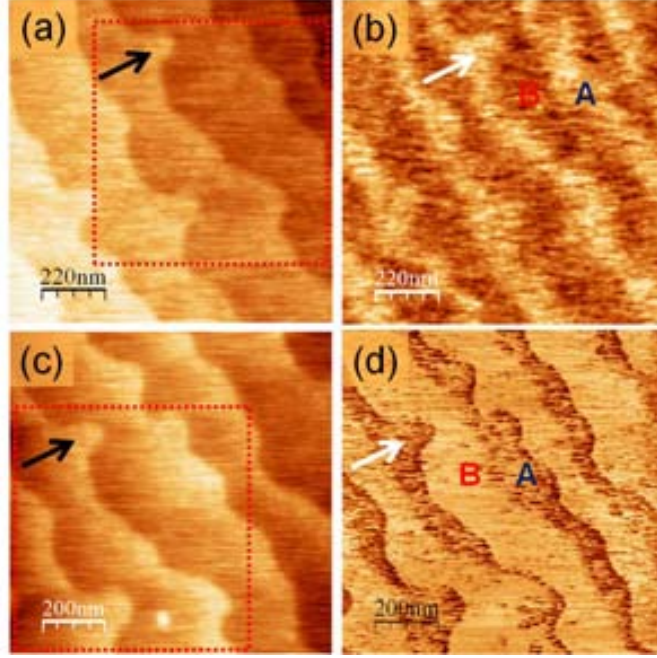
Figure 6.10. Topography (a, c) and the corresponding SP (b) and CSFM (taken at -800mV) (d) maps of the LSMO//LSAT surface. Total color range equals absolute values of 70mV (b) and 300pA (d). The dash lined areas and arrows illustrate that the same surface location was recorded in both cases. As shown in the (b) and (d) regions, A´O (A) terminated exhibit a higher (lower) surface potential (work function) than regions B´O$_2$ (B) terminated, where lower current values are detected. Taken from [200].

6.4.2 STO(001) Substrates

Comparison of the topographic image of the bare STO (see Figure 6.11 (a)) with the corresponding SP map and profile (b, c) shows that the SrO regions (bright areas) have higher SP than the surrounding TiO$_2$ regions; this result implies SP(AO)>SP(BO$_2$), as observed for LSAT. Statistical estimation including data from different samples [12] gives a difference of SP(SrO) - SP(TiO$_2$)≈45 mV (c). In the topographic image of the LSMO//STO (d), approximately equally spaced and nearly parallel distinct terraces separated by ≈ $\frac{1}{2}$ u.c steps are visible (see profile in (g)), reflecting the existence of A´O and B´O$_2$ stripes. The developed quasi-periodic pattern is also clearly visible in the CSFM and the SP maps (e, h), respectively. Line scans across each image (f, i) have

been connected with vertical arrows to indicate the spatial correspondence. Maxima (minima) values in surface potential are accompanied by maxima (minima) values in conductance. The surface potential difference is SP(A´O) - SP(B´O$_2$)≈30mV about the same that for LSMO//LSAT.
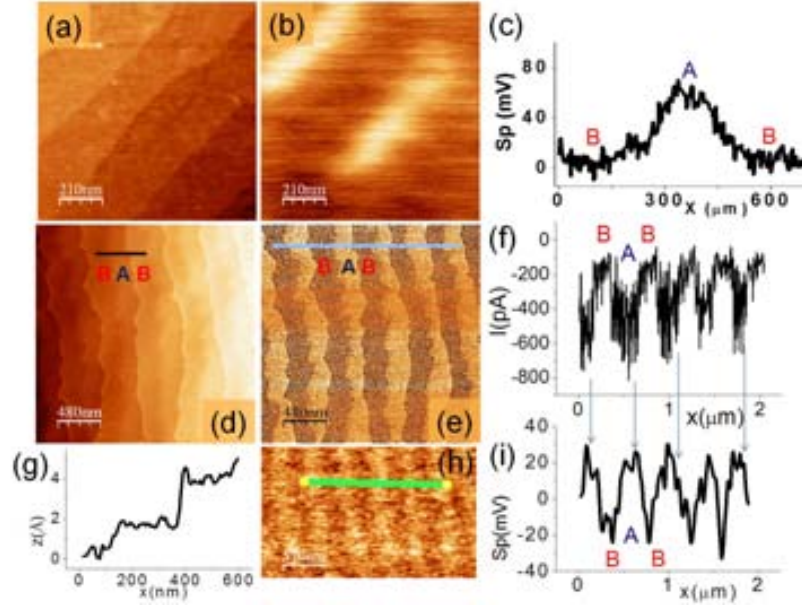
Figure 6.11. Top panels: topographic image (a) and the corresponding SP map (b) of the treated STO substrate exhibiting AO and BO$_2$ terminated terraces, appearing as bright and dark in (b), respectively. A SP profile crossing the different terminations is presented in (c). Bottom panels: topography, current, and SP images (d, e, and h, respectively) and the corresponding line profiles (g, f, and i, respectively). The $\frac{1}{2}$ u.c high steps separating AO and BO$_2$ terraces evidence that they correspond to alternate planes of the perovskite LSMO film. Line scans across SP and CSFM images are connected with vertical arrows to indicate the spatial correspondence between them. Taken from [200].

The 4ML thick BTO film grown on LSMO grown on STO (BTO/LSMO//STO) was characterized (see Figure 6.12). The topographic relief images of two locations (a, e) and their corresponding SP and CSFM maps (b, f), respectively are shown. As already described, the $\frac{1}{2}$ u.c steps at the BTO surface (c) indicate the existence of the BaO and TiO$_2$ terminations. The contrast in the corresponding SP map (b) is about 25mV (d)

with $SP(B''O_2) > SP(A''O)$, slightly smaller in magnitude and opposite in sign to that obtained for the LSMO//STO underneath. Consistent with all data described above, in the conductance map (f) the $B''O_2$ regions have higher conductance. The measured current is extremely low (tens of pA for positive voltages of some volts) due to the fact that the BTO film adds an extra thin insulating barrier to the tip-LSMO junction. It is worth highlighting that higher current is measured on the $B''O_2$ regions of BTO that are stacked with the less conducting regions $B'O_2$ of the free LSMO surface. This indicates that conduction at the surface is determined by the local electrostatic barrier height at the oxide surface but depends on the interfacial BTO/LSMO properties. As a final remark, we note that in all cases, regions of high(low) SP are always regions of high(low) conductance, no matter to which termination they correspond, indicating the direct relation between these magnitudes.

First, we focus on the KPFM contrast (ΔSP) observed at the bare $SrTiO_3$ surface. The TiO_2 and SrO terminations of STO are nonpolar, and therefore, the observed SP corrugation is expected to be due to intrinsic properties of the oxide. In particular, each termination are characterized by distinct electronic and/or ionic relaxation patterns, which will produce (via changes in the surface dipole) a lateral modulation of the local IP. First-principles calculations indeed show a marked termination-dependent difference in the IP: $IP(TiO_2) = 6.41$ eV and $IP(SrO) = 4.07$ eV. However, the experimental observation of $\Delta SP \approx 45mV$ is by far lower than the calculated $\Delta IP \approx 2.34eV$.

To account for this discrepancy, one can think of different possible scenarios, which we can group into two main categories: (i) the surface terminations themselves physically differ from the calculated models; (ii) the measuring technique is inadequate to quantify the ionization potential differences in these nanostructured surfaces. Within (i), we note that even though all measurements are performed at low RH conditions, the sample is brought through air from the preparation chamber to the SFM equipment and, therefore, it cannot be excluded that its surface is covered with adsorbates, in particular with H_2O. The adsorption of one full single monolayer of H_2O could reduce the predicted ΔIP down to 1.44 eV [204], still far from the experimentally measured ΔSP. It is likely that other species, such as ionized adsorbates, might produce more drastic effects. Additional factors altering the local IP include surface reconstructions
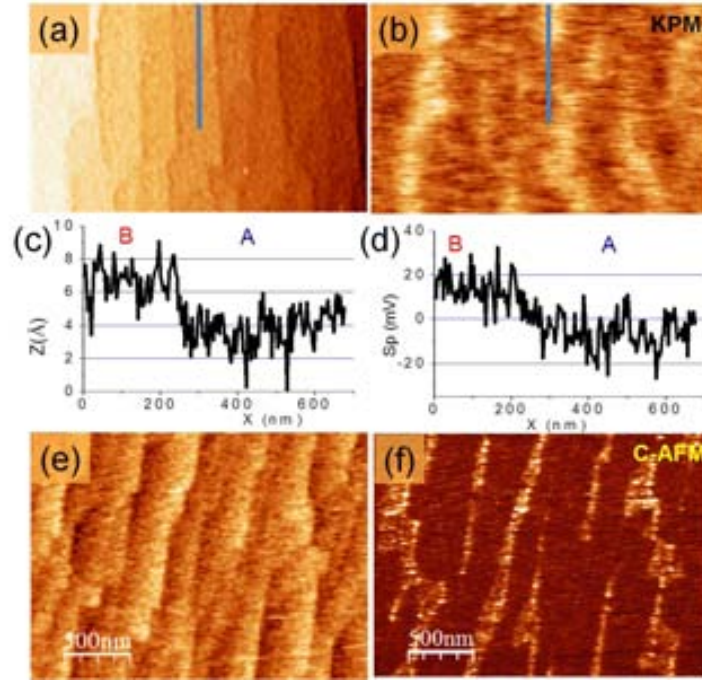
Figure 6.12. Topographic images (a, e) with their corresponding simultaneously measured surface potential (b) and current (f) maps for two locations of the same surface of the ultrathin BTO//LSMO//STO surface. Line profiles obtained along the lines marked in (a) and (b) are depicted in panels (c) and (d) to illustrate the correspondence between surface termination (A´´O or B´´O_2) with a lower or higher surface potential value. The same correspondence made for the CSFM data (taken at 4.5V) indicates that the current measured on A´´O is rather small but still larger than that in the B terminated regions. Total color scales correspond to absolute values of 25mV (b) and 55pA (f).

and/or defects such as oxygen vacancies. Concerning possibility (ii), we note that the regions of AO and BO_2 are about 50-100 nm wide, at the limit of our KPFM lateral resolution. Therefore, a reduced ΔSP might result from the otherwise unavoidable averaging produced by the tip-cantilever ensemble.

6.4.3   Discussion

In the sketches (not scaled) of Figure 6.13, we summarize the SP (a, b), conductance profiles (c), and current-voltage characteristics (d) of the systems studied, (left: LSAT and LSMO on LSAT; center: STO and LSMO on STO; right: STO and BTO/LSMO

on STO).
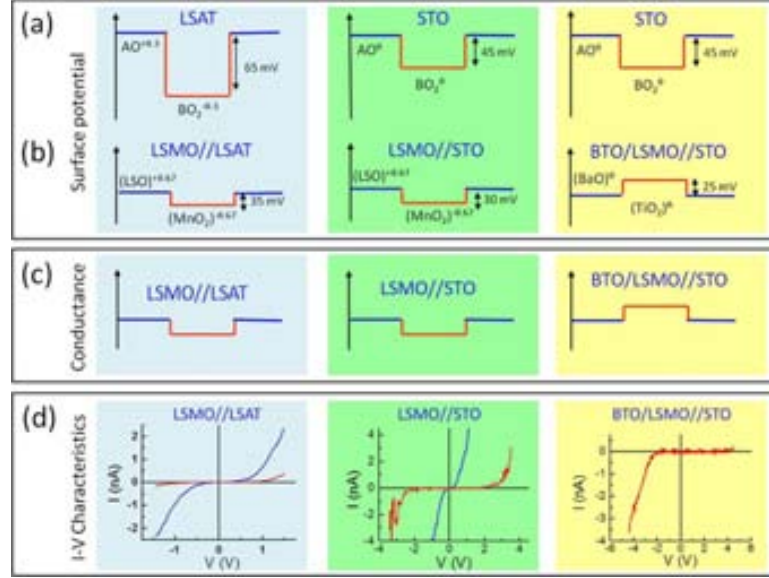
Figure 6.13. Illustrating the results of SP (a, b), conductance profiles (c) and current-voltage (IV) curves on each termination of the corresponding surfaces.

Moving now to the bare LSAT substrates, the most striking observation when analyzing the data is that the ΔSP contrast (a, left) is considerably larger than, but coincides in sign to, that of STO (a, left), that is, SP(A´O) > SP(B´O$_2$). As mentioned before, in clean LSAT, these terminations are polar, and therefore, the larger magnitude of ΔSP could arise from additional ionic and/or electronic compensation mechanisms.

We turn next to the SP profiles of LSMO grown on STO and LSAT sketched in (b, central and left panels), respectively. In both cases, the SP of LSMO films replicates the SP contrast of the corresponding substrate, that is, SP(A´O) > SP(B´O$_2$) for both LSMO//STO and LSMO//LSAT surfaces. The values of ΔSP measured at the LSMO surfaces are quite similar, about 30 and 35 mV, and smaller than ΔSP at the substrates, ΔSP(LSAT)$\approx$65mV and ΔSP(STO)$\approx$45mV. To understand the physical origin of the observed contrast, we invoke again two different extreme scenarios where the LSMO overlayer behaves as (i) a metal or (ii) an insulator. In case (i), the Fermi level of different LSMO regions are aligned, implying that right

below the topmost LSMO surface the electrostatic potential is uniform. Then, the only source of surface potential modulation should originate from the termination-dependent local work function of LSMO, regardless of the underlying substrate. The similar ΔSP measured in LSMO//STO and LSMO//LSAT indeed suggests that this might be a reasonable hypothesis. Conversely, in the scenario (ii), we expect the electronic levels of the LSMO film to align separately to the underlying substrate. In this case, in addition to the termination dependence of the LSMO work function described above, we must also take into account the band offset at the buried LSMO//STO (and LSMO//LSAT) interface.

We now briefly address the conductance profiles of LSMO on STO and LSAT as sketched in (c, center and left panels), respectively. As already commented, in all cases, the conductance profiles mimic the SP modulation of the LSMO film. As higher SP corresponds in our experiments to lower electron barrier height, the higher conductance in those regions is in agreement with expectations. The current-voltage (IV) characteristics measured on each termination (d) of the corresponding LSMO surfaces agree with this local electronic property, which results in lateral modulation.

The SP and conductance profiles at the surface of the BTO/LSMO//STO are sketched in (b, c) right. The persistence of the STO bimodal signature (a, right) up to the free topmost surface of BTO is remarkable. However, the BTO covered surface has a SP profile reversed to those of the bare STO and LSMO//STO surfaces, being SP(BaO) < SP(TiO$_2$). Accordingly, the corresponding conductance profile (c, right) is also reversed. Interestingly, the IV curve obtained on the higher SP region (d, right) does present a nearly perfect n-type rectifying behavior of the new junction. The overall observations deserve deeper investigation out of the scope of the present work, since it may result either from the charge transfer at the newly formed BTO//LSMO interface or from the ferroelectric nature and domain structure of BTO and/or the concomitant charge screening due to adsorbates at the two BTO surface terminations. As a closing remark, we note that the complete consistency of the KPFM and CSFM measurements (which are done in very different operation modes) gives strong support to the experimental procedures and data analysis and gives further evidence of the dramatic impact of interfacial properties via substrate termination design.

6.5 Complex Oxides Functionalized With Organic Molecules

Hybrid materials based on oxide supported organic films are the subject of increasing interest because of the many practical applications they may find in nanotechnology. The control of growth and properties of these hybrid structures, on a length scale down to nanometric dimensions, is one of the major challenges in the field and surface science strategies based on the use of nanostructured substrate surfaces can be employed to initiate and control the growth in a bottom-up fashion. Organic self-assembled monolayers are of particular relevance in a wide variety of fields to improve or modify the characteristics of the materials surfaces. They are, for instance, employed in relatively conventional electromechanical devices as lubricating layers, or used to induce specific interface dipoles upon adsorption, which tune the surface work function in optoelectronic systems. Thus both, the nanotribological properties of the organic films themselves and the surface contact potential modifications they induce on the substrates, are decisive and deserve in depth investigation.

6.5.1 Selective Growth of Stearic Acid on the TiO_2 Termination

The role of chemical surface termination of STO has been observed down to the atomistic level and because titanium dioxide (TiO_2) terminated surfaces are preferred in many applications, obtaining nanostructured surfaces having tailored TiO_2 termination is of enormous interest for further developments. Moreover, besides the appealing properties of the substrates and those of the materials growing on that surface, the capability of confining these properties at the nanoscale in a controlled way, although challenging, is of major technological interest in a variety of fields. Here we will show that STO is a promising substrate because of the flexibility in this type of design.

$SrTiO_3(001)$ single-crystal surfaces have two possible chemical terminations (TiO_2 and SrO) which coexist on as-received substrates. Annealing at relatively high temperature (1000-1200°C) causes atomic surface diffusion. By tuning the annealing conditions (temperature and time), the size and distribution of SrO-terminated areas can be controlled, from nanometer scale patches to highly ordered 1D-structures. The unknown possibility of using these chemically-patterned substrates for selective growth of others materials such as stearic acid is shown.

Stearic acid (n-$C_{17}H_{35}COOH$) was chosen as an adsorbate because the carboxylate function can interact favourably with oxide surfaces as well as the fact that the alkyl chain can lead to ordering of the hydrophobic section (the alkyl chain) of the molecule through van der Waals interactions, a situation that arises in different types of self-assembled monolayers. Furthermore, the dimensions of the molecule make it easy to locate on the surface and to determine its orientation. In addition, since this saturated fatty acid is commonly used as lubricant and is expected to present a conveniently oriented molecular dipole of measurable magnitude this molecule appears suitable to explore changes on the STO surface properties.

We first attempted incubation of the surface in a 2mM solution of the acid in absolute ethanol. Even after standing for long periods of time (up to 25 hours), removal of the sample and washing with ethanol gave only signs of very little non-specific adsorption. This observation indicates that the surface sites of the STO as it is prepared and subsequently handled in air are not sufficiently active to form covalent links with the acid. In an alternative approach, the ethanolic solution of the acid was cast from a pipette onto the freshly prepared nanopatterned STO and the solvent was allowed to evaporate. The surface was then rinsed with absolute ethanol and dried under a N_2 stream.

SFM images of this kind of cast films are presented for different surface coverages (see Figure 6.14) showing that specific adsorption of the acid onto the TiO_2 termination exists. Growth of the first monolayer seemed to inhibit the growth of further organic layers on top and a nearly perfect self-assembled monolayer following the nanostructured chemical pattern of the underlying substrate is formed (a). The casting procedure was tested at different deposition conditions, including sample post-annealing, without noticeable changes.

In very few cases, local excess of stearic acid was found to give rise to slight SrO occupation (b) or even isolated multilayer islands formation (c, d). These crystallite-like structures, 5.3 ± 0.2 nm in height (e), exhibited a top with two levels with extremely well defined inter-plane distance of $\approx1.3\pm0.2$ nm. Stearic acid molecules are ≈2 nm in length and thus the measured heights are consistent with layers consisting of molecules standing up with a tilt angle of about $50°$ with respect to the surface normal. If this
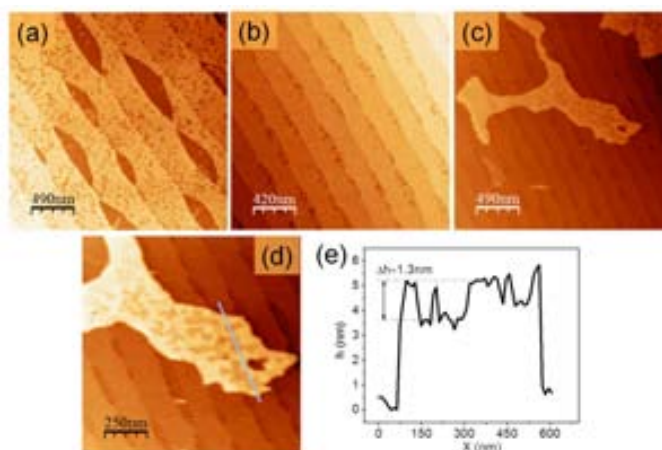
Figure 6.14. Topographic SFM data for three different stearic acid coverages (a, b and c) obtained on three different STO substrates. A magnified region showing a multilayer of stearic acid (d) and a line profile (e) as indicated in (d). The total height (5.3 nm) is a multiple of the difference between the two superior levels (1.3 nm), which coincides with the monolayer thickness.

is the case, the three dimensional islands would consist of 4 molecular layers grown on one monolayer in direct contact with the TiO_2-terminated terraces of the substrate, which could then be considered as a wetting layer. We suggest that these 3D structures resulting from multilayer formation are observed rarely and are non-expected because the CH_3 terminal group of the monolayer surface does not favour vertical growth. On the contrary, the selectively grown single layer shown in (a) was observed to form over the vast majority of the surface and was obtained repeatedly.

This can be seen in Figure 6.15, where a line profile crossing two surface steps and a bare SrO terminated region, allows measurement of the organic layer thickness of 1.2-1.3 nm, which coincides with the inter-plane distance measured in the multilayered islands. This observation further supports molecular self-assembly with stearic acid molecules tilted about 50° with respect to the surface normal. The selective patterning of the SrTiO3(001) surface with these organic molecules could arise from (i) specific adsorbate-surface interaction leading to a more favourable non-covalent interaction with one substrate termination or another, or (ii) selectivity could be driven by general polarity factors, i.e. the polar head group of the organic molecule would assemble in

200
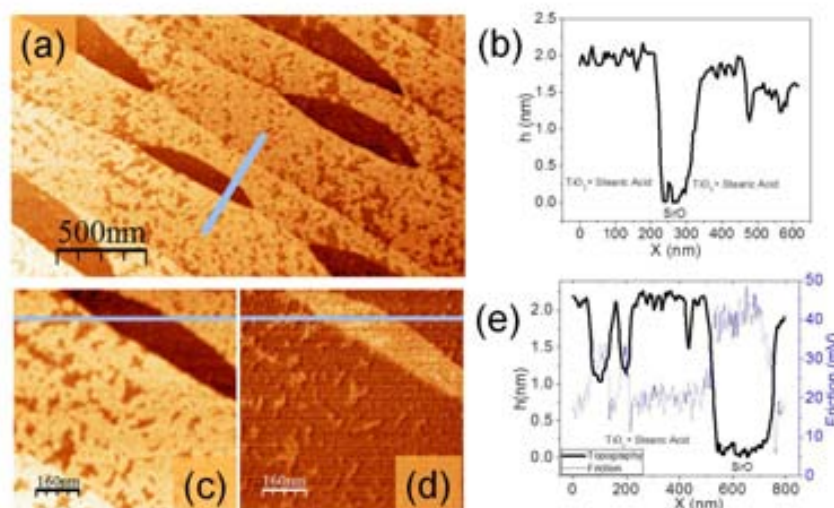
Figure 6.15. (a) Topographic image of stearic acid deposited onto a nanostructured STO substrate, (b) relief profile taken along the line indicated in (a). Topographic (c) and friction (d) images. Topographic profile and the corresponding friction obtained from (c, d) are shown in (e).

the area which is most hydrophilic. Previous results indicate that the SrO areas of the surface are more hydrophilic than the TiO_2 areas, and therefore we rule out option (ii). Rather, based on the chemical states proposed for similarly terminated carboxylic molecules adsorbed on ITO oxide surfaces [205], we hypothesise an (i)-type situation, where the carboxylic acid group forms hydrogen bonds with the TiO_2 in preference to the SrO areas.

In order to know the change in the surface frictional response induced by the organic layer, simultaneous topographic and lateral force (forward and backward) images were acquired for both, the clean as-prepared STO substrate and the same surface after stearic acid deposition. FFM measurements were always performed under low-humidity conditions (RH $\approx$ 2%). Friction plots were calculated from the forward and backward profiles of lateral force images and correlated with the corresponding line profile of the simultaneous topographic image. The difference in frictional response between SrO and TiO_2 terminated regions previous to the organic layer deposition was found to be about $\approx$10%, in accordance to the reported value of 15% for low humidity [186, 12].

6.5 Complex Oxides Functionalized With Organic Molecules

The friction map reveals a clear frictional contrast between the uncovered SrO regions and the surrounding stearic covered TiO_2 terraces (see Figure 6.15 (d)). The friction is quantified to be $\approx 60\%$ lower in the latter, i.e. the resistance to relative motion of the initial TiO_2 has been reduced about 50% after the organic coating. We remark that this percentage could be even larger because of the highly hydrophobic character of the CH_3 terminated organic layer as compared to the hydrophilic character of the SrO regions. Although film exposure to air was minimized (less than a few minutes at RHs larger than 10%) a fine water film cannot be excluded on the exposed SrO surface locations.

The organic layer deposition constitutes a convenient method to change the contact potential difference between the chemically differentiated substrate surface regions, in other words, the local surface potential of the STO substrate is reduced upon adsorption of the stearic acid on the TiO_2 terraces. In order to quantify this effect, we conducted KPFM measurements on two types of surfaces in which SrO nanostructures coexist with either bare or stearic acid covered TiO_2 terraces. The contact potential difference between chemically differentiated regions on the thermally treated STO substrate $\Delta CPD_{STO} = CPD_{SrO}$ - CPD_{TiO} is independent of the material the tip is made of. Topography, friction and surface potential data were obtained in the very same STO surface area, obtaining a $\Delta CPD_{STO} \approx 45 \pm 10mV$, thus implying $CPD_{SrO} >$ CPD_{TiO}. As the stearic acid selectively adsorbs on the TiO_2 terminated regions, we can estimate the change in surface potential of these regions referred to that of non-covered SrO terminated patches, i.e., using ΔCPD_{STO} as a reference, regardless of the actual absolute value of CPD_{SrO}.

Topographic and KPFM maps for a stearic acid covered STO substrate were recorded simultaneously. From the topographic relief and its corresponding surface potential profiles on the stearic acid terminated TiO_2 terraces (CPD_{AcTiO}), we estimate a $\Delta CPD_{AcTiO-SO} = CPD_{AcTiO}$ - $CPD_{SrO} \approx 70 \pm 25mV$. In addition, we estimated the contact potential difference ($\Delta CPD_{AcTiOSO} \approx 110 \pm 15mV$) by the shift of the electrostatic parabolas obtained with the 3D approach measured on specific point locations (see details in [12]). In the frame of the present work, it is not the exact specific absolute value of $\Delta CPD_{AcTiO-SO}$ which is relevant for our purposes, but the fact that for the

bare substrate we found $\mathrm{CPD}_{SrO} > \mathrm{CPD}_{TiO}$, whereas after stearic acid adsorption $\mathrm{CPD}_{SrO} < \mathrm{CPD}_{AcTiO}$. This fact allows us to clearly conclude that the specific stearic acid adsorption increases locally the contact surface potential of the substrate.

6.6 Conclusions

Self-separation of the surface chemical terminations has been effectively handled to obtain surfaces with laterally modulated properties capable of hosting low dimensional nanostructures of complex oxides.

A simple high-temperature annealing process, by which SrO terminations on SrTiO3(001) surface spontaneously form ordered nanotrenches along step-edges separated by atomically flat terraces in between has been exposed. Exploiting the difference in adatom sticking coefficients between both chemical terminations, the chemically self-patterned $SrTiO_3$(001) surfaces can be used as template for fabrication of oxide nanostructures by selective nucleation and growth.

It has been shown that chemical terminations existing at the as-received LSAT and STO surfaces self-arrange after the appropriate thermal treatment to form a pattern of AO and BO_2 terraces separated by $\frac{1}{2}$ u.c high steps. The width of the AO and BO_2 regions, being of about some tens of nanometers (50-150 nm) on the crystals analyzed, can be controlled by substrate miscut. Associated with the topographic nanostructuration, the chemical terminations of the substrates promote the formation of a patterned surface potential. We have found that the SP contrast at surfaces of STO and LSAT substrates originates from the different electrostatic potential at the (possibly reconstructed and adsorbate-covered) AO and BO_2 terminations.

LSAT substrates thermally treated display atomically flat surface morphology and self-separation of the chemical terminations with tunable period. The resulting chemically modulated surface has been subsequently used for selective growth of other oxide that preserve the lateral ordering of the substrate. Moreover, an appropriate combination of substrate and epilayer allows promoting 3D epitaxial growth that ultimately produces self-ordered arrays of dots ($SrRuO_3$).

The surface potential profiles of LSMO grown on STO and LSAT mimic those of the substrate. Therefore, the substrate acts not only as template determining morphology and chemical termination but also allows for the lateral tuning of the electrical proper-

ties of the film surface. We have also shown that the SP contrast of the nanostructured LSMO films is slightly smaller than that of the underlying substrates; however, ΔSP shows only a weak dependence on the nature of the substrate, suggesting that the distinct (La, SrO) and (Mn$_{O2}$) termination might have the dominant role on the SP contrast. Interestingly, the SP contrast at the surface of BTO appears reversed with respect to that of the underlying substrate and electrode, suggesting that the ferroelectric nature of BTO, e.g. via a hypothetical selective formation of ferroelectric domains on distinct polar terminations, could play a role.

The conductance maps of all the investigated surfaces indicate that higher conductance is ubiquitously associated to higher SP. This close correlation, that is interpreted by arguing that high(low) surface potential correspond to low(high) local electrostatic barrier height, should contribute to a better understanding of the KPFM on insulating materials.

CHAPTER 7

FUTURE WORK AND OUTLOOK

In this work, we have shown strategies for producing self-assembled monolayers (SAMs) exhibiting bi-chemically terminated organic surfaces on Au(111) substrates and molecular growth on complex oxides, in particular STO(001). In addition to SFM measurements, we carried out Infrared Reflection Absorption Spectroscopy (IRRAS) and Polarization modulation-infrared reflection-absorption spectroscopy (PM-IRRAS) experiments on Au(111) surfaces after immersing for prolonged times from 100μM MMTA solutions (acetic acid and THF solvents) plus annealing . A characteristic feature of this method is the surface selection rule, which states that only the vibrations with a component of the transition dipole moment aligned perpendicular to the surface plane can interact with the incident light and contribute to the infrared spectrum [206]. In this sense, our objective was clearly to find the fingerprint of the terminated surfaces SAMs (-SH and -COOH) by means of the spectroscopic technique. Despite the effort, for instance, by preparing samples in minimum contact with the environment or shifting the frequency in PM-module to enhance details for the region of interest, the SH vibrational band was not observed.

7.1 IRRAS and PM-IRRAS

PM-IRRAS studies performed by Rajalingam et al. [207] revealed that the SH vibrational band observed at 2565 cm^{-1} and 2572 cm^{-1} in the bulk are absent in the IR spectra recorded for the benzylmercaptan (BM) and para-cyanobenzylmercaptan (pCBM) SAMs, respectively. They suggested that the BM and pCBM thiol adsorb on gold as thiolate. SH-terminated surfaces studied by Niklewski et al. [208] by means of IR spectroscopy did not record the SH vibrational band either, which was associated to its weak transition dipole moment.

7.1 IRRAS and PM-IRRAS

IRRAS and PM-IRRAS spectra were recorded with a Bruker VERTEX 70 FT-IR spectrometer for the signal acquisition from the far IR (15cm^{-1}) to visible (28000cm^{-1}) region, equipped with a Polarization Modulation Accessory (PMA) 50 unit (Bruker Optik GmbH, Germany) which allows recording both IRRAS and PM-IRRAS data. For PM-IRRAS experiments, each sample was placed in the external beam of a Fourier transform infrared (FT-IR) instrument, and reflected light is focused onto a nitrogen-cooled mercury cadmium telluride (MCT) detector at an optimal incident angle of 80-82° relative to the surface normal.
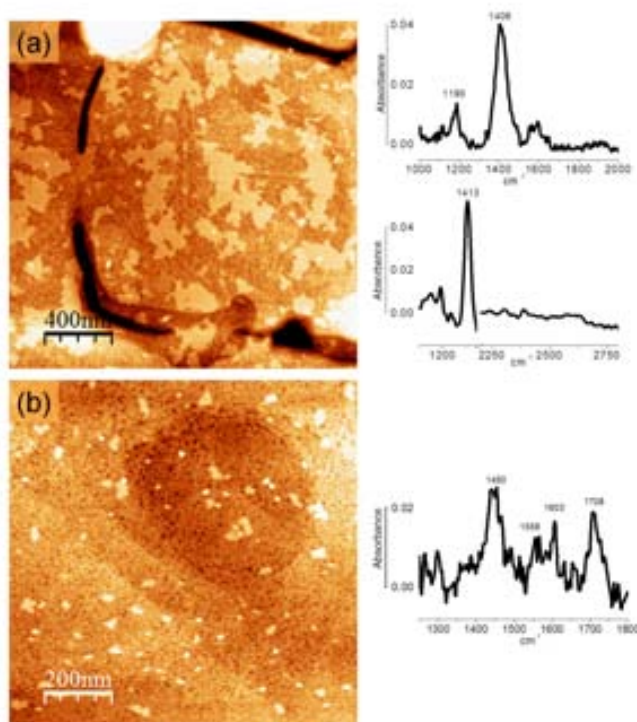
Figure 7.1. SFM topographic image of MMTA islands on Au(111) after immersing from a 100μM acetic acid (a) and THF (b) solution for 16 hours and post-annealing at 115°C for 16 hours. (a, top) PM-IRRAS of the bi-chemically terminated surface after annealing process for 1000-2000 cm^{-1} region and shifting the maximum efficiency for the wave retardation at 1000cm^{-1} to detect the SH stretching mode at 2500cm^{-1} (a, down). (b) Topographic image and IR spectra showing the stretching modes of the carbonyl group at 1450cm^{-1} and 1710cm^{-1} as well as the fingerprint of aromatic rings at 1600cm^{-1}.

In Figure 7.1, we display the PM-IRRAS spectra recorded for -COOH and SH-terminated surfaces on Au(111) substrates plus annealing. IR spectra (a, top) revealed band intensities at $\approx 1200 cm^{-1}$, $\approx 1410 cm^{-1}$ and $\approx 1600 cm^{-1}$. Interestingly, we observed the band located at $1410 cm^{-1}$, closely at $1435 cm^{-1}$ whose value is assigned to the carboxylate symmetric stretch vibration [75, 209]. The presence of bands in the (1200-1300 cm^{-1}) range could indicate formation of ester groups after the formation of SAMs. The width stretch vibration at $\approx 1600 cm^{-1}$ corresponds to the fingerprint of the aromatics rings of the MMTA molecule. IR-retarded spectra recorded at $1000 cm^{-1}$ to enhance details in the range 2000-3000cm^{-1} is displayed (down). The absence of the -SH vibrational band for these type of samples not only suggests that thiol molecules were anchored to the Au(111) surface, but the SH-terminated surface poses a weak transition dipole moment.

The frequency of 1710 cm^{-1} observed in (b) is typical for cyclic dimers of carboxylic acids, this fact provides also support for the presence of a second layer of MMTA hydrogen-bonded to the first layer as proposed Arnold et al. [75]. However, this stretch mode is absent in the IR spectra of (a).

7.2 Selective Growth of Metal Organics

On the another hand, it is known that self-assembled monolayers of molecules on gold can be utilized as chemically sticky surface for attachment of metal clusters and layers, we investigated the possibility that on -COOH or SH-terminated surface bind chemically to the deposited metal atoms. In our first attempt, we used dinuclear copper(II) acetate complexes ($Cu_2(CH_3COO)_4 \bullet 2H_2O$) (hereafter CuAc) on the bi-chemically terminated islands. For each experiment, the CuAc was deposited by immersing the (-SH and COOH)-terminated surfaces Au(111) substrate in 1mM aqueous for 3 hours, 24 hours and 2 days at room temperature in absence of light (see Figure 7.2), described in [10]. We did not observe a selective growth on the (-SH) or (-COOH)-end groups, but 2D and 3D structures were observed by SFM technique. In addition, we performed KPFM, high resolution lateral force and friction experiments on the resulting surface. We propose as future works, depth studies in the theoretical and experimental frame to understand the type of interaction with the surface and

design experiments with CuAc solutions more diluted.
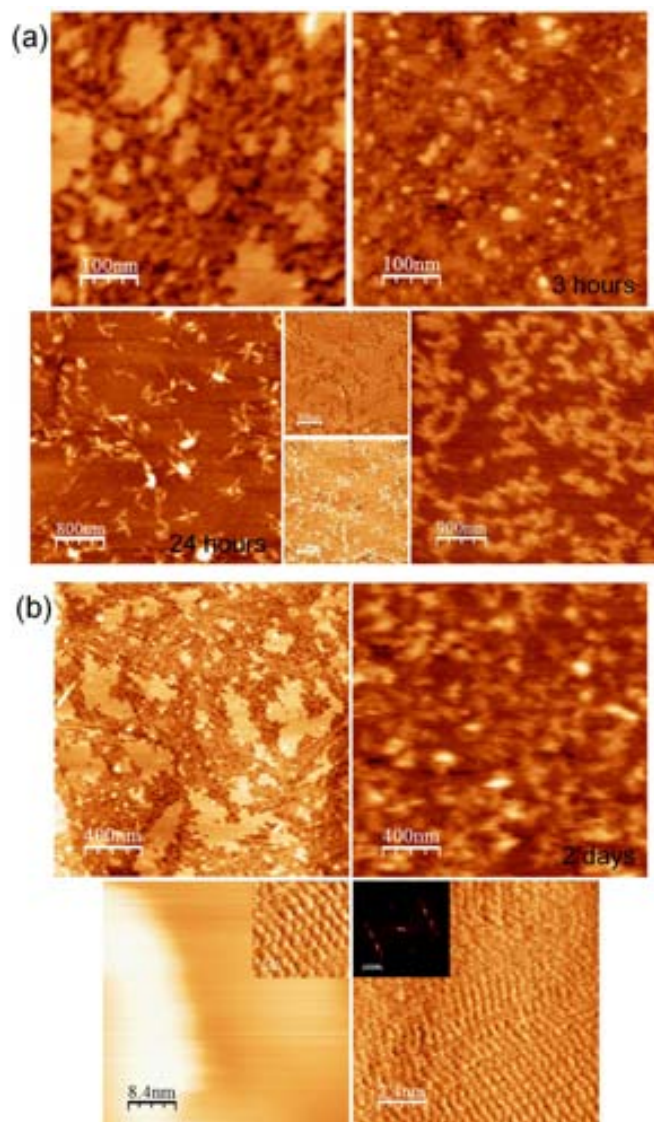
Figure 7.2. (a, b) SFM images of CuAc deposited by immersion on MMTA islands on Au(111). (a, top) Topographic image before (left) and after immersing for 3 hours in CuAc solution of the MMTA islands (right). (down) Topographic image of CuAc after 24 hours, lateral force images(Fw&Bw)(middle) and surface potential image in different region. (b, top) Topographic image before (left) and after immersing for 2 days in CuAc solution (right). (down) magnified topographic image on the formed structure. High resolution image reveals a molecular order as shown FFT (inset).

REFERENCES

[1] J. Chen and M. A. Reed. Electronic transport of molecular systems. *Chemical Physics*, 281(2-3):127–145, 2002. 1

[2] Hadley D. Sikes, John F. Smalley, Stephen P. Dudek, Andrew R. Cook, Marshall D. Newton, Christopher E. D. Chidsey, and Stephen W. Feldberg. Rapid electron tunneling through oligophenylenevinylene bridges. *Science*, 291(5508):1519–1523, 2001. 1, 140

[3] Abraham Nitzan. Electron transmission through molecules and molecular interfaces. *Annual Review of Physical Chemistry*, 52(1):681–750, 2001. 1

[4] Xu Qingmin, Ma Hong, Yip Hinlap, and Alex K-Y Jen. Controlled assembly of large pi-conjugated aromatic thiols on Au(111). *Nanotechnology*, 19(13):X; 11 pages, 2008. 1

[5] Jian Liang and Giacinto Scoles. An analysis of conductive-probe atomic force microscopy applied to the study of electron transport mediating properties of self-assembled monolayers. *The Journal of Physical Chemistry C*, 114(24):10836–10842, 2010. 1

[6] K. Heister, H. T. Rong, M. Buck, M. Zharnikov, M. Grunze, and L. S. O. Johansson. Odd-even effects at the s-metal interface and in the aromatic matrix of biphenyl-substituted alkanethiol self-assembled monolayers. *The Journal of Physical Chemistry B*, 105(29):6888–6894, 2001. 1, 39

[7] P. Cyganik and M. Buck. Polymorphism in biphenyl-based self-assembled monolayers of thiols. *J Am Chem Soc*, 126(19):5960–1, 2004. 1, 37

[8] Hai-Tao Rong, Stefan Frey, Yong-Jie Yang, Michael Zharnikov, Manfred Buck, Mario Wühn, Christof Wöll, and Günter Helmchen. On the importance of the headgroup substrate bond in thiol monolayers: A study of biphenyl-based thiols on gold and silver. *Langmuir*, 17(5):1582–1593, 2001. 1

[9] Nikin Patel, Martyn C. Davies, Mark Hartshorne, Richard J. Heaton, Clive J. Roberts, Saul J. B. Tendler, and Philip M. Williams. Immobilization of protein molecules onto homogeneous and mixed carboxylate-terminated self-assembled monolayers. *Langmuir*, 13(24):6485–6490, 1997. 2

[10] R. Urcuyo, E. Cortés, A. A. Rubert, G. Benitez, M. L. Montero, N. G. Tognalli, A. Fainstein, M. E. Vela, and R. C. Salvarezza. Aromatic and aliphatic thiol self-assembled monolayers on Au: Anchoring and delivering copper species. *The Journal of Physical Chemistry C*, 115(50):24707–24717, 2011. 2, 207

[11] Ketheeswari Rajalingam, Thomas Strunskus, Andreas Terfort, Roland A. Fischer, and Christof Wöll. Metallization of a thiol-terminated organic surface using chemical vapor deposition. *Langmuir*, 24(15):7986–7994, 2008. 2

[12] M. Paradinas, L. Garzon, F. Sanchez, R. Bachelet, D. B. Amabilino, J. Font-cuberta, and C. Ocal. Tuning the local frictional and electrostatic responses of nanostructured *SrTiO3*-surfaces by self-assembled molecular monolayers. *Phys Chem Chem Phys*, 12(17):4452–8, 2010. 2, 176, 192, 201, 202

[13] R. Bachelet. Atomically flat sro-terminated *SrTiO3*(001) substrate. *Appl. Phys. Lett.*, 95(14):141915, 2009. 3

[14] R. Bachelet. Atomically flat sro-terminated *SrTiO3*(001) substrate. *Appl. Phys. Lett.*, 95(14):141915, 2009. 3

[15] G. Binnig, C. F. Quate, and Ch. Gerber. Atomic force microscope. *Physical Review Letters*, 56(9):930, 1986. 5

[16] D. Rugar. Atomic force microscopy. *Phys. Today*, 43(10):23, 1990. 5

[17] W. F. Kolbe, D. F. Ogletree, and M. B. Salmeron. Atomic force microscopy imaging of t4 bacteriophages on silicon substrates. *Ultramicroscopy*, 42-44, Part 2:1113–1117, 1992. doi: 10.1016/0304-3991(92)90411-C. 6

[18] Nanotec™. http://www.nanotec.es. 6, 11

[19] Nanosensors™. http://www.nanosensors.com/. 6, 7

[20] Budgetsensors. http://www.budgetsensors.com/. 6

[21] Bruker. http://www.brukerafmprobes.com/. 6, 7

[22] John E. Sader, James W. M. Chon, and Paul Mulvaney. Calibration of rectangular atomic force microscope cantilevers. *Review of Scientific Instruments*, 70(10):3967–3969, 1999. 8

[23] A. Clifford Charles and P. Seah Martin. The determination of atomic force microscope cantilever spring constants via dimensional methods for nanomechanical analysis. *Nanotechnology*, 16(9):1666, 2005. 8

[24] Christopher P. Green, Hadi Lioe, Jason P. Cleveland, Roger Proksch, Paul Mulvaney, and John E. Sader. Normal and torsional spring constants of atomic force microscope cantilevers. *Review of Scientific Instruments*, 75(6):1988–1996, 2004. 8

[25] NT-MDT. http://www.ntmdttips.com/usa/. 9

[26] I. Horcas. *WSxM*: A software for scanning probe microscopy and a tool for nanotechnology. *Rev. Sci. Instrum.*, 78(1):013705, 2007. 10.1063/1.2432410. 10, 41

[27] Jacob Israelachvili. *Intermolecular and Surface Forces.* Academic Press, London, 1992. 13

[28] C. Argento. Parametric tip model and force-distance relation for hamaker constant determination from atomic force microscopy. *J. Appl. Phys.*, 80(11):6081, 1996. 10.1063/1.363680. 15

[29] T. R. Albrecht, P. Grutter, D. Horne, and D. Rugar. Frequency modulation detection using high-q cantilevers for enhanced force microscope sensitivity. *Journal of Applied Physics*, 69(2):668–673, 1991. 19

[30] Roland Bennewitz. *Fundamentals of Friction and Wear*, volume 1. Springer, 2007. 21

[31] C. Mathew Mate, Gary M. McClelland, Ragnar Erlandsson, and Shirley Chiang. Atomic-scale friction of a tungsten tip on a graphite surface. *Physical Review Letters*, 59(17):1942–1945, 1987. 21

[32] Seizo Morita, Satoru Fujisawa, and Yasuhiro Sugawara. Spatially quantized friction with a lattice periodicity. *Surface Science Reports*, 23(1):1–41, 1996. 21

[33] Y. Martin, C. C. Williams, and H. K. Wickramasinghe. Atomic force microscope-force mapping and profiling on a sub $100\AA$- scale. *Journal of Applied Physics*, 61(10):4723–4729, 1987. 22

[34] Q. Zhong, D. Inniss, K. Kjoller, and V. B. Elings. Fractured polymer/silica fiber surface studied by tapping mode atomic force microscopy. *Surface Science*, 290:L688–L692, 1993. doi: 10.1016/0039-6028(93)90582-5. 22

[35] Hans-Jürgen Butt, Brunero Cappella, and Michael Kappl. Force measurements with the atomic force microscope: Technique, interpretation and applications. *Surface Science Reports*, 59:1–152, 2005. doi: 10.1016/j.surfrep.2005.08.003. 23

[36] Ricardo García and Rubén Pérez. Dynamic atomic force microscopy methods. *Surface Science Reports*, 47:197–301, 2002. doi: 10.1016/S0167-5729(02)00077-8. 23

[37] D. Sarid. The role of adhesion in tapping-mode atomic force microscopy. *Applied Physics A: Materials Science and Processing*, 66:s283–S286, 1998. 23

[38] S. H. Ke, T. Uda, and K. Terakura. Quantity measured in frequency-shift-mode atomic-force microscopy: An analysis with a numerical model. *Physical Review B*, 59(20):13267–13272, 1999. 23

[39] C. Gómez-Navarro, A. Gil, M. Álvarez, P. J. De Pablo, F. Moreno-Herrero, I. Horcas, R. Fernández-Sánchez, J. Colchero, J. Gómez-Herrero, and A. M. Baró. Scanning force microscopy three-dimensional modes applied to the study of the dielectric response of adsorbed *DNA* molecules. *Nanotechnology*, 13(3):314, 2002. 23, 137

[40] Elisa Palacios-Lidón and Colchero Jaime. Quantitative analysis of tip-sample interaction in non-contact scanning force spectroscopy. *Nanotechnology*, 17(21):5491, 2006. 23, 137

[41] C. Munuera., Esther. Barrena, and C. Ocal. Scanning force microscopy three-dimensional modes applied to conductivity measurements through linear-chain organic sams. *Nanotechnology*, 18(12):125505, 2007. 23

[42] Sheng Liao, Yitzhak Shnidman, and Abraham Ulman. Adsorption kinetics of rigid 4-mercaptobiphenyls on gold. *Journal of the American Chemical Society*, 122(15):3688–3694, 2000. doi: 10.1021/ja9905804. 29

[43] D. S. Karpovich and G. J. Blanchard. Direct measurement of the adsorption kinetics of alkanethiolate self-assembled monolayers on a microcrystalline gold surface. *Langmuir*, 10(9):3315–3322, 1994. doi: 10.1021/la00021a066. 29

[44] R. L. David. *Hand Book of Chemistry and Physics.* CRC press, 1998. 79 ed. 30

[45] Younan Xia and George M. Whitesides. Soft lithography. *Angewandte Chemie International Edition*, 37(5):550–575, 1998. 31

[46] John A. Rogers and Ralph G. Nuzzo. Recent progress in soft lithography. *Materials Today*, 8(2):50–56, 2005. doi: 10.1016/S1369-7021(05)00702-9. 31

[47] Younan Xia, Enoch Kim, Xiao-Mei Zhao, John A. Rogers, Mara Prentiss, and George M. Whitesides. Complex optical surfaces formed by replica molding against elastomeric masters. *Science*, 273(5273):347–349, 1996. 31

[48] Enoch Kim, Younan Xia, and George M. Whitesides. Polymer microstructures formed by moulding in capillaries. *Nature*, 376(6541):581–584, 1995. 31

[49] Enoch King, Younan Xia, Xiao-Mei Zhao, and George M. Whitesides. Solvent-assisted microcontact molding: A convenient method for fabricating three-dimensional structures on surfaces of polymers. *Advanced Materials*, 9(8):651–654, 1997. 31

[50] Xiao-Mei Zhao, Younan Xia, and George M. Whitesides. Fabrication of three-dimensional micro-structures: Microtransfer molding. *Advanced Materials*, 8(10):837–840, 1996. 32

[51] Sungil Chung, Yonggwan Im, Jaeyoung Choi, and Haedo Jeong. Microreplication techniques using soft lithography. *Microelectronic Engineering*, 75(2):194–200, 2004. 32

[52] Xinhong Yu, Zhe Wang, Rubo Xing, Shifang Luan, and Yanchun Han. Fabrication of structures with tunable morphologies and sizes by soft molding. *Applied Surface Science*, 252(5):1947–1953, 2005. 32

[53] J. N. Lee, C. Park, and G. M. Whitesides. Solvent compatibility of poly(dimethylsiloxane)-based microfluidic devices. *Anal Chem*, 75(23):6544–54, 2003. 32, 34

[54] M. Morra, E. Occhiello, R. Marola, F. Garbassi, P. Humphrey, and D. Johnson. On the aging of oxygen plasma-treated polydimethylsiloxane surfaces. *Journal of Colloid and Interface Science*, 137(1):11–24, 1990. doi: 10.1016/0021-9797(90)90038-P. 34

[55] J. C. Chang, G. J. Brewer, and B. C. Wheeler. A modified microstamping technique enhances polylysine transfer and neuronal cell patterning. *Biomaterials*, 24(17):2863–70, 2003. 34

[56] Andreas Offenhausser, Simone Bocker-Meffert, Tanja Decker, Rita Helpenstein, Peter Gasteier, Jurgen Groll, Martin Moller, Anna Reska, Susanne Schafer, Petra Schulte, and Angela Vogt-Eisele. Microcontact printing of proteins for neuronal cell guidance. *Soft Matter*, 3(3):290–298, 2007. 34

[57] M. Zharnikov and M. Grunze. Spectroscopic characterization of thiol-derived self-assembling monolayers. *Journal of Physics: Condensed Matter*, 13(49):11333, 2001. 36

[58] Cindra A. Widrig, Carla A. Alves, and Marc D. Porter. Scanning tunneling microscopy of ethanethiolate and n-octadecanethiolate monolayers spontaneously absorbed at gold surfaces. *Journal of the American Chemical Society*, 113(8):2805–2810, 1991. doi: 10.1021/ja00008a001. 36

[59] Ralph G. Nuzzo, Lawrence H. Dubois, and David L. Allara. Fundamental studies of microscopic wetting on organic surfaces. formation and structural characterization of a self-consistent series of polyfunctional organic monolayers. *Journal of the American Chemical Society*, 112(2):558–569, 1990. 36

[60] Lou Strong and George M. Whitesides. Structures of self-assembled monolayer films of organosulfur compounds adsorbed on gold single crystals: electron diffraction studies. *Langmuir*, 4(3):546–558, 1988. doi: 10.1021/la00081a009. 36

[61] P. Fenter, P. Eisenberger, and K. S. Liang. Chain-length dependence of the structures and phases of $CH3(CH2)_{n-1} SH$ self-assembled on $Au(111)$. *Physical Review Letters*, 70(16):2447–2450, 1993. 36

[62] Harrell Sellers, Abraham Ulman, Yitzhak Shnidman, and James E. Eilers. Structure and binding of alkanethiolates on gold and silver surfaces: implications for self-assembled monolayers. *Journal of the American Chemical Society*, 115(21):9389–9401, 1993. 36

[63] Henrik Grönbeck, Alessandro Curioni, and Wanda Andreoni. Thiols and disulfides on the $Au(111)$ surface: The headgroup-gold interaction. *Journal of the American Chemical Society*, 122(16):3839–3842, 2000. 36

[64] Tomohiro Hayashi, Yoshitada Morikawa, and Hisakazu Nozoye. Adsorption state of dimethyl disulfide on $Au(111)$: Evidence for adsorption as thiolate at the bridge site. *The Journal of Chemical Physics*, 114(17):7615–7621, 2001. 36

[65] Yashar Yourdshahyan and Andrew M. Rappe. Structure and energetics of alkanethiol adsorption on the $Au(111)$ surface. *The Journal of Chemical Physics*, 117(2):825–833, 2002. 37

[66] Peter Maksymovych, Dan C. Sorescu, and Jr. Yates, John T. Gold-adatom-mediated bonding in self-assembled short-chain alkanethiolate species on the $Au(111)$ surface. *Physical Review Letters*, 97(14):146103, 2006. 37

[67] Natalie A. Kautz and S. Alex Kandel. Alkanethiol/$Au(111)$ self-assembled monolayers contain gold adatoms: Scanning tunneling microscopy before and after reaction with atomic hydrogen. *Journal of the American Chemical Society*, 130(22):6908–6909, 2008. 37

[68] D. C. Jackson, A. Chaudhuri, T. J. Lerotholi, D. P. Woodruff, Robert G. Jones, and V. R. Dhanak. The local adsorption site of methylthiolate on $Au(111)$: Bridge or atop? *Surface Science*, 603(5):807–813, 2009. 37

[69] Li-Jun Wan, Mimi Terashima, Hiroyuki Noda, and Masatoshi Osawa. Molecular orientation and ordered structure of benzenethiol adsorbed on gold (111). *The Journal of Physical Chemistry B*, 104(15):3563–3569, 2000. 37

[70] Claus Fuxen, Waleed Azzam, Ralf Arnold, Gregor Witte, Andreas Terfort, and Christof Wöll. Structural characterization of organothiolate adlayers on gold: The case of rigid, aromatic backbones. *Langmuir*, 17(12):3689–3695, 2001. doi: 10.1021/la0018033. 37, 62

[71] S. Frey, V. Stadler, K. Heister, W. Eck, M. Zharnikov, M. Grunze, B. Zeysing, and A. Terfort. Structure of thioaromatic self-assembled monolayers on gold and silver. *Langmuir*, 17(8):2408–2415, 2001. doi: 10.1021/la001540c. 37, 39

[72] M. David Curtis, Jie Cao, and Jeff W. Kampf. Solid-state packing of conjugated oligomers:from pi-stacks to the herringbone structure. *Journal of the American Chemical Society*, 126(13):4318–4328, 2004. 37

[73] R. F. Dou, X. C. Ma, L. Xi, H. L. Yip, K. Y. Wong, W. M. Lau, J. F. Jia, Q. K. Xue, W. S. Yang, H. Ma, and A. K. Jen. Self-assembled monolayers of aromatic thiols stabilized by parallel-displaced pi-pi stacking interactions. *Langmuir*, 22(7):3049–56, 2006. 37

[74] Karsten Walzer, Eike Marx, Neil C. Greenham, Robert J. Less, Paul R. Raithby, and Kurt Stokbro. Scanning tunneling microscopy of self-assembled phenylene ethynylene oligomers on $Au(111)$ substrates. *Journal of the American Chemical Society*, 126(4):1229–1234, 2004. 37

[75] R. Arnold, W. Azzam, A. Terfort, and C. Woll. Preparation, modification, and crystallinity of aliphatic and aromatic carboxylic acid terminated self-assembled monolayers. *Langmuir*, 18(10):3980–3992, 2002. 37, 38, 91, 96, 207

[76] T. Ishida, W. Mizutani, Y. Aya, H. Ogiso, S. Sasaki, and H. Tokumoto. Electrical conduction of conjugated molecular *SAMs* studied by conductive atomic force microscopy. *Journal of Physical Chemistry B*, 106(23):5886–5892, 2002. 38, 133

[77] Hans-Jörg Himmel, Andreas Terfort, and Christof Wöll. Fabrication of a carboxyl-terminated organic surface with self-assembly of functionalized terphenylthiols: The importance of hydrogen bond formation. *Journal of the American Chemical Society*, 120(46):12069–12074, 1998. doi: 10.1021/ja981872s. 38, 48, 91

[78] Ralf Arnold. *Struktur und Ordnung selbstordnender Monolagen aliphatischer und aromatischer Thiole auf Goldoberflächen.* PhD thesis, Ruhr-Universität Bochum, 2001. 38

[79] Eyal Sabatani, Joseph Cohen-Boulakia, Merlin Bruening, and Israel Rubinstein. Thioaromatic monolayers on gold: a new family of self-assembling monolayers. *Langmuir*, 9(11):2974–2981, 1993. 39

[80] Yu-Tai Tao, Chien-Ching Wu, Ji-Yang Eu, Wen-Ling Lin, Kwang-Chen Wu, and Chun-hsien Chen. Structure evolution of aromatic-derivatized thiol monolayers on evaporated gold. *Langmuir*, 13(15):4018–4023, 1997. 39

[81] W. Azzam, A. Bashir, A. Terfort, T. Strunskus, and Ch Woll. Combined *STM* and *FTIR* characterization of terphenylalkanethiol monolayers on *Au*(111): effect of alkyl chain length and deposition temperature. *Langmuir*, 22(8):3647–55, 2006. 39, 40

[82] W. Azzam, P. Cyganik, G. Witte, M. Buck, and Ch Wöll. Pronounced odd-even changes in the molecular arrangement and packing density of biphenyl-based thiol sams: A combined stm and leed study. *Langmuir*, 19(20):8262–8270, 2003. 39, 40

[83] Kaoru Tamada, Masahiko Hara, Hiroyuki Sasabe, and Wolfgang Knoll. Surface phase behavior of n-alkanethiol self-assembled monolayers adsorbed on *Au*(111): An atomic force microscope study. *Langmuir*, 13(6):1558–1566, 1997. 40

[84] Schreiber Frank. Structure and growth of self-assembling monolayers. *Progress in Surface Science*, 65(5-8):151–257, 2000. 40

[85] Mathematica. http://www.wolfram.com/mathematica/. 47

[86] Farid Bensebaa, Raluca Voicu, Laurent Huron, Thomas H. Ellis, and Erik Kruus. Kinetics of formation of long-chain n-alkanethiolate monolayers on polycrystalline gold. *Langmuir*, 13(20):5335–5340, 1997. 56

[87] C. Munuera, J. Puigmarti-Luis, M. Paradinas, L. Garzon, D. B. Amabilino, and C. Ocal. Layer-by-layer electropeeling of organic conducting material imaged in real time. *Small*, 5(2):214–20, 2009. 59

[88] R. Aguilar-Sanchez, G. J. Su, M. Homberger, U. Simon, and Th Wandlowski. Structure and electrochemical characterization of $4-methyl-4'-(n-mercaptoalkyl)$biphenyls on $Au(111)$. *The Journal of Physical Chemistry C*, 111(46):17409–17419, 2007. doi: 10.1021/jp0744634. 62

[89] Gujin J. Su, Rocio Aguilar-Sanchez, Zhihai Li, Ilya Pobelov, Melanie Homberger, Ulrich Simon, and Thomas Wandlowski. Scanning tunneling microscopy and spectroscopy studies of $4-methyl-4'-(n-mercaptoalkyl)$biphenyls on $Au(111)$. *Chemphyschem*, 8(7):1037–1048, 2007. 62

[90] E. Delamarche, B. Michel, H. Kang, and Ch Gerber. Thermal stability of self-assembled monolayers. *Langmuir*, 10(11):4103–4108, 1994. 65

[91] Carmen Munuera. *Structural, mechanical and transport characterization of organosulphur nanoscaled molecular films*. PhD thesis, Universidad Autonoma de Madrid, 2007. 65, 116, 129

[92] M. Radmacher. Measuring the elastic properties of biological samples with the afm. *Engineering in Medicine and Biology Magazine, IEEE*, 16(2):47–57, 1997. 73

[93] V. I. Uricanu, M. H. G. Duits, R. M. F. Nelissen, M. L. Bennink, and J. Mellema. Local structure and elasticity of soft gelatin gels studied with atomic force microscopy. *Langmuir*, 19(20):8182–8194, 2003. 73

[94] H. Bei, E. P. George, J. L. Hay, and G. M. Pharr. Influence of indenter tip geometry on elastic deformation during nanoindentation. *Physical Review Letters*, 95(4):045501, 2005. 73

[95] C. Munuera, E. Barrena, and C. Ocal. Deciphering structural domains of alkanethiol self-assembled configurations by friction force microscopy. *J Phys Chem A*, 111(49):12721–6, 2007. 73, 93, 100

[96] M. A. Monclus, T. J. Young, and D. Di Maio. Afm indentation method used for elastic modulus characterization of interfaces and thin layers. *Journal of Materials Science*, 45(12):3190–3197, 2010. 73

[97] M. Radmacher, M. Fritz, and P. K. Hansma. Imaging soft samples with the atomic force microscope: gelatin in water and propanol. *Biophysical Journal*, 69(1):264–270, 1995. 73

[98] Ian N. Sneddon. The relation between load and penetration in the axisymmetric boussinesq problem for a punch of arbitrary profile. *International Journal of Engineering Science*, 3(1):47–57, 1965. 76

[99] E. Delamarche, H. Schmid, A. Bietsch, N. B. Larsen, H. Rothuizen, B. Michel, and H. Biebuyck. Transport mechanisms of alkanethiols during microcontact printing on gold. *The Journal of Physical Chemistry B*, 102(18):3324–3334, 1998. 90

[100] Laurent Libioulle, Alexander Bietsch, Heinz Schmid, Bruno Michel, and Emmanuel Delamarche. Contact-inking stamps for microcontact printing of alkanethiols on gold. *Langmuir*, 15(2):300–304, 1998. 90

[101] Nicholas J. Brewer, Ben D. Beake, and Graham J. Leggett. Friction force microscopy of self-assembled monolayers: Influence of adsorbate alkyl chain length, terminal group chemistry, and scan velocity. *Langmuir*, 17(6):1970–1974, 2001. 93

[102] Susannah C. Clear and Paul F. Nealey. Chemical force microscopy study of adhesion and friction between surfaces functionalized with self-assembled monolayers and immersed in solvents. *Journal of Colloid and Interface Science*, 213(1):238–250, 1999. 93

[103] Eric W. van der Vegte, Andrei Subbotin, Georges Hadziioannou, Peter R. Ashton, and Jon A. Preece. Nanotribological properties of unsymmetrical n-dialkyl sulfide monolayers on gold:effect of chain length on adhesion, friction, and imaging. *Langmuir*, 16(7):3249–3256, 2000. 93

[104] Martin H. Müser, Ludgar Wenning, and Mark O. Robbins. Simple microscopic theory of amontons's laws for static friction. *Physical Review Letters*, 86(7):1295–1298, 2001. 93

[105] R. Bennewitz, E. Gnecco, T. Gyalog, and E. Meyer. Atomic friction studies on well-defined surfaces. *Tribology Letters*, 10(1):51–56, 2001. 93

[106] E. Barrena, C. Ocal, and M. Salmeron. Molecular packing changes of alkanethiols monolayers on $Au(111)$ under applied pressure. *The Journal of Chemical Physics*, 113(6):2413–2418, 2000. 93

[107] Markos Paradinas, Carmen Munuera, Christophe Silien, Manfred Buck, and Carmen Ocal. Heterogeneous nanotribological response of polymorphic self-assembled monolayers arising from domain and phase dependent friction. *Physical Chemistry Chemical Physics*, 15(4):1302–1309, 2013. 94, 100

[108] John-Bruce D. Green, Mark T. McDermott, Marc D. Porter, and Lorraine M. Siperko. Nanometer-scale mapping of chemically distinct domains at well-defined organic interfaces using frictional force microscopy. *The Journal of Physical Chemistry*, 99(27):10960–10965, 1995. 94

[109] Nicholas J. Brewer, Trevor T. Foster, Graham J. Leggett, Morgan R. Alexander, and Eoghan McAlpine. Comparative investigations of the packing and ambient stability of self-assembled monolayers of alkanethiols on gold and silver by friction force microscopy. *The Journal of Physical Chemistry B*, 108(15):4723–4728, 2004. 94

[110] Z. H. Xia, J. Lou, and W. A. Curtin. A multiscale experiment on the tribological behavior of aligned carbon nanotube/ceramic composites. *Scripta Materialia*, 58(3):223–226, 2008. 94

[111] K. L. Johnson, K. Kendall, and A. D. Roberts. Surface energy and the contact of elastic solids. *Proceedings of the Royal Society of London. A. Mathematical and Physical Sciences*, 324(1558):301–313, 1971. 95

[112] B. V. Derjaguin, V. M. Muller, and Yu P. Toporov. Effect of contact deformations on the adhesion of particles. *Journal of Colloid and Interface Science*, 53(2):314–326, 1975. doi: 10.1016/0021-9797(75)90018-1. 95

[113] J. te Riet, T. Smit, J. W. Gerritsen, A. Cambi, J. A. Elemans, C. G. Figdor, and S. Speller. Molecular friction as a tool to identify functionalized alkanethiols. *Langmuir*, 26(9):6357–66, 2010. 96

[114] M. Liley, D. Gourdon, D. Stamou, U. Meseth, T. M. Fischer, C. Lautz, H. Stahlberg, H. Vogel, N. A. Burnham, and C. Duschl. Friction anisotropy and asymmetry of a compliant monolayer induced by a small molecular tilt. *Science*, 280(5361):273–5, 1998. 100

[115] C. Munuera and C. Ocal. Real time scanning force microscopy observation of a structural phase transition in self-assembled alkanethiols. *J Chem Phys*, 124(20):206102, 2006. 100

[116] Musun Kwak and Hitoshi Shindo. Frictional force microscopic detection of frictional asymmetry and anisotropy at (1014) surface of calcite. *Physical Chemistry Chemical Physics*, 6(1):129–133, 2004. 100

[117] J. J. Segura, A. Verdaguer, L. Garzon, E. Barrena, C. Ocal, and J. Fraxedas. Strong water-mediated friction asymmetry and surface dynamics of zwitterionic solids at ambient conditions: L-alanine as a case study. *The Journal of Chemical Physics*, 134(12):124705–9, 2011. 100

[118] Hendrik Bluhm, Udo D. Schwarz, and Roland Wiesendanger. Origin of the ferroelectric domain contrast observed in lateral force microscopy. *Physical Review B*, 57(1):161–169, 1998. 102

[119] Bharat Bhushan and Huiwen Liu. Nanotribological properties and mechanisms of alkylthiol and biphenyl thiol self-assembled monolayers studied by *AFM*. *Physical Review B*, 63(24):245412, 2001. 121, 122

[120] James L. Wilbur, Hans A. Biebuyck, John C. MacDonald, and George M. Whitesides. Scanning force microscopies can image patterned self-assembled monolayers. *Langmuir*, 11(3):825–831, 1995. doi: 10.1021/la00003a025. 129

[121] G. Bar, S. Rubin, A. N. Parikh, B. I. Swanson, T. A. Zawodzinski, and M. H. Whangbo. Scanning force microscopy study of patterned monolayers of alkanethiols on gold. importance of tip-sample contact area in interpreting force modulation and friction force microscopy images. *Langmuir*, 13(3):373–377, 1997. doi: 10.1021/la960935m. 129

[122] C. Munuera, O. Shekhah, H. Wang, C. Wöll, and C. Ocal. The controlled growth of oriented metal-organic frameworks on functionalized surfaces as followed by scanning force microscopy. *Phys Chem Chem Phys*, 10(48):7257–61, 2008. 129

[123] Sergey Kubatkin, Andrey Danilov, Mattias Hjort, Jerome Cornil, Jean-Luc Bredas, Nicolai Stuhr-Hansen, Per Hedegard, and Thomas Bjornholm. Single-electron transistor of a single organic molecule with access to several redox states. *Nature*, 425(6959):698–701, 2003. 10.1038/nature02010. 133

[124] James G. Kushmerick, David B. Holt, Steven K. Pollack, Mark A. Ratner, John C. Yang, Terence L. Schull, Jawad Naciri, Martin H. Moore, and Ranganathan Shashidhar. Effect of bond-length alternation in molecular wires. *Journal of the American Chemical Society*, 124(36):10654–10655, 2002. 133

[125] Wenyong Wang, Takhee Lee, and M. A. Reed. Mechanism of electron conduction in self-assembled alkanethiol monolayer devices. *Physical Review B*, 68(3):035416, 2003. 133, 137

[126] C. Zhou, M. R. Deshpande, M. A. Reed, L. Jones Ii, and J. M. Tour. Nanoscale metal/self-assembled monolayer/metal heterostructures. *Applied Physics Letters*, 71(5):611–613, 1997. 133

[127] J. Chen, L. C. Calvet, M. A. Reed, D. W. Carr, D. S. Grubisha, and D. W. Bennett. Electronic transport through metal-1,4-phenylene diisocyanide-metal junctions. *Chemical Physics Letters*, 313:741–748, 1999. doi: 10.1016/S0009-2614(99)01060-X. 133

[128] Seong Ho Choi, Chad Risko, M. Carmen Ruiz Delgado, BongSoo Kim, Jean-Luc Breidas, and C. Daniel Frisbie. Transition from tunneling to hopping transport in long, conjugated oligo-imine wires connected to metals. *Journal of the American Chemical Society*, 132(12):4358–4368, 2010. 134, 146

[129] Jeremy M. Beebe, BongSoo Kim, J. W. Gadzuk, C. Daniel Frisbie, and James G. Kushmerick. Transition from direct tunneling to field emission in metal-molecule-metal junctions. *Physical Review Letters*, 97(2):026801, 2006. 134, 147

[130] Yoram Selzer, Lintao Cai, Marco A. Cabassi, Yuxing Yao, James M. Tour, Theresa S. Mayer, and David L. Allara. Effect of local environment on molecular conduction: Isolated molecule versus self-assembled monolayer. *Nano Letters*, 5(1):61–65, 2004. doi: 10.1021/nl048372j. 134

[131] John G. Simmons. Electric tunnel effect between dissimilar electrodes separated by a thin insulating film. *Journal of Applied Physics*, 34(9):2581–2590, 1963. 134

[132] J. Simmons. Generalized formula for the electric tunnel effect between similar electrodes separated by a thin insulating film. *J. Appl. Phys.*, 34(6):1793, 1963. 10.1063/1.1702682. 134

[133] J. G. Simmons. Conduction in thin dielectric films. *Journal of Physics D: Applied Physics*, 4(5):613, 1971. 134

[134] S. Hong, R. Reifenberger, W. Tian, S. Datta, J. I. Henderson, and C. P. Kubiak. Molecular conductance spectroscopy of conjugated, phenyl-based molecules on Au(111): the effect of end groups on molecular conduction. *Superlattices and Microstructures*, 28(4):289–303, 2000. 134

[135] Obadiah G. Reid, Keiko Munechika, and David S. Ginger. Space charge limited current measurements on conjugated polymer films using conductive atomic force microscopy. *Nano Letters*, 8(6):1602–1609, 2008. 135

[136] Jianwei Zhao and Jason J. Davis. Molecular electron transfer of protein junctions characterized by conducting atomic force microscopy. *Colloids and Surfaces B: Biointerfaces*, 40:189–194, 2005. 135

[137] C. Ramirez, L. Garzón, P. Miranzo, M. I. Osendi, and C. Ocal. Electrical conductivity maps in graphene nanoplatelet/silicon nitride composites using conducting scanning force microscopy. *Carbon*, 49(12):3873–3880, 2011. 135

[138] F. Yamada. Control of surface morphology and electronic properties of iii-v semiconductors using molecular modification. *J. Vac. Sci. Technol. B*, 28(4):C5F28, 2010. 135

[139] R. Lloyd Carroll and Christopher B. Gorman. The genesis of molecular electronics. *Angewandte Chemie International Edition*, 41(23):4378–4400, 2002. 135

[140] Yves Martin, David W. Abraham, and H. Kumar Wickramasinghe. High-resolution capacitance measurement and potentiometry by force microscopy. *Applied Physics Letters*, 52(13):1103–1105, 1988. 135

[141] V. Palermo, M. Palma, and P. Samorì. Electronic characterization of organic thin films by kelvin probe force microscopy. *Advanced Materials*, 18(2):145–164, 2006. 135, 159

[142] Stephen D. Evans, Edward Urankar, Abraham Ulman, and Nancy Ferris. Self-assembled monolayers of alkanethiols containing a polar aromatic group: effects of the dipole position on molecular packing, orientation, and surface wetting properties. *Journal of the American Chemical Society*, 113(11):4121–4131, 1991. 135

[143] Paul C. Rusu and Geert Brocks. Surface dipoles and work functions of alkylthiolates and fluorinated alkylthiolates on Au(111). *The Journal of Physical Chemistry B*, 110(45):22628–22634, 2006. 135, 169, 171

[144] G. H. Enevoldsen, T. Glatzel, M. C. Christensen, J. V. Lauritsen, and F. Besenbacher. Atomic scale kelvin probe force microscopy studies of the surface potential variations on the $TiO2$ (110) surface. *Physical Review Letters*, 100(23):236104, 2008. 135

[145] Antoine Hinaut, Adeline Pujol, Florian Chaumeton, David Martrou, André Gourdon, and Sébastien Gauthier. An *NC-AFM* and *KPFM* study of the adsorption

of a triphenylene derivative on *KBr*(001). *Beilstein Journal of Nanotechnology*, 3:221–229, 2012. 135

[146] Maria L. Sushko and Alexander L. Shluger. Dipole-dipole interactions and the structure of self-assembled monolayers. *The Journal of Physical Chemistry B*, 111(16):4019–4025, 2007. 135

[147] Stephen D. Evans and Abraham Ulman. Surface potential studies of alkyl-thiol monolayers adsorbed on gold. *Chemical Physics Letters*, 170(5-6):462–466, 1990. 136

[148] R. Erik Holmlin, Rainer Haag, Michael L. Chabinyc, Rustem F. Ismagilov, Adam E. Cohen, Andreas Terfort, Maria Anita Rampi, and George M. Whitesides. Electron transport through thin organic films in metal - insulator - metal junctions based on self-assembled monolayers. *Journal of the American Chemical Society*, 123(21):5075–5085, 2001. 137

[149] Ayelet Vilan. Analyzing molecular current-voltage characteristics with the simmons tunneling model:scaling and linearization. *The Journal of Physical Chemistry C*, 111(11):4431–4444, 2007. doi: 10.1021/jp066846s. 137

[150] Michael Galperin, Abraham Nitzan, Slawomir Sek, and Marcin Majda. Asymmetric electron transmission across asymmetric alkanethiol bilayer junctions. *Journal of Electroanalytical Chemistry*, 550-551:337–350, 2003. 137

[151] M. A. Reed, C. Zhou, C. J. Muller, T. P. Burgin, and J. M. Tour. Conductance of a molecular junction. *Science*, 278(5336):252–254, 1997. 137

[152] C. Kergueris, J. P. Bourgoin, S. Palacin, D. Esteve, C. Urbina, M. Magoga, and C. Joachim. Electron transport through a metal-molecule-metal junction. *Physical Review B*, 59(19):12505–12513, 1999. 137

[153] L. A. Bumm, J. J. Arnold, T. D. Dunbar, D. L. Allara, and P. S. Weiss. Electron transfer through organic molecules. *The Journal of Physical Chemistry B*, 103(38):8122–8127, 1999. 137

[154] C. Munuera, Esther Barrena, and C. Ocal. Scanning force microscopy three-dimensional modes applied to conductivity measurements through linear-chain organic sams. *Nanotechnology*, 18(12):125505, 2007. 137

[155] Harry O. Finklea and Dwight D. Hanshew. Electron-transfer kinetics in organized thiol monolayers with attached pentaammine(pyridine)ruthenium redox centers. *Journal of the American Chemical Society*, 114(9):3173–3181, 1992. 140

[156] David J. Wold and C. Daniel Frisbie. Fabrication and characterization of metal - molecule - metal junctions by conducting probe atomic force microscopy. *Journal of the American Chemical Society*, 123(23):5549–5556, 2001. doi: 10.1021/ja0101532. 140, 143

[157] X. D. Cui, X. Zarate, J. Tomfohr, O. F. Sankey, A. Primak, A. L. Moore, T. A. Moore, D. Gust, G. Harris, and S. M. Lindsay. Making electrical contacts to molecular monolayers. *Nanotechnology*, 13(1):5, 2002. 140

[158] Yoram Selzer, Adi Salomon, and David Cahen. The importance of chemical bonding to the contact for tunneling through alkyl chains. *The Journal of Physical Chemistry B*, 106(40):10432–10439, 2002. doi: 10.1021/jp026324m. 140

[159] Stephen Creager, C. J. Yu, Cindy Bamdad, Steve O :'Connor, Tanya MacLean, Eric Lam, Yoochul Chong, Gary T. Olsen, Jiye Luo, Michael Gozin, and Jon Faiz Kayyem. Electron transfer at electrodes through conjugated molecular wire bridges. *Journal of the American Chemical Society*, 121(5):1059–1064, 1999. 140

[160] Sandra B. Sachs, Stephen P. Dudek, Richard P. Hsung, Lawrence R. Sita, John F. Smalley, Marshall D. Newton, Stephen W. Feldberg, and Christopher E. D. Chidsey. Rates of interfacial electron transfer through pi-conjugated spacers. *Journal of the American Chemical Society*, 119(43):10563–10564, 1997. 140

[161] Takao Ishida, Wataru Mizutani, Nami Choi, Uichi Akiba, Masamichi Fujihira, and Hiroshi Tokumoto. Structural effects on electrical conduction of conjugated molecules studied by scanning tunneling microscopy. *The Journal of Physical Chemistry B*, 104(49):11680–11688, 2000. doi: 10.1021/jp0018450. 140

[162] Hongmei Liu, Nan Wang, Jianwei Zhao, Yan Guo, Xing Yin, Freddy Y. C. Boey, and Hua Zhang. Length-dependent conductance of molecular wires and contact resistance in metalmoleculemetal junctions. *Chemphyschem*, 9(10):1416–1424, 2008. 140

[163] Fu-Ren F. Fan, Jiping Yang, Lintao Cai, David W. Price, Shawn M. Dirk, Dmitry V. Kosynkin, Yuxing Yao, Adam M. Rawlett, James M. Tour, and Allen J. Bard. Charge transport through self-assembled monolayers of compounds of interest in molecular electronics. *Journal of the American Chemical Society*, 124(19):5550–5560, 2002. doi: 10.1021/ja017706t. 140

[164] G. Heimel, L. Romaner, J. L. Bredas, and E. Zojer. Odd-even effects in self-assembled monolayers of omega-(biphenyl-4-yl)alkanethiols: a first-principles study. *Langmuir*, 24(2):474–82, 2008. 140

[165] A. Salomon, D. Cahen, S. Lindsay, J. Tomfohr, V. B. Engelkes, and C. D. Frisbie. Comparison of electronic transport measurements on organic molecules. *Advanced Materials*, 15(22):1881–1890, 2003. 140

[166] H. McNally, D. B. Janes, B. Kasibhatla, and C. P. Kubiak. Electrostatic investigation into the bonding of poly(phenylene) thiols to gold. *Superlattices and Microstructures*, 31(5):239–245, 2002. 158

[167] B. de Boer, A. Hadipour, M. M Mandoc, T. van Woudenbergh, and P. W M Blom. Tuning of metal work functions with self-assembled monolayers. *Advanced Materials*, 17(5):621–625, 2005. 169, 173

[168] Dana M. Alloway, Amy L. Graham, Xi Yang, Anoma Mudalige, Ramon Colorado, Vicki H. Wysocki, Jeanne E. Pemberton, T. Randall Lee, Ronald J. Wysocki, and Neal R. Armstrong. Tuning the effective work function of gold and silver using w-functionalized alkanethiols: Varying surface composition through dilution and choice of terminal groups. *The Journal of Physical Chemistry C*, 113(47):20328–20334, 2009. 169

[169] Dana M. Alloway, Michael Hofmann, Darrin L. Smith, Nadine E. Gruhn, Amy L. Graham, Ramon Colorado, Vicki H. Wysocki, T. Randall Lee, Paul A. Lee, and Neal R. Armstrong. Interface dipoles arising from self-assembled monolayers on gold: *UV-Photoemission* studies of alkanethiols and partially fluorinated alkanethiols. *The Journal of Physical Chemistry B*, 107(42):11690–11699, 2003. 169

[170] V. De Renzi, R. Rousseau, D. Marchetto, R. Biagi, S. Scandolo, and U. del Pennino. Metal work-function changes induced by organic adsorbates: A combined experimental and theoretical study. *Physical Review Letters*, 95(4):046804, 2005. 170

[171] Ante Bilic, Jeffrey R. Reimers, Noel S. Hush, and Jurgen Hafner. Adsorption of ammonia on the gold (111) surface. *The Journal of Chemical Physics*, 116(20):8981–8987, 2002. 170

[172] D. M. Taylor. Developments in the theoretical modelling and experimental measurement of the surface potential of condensed monolayers. *Advances in Colloid and Interface Science*, 87:183–203, 2000. doi: 10.1016/S0001-8686(99)00044-5. 171

[173] C. R. Martin and I. A. Aksay. Submicrometer-scale patterning of ceramic thin films. *Journal of Electroceramics*, 12(1-2):53–68, 2004. 175

[174] C. S. Ganpule, A. Stanishevsky, Q. Su, S. Aggarwal, J. Melngailis, E. Williams, and R. Ramesh. Scaling of ferroelectric properties in thin films. *Applied Physics Letters*, 75(3):409–411, 1999. 175

[175] Catalin Harnagea, Marin Alexe, Jorg Schilling, Jinsub Choi, Ralf B. Wehrspohn, Dietrich Hesse, and Ulrich Gosele. Mesoscopic ferroelectric cell arrays prepared by imprint lithography. *Applied Physics Letters*, 83(9):1827–1829, 2003. 175

[176] Zixiao Pan, Nasim Alem, Tao Sun, and Vinayak P. Dravid. Site-specific fabrication and epitaxial conversion of functional oxide nanodisk arrays. *Nano Letters*, 6(10):2344–2348, 2006. 175

[177] S. Clemens, T. Schneller, A. van?der?Hart, F. Peter, and R. Waser. Registered deposition of nanoscale ferroelectric grains by template-controlled growth. *Advanced Materials*, 17(11):1357–1361, 2005. 175

[178] Catherine Y. Han, Gerold A. Willing, Zhili Xiao, and H. Hau Wang. Control of the anodic aluminum oxide barrier layer opening process by wet chemical etching. *Langmuir*, 23(3):1564–1568, 2006. 175

[179] Woo Lee, Ran Ji, Ulrich Gosele, and Kornelius Nielsch. Fast fabrication of long-range ordered porous alumina membranes by hard anodization. *Nat Mater*, 5(9):741–747, 2006. 175

[180] Paul M. te Riele, Guus Rijnders, and Dave H. A. Blank. Ferroelectric devices created by pressure modulated stencil deposition. *Applied Physics Letters*, 93(23):233109–3, 2008. 175

[181] Johannes V. Barth, Giovanni Costantini, and Klaus Kern. Engineering atomic and molecular nanostructures at surfaces. *Nature*, 437(7059):671–679, 2005. 176

[182] O. Marchenko and J. Cousty. Molecule length-induced reentrant self-organization of alkanes in monolayers adsorbed on $Au(111)$. *Physical Review Letters*, 84(23):5363–5366, 2000. 176

[183] Esther Barrena, Dimas G. de Oteyza, Stefan Sellner, Helmut Dosch, J. Oriol Ossó, and Bernd Struth. In situ study of the growth of nanodots in organic heteroepitaxy. *Physical Review Letters*, 97(7):076102, 2006. 176

[184] J. de la Figuera, M. A. Huerta-Garnica, J. E. Prieto, C. Ocal, and R. Miranda. Fabrication of magnetic quantum wires by step-flow growth of cobalt on copper surfaces. *Applied Physics Letters*, 66(8):1006–1008, 1995. 176

[185] Christian Teichert. Self-organization of nanostructures in semiconductor heteroepitaxy. *Physics Reports*, 365:335–432, 2002. 176

[186] R. Bachelet, F. Sánchez, J. Santiso, C. Munuera, C. Ocal, and J. Fontcuberta. Self-assembly of $SrTiO3(001)$ chemical-terminations: A route for oxide-nanostructure fabrication by selective growth. *Chemistry of Materials*, 21(12):2494–2498, 2009. 176, 179, 184, 187, 201

[187] R. Bachelet, F. Sanchez, F. J. Palomares, C. Ocal, and J. Fontcuberta. Atomically flat sro-terminated $SrTiO3(001)$ substrate. *Applied Physics Letters*, 95(14):141915–3, 2009. 176, 187

[188] Josée E. Kleibeuker, Gertjan Koster, Wolter Siemons, David Dubbink, Bouwe Kuiper, Jeroen L. Blok, Chan-Ho Yang, Jayakanth Ravichandran, Ramamoorthy Ramesh, Johan E. ten Elshof, Dave H. A. Blank, and Guus Rijnders. Atomically defined rare-earth scandate crystal surfaces. *Advanced Functional Materials*, 20(20):3490–3496, 2010. 176, 187

[189] A. P. Ramirez. Colossal magnetoresistance. *Journal of Physics: Condensed Matter*, 9(39):8171, 1997. 177

[190] N. Bickel, G. Schmidt, K. Heinz, and K. Müller. Ferroelectric relaxation of the $SrTiO3(100)$ surface. *Physical Review Letters*, 62(17):2009–2011, 1989. 177

[191] Tokihisa Hikita, Takashi Hanada, Masahiro Kudo, and Maki Kawai. Structure and electronic state of the tio2 and sro terminated $SrTiO3(100)$ surfaces. *Surface Science*, 287-288, Part 1:377–381, 1993. 177

[192] A. Ikeda, T. Nishimura, T. Morishita, and Y. Kido. Surface relaxation and rumpling of $TiO2$-terminated $SrTiO3$(001) determined by medium energy ion scattering. *Surface Science*, 433-435:520–524, 1999. 177

[193] G. Charlton, S. Brennan, C. A. Muryn, R. McGrath, D. Norman, T. S. Turner, and G. Thornton. Surface relaxation of $SrTiO3$(001). *Surface Science*, 457(1-2):L376–L380, 2000. 177

[194] P. A. W. van der Heide, Q. D. Jiang, Y. S. Kim, and J. W. Rabalais. X-ray photoelectron spectroscopic and ion scattering study of the $SrTiO3$(001) surface. *Surface Science*, 473(1-2):59–70, 2001. 177

[195] W. Maus-Friedrichs, M. Frerichs, A. Gunhold, S. Krischok, V. Kempter, and G. Bihlmayer. The characterization of $SrTiO3$(001) with *MIES*, *UPS(HeI)* and first-principles calculations. *Surface Science*, 515(2-3):499–506, 2002. 177

[196] T. Ohnishi, K. Shibuya, M. Lippmaa, D. Kobayashi, H. Kumigashira, M. Oshima, and H. Koinuma. Preparation of thermally stable TiO_2-terminated $SrTiO3$(100) substrate surfaces. *Applied Physics Letters*, 85(2):272–274, 2004. 181

[197] M. Esser, K. Morgenstern, G. Rosenfeld, and G. Comsa. Dynamics of vacancy island coalescence on $Ag(111)$. *Surface Science*, 402-404:341–345, 1998. 182

[198] J. de la Figuera, J. E. Prieto, C. Ocal, and R. Miranda. Creation and motion of vacancy islands on solid surfaces: A direct view. *Solid State Communications*, 89(9):815–818, 1994. 182

[199] Gertjan Koster, Guus Rijnders, Dave H. A. Blank, and Horst Rogalla. Surface morphology determined by (001) single-crystal $SrTiO3$ termination. *Physica C: Superconductivity*, 339(4):215–230, 2000. 182

[200] Carmen Ocal, Romain Bachelet, Luis Garzón, Massimiliano Stengel, Florencio Sánchez, and Josep Fontcuberta. Nanoscale laterally modulated properties of oxide ultrathin films by substrate termination replica through layer-by-layer growth. *Chemistry of Materials*, 24(21):4177–4184, 2012. 183, 190, 191, 192, 193

[201] Koichiro Iwahori, Shunji Watanabe, Maki Kawai, Kei Kobayashi, Hirofumi Yamada, and Kazumi Matsushige. Effect of water adsorption on microscopic friction force on $SrTiO3$(001). *Journal of Applied Physics*, 93(6):3223–3227, 2003. 185

[202] R. Bachelet, C. Ocal, L. Garzon, J. Fontcuberta, and F. Sanchez. Conducted growth of $SrRuO3$ nanodot arrays on self-ordered $LSAT$(001) surfaces. *Applied Physics Letters*, 99(5):051914–3, 2011. 186, 188

[203] Tsuyoshi Ohnishi, Kazuhiro Takahashi, Masashi Nakamura, Masashi Kawasaki, Mamoru Yoshimoto, and Hideomi Koinuma. A-site layer terminated perovskite substrate: $NdGaO3$. *Applied Physics Letters*, 74(17):2531–2533, 1999. 189

[204] Hannes Guhl, Wolfram Miller, and Karsten Reuter. Water adsorption and dissociation on $SrTiO3$(001) revisited: A density functional theory study. *Physical Review B*, 81(15):155455, 2010. 194

[205] Chet Carter, Michael Brumbach, Carrie Donley, Richard D. Hreha, Seth R. Marder, Benoit Domercq, SeungHyup Yoo, Bernard Kippelen, and Neal R. Armstrong. Small molecule chemisorption on indium-tin oxide surfaces: Enhancing probe molecule electron-transfer rates and the performance of organic light-emitting diodes . *The Journal of Physical Chemistry B*, 110(50):25191–25202, 2006. 201

[206] Hoffmann Friedrich M. Infrared reflection-absorption spectroscopy of adsorbed molecules. *Surface Science Reports*, 3:107–192, 1983. 205

[207] K. Rajalingam, L. Hallmann, T. Strunskus, A. Bashir, C. Woll, and F. Tuczek. Self-assembled monolayers of benzylmercaptan and para-cyanobenzylmercaptan on gold: surface infrared spectroscopic characterization. *Physical Chemistry Chemical Physics*, 12(17), 2010. 205

[208] A. Niklewski, W. Azzam, T. Strunskus, R. A. Fischer, and Ch Woll. Fabrication of self-assembled monolayers exhibiting a thiol-terminated surface. *Langmuir*, 20(20):8620–4, 2004. 205

[209] Frederik Tielens, Dominique Costa, Vincent Humblot, and Claire-Marie Pradier. Characterization of w-functionalized undecanethiol mixed self-assembled monolayers on Au(111): A combined polarization modulation infrared reflection - absorption spectroscopy/x-ray photoelectron spectroscopy/periodic density functional theory study. *The Journal of Physical Chemistry C*, 112(1):182–190, 2007. doi: 10.1021/jp074023c. 207